ISIM & ISWIM 2025

20-22 November 2025

Bucharest, Romania

www.isimconference.eu

NATIONAL UNIVERSITY OF SCIENCE AND TECHNOLOGY POLITEHNICA BUCHAREST
Center for Research and Training in Innovative Techniques of Applied Mathematics in Engineering "*Traian Lalescu*" (CiTi)
&
FACULTY OF INDUSTRIAL ENGINEERING AND ROBOTICS

BOOK OF ABSTRACTS ISIM & ISWIM

International Symposium & International Student Workshop on Interdisciplinary Mathematics in the CiTi areas

Volume IV

ISSN-L 2821 – 8779

2025
BUCHAREST, ROMANIA

ISIM & ISWIM 2025

The National University of Science and Technology POLITEHNICA Bucharest (NUSTPB)- Center for Research and Training in Innovative Applied Mathematics Techniques in Engineering "Traian Lalescu" (CiTi), in partnership with the **Romanian Mathematical Society** and with the support of the **Faculty of Industrial Engineering and Robotics** and the **Faculty of Applied Sciences**, under the auspices of the **Ministry of Education and Research**, is honored to invite you to participate in the **4th Edition of the International Symposium & International Student Workshop on Interdisciplinary Mathematics (ISIM & ISWIM)**.

The symposium welcomes professors, researchers, and students from Romania and abroad and aims to foster collaboration, dialogue, and dissemination of original research works and innovative ideas in CiTi interdisciplinary areas and applications, including but not limited to: **Fractional Calculus, Wavelet Analysis, Evolutionary Algorithms, Data Analysis and Information Security, Game Theory - including Quantum, Partial and Ordinary Differential Equations, Mathematical Statistics, Graph Theory, Non-classical sets (algebraic and topological aspects), Generalized matrices and applications, AI Algorithms for Autonomous Robots, Research in Mathematics Education.**

Keynote Speakers:

- **Jorge Jimenez URROZ**, Universidad Politécnica de Madrid, Spain
- **Radu STATE**, University of Luxembourg, Luxembourg
- **Ion TURCANU**, Luxembourg Institute of Science and Technology, Luxembourg
- **Ștefan CRUCEANU**, "Gheorghe Mihoc - Caius Iacob" Institute of Mathematical Statistics and Applied Mathematics, Romanian Academy, Romania
- **Cristian DOICIN**, National University of Science and Technology POLITEHNICA Bucharest, Romania
- **Emil SIMION**, National University of Science and Technology POLITEHNICA Bucharest, Romania

Symposium Contact
E-mail: office@isimconference.eu
Website: https://isimconference.eu

Antonela Toma

University POLITEHNICA of Bucharest, Romania

Cristian Doicin

Faculty of Industrial Engineering and Robotics

BOUNDARY VALUE PROBLEMS FOR FRACTIONAL DIFFERENTIAL INCLUSIONS WITH CAPUTO-HADAMARD TYPE DERIVATIVE

Abdelaziz OUALID[1], Samira HAMANI[2]

[1,2]Abdelhamid Ibn Badis University Mostaganem, Department of Mathematics and Computer Science, ACSY Team-Laboratory of Pure and Applied Mathematics,
Faculty SEI-BP 227/118 Mostaganem 27000, Algeria.

Corresponding author email: abdelaziz.oualid.etu@univ-mosta.dz [1]

samira.hamani@univ-mosta.dz [2]

Abstract

In this manuscript, we discuss the existence of solutions in a Banach space of boundary value problem for Caputo-Hadamard fractional differential inclusions.

Key words*: fractional differential inclusion; Caputo-Hadamard fractional derivate; fixed point theorem; Mönch's fixed point theorem; Kuratowski measure of noncompactness.*

.

1. INTRODUCTION

The Fractional calculus has evolved into an important and interesting field of research in view of its numerous applications in technical and applied sciences. The mathematical modeling of many real world phenomena based on fractional-order operators is regarded as better and improved than the one depending on integer-order operators. In particular, fractional calculus has played a significant role in the recent development of special functions and integral transforms, signal processing, control theory, bioengineering and biomedical, viscoelasticity, finance, stochastic processes, wave and diffusion phenomena, plasma physics, social sciences, etc. For further details and applications.

The history of quantum calculus(QC) dates back to the work of the British mathematician Frank Hilton Jackson. In 1910, he gave a new definition of the derivative, by which the basic principles of quantum calculus. Jackson removed the concept of limit from the definition of the derivative and introduced two types of operators, namely q-derivative and h-derivative. Of course, q-derivative's growth was higher than h-derivative and it didn't take long for it to enter the field of Fractional Calculus. Fractional q-derivative has both the a dvantages of Fractional Calculus and due to the discreteness of the space, it provides the possibility of using the computer in solving and simulating complex equations. For the same reason, in the last decade, q-derivative has received a lot of attention from researchers and many articles have been published in this field. On the other hand, Set-Valued mappings, namely Multifunction, have interesting features whose properties have been investigated from different aspects and recently used in modeling due to their ability to interpret physical phenomena with shock.

2. CONTENT

This article deals the existence of solutions for boundary value problems for fractional order differential inclusions. We consider the boundary-value problem
.

$$ {}_{\mathrm{H}}^{\mathrm{c}}\mathrm{D}^{\alpha}\, y(t) \in F\big(t, y(t)\big), \quad \text{for almost all } \mathrm{t} \in \mathrm{J} = [1, \mathrm{T}],\ 0 < \alpha \leq 1 \quad (1.1) $$

$$ \mathrm{a}y(1) = c, \quad (1.2) $$

Where $\mathrm{T} > 0$, $q \in [0,1]$ and ${}_{\mathrm{H}}^{\mathrm{c}}\mathrm{D}^{\alpha}$ is the Caputo-Hadamard fractional derivative, $\mathrm{F} : \mathrm{J} \times \Re \to \wp(\Re)$ is a multivalued map, $\wp(\Re)$ is the family of all nonamply subsets of $\Re$ and $a, c \in \Re$.

3. CONCLUSIONS

In this paper, we present existence results for the problems (1)–(2) in the case where the right hand side is convex-valued. This result relies on the set-valued analog of Mönch's fixed point theorem combined with the technique of measure of noncompactness. Recently, this has proved to be a valuable tool in studying fractional differential equations and inclusions in Banach spaces;

4. REFERENCES

[1] N. Guerraiche, S. Hamani and J.Henderson, Boundary value problems for Differential Inclusions with Integral and Anti-periodie Conditions, Communication on Applied Nonlinear Analyses 23(2016), 3,33-46

ON THE LMI FEASIBILITY IN ANALYZING THE STABILITY OF 2D DYNAMICAL SYSTEMS. THE CASE OF SYSTEMS ARISING FROM EXCITABLE MEDIA

Adela IONESCU[1]

[1]University of Craiova, 13 A.I. Cuza, Craiova, Romania

adelajaneta2015@gmail.com

Abstract
Construction of a Control Lyapunov Function (CLF) for a nonlinear system is generally a difficult problem, but once a CLF is found, stabilization of the system is straight-forward. The present paper focuses on the efficiency of using linear matrix inequalities (LMIs) and convex programming in process control applications. Mathematical models arising from excitable media are taken into account.

Key words*: mixing flow; kinematics; linear matrix inequality; convex programming; Lyapunov inequality.*

1. INTRODUCTION

A very wide variety of problems arising in system and control theory can be reduced to a few standard convex or quasi-convex optimization problems involving linear matrix inequalities (LMIs).
The types of problems where LMIs are implied are widespread, including:

- construction of quadratic Lyapunov functions for stability and performance analysis of linear differential inclusions;
- synthesis of state-feedback and quadratic Lyapunov functions for stochastic and delay systems.

A linear matrix inequality (LMI) is a convex constraint. Consequently, optimization problems with convex objective functions and LMI constraints are solvable relatively efficiently with software. The form of an LMI is quite general. Linear inequalities, convex quadratic inequalities, matrix norm inequalities, and various constraints from control theory such as Lyapunov and Riccati inequalities *can all be written as LMIs.*
A LMI has the following form:

$$F(x) = F_0 + \sum_{i=1}^{m} x_i F_i \ > 0, \ \ x \in R^m, \ \ F_i \in R^{nxn} \tag{1}$$

where F(x) is a positive definite matrix, and the symetric matrices F_i are fixed, x being the variable. Thus, F(x) is an affine funcion of the elements of x.

In this context, a necessary and sufficient condition for the linear system:

$$\dot{x} = Ax \tag{2}$$

to be stable is the existence of a Lyapunov function

$$V(x) = x^T P x \tag{3}$$

with P a symetric positive matrix with the derivative negative for all nonzero x, which implies the well known Lyapunov inequality:

$$A^T P + PA < 0 \tag{4}$$

The relation (4) is a LMI, with the variable P.
There are a lot of inequalities and control properties of interest which can be expressed in terms of LMI.
Let us take into account the problem of analyzing the stability of a system like (2), in the form:

$$\dot{x} = Ax, A = \sum_{i=1}^{L} \lambda_i A_i, \ \ \forall \ \lambda_i \geq 0, \sum_{i=1}^{L} \lambda_i = 1 \tag{5}$$

A necessary and sufficient condition for the existence of a quadratic Lyapunov function (3) which proves the stability of (5) is the existence of a positive $P = P^T$ that satisfies

$$\frac{dV(x)}{dt} = \dot{x}^T P x + x^T P \dot{x} < 0, \forall x \neq 0 \tag{6}$$

which implies the system of inequalities

$$A_i^T P + P A_i \ < 0, \forall \ i = 1,2, \dots, L \tag{7}$$

The search of a P satisfying the inequalities (7) is a *LMI feasibility problem* .

2. CONTENT

In this paper the LMI feasibility problem context will be analysed for systems arising from mixing flow dynamics.
In the kinematics of mixing, models are focused on *stretching and folding phenomena* for material elements in a basic fluid, where basic mechanisms can act in simple chaotic flows, and thus some "windows" for some complicated situations are opened.
When approaching the mixing model as a dynamical system, it is convenient to start from the widespread basic 2d mathematical form:

$$\begin{cases} \dot{x_1} = G x_2 \\ \dot{x_2} = KG x_1, \end{cases} \ -1 < K < 1, \ \ G \in R \tag{8}$$

For this system, the solution of the associated Cauchy problem has an interesting geometry: the streamlines correspond to some ellipses for K negative, and to some hyperbolas for K positive.
The stability analysis from the LMI standpoint will be applied both for this system, and for a slightly perturbed form of it, namely

$$\begin{cases} \dot{x_1} = G x_2 + x_1 \\ \dot{x_2} = KG x_1 - x_2 \end{cases} \ -1 < K < 1, \ \ G \in R \tag{9}$$

For the system (9), the construction of a convex hull for the Jacobian of the system is taken into account, since it is a nonlinear system and in the nonlinear case, the construction of the convex hull must be approached.

3. CONCLUSIONS

In the paper it is found that in some feasible conditions for the parameters, the 2d mixing model dynamical system can admit a quadratic Lyapunov function, so it can be stabilized from the LMI standpoint.
In the perturbed form of the system, it is found that for some basic testing values of the matrix P, a set of coefficients can be generated, so that the LMI feasibility problem can be approached. A set of feasible conditions for the parameters is obtained in this case too, which allows the further study of the stability in some other perturbation cases for the mixing model.

VISUAL AI-BASED ASSISTANT FOR ENHANCED DRIVING AWARENESS AND SAFETY

Alexandra-Maria BORȘ[1,4], Simona Mihaela BIBIC[2,4], Andreea MILOSTEANU[3,4]

[1]Faculty of Applied Sciences, National University of Science and Technology POLITEHNICA Bucharest, Romania

[2]Departament of Applied Mathematics, National University of Science and Technology POLITEHNICA Bucharest, Romania

[3]Faculty of Mathematics and Computer Science, University of Bucharest, Romania
[4]Center for Research and Training in Innovative Techniques of Applied Mathematics in Engineering, National University of Science and Technology POLITEHNICA Bucharest, Romania

Corresponding author email: alexandra.bors@stud.fsa.upb.ro, simona.bibic@upb.ro, andreea.milosteanu@s.unibuc.ro

Abstract
This research paper proposes a Visual AI-Based Assistant designed to improve driver awareness and road safety through intelligent monitoring and adaptive feedback. The system uses computer vision and machine learning techniques to analyse facial expressions, eye movement, posture enabling real-time detection of fatigue, distraction and stress while driving. By interpreting behavioural and environmental data, such as blink rate, yawning frequency and sitting posture, the designed driving assistant can send visual and vocal alerts to prevent accidents caused by inattention or tiredness. The systems innovation lies in both internal and external factors providing personalized recommendations for safer driving, such as suggesting rest breaks during high-risk conditions, representing a step toward smarter, more responsible, and safer driving experiences.

Key words*: AI assistant, Computer Vision, Intelligent Transportation Systems, Smart Driving, Machine Learning*

1. INTRODUCTION

Road safety remains one of the most important global challenges, as tiredness, distraction and stress are among the leading causes of traffic accidents. According to recent studies, driver inattention contributes to a significant percentage of fatal crashes each year. As vehicles become increasingly equipped with digital systems, integrating Artificial Intelligence (AI), Machine Learning (ML) into transportation has appeared as a promising approach to enhancing driver awareness and minimizing risk.

In this context, the development of intelligent driver assistance systems has shifted from traditional sensor-based alerts to advanced visual monitoring and predictive analytics. AI technologies enable continuous assessment of human interactions with a variety of factors, allowing the system not to only detect risky situations, but also to anticipate them before they escalate.

2. CONTENT

This research paper proposes the development of an Artificial Intelligence-based Assistant (AIA), see Figure 1, to increase drivers' awareness and boost road safety by monitoring their behavior, physical condition, and the vehicle's interior environment.

The system integrates computer vision and machine learning to evaluate facial expressions and ocular activity (such as blink rate, yawning frequency, and eye closure duration) in order to detect exhaustion and tiredness in real-time.

Also, the AIA provides vocal feedback to alert the driver and prevent accidents caused by inattention or sleep episodes. Beyond detection of fatigue, the system can identify forgotten objects inside the car, such as mobile phones, bags, or even living beings like pets or children, reducing the risk of dangerous mistakes. It can also alert when it detects unsafe behaviors while driving, such as sitting too close to the wheel, driving with only one hand on it, or even with no hands. To further improve situational awareness, the AIA has facial tension analysis by evaluating movements in facial muscles,

the jaw, and eyebrows to identify signs of stress, and it can suggest relaxing actions or audio content to help the driver remain calm and focused.

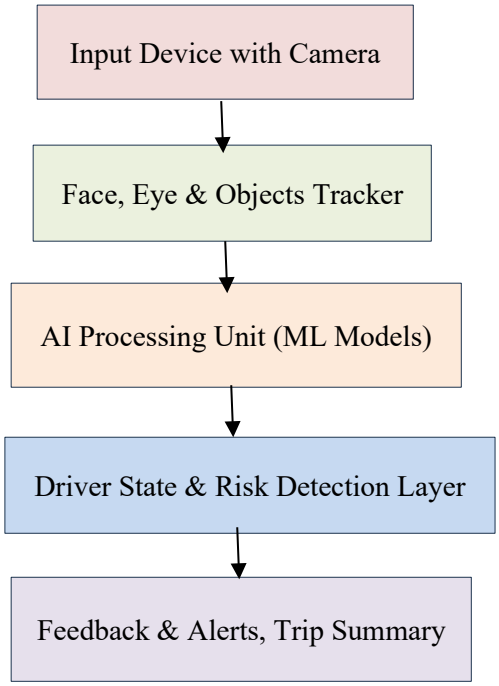

Figure 1: AIA System Architecture Overview

A significant innovation of the system is its ability to combine internal data (driver behaviour and environment) with external factors like nighttime, traffic, and storms. When combined with fatigue indicators, this enables the AIA to provide suggestions such as taking a break to minimize accident risks. Distraction detection is another feature of the system that detects when a driver is not paying attention to the road. After each trip, the assistant generates a performance summary, providing comments on the driver's actions and underlining areas that require improvement for a better awareness of personal driving habits and the promotion of safer practices.

3. CONCLUSIONS

The AIA system represents a step forward in integrating AI and computer vision into intelligent transportation systems. By continuously analysing facial expressions, ocular movements and driver posture, the assistant can significantly improve awareness and prevent accidents caused by human error. This integration allows the AIA to provide personalized feedback fostering proactive and responsible driving habits.

Python-Based Data Fitting for Gaussian, Poisson, and Landau Distributions

Alexandru-Valentin AVRAM[1,2], Ruxandra-Mihaela CEAUȘU[1,2]

[1]Faculty of Applied Sciences, National University of Science and Technology Politehnica Bucharest (NUSTPB), Splaiul Independentei 313, Bucharest, Romania
[2]"Centre for Research and Training in Innovative Techniques of Applied Mathematics in Engineering "Traian Lalescu" (CiTi), National University of Science and Technology Politehnica Bucharest, Splaiul Independentei 313, Bucharest, Romania

Corresponding author email: alexandru.avram1402@upb.ro

Abstract
This paper presents a study on data fitting techniques based on analytical probability distributions, including Gaussian, Poisson, and Landau distributions. The work focuses on comparing these models and evaluating their ability to describe various types of experimental data. The mathematical approach involves parameter estimation, error propagation, and statistical goodness-of-fit analysis, combining concepts from applied mathematics, statistics, and computational modeling. As a practical implementation, a Python-based application with a graphical user interface (GUI) has been developed, allowing users to upload x–y datasets, select the desired fitting function, and visualize both the data and the fitted curve interactively. This tool supports data-driven analysis and enables intuitive exploration of model performance. The results emphasize the importance of mathematical modeling and computational tools in the quantitative interpretation and optimization of experimental measurements.

Key words: data fitting; Gaussian distribution; Poisson statistics; applied mathematics; Python interface; computational modeling.

1. INTRODUCTION

The mathematical modeling of physical phenomena often involves fitting experimental data to analytical distributions that describe underlying stochastic processes. Gaussian, Poisson and Landau distributions are widely used in experimental physics for modeling noise, fluctuations, and asymmetric peak structures. This paper explores these functions both from a mathematical perspective and through computational implementation. The approach is complemented by the development of a Python-based software tool designed to perform real-time data fitting with graphical visualization capabilities.

2. CONTENT

The study focuses on understanding how different probability distributions can describe various types of experimental data. Each function models a specific type of behavior: the Gaussian function represents normal statistical fluctuations, the Poisson distribution describes discrete counting processes, and the Landau distribution is typically used for energy loss in particle detection experiments. By comparing these models, we can observe how different mathematical shapes fit real or simulated datasets and what parameters influence the quality of the fit.

A **Python**-based application with a graphical user interface (GUI) has been developed to allow interactive data analysis. Users can import *(x,y)* datasets, select the desired fitting model, and visualize both the experimental data and fitted curve in real time. The fitting procedure employs numerical optimization methods, including least-squares and maximum-likelihood estimation, to iteratively

determine the parameters that best represent the data. Goodness-of-fit is evaluated using the chi-squared (χ^2) statistic, the coefficient of determination (R^2), and residual analysis.

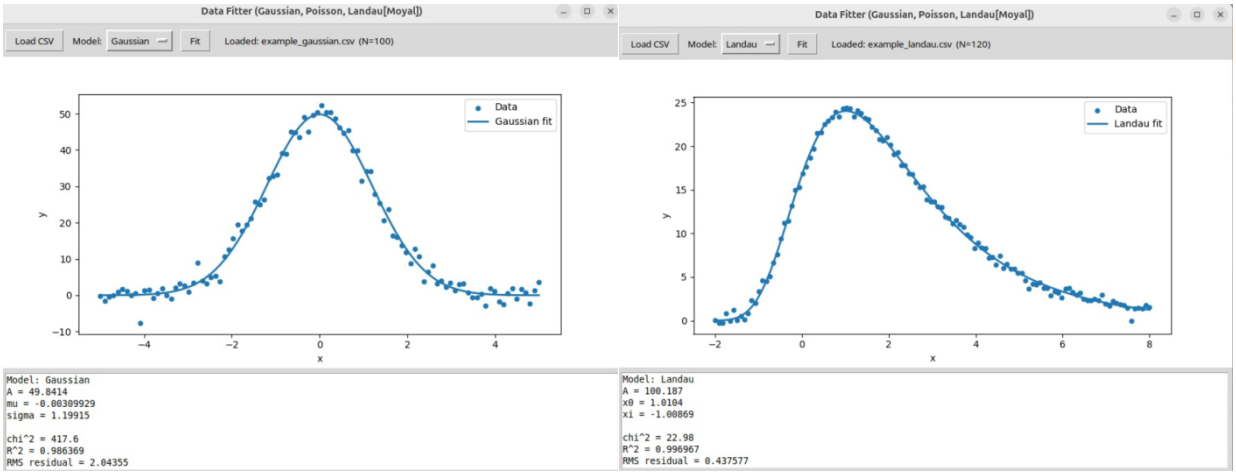

Mathematically, the fitting functions are expressed as:

- **Gaussian**: $f(x) = A \exp\left(-\frac{(x-\mu)^2}{2\sigma^2}\right)$, where A represents the amplitude, μ the mean, and σ the standard deviation controlling the peak width.
- **Poisson**: $f(x) = e^{-\lambda} \cdot \frac{\lambda^x}{x!}$, where k is the observed number of events and λ is the expected mean count per interval.
- **Landau** (Moyal approximation): $f(x) = A\exp\left(-\frac{\lambda+e^{-\lambda}}{2}\right)$, where $\lambda = \frac{x-x_0}{\xi}$, where $A$is the amplitude, x_0 is the most probable value (peak position), ξ controls the width and asymmetry of the distribution, and λ is a dimensionless variable.

In essence, the parameters (A, μ, σ, λ, x_0, ξ) have specific physical and statistical meanings that define the position, width, and scale of each distribution. By adjusting these parameters through optimization, the program finds the best mathematical representation of the given data. This approach not only demonstrates the use of applied mathematics in data analysis but also highlights the importance of computational tools in supporting experimental interpretation and visualization.

Results show that the three models can effectively describe different types of datasets depending on the underlying stochastic process. Gaussian fitting is particularly suitable for normally distributed noise, Poisson accurately captures counting statistics, and Landau provides a reliable representation for skewed peak structures, such as energy-loss measurements in particle detectors.

3. CONCLUSIONS

This study highlights the importance of combining applied mathematics with computational tools in experimental analysis, enabling users to test multiple models and explore data-driven interpretations. Future work may include automated model selection, uncertainty estimation, and extension to additional distributions relevant to experimental physics and engineering applications.

REFERENCES

[1] Hermann Kolanoski & Norbert Wermes**,** *Particle Detectors Fundamentals and Applications,* Oxford University Press, 2020.
[2] W. H. Press, S. A. Teukolsky, W. T. Vetterling, B. P. Flannery, *Numerical Recipes in Python: The Art of Scientific Computing*, 3rd Edition, Cambridge University Press, 2007.

CONVEX FORMULATION OF APPROXIMATE FEEDBACK LINEARIZATION AND CONVERGENCE RATE CONTROL

Alina-Claudia PRECUP, Mircea ȘUȘCĂ, Vlad Mihai MIHALY

Technical University of Cluj-Napoca, 28 Memorandumului Street, 400114 Cluj-Napoca, Romania

Corresponding author email: precup.gr.alina@student.utcluj.ro

Abstract
This paper investigates a mathematical formulation of approximate feedback linearization for nonlinear systems in which the relative degree is not constant or globally defined. To compensate for the residual nonlinearities that arise from this approximation, an auxiliary input is introduced to control the convergence rate. The formulation integrates Lyapunov stability theory with the feedback linearization framework and introduces a control barrier function-type auxiliary input expressed through linear matrix inequalities, resulting in a convex optimization structure. The results show that local asymptotic behavior and a controllable convergence rate can be ensured.

Key words*: approximate feedback linearization; coordinate transformation; Lyapunov stability; convergence rate; control barrier function; linear matrix inequalities.*

1. INTRODUCTION

Exact feedback linearization (EFL) is a fundamental method in nonlinear control, enabling the transformation of a set of first order nonlinear equations into an equivalent set of first order linear differential equations through a suitable coordinate change. To address its limitation in the presence of singularities, this paper proposes an approximate feedback linearization approach that preserves local linear behavior while compensating for residual nonlinearities. The objective is to ensure stability and regulate the convergence rate toward equilibrium through a compensation strategy based on *control barrier functions (CBFs)* and a *linear matrix inequality (LMI)*-based optimization framework. This formulation extends classical linearization techniques to systems where exact cancellation of nonlinearities is not feasible.

2. CONTENT

Consider an n-dimensional, input-affine nonlinear system described by the ordinary differential equation (ODE) model:

$$\Sigma_n: \begin{cases} \dot{x}(t) = f\big(x(t)\big) + g\big(x(t)\big)u(t); \\ y(t) = h(x(t)), \end{cases} \tag{1}$$

where $x(t) \in D \subseteq \mathbb{R}^n$ denotes the state, $u(t) \in \mathbb{R}$ the input and $y(t) \in \mathbb{R}$ the output. Mappings $f, g: D \subseteq \mathbb{R}^n \to \mathbb{R}^n$ and $h: D \subseteq \mathbb{R}^n \to \mathbb{R}$ are assumed to be sufficiently smooth, i.e. $f, g, h \in \mathcal{C}^\infty(D)$.

Theorem 1. The system Σ_n is *feedback linearizable* on an open domain $D_0 \subset D$ if the following conditions hold:

i) The vectors $g_i(x),\ i = \overline{1,n}$ form a basis in $\mathbb{R}^n$ for all $x \in D_0$;

ii) The distribution generated by the vector fields $g_i(x),\ i = \overline{1,n-1}$ is involutive on D_0.

Definition 1. System Σ_n has full *relative degree* at a point $x_e \in D$ if:

i) $\nabla h_i(x) g(x) = 0,\ i = \overline{1,n-1}, \forall x \in \mathcal{V}(x_e)$;

ii) $\nabla h_\rho(x_e) g(x_e) \neq 0$,

where $\mathcal{V}(x_e)$ denotes a neighborhood of x_e and functions $h_i: D \to \mathbb{R}$ are recursively defined as: $h_1(x) = h(x),\ h_{i+1}(x) = \nabla h_i(x)\, f(x), i = \overline{1,n-1}$.

The feedback linearization procedure transforms the nonlinear model Σ_n into an equivalent linear representation through a smooth coordinate change and an input redefinition, defined by

$$z = \Phi(x), \qquad z_i = \Phi_i(x) = \nabla h_{i-1}(x) f(x), \qquad i = \overline{1,n}, \tag{2}$$

where $\Phi : D \to \mathbb{R}^n$ is a diffeomorphism with inverse $x = \Phi_i^{-1}(z)$.
The feedback transformation is expressed as: $v(t) = -\alpha(x)\gamma(x) + \gamma(x)u(t)$, where

$$\gamma(x) = \nabla h_{n-1}(x) g(x), \qquad \alpha(x) = \frac{\nabla h_n(x) f(x)}{\nabla h_{n-1}(x) g(x)}. \tag{3}$$

Under this transformation, system Σ_n takes the *normal form* based on the controllable canonical form:

$$\begin{cases} \dot{z}(t) = A_c\, z(t) + B_c\, v(t); \\ y(t) = C_c\, z(t). \end{cases} \tag{4}$$

Definition 2. A function $b(x)$ is a *control barrier function (CBF)* for the system (1) if there exists a class-$\mathcal{K}$ function δ and a safety set $\mathcal{C} = \{x \in \mathbb{R}^n \mid b(x) \geq 0\}, b \in \mathcal{C}^1(\mathbb{R}^n, \mathbb{R})$, such that

$$\sup_{u \in \mathcal{U}} [\nabla b(x) f(x) + \nabla b(x) g(x)] \geq -\delta\big(b(x)\big), \quad \forall x \in \mathbb{R}^n, \tag{5}$$

and $\nabla b(x) \neq 0$ whenever $b(x) = 0$, which guarantees forward invariance of $\mathcal{C}$ and prevents trajectories from leaving the safe set.
Consider the linearized system in normal form and its autonomous version:

$$\Sigma: \dot{z} = \tilde{A}z + \tilde{B}w + \nabla(z), \qquad \tilde{\Sigma}_{\mathcal{L}}: \dot{z} = \tilde{A}z, \tag{6}$$

where w denotes an auxiliary compensation input, $\nabla(z)$ represents the residual nonlinearities, and the matrices $\tilde{A} \coloneqq A_c + B_c K$, $\tilde{B} \coloneqq B_c$, are defined such that $\tilde{A}$ is Hurwitz; its eigenvalues characterize the convergence rate of the solutions of the corresponding differential equation toward the equilibrium point. Let the quadratic Lyapunov candidate be

$$\tilde{V}(z) = z^T P\, z > 0, \qquad \dot{\tilde{V}}(z) = z^T(\tilde{A}^T P + P\tilde{A})z < 0, \qquad \forall z \neq 0, \tag{7}$$

with $P = P^T \succeq 0$ satisfying the Lyapunov inequality $\tilde{A}^T P + P\tilde{A} \prec 0$. Hence, the equilibrium $point$ of $\tilde{\Sigma}_{\mathcal{L}}$ is exponentially stable.
Including compensation and residuals gives

$$\dot{\tilde{V}}(z) = z^T\big(\tilde{A}^T P + P\tilde{A}\big)z + w^T \tilde{B}^T P z + z^T P \tilde{B} w + \nabla^T(z) P z + z^T P \nabla(z). \tag{8}$$

To ensure stability and safety, the auxiliary input w is computed by solving the convex optimization:

$$min\, t \;\; s.t. \begin{pmatrix} -t & w \\ w & -t \end{pmatrix} \preccurlyeq 0, \tag{9}$$

$$w\varphi(z) + \psi(z) \leq 0, \tag{10}$$

$$(\bar{\varphi}(z)w + \bar{\psi}(z) I(\psi(z)) \leq 0, \tag{11}$$

where $I : \mathbb{R} \to \mathbb{R}$ is the indicator function, $\varphi(z) = \big(2\tilde{B}^T P\big)z$, $\psi(z) = (2\nabla^T(z)P)z$, $\bar{\varphi}(z) = -\big[8\big(\tilde{B}^T P z\big)\big(\tilde{B}^T P\big)\tilde{B}\big]$, $\bar{\psi}(z) = -\Big[8\big(\tilde{B}^T P z\big)\big(\tilde{B}^T P\big)\Big(\tilde{A}z + \nabla(z)\Big)\Big] - \mu \cdot b(z)$.
The linear constraint activation condition (11) is introduced for cases in which $\varphi(z) \approx 0$, which may lead to an ill-posed optimization. To prevent this, it is required that $z \in ker\big(2\tilde{B}^T P\big)$, resulting in the following *CBF-based safety constraint*: : $b(z) = \varphi(z)^2 - \varepsilon$, $b(z) \geq 0$, $\varepsilon > 0$, which activates only when the state approaches regions where the barrier condition becomes critical.

3. CONCLUSIONS

An approximate feedback linearization framework was developed for nonlinear systems with an ill-defined relative degree. Through a locally defined coordinate transformation, the nonlinear dynamics are mapped into an approximate linear representation, while residual terms are compensated by a barrier-type auxiliary input formulated via linear matrix inequalities. This structure ensures local asymptotic stability and provides control over the convergence rate of the solutions of the corresponding differential equation toward the equilibrium point.

Probabilistic Analysis of Skip List Search Complexity

Alin-Teodor Bratu

October 30, 2025

Abstract

Skip lists, introduced by William Pugh in 1990 [1], represent a probabilistic alternative to balanced tree structures such as AVL or Red-Black trees. They achieve expected logarithmic time complexity for search, insertion, and deletion through randomized level assignment. This randomness ensures average efficiency without the structural rigidity or rebalancing overhead of deterministic trees. The present paper develops an analytical framework for determining the expected runtime complexity $T(n)$ of skip list search operations, based on probabilistic modeling of level distributions and traversal dynamics.

A skip list is essentially a hierarchy of linked lists layered on top of one another. The bottom layer contains all the elements in sorted order, while higher levels act as express lanes that skip over multiple elements, allowing faster traversal. Each element is assigned a random height that determines how many levels it appears in, typically following a geometric distribution. Search operations begin at the topmost level and move forward until the target is surpassed, at which point the algorithm drops one level and continues. This combination of horizontal and vertical traversal ensures that, on average, only $O(\log n)$ nodes are visited per search. Insertions and deletions follow a similar pattern, maintaining probabilistic balance without explicit rotations or restructuring.

The proposed analysis decomposes $T(n)$ into contributions from the top level and the lower levels, reflecting the skip list's hierarchical design. The top-level traversal is modeled as $n \cdot p$, where p denotes the probability that an element from the lowest level is also present on the top level. The lower levels are characterized using conditional probabilities p_k, representing the likelihood that an element's maximum level equals k given its presence on level k. This probabilistic framework enables deriving a general formula for the expected execution time, accounting for arbitrary level distributions rather than restricting to geometric ones.

$$\begin{aligned} p_k &= P\big(\text{the max level of the element is } k \,\big|\, \text{the element can be found on level } k\big) \\ &= \frac{P(\text{element is on level } k) - P(\text{element is on level } k+1)}{P(\text{element is on level } k)} \\ &\quad \forall\, k < \text{top level} \end{aligned}$$

The derivation leverages concepts from geometric random variables, which model the number of independent trials until the first success. The skip list's level assignment mimics a sequence of coin flips, where each "heads" indicates an additional level. Consequently, the expected number of elements between nodes of consecutive higher levels follows the same probabilistic pattern. This relationship provides

theoretical justification for the term in the final expression for $T(n)$:

$$\sum_{k=1}^{\text{top}-1} \frac{p_k}{(1-p_k)^2}$$

Combining the top level search with the lower levels search, the formula for $T(n)$ is:

$$T(n) = \frac{1}{2} \cdot (n \cdot p_{\text{top}} + \sum_{k=1}^{top-1} \frac{p_k}{(1-p_k)^2})$$

Empirical and theoretical results confirm that for a geometric distribution with $p = \frac{1}{2}$, the expected runtime approaches $O(\log n)$ ($T(n) = \frac{1}{2} \cdot (n \cdot \frac{1}{n} + \sum_{k=1}^{log_2(n)} \frac{p}{(1-p)^2}) = \frac{1}{2} \cdot (1 + \sum_{k=1}^{log_2(n)} 2) \approx log_2(n)$), consistent with classical findings [1, 2]. Moreover, for degenerate cases such as $p = 1$, where the structure collapses to a simple linked list, the model correctly yields a linear behavior $O(n)$ ($T(n) = \frac{1}{2} \cdot (n \cdot 1 + 0) = \frac{n}{2}$). Additional tests examined decaying probabilities, where the likelihood of promotion decreased for higher levels, and the observed results aligned with the expected complexity. This demonstrates the robustness and generality of the proposed probabilistic decomposition approach.

Skip lists remain a subject of continued research interest due to their simplicity, cache efficiency, and suitability for concurrent environments [3, 4]. Recent studies have expanded their application in distributed systems, memory-efficient data stores, and blockchain indexing [5, 6]. The probabilistic analysis developed in this paper provides a foundational step toward extending the theoretical understanding of such variants, including weighted skip lists, dynamic rebalancing models, and adaptive probability schemes.

In summary, this work refines the mathematical modeling of skip list search complexity by incorporating conditional probabilities for level distribution. The derived formula offers a flexible framework for analyzing both classical and non-geometric skip list configurations, bridging the gap between probabilistic modeling and empirical performance.

References

[1] William Pugh, "Skip lists: a probabilistic alternative to balanced trees," *Communications of the ACM*, vol. 33, no. 6, pp. 668–676, 1990.

[2] Robert Sedgewick and Kevin Wayne, *Algorithms*, 4th Edition, Addison-Wesley, 2011.

[3] Maurice Herlihy and Nir Shavit, *The Art of Multiprocessor Programming*, Morgan Kaufmann, 2012.

[4] H. Sundell and P. Tsigas, "Lock-free and practical doubly linked list-based deques using single-word compare-and-swap," in *Proceedings of the 8th International Conference on Principles of Distributed Systems*, 2004.

[5] J. Aspnes and G. Shah, "Skip graphs," *ACM Transactions on Algorithms*, vol. 3, no. 4, p. 37, 2007.

[6] N. Viennot et al., "SkipChains: Decentralized, tamper-evident logs with skip list replication," in *USENIX Security Symposium*, 2018.

NUMERICAL METHODS FOR SOLVING SYLVESTER AND LYAPUNOV EQUATIONS: CHALLENGES AND IMPLEMENTATION IN MATLAB

Ana-Gabriela TĂMAȘ[1], Mircea ȘUȘCĂ[2]

[1, 2] Technical University of Cluj-Napoca, 28 Memorandumului Street, 400114 Cluj-Napoca, Romania

Corresponding author email: tamas.an.ana@student.utcluj.ro

Abstract

This paper presents a comparative numerical analysis of several methods for solving the Sylvester and Lyapunov equations, which play a fundamental role in stability analysis and control design. The investigated algorithms include the Kronecker product formulation and Schur-based approaches combined with orthogonal transformations: Gram-Schmidt, Householder reflectors and Givens rotations. All methods were implemented in MATLAB and evaluated in terms of computational effort, numerical stability and residual error. The results indicate that Gram-Schmidt produces the largest residuals, making it less suitable for high-precision applications. The Kronecker formulation yields satisfactory results for small-scale matrices but becomes costly as size grows. For medium and large problems, Schur decomposition with Householder reflectors provides improved stability and efficiency, while Givens rotations are advantageous when operating on sparse or structured matrices. The study clarifies accuracy-cost trade-offs and offers practical guidance on selecting appropriate solvers for control-oriented computations.

Key words*: Sylvester equation; Lyapunov equation; numerical methods; MATLAB implementation; Schur decomposition; Householder transformation; Givens rotations; stability analysis.*

1. INTRODUCTION

Matrix equations of the Sylvester and Lyapunov type are fundamental in control theory and numerical linear algebra. The general Sylvester equation

$$- \quad = C \ ,$$

and its particular form, the continuous Lyapunov equation

$$A \quad P \ + \quad = -Q \ ,$$

are essential tools for studying the stability of linear time-invariant systems and for designing state feedback controllers. Their numerical solution requires efficient and stable algorithms, since the conditioning of matrices A and B strongly influences the accuracy of the results. Several numerical approaches have been proposed, including the Kronecker product formulation and Schur-based methods combined with orthogonal transformations such as Gram-Schmidt, Householder and Givens. The objective of this paper is to compare these representative algorithms implemented in MATLAB and to evaluate their efficiency, precision and numerical robustness.

2. CONTENT

The Sylvester equation

$$- \quad = C \ ,$$

with $A \ \in \mathbb{C}^{m \times m}$, $B \ \in \mathbb{C}^{n \times n}$, $C \ \in \mathbb{C}^{m \times}$, $A \ \in \mathbb{C}^{m \times n}$ can be written in vectorized form using the Kronecker product identity

$$(\quad) = (B^{T} \otimes A \ ) \quad (A \ ),$$

which yields

$$(I_n \otimes A - B^T \otimes I_m)\, vec(X) = vec(C). \tag{1}$$

If the matrix $K = (I_n \otimes A - B^T \otimes I_m)$ is nonsingular, the unique solution is $vec(X) = K^{-1}\, vec(C)$.

To increase efficiency, both A and B can be transformed into upper triangular matrices via Schur decomposition:

$$A = Q_A T_A Q_A^T, \qquad B = Q_B T_B Q_B^T,$$

where Q_A, Q_B are orthogonal and T_A, T_B are upper triangular.
Substituting these in the Sylvester equation and defining $Y = Q_A^T X Q_B$ gives:

$$T_A Y - Y T_B = Q_A^T C Q_B.$$

Each element y_{ij} of Y can then be computed recursively as:

$$y_{ij} = \frac{(Q_A^T C Q_B)_{ij} - \sum_{k=i+1}^{m} (T_A)_{ik} y_{kj} + \sum_{k=1}^{j-1} y_{ik} (T_B)_{kj}}{(T_A)_{ii} - (T_B)_{jj}}.$$

The orthogonal matrices Q_A, Q_B are obtained through QR factorization, using one of several orthogonalization techniques:

a) Classical Gram-Schmidt:

$$q_k = a_k - \sum_{j=1}^{k-1} (q_j^T a_k)\, q_j, \qquad q_k := \frac{q_k}{\|q_k\|}.$$

b) Householder Reflectors:

$$H = I - 2\,\frac{v\, v^T}{v^T v}, \qquad v = x + sign(x_1)\, \|x\|\, e_1.$$

c) Givens Rotations:

$$G(i,j,\theta) = \begin{pmatrix} \cos\theta & \sin\theta \\ -\sin\theta & \cos\theta \end{pmatrix}, \qquad \cos\theta = \frac{a_{ii}}{\sqrt{a_{ii}^2 + a_{ji}^2}}, \qquad \sin\theta = \frac{-a_{ji}}{\sqrt{a_{ii}^2 + a_{ji}^2}},$$

$$A' = G^T \cdot A, \qquad a'_{ij} = 0.$$

A particular case of (1) is the continuous-time Lyapunov equation:

$$A^T P + PA = -Q,$$

which can be solved using the same Schur-based framework, by setting $A = A^T, B = -A, C = -Q$.
The uniqueness of the solution to the Sylvester equation is guaranteed if

$$\lambda_i(A) - \lambda_j(B) \neq 0, \qquad \forall i,j.$$

The numerical accuracy of each method can be evaluated by the Frobenius norm of the residual:

$$r = \|AX - XB - C\|_F.$$

3. CONCLUSIONS

The comparative analysis of several numerical methods for solving the Sylvester and Lyapunov matrix equations revealed clear differences in precision and computational effort. The Schur decomposition combined with Householder transformations proved to be the most stable and efficient for larger matrices. The Kronecker formulation remains adequate for small systems, while the Gram-Schmidt method is more affected by round-off errors. Givens rotations offer a balanced compromise between accuracy and cost. The results emphasize that the solver choice should depend on matrix size and conditioning to ensure reliable computations in control applications.

ELEMENTS OF CLIMATE AND RELATED ANALYSIS IN THE CONTEXT OF PSEUDOMATRIX TECHNOLOGIES

Ana-Maria MARIN[1,3,4], Calin-Tudor TOPAN[2,3], Dr. Mihai REBENCIUC[1,3,5], Associate Professor Antonela TOMA[1,3,5]

[1]University Politehnica of Bucharest, 313 Splaiul Independentei, District 6, Bucharest, Romania
[2]Karlsruhe Institute of Technology, 12 Kaiserstrasse, Karlsruhe, Germany
[3]Center for Research and Training in Innovative Techniques of Applied Mathematics in Engineering "Traian Lalescu" (CiTi)
[4]Faculty of Electrical Engineering
[5]Faculty of Applied Sciences

Corresponding author email: ana_maria.marin1007@stud.electro.upb.ro, ubqpy@student.kit.edu , mihai.rebenciuc@upb.ro, antonela.toma@upb.ro

Abstract

Using collections of meteorological data as a starting point, this paper aims to analyse and compare variations of temperature across settlements in the climate zones of Bucharest and Karlsruhe, respectively. The study expands upon the methods of R. di Francesco by refining mathematical formulations and extending the range of datasets and applications. Employing matrices of intervals, we investigate annual temperature variations to identify trends that can support decision-making in engineering, travel, and industrial contexts. The mathematical framework focuses on expanding matrix multiplication principles to better represent geographical and climatic dependencies by making use of the Jaccard Similarity Index. The results demonstrate potential benefits in optimizing material selection, mechanical behaviour, and electrical performance under varying thermal conditions. Overall, geographically oriented matrices of sets represent a promising field of research within pseudomatrix technologies viable for practical implementations.

Key words*:* Pseudomatrix technologies, Matrices of intervals, Climate zones, Jaccard Similarity Index

1. INTRODUCTION

Using collections of data, it is often useful to analyze, compare, and predict temperature conditions in the field of engineering, whether they stem from the environment or from the application itself. This paper aims to build upon our previous study on the methods proposed by R. Di Francesco by expanding the mathematical base and applicability.

2. CONTENT

Applying matrices of sets, specifically intervals, and proceeding with matrix calculations adapted to this datatype, temporal and spatial variations in temperature are mapped out to optimize engineering solutions, travel considerations and more. Mathematically, our scope is refining and expanding the basis of matrix computation. Aspects such as material choice in construction and machine components in 3D can be greatly influenced by temperature, such as in the case of thermal expansion and elastic behaviour.

Using the Jaccard similarity Index, comparative relationships between temperature interval matrices can be instated, and different operational parameters may be accounted for, operating locations may be considered and failure may be prevented. The concepts are to be exemplified using two sets of meteorological data, representing the areas of southern Romania around the Bucharest region and

southwestern Germany respectively, around the Karlsruhe district and the Black Forest region, as well as several nearby key cities.

City \ Month	1	2	3	4	5	6	7	8	9	10	11	12
București	[-2, 6]	[0, 7]	[3, 14]	[8, 20]	[12, 26]	[16, 30]	[19, 33]	[18, 32]	[14, 26]	[9, 19]	[4, 13]	[0, 7]
Otopeni	[-2, 6]	[0, 7]	[3, 13]	[7, 19]	[12, 26]	[16, 30]	[18, 32]	[18, 32]	[14, 26]	[9, 19]	[4, 12]	[0, 7]
Buftea	[-2, 6]	[0, 7]	[3, 13]	[7, 19]	[12, 25]	[16, 30]	[18, 32]	[18, 31]	[14, 26]	[9, 19]	[4, 12]	[0, 7]
Voluntari	[-2, 6]	[0, 7]	[3, 14]	[7, 20]	[12, 26]	[16, 30]	[19, 33]	[18, 32]	[14, 26]	[9, 19]	[4, 12]	[0, 7]
Chitila	[-2, 6]	[0, 7]	[3, 13]	[7, 19]	[12, 26]	[16, 30]	[19, 32]	[18, 32]	[14, 26]	[9, 19]	[4, 12]	[0, 7]
Pantelimon	[-2, 7]	[0, 7]	[3, 14]	[8, 20]	[12, 26]	[16, 30]	[19, 33]	[18, 32]	[14, 26]	[9, 19]	[4, 13]	[0, 7]
Popești-Leordeni	[-1, 7]	[0, 8]	[3, 14]	[8, 20]	[13, 26]	[17, 31]	[19, 33]	[19, 32]	[14, 27]	[9, 20]	[5, 13]	[0, 8]
Măgurele	[-1, 7]	[0, 7]	[3, 14]	[8, 20]	[12, 26]	[17, 31]	[19, 33]	[18, 32]	[14, 27]	[9, 19]	[5, 13]	[0, 7]
Bragadiru	[-2, 6]	[0, 7]	[3, 14]	[8, 20]	[12, 26]	[16, 30]	[19, 33]	[18, 32]	[14, 26]	[9, 19]	[4, 13]	[0, 7]
Domnești	[-2, 6]	[0, 7]	[3, 13]	[7, 20]	[12, 26]	[16, 30]	[19, 33]	[18, 32]	[14, 26]	[9, 19]	[4, 12]	[0, 7]

(1) Bucharest Region

	1	2	3	4	5	6	7	8	9	10	11	12
Karlsruhe	[-12,14]	[-2,17]	[-1,19]	[0,28]	[7,27]	[6,32]	[11,33]	[9,34]	[3,32]	[3,22]	[-3,18]	[-4,13]
Stuttgart	[8,14]	[0,16]	[0,20]	[-1,28]	[7,26]	[9,32]	[12,33]	[11,34]	[4,31]	[4,21]	[-2,19]	[-5,14]
Mannheim	[-13,14]	[-1,18]	[0,20]	[-1,28]	[6,28]	[7,33]	[9,34]	[9,36]	[4,33]	[3,23]	[-2,17]	[-4,13]
Pforzheim	[-10,13]	[-2,16]	[0,19]	[-2,27]	[5,25]	[6,32]	[11,32]	[8,35]	[3,31]	[4,21]	[-4,20]	[-7,15]
Ettlingen	[-12,14]	[-2,18]	[-1,20]	[-1,28]	[6,27]	[6,33]	[11,33]	[9,35]	[3,32]	[3,22]	[-3,19]	[-5,14]
Baden-Baden	[-9,15]	[-1,17]	[0,19]	[-3,29]	[5,28]	[6,31]	[10,33]	[9,33]	[3,31]	[4,22]	[-4,22]	[-7,16]
Heidelberg	[-8,12]	[-1,16]	[1,22]	[-1,25]	[7,26]	[8,31]	[12,31]	[11,32]	[6,32]	[4,21]	[-2,16]	[-3,12]
Heilbronn	[-9,14]	[-1,17]	[-1,20]	[-2,28]	[6,27]	[6,35]	[10,34]	[9,35]	[3,33]	[2,22]	[-2,19]	[-5,13]
Rastatt	[-8,13]	[-1,17]	[0,18]	[0,28]	[8,27]	[7,30]	[11,32]	[11,34]	[4,30]	[4,21]	[-4,19]	[-4,14]
Frankfurt am Main	[-8,14]	[1,16]	[1,20]	[0,28]	[7,28]	[10,32]	[12,33]	[11,35]	[6,33]	[3,22]	[-2,16]	[-3,13]

(2) Karlsruhe Region

The Jaccard Similarity Index is mathematically defined as the ratio between the length of the common temperature interval and the length of the total temperature interval:

$$\mathrm{J(T(i\_1, j),T(i\_2, j)) = \frac{|T(i_1,j) \cap T(i_2,j)|}{|T(i_1,j) \cup T(i_2,j)|}} \qquad (5)$$

The Jaccard Index for 4 cities in the Bucharest region during June 2024 will now be computed and organized within a table:

	Bucharest	Otopeni	Popești-Leordeni	Măgurele
Bucharest	1	1	0.86	0.86
Otopeni	1	1	0.86	0.86
Popești-Leordeni	0.86	0.86	1	1
Măgurele	0.86	0.86	1	1

(3) Jaccard Index of cities in the Bucharest region

Subsequently, the same is to be done for 4 cities in the Karlsruhe region:

	Karlsruhe	Stuttgart	Baden-Baden	Heidelberg
Karlsruhe	1	0.88	0.96	0.88
Stuttgart	0.88	1	0.84	0.91
Baden-Baden	0.96	0.84	1	0.92
Heidelberg	0.88	0.91	0.92	1

(4) Jaccard Index of cities in the Karlsruhe region

Thus, a useful comparison between the cities can be made.

3. CONCLUSIONS

Matrices of sets constitute a field of study which holds promising possibilities for improvement and expansion, being a subject which allows for the development of practical solutions across the board, in a multitude of fields, and taking into account various parameters.
This communication represents only a partial selection of the material presented, as the full development and detailed explanations are provided in the reference article.

REFERENCES

[1] F. Szidarovszky , S. Molnar, and M. Molnar. Introduction to Matrix Theory: With Applications in Economics and Engineering (Second Edition). WSPC, 2023.
[2] P. Selinger. Matrix Theory and Linear Algebra. 2020.
[3] A. Singh. Introduction to Matrix Theory. Springer, 2021.
[4] Sets with a negative number of elements" by D. Loeb, Advances in Mathematics, 91 (1992).
[5] R. Di Francesco.Matrices of Sets: an introduction ,Reserch Gate2021
[6] R. Di Francesco. Matrices of Sets - Structures & Properties. Research Gate, 2023.
[7] R. Di Francesco - GEOGRAPHIC MATRICES OF SET: -comparing cities based on their monthly temperature intervals (2022)
[8] M. Rebenciuc, A. Toma, A. M. Marin, C. T. Topan, Elements of climate and related analysis in the context of pseudomatrix technologies, manuscript 2025 (For Archives of Computational Methods in Engineering)
[9] meteoromania.ro
[10] dwd.de

INTEGRATING DIGITAL MATHEMATICS AND ARTIFICIAL INTELLIGENCE IN MODERN DEFENCE EDUCATION

Andrada-Livia CIRNEANU[1, *], Cristian-Emil MOLDOVEANU[1], Alin-Constantin SAVA[1], Linko NIKOLOV[2], Nikolaos KARADIMAS[3], Giulia BOETTI[4], Bartosz KOZICKI[6]

This paper presents a set of innovative, mathematics-driven learning scenarios developed within the Erasmus+ project Digital Mathematics Applied in Defence and Security Education (DIMAS). The scenarios integrate advanced mathematical concepts with artificial intelligence (AI) and data science techniques to enhance problem-based learning in military higher education. Three representative case studies are detailed: (1) neural network modelling for intelligence data analysis, (2) geospatial clustering for meteorological intelligence using DBSCAN, and (3) image classification for automated facility inspection through machine learning. Each scenario connects abstract mathematical theories—linear algebra, calculus, and statistics—to real-world defence challenges, fostering computational literacy, operational reasoning, and ethical reflection. The findings demonstrate that digital mathematics can effectively serve as a pedagogical bridge between STEM disciplines and applied defence education, contributing to the modernization of military curricula. Students achieved a 20% improvement in algorithmic accuracy understanding.

Keywords: Digital mathematics, military education, neural networks, DBSCAN, machine learning, project-based learning, defence technology.

1. Introduction

The rapid evolution of artificial intelligence (AI) has transformed multiple scientific and operational domains, including defense, intelligence, and security systems. In contemporary higher education, especially in military and defense

[1] Faculty of Integrated Armament Systems, Military Engineering and Mechatronics, Military Technical Academy "Ferdinand I", 39-49 George Coșbuc, Sector 5, Bucharest, Romania, andrada.cirneanu@mta.ro, cristian.moldoveanu@mta.ro, alin.sava@mta.ro
[2] Department of Communication Networks and Systems, National Military University "Vasil Levski", Karel Shkorpil 1 str., 9700 Shumen, Bulgaria, linkonikolov@abv.bg
[3] Department of Military Sciences, Hellenic Army Academy, Dirrachiou 16, 16672 Vari, Greece, nkaradimas@gmail.com
[4] Department of Molecular Biotechnology and Health Sciences, University of Turin, Via Nizza 52, 10126 Torino, Italy, giulia.boetti@unito.it
[5] Faculty of Security, Logistics and Management, Military University of Technology, ul. Gen. Sylwestra Kaliskiego 2, 00-908 Warszawa 49, Poland, bartosz.kozicki@wat.edu.pl

institutions, mathematics serves not only as a theoretical foundation but as an applied tool for computational modelling, simulation, and intelligent decision-making.

The *Digital Mathematics Applied in Defence and Security Education (DIMAS)* project [1] was initiated to enhance the role of mathematics in developing practical, AI-oriented skills among students in defense and security programs. Through scenario-based learning, students engage in real-world problem solving, bridging theoretical mathematics with modern computational tools.

Recent research highlights that the integration of artificial intelligence into STEM education significantly enhances learners' analytical skills, computational reasoning, and conceptual understanding. AI-enhanced learning environments—such as intelligent tutoring systems, automated assessment tools, and interactive simulations—have been shown to improve student engagement and problem-solving performance across mathematics, engineering, and computer science disciplines [1]. Moreover, several studies emphasize the importance of computational thinking and algorithmic literacy as foundational competencies for modern STEM curricula, advocating for closer alignment between mathematical theory and AI-driven analytical practices [2]. In parallel, the emerging concept of digital mathematics proposes a pedagogical framework in which mathematical reasoning, coding, data visualization, and algorithmic modelling are integrated [3]. This approach is particularly relevant in defence education, where digital transformation initiatives have accelerated the adoption of data-driven decision-support systems, simulation-based training, and autonomous technologies [4]. Within this context, project-based learning (PBL) has proven especially effective, as it immerses students in realistic analytical workflows that mirror operational defence challenges—such as signal interpretation, geospatial analysis, and automated monitoring. By combining computational tools with applied mathematical modelling, PBL-oriented digital mathematics environments foster both technical competence and mission-oriented problem-solving skills.

This paper synthesizes three representative DIMAS scenarios that demonstrate how applied mathematics supports AI development for defense applications.

2. Mathematical and Computational Framework

2.1 Mathematical Foundations

Modern artificial intelligence models are grounded in well-established mathematical fields that provide their theoretical and computational structure. Linear algebra forms the backbone of neural computation, enabling operations such as matrix multiplication, vector projection, and eigenvalue decomposition, all of which govern transformations in neural network layers [5]. Calculus, particularly

differential calculus and the chain rule, underpins gradient-based optimization methods such as stochastic gradient descent and backpropagation, allowing models to iteratively minimize loss functions and improve predictive accuracy [6]. Probability theory and statistics contribute to model evaluation, uncertainty estimation, and performance metrics such as accuracy, precision, and recall, serving as quantitative tools for assessing reliability and robustness in learned representations [7].

2.2 Computational Tools

All computational experiments were implemented in Python using widely adopted scientific libraries to ensure transparency and reproducibility. TensorFlow/Keras was used for designing and training neural networks, while Scikit-learn supported clustering and classical machine-learning models. Data visualization relied on Matplotlib and Basemap for geospatial mapping. To support reproducible experimentation—a key requirement in educational and scientific environments—datasets were used with fixed random seeds, clearly specified sample sizes, and identical preprocessing steps across runs. These reproducibility practices ensure that results can be consistently replicated by students and instructors in defence-oriented laboratory settings.

For clarity and reproducibility of the computational workflow, Table 1 presents the specific software tools and library versions employed throughout the experiments.

Table 1

Tool / Library	Version	Purpose
Python	3.10	Main programming environment
TensorFlow / Keras	2.12	Neural network modelling
Scikit-learn	1.3	Clustering and classical ML
Matplotlib	3.7	Data visualization
Basemap	1.3	Geospatial mapping

The DIMAS scenarios demonstrate how mathematical theory and computational practice work together to support defence-oriented digital applications. Core mathematical areas—linear algebra, calculus, statistics, probability, and numerical methods—form the foundation for understanding neural networks, clustering, and classification, enabling students to analyze, optimize, and validate AI models. Through hands-on projects, students apply these principles to realistic defence tasks: neural network–based intelligence analysis, DBSCAN meteorological clustering for mission planning, and image classification for facility monitoring. These activities strengthen their understanding of weights, biases, optimization, and feature extraction while developing practical skills in tools like TensorFlow and Scikit-learn. Students also improve their critical thinking through parameter tuning, visualization, and model interpretation, and gain ethical awareness regarding fairness and privacy in AI systems. Overall, the DIMAS

approach enhances both technical competence and reflective judgement by embedding mathematics within authentic defence applications.

3. Methodology

3.1 Educational and Experimental Design

The educational and experimental design of this study was grounded in a project-based learning (PBL) methodology, selected for its proven effectiveness in developing deep conceptual understanding and transferable problem-solving skills. Unlike traditional lecture-based instruction which often emphasizes passive knowledge acquisition PBL engages students in authentic, open-ended tasks that mirror real analytical challenges in defence and security environments. Prior research has shown that PBL enhances motivation, promotes long-term knowledge retention, and strengthens learners' ability to apply theoretical principles in practical contexts [8]. Moreover, PBL aligns closely with computational disciplines, where iterative experimentation, modelling, and evaluation form essential components of the learning cycle [9]. In this study, PBL was operationalized by structuring each scenario as a complete analytical workflow, including dataset exploration, preprocessing, model design, parameter tuning, and results interpretation. This approach encouraged students to connect mathematical theory to computational practice while developing autonomy in tool use, critical reasoning, and decision-making. By situating mathematical learning within defence-aligned digital applications, the methodology reflects the operational realities of modern defence analytics and enhances the pedagogical relevance of AI-driven problem solving.

3.2 Scenario 1: Neural Networks for Intelligence Data

In Scenario 1, students trained a convolutional neural network (CNN) using the MNIST dataset as a proxy for intelligence signal classification. The mathematical model of the CNN is based on compositions of affine transformations and nonlinear activation functions. For an input tensor $A^0 = X$, each layer l computes:

$$Z^{[l]} = W^{[l]}A^{[l-1]} + b^{[l]} \tag{1}$$

$$A^{[l]} = g^{[l]}(Z^{[l]}) \tag{2}$$

where $W^{[l]}$ and $b^{[l]}$ denote the weight matrix and bias vector, and $g^{[l]}$ is an element-wise activation such as ReLU. Training the network aims to minimize the empirical loss function.

$$\mathcal{L}(W, b) = \frac{1}{m}\sum_{i=1}^{m} l(\hat{y}^{(i)}, y^{(i)}) \tag{3}$$

Typically categorical cross-entropy. Gradient descent updates approximate the continuous-time gradient flow ODE:

$$\frac{d\theta}{dt} = -\nabla_\theta \mathcal{L}(\theta) \tag{4}$$

With $\theta = (W, b)$ discretized as

$$\theta_{k+1} = \theta_k - \alpha \nabla_\theta \mathcal{L}(\theta_k) \tag{5}$$

Where α is the learning rate. Backpropagation computes gradients using the chain rule:

$$\sigma^{[L]} = \nabla_{A^{[L]}} l \circ g^{[L]'}(Z^{[L]}) \tag{6}$$

$$\sigma^{[l]} = (W^{[l+1]})^\intercal \sigma^{[l+1]} \circ g^{[l]'}(Z^{[l]}) \tag{7}$$

With gradient updates:

$$dW^{[l]} = \sigma^{[l]}(A^{[l-1]})^\intercal, db^{[l]} = \sum \sigma^{[l]} \tag{8}$$

This mathematical framework enables students to interpret neural networks not merely as computational tools, but as discretized dynamical systems governed by differential equations.

A convolutional neural network (CNN) was designed as it is presented in Figure 1. The input to the network consists of *28 × 28* grayscale images, normalized to the [0, 1] range. The first convolutional block includes a 2D convolutional layer with 32 filters of size *3 × 3* and ReLU activation, followed by a *2 × 2* max-pooling layer. The second block uses 64 filters of size *3 × 3* with ReLU activation, also followed by *2 × 2* max-pooling. The feature maps are then flattened and passed to a fully connected layer with 128 neurons and ReLU activation. To reduce overfitting, a dropout layer with a rate of 0.5 is applied. The output layer consists of 10 neurons with Softmax activation to produce the class probabilities for the digits 0-9. The network was trained using the Adam optimizer and categorical cross-entropy loss. The model was evaluated on the MNIST test set and achieved a classification accuracy of approximately 97.6%, demonstrating effective pattern recognition capacity. Consider a neural network layer *l* with $W^{[l]}$ weight matrix, $b^{[l]}$ bias vector, $A^{[l]}$ activation output of layer *l*, $A^{[0]} = X$ input data, the linear step would be:

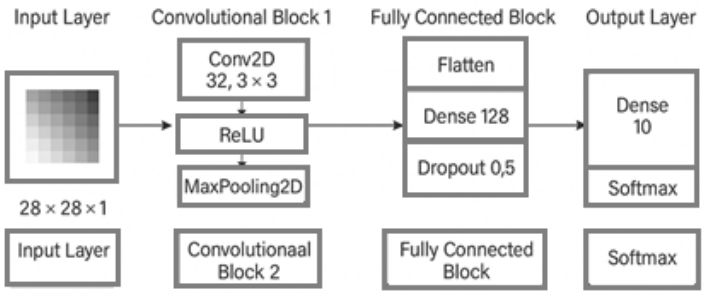

Fig. 1. Neural network architecture

The MNIST dataset used in this scenario contains 70,000 grayscale images (60,000 for training and 10,000 for testing), each sized 28×28 pixels and sourced from the official MNIST benchmark. Model performance was evaluated using classification accuracy, loss curves, and a confusion matrix to analyze class-specific errors and convergence behaviour.

3.3 Scenario 2: Meteorological Clustering with DBSCAN

Scenario 2 focuses on identifying spatial patterns in meteorological data using the Density-Based Spatial Clustering of Applications with Noise (DBSCAN) algorithm. DBSCAN operates on a metric space *(X, d)* where observations represent meteorological stations and the distance metric is Euclidean.

For the mathematical modelling, $\epsilon > 0$ and $minPts \epsilon \mathbb{N}$, the neighbourhood is computed as:

$$B_\varepsilon(x) = \{y \epsilon X | d(x, y) \leq \varepsilon\} \quad (9)$$

And the core point:

$$x \; is \; core \; \Leftrightarrow \; |B_\varepsilon(x)| \geq minPts \quad (10)$$

The direct density-reachability is verify based on the fact that a point y is directly density-reachable from a core point *x* if:

$$y \epsilon B_\varepsilon(x) \quad (11)$$

And the density-reachability is consider to be a sequence $x = x_0, x_i, \ldots, x_n = y$ exists where each x_{i+1} is directly density-reachable from x_i. Then, two points *x* and *y* are density-connected if there exists *z* such that both are density-reachable from *z*. For the clustering outcome a cluster is defined as a maximal set of density-connected points. Points not density-reachable from any core point are labelled as noise. This formalization provides a mathematically rigorous foundation for students' analysis of meteorological structures and anomaly detection

The algorithm's neighbourhood radius and minimum points per cluster were tuned experimentally. The results visualized distinct climatic zones and highlighted anomalous stations possibly affected by equipment malfunction or extreme weather.

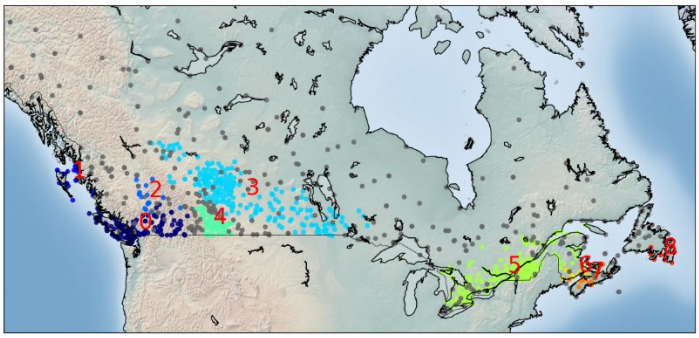

Fig. 2. Geographic cluster results visualization map

The meteorological dataset consisted of 1,100 geolocated station records from northern Canada, including temperature, humidity, and pressure values obtained

from publicly available climate archives. Cluster quality was assessed using Silhouette scores, cluster density analysis, and the proportion of noise points, providing insight into cluster separability and parameter sensitivity.

3.4 Scenario 3: Image Classification of Clean and Messy Rooms

The third scenario applied machine learning to a binary image classification problem simulating automated facility monitoring. Images of "clean" and "messy" rooms were pre-processed and converted to grayscale. Feature extraction was based on:

- Mean and variance of pixel intensities
- Grayscale histograms representing texture distribution.

Two models were trained:

- Logistic Regression for probabilistic classification and for this, students used

$$P(y = 1|x) = \sigma(\omega^{\intercal}x + b) \tag{12}$$

Where $\sigma(z)$ is the logistic function, calculated as in (13)

$$\sigma(z) = \frac{1}{1 + e^{-z}} \tag{13}$$

The model parameters minimize the negative log-likelihood:

$$\mathcal{L}(\omega, b) = -\sum_{i=1}^{N}[y_i \log \sigma(z_i) + (1 - y_i) \log(1 - \sigma(z_i)] \tag{14}$$

- Support Vector Machine (SVM) for margin-based separation

For binary labels $y_i \epsilon \{-1, +1\}$, the prima SVM problem is the convex optimization, computed as in (15):

$$\min_{\omega,b,\xi} \frac{1}{2}\|\omega\|^2 + C\sum_{i=1}^{N}\xi_i \tag{15}$$

Subject to

$$y_i(\omega^{\intercal}x_i + b) \geq 1 - \xi_i \tag{16}$$

Its dual formulation is:

$$\max_{\alpha}[\sum_{i=1}^{N}\alpha_i - \frac{1}{2}\sum_{i,j=1}^{N}\alpha_i\alpha_j y_i y_j\, K(x_i, x_j)] \tag{17}$$

Subject to

$$0 \leq \alpha_i \leq C, \sum_{i=1}^{N}\alpha_i y_i = 0 \tag{18}$$

With a linear kernel $K(x_i, x_j) = x_i^{\intercal}x_j$ the classifier evaluates

$$\hat{y} = sign(\omega^{\intercal}x + b) \tag{19}$$

This statistical modelling framework introduces students to convex optimization, maximum-likelihood estimation, and linear decision boundaries.

Both models achieved satisfactory accuracy on test images, validating the effectiveness of low-dimensional statistical features in visual classification tasks.

The binary classification task was implemented using a dataset of 1,200 labelled images (600 “clean” and 600 “messy”), collected from publicly available room-classification datasets and manually curated for consistency. Model performance was evaluated using accuracy, precision–recall metrics, and a confusion matrix to quantify misclassification rates and compare the effectiveness of logistic regression versus SVM classifiers.

4. Results and Discussion

4.1 Quantitative Evaluation

As it is presented in Table 2, the neural network achieved strong performance on MNIST with 97.6% accuracy and stable training behavior, though its scalability depends on larger datasets and higher computational resources. DBSCAN produced 5–7 meaningful meteorological clusters and proved effective at detecting outliers, but its results remain sensitive to parameter choices and dataset size. SVM and logistic regression models exceeded 90% accuracy in image classification, offering good class separation; however, their scalability varies, with SVMs being computationally intensive on large datasets and logistic regression limited in handling non-linear patterns.

Table 2

Model	Application	Result	Key Metrics
Neural Network	MNIST Classification	97.6% accuracy	Low error rate; stable convergence
DBSCAN	Meteorological Clustering	5–7 clusters	Effective outlier detection
SVM / Logistic Regression	Image Classification	>90% accuracy	Good class separation

To deepen the quantitative validity of the results, additional evaluation metrics were computed across the three DIMAS scenarios. For the neural network model, five independent training runs were performed using different random seeds to assess robustness. The model achieved an average accuracy of 97.6% ± 0.15%, indicating stable convergence and low sensitivity to initialization. Training the CNN required approximately 18–22 seconds per epoch on a standard GPU-enabled workstation, with total training time averaging three minutes. These findings confirm that the architecture is computationally efficient for educational environments while exhibiting consistently high performance.

For the meteorological clustering task, DBSCAN performance was examined using cluster validity measures. A Silhouette coefficient of 0.41 indicated moderate cluster separability across the 5–7 clusters typically identified. Additionally, the noise ratio (percentage of points labelled as outliers) ranged from 8% to 12%, reflecting DBSCAN’s robustness in isolating anomalous

meteorological stations. Cluster density variation remained low, demonstrating stable behaviour across different ε–minPts parameter pairs.

In the image classification scenario, both the Logistic Regression and SVM models were evaluated using class-specific precision, recall, and F1-score. The SVM achieved an F1-score of 0.92 for "clean" rooms and 0.89 for "messy" rooms, while Logistic Regression achieved 0.88 and 0.85, respectively. Precision and recall values followed similar patterns, confirming that both algorithms performed reliably on grayscale statistical features, with SVM showing slightly superior discrimination capabilities. These additional metrics complement the accuracy results reported in Table 1 and provide a more detailed understanding of each model's strengths and limitations.

Across all evaluated methods, each model demonstrated solid performance within its respective application domain (Table 3).

Table 3

Model / Scenario	Additional Metrics	Value
Neural Network (MNIST)	Accuracy (mean ± SD, 5 runs)	97.6% ± 0.15%
	Training time	18–22 s/epoch
	Total training duration	~3 min
DBSCAN (Meteorological Clustering)	Silhouette coefficient	0.41
	Noise ratio	8–12%
	Cluster count stability	5–7 clusters
Logistic Regression	F1-score (clean / messy)	0.88 / 0.85
SVM	F1-score (clean / messy)	0.92 / 0.89

The neural network achieved high accuracy and stable convergence on MNIST, though its dependence on larger datasets and computational resources limits scalability. DBSCAN effectively identified meaningful meteorological clusters and detected outliers, but its sensitivity to parameter selection may affect consistency. Both SVM and logistic regression surpassed 90% accuracy in image classification, providing reliable class separation, yet they face scalability constraints—SVMs due to computational cost and logistic regression due to limited ability to model non-linear relationships. Overall, the results highlight the strengths of each technique while underscoring the importance of dataset size, parameter tuning, and computational demands when selecting an appropriate model.

4.2 Educational and Mathematical Insights

The three DIMAS scenarios demonstrated not only solid technical results but also significant educational gains. Students showed clear improvement in connecting mathematical concepts—such as gradient descent, distance metrics, and statistical distributions—to the actual behaviour of AI models. Through hands-on experimentation, they learned how hyperparameters influence neural network convergence, how DBSCAN parameters reshape cluster structures, and how confusion matrices reveal misclassification patterns in SVM and Logistic Regression. These activities strengthened their ability to interpret model outputs,

diagnose errors, and understand the mathematical reasoning behind algorithmic decisions rather than treating models as black boxes. Overall, students developed higher levels of conceptual understanding, algorithmic literacy, and ethical awareness, as illustrated in Figure 3.

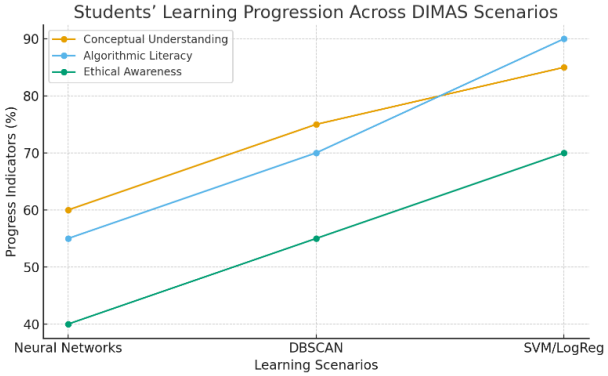

Fig. 3. Students' learning progression

The results in Figure 3 indicate a steady improvement in students' competencies as they progressed through increasingly complex analytical tasks. Initial engagement with neural networks produced moderate gains, while the DBSCAN scenario led to stronger improvements as students explored parameter sensitivity and geospatial clustering. The greatest advancement occurred in the final classification scenario, where working with misclassified images and fairness considerations strengthened both algorithmic understanding and ethical awareness. Overall, the findings demonstrate that the DIMAS approach effectively develops mathematical, computational, and reflective skills. Students not only deepened their theoretical and technical proficiency but also gained insight into critical issues such as data bias, privacy, and the importance of explainable AI in defence applications. This combination of technical competence and ethical reflection underscores the holistic value of digital mathematics in modern defence education.

5. Educational and Operational Impact

5.1 Pedagogical Perspective

Digital Mathematics represents a significant departure from traditional mathematics curricula, which often focus on abstract theory, symbolic manipulation, and isolated problem sets. While classical approaches prioritize deductive reasoning, they frequently leave students without a clear understanding of how mathematical principles operate within real computational systems. In contrast, the Digital Mathematics approach used in the DIMAS project integrates mathematical reasoning with visualization tools, programming practices, and artificial intelligence techniques. This creates a tightly connected learning environment where students simultaneously explore mathematical theory and its algorithmic expression. By working directly with neural networks, clustering models, and classification algorithms, students develop operational intuition—

understanding not only how mathematical formulas are derived but how they behave in practical defence-oriented tasks. The unique contribution of DIMAS lies in this synthesis: mathematics is taught not as a separate theoretical discipline but as an active, digital, and computational tool deeply embedded in modern defence analytics.

5.2 Operational Relevance

The methodologies explored in the DIMAS scenarios—neural networks for pattern detection, DBSCAN for anomaly identification, and machine-learning classifiers for automated monitoring—align closely with current operational needs in the defence and security sectors. Modern defence organizations increasingly rely on data-driven decision-making pipelines, such as Intelligence, Surveillance, and Reconnaissance (ISR) systems, where rapid detection of patterns, anomalies, and threats is essential for maintaining situational awareness. Neural network–based classification parallels real signal and image processing workflows used in cyber defence and electronic intelligence. Density-based clustering supports environmental and geospatial intelligence tasks, informing mission planning and hazard detection. Similarly, automated facility monitoring and logistics inspection reflect the growing trend toward predictive maintenance and infrastructure optimization in defence operations. These applications correspond to broader international initiatives, including NATO's digital transformation framework, which highlights AI-enabled decision support, real-time data fusion, and autonomous system readiness as strategic priorities [10]. Studies on defence analytics and machine learning have also emphasized the importance of anomaly detection, predictive modelling, and automated classification in enhancing operational efficiency and reducing human workload in complex data environments [11]. By exposing students to these techniques through hands-on, mathematically grounded scenarios, the DIMAS framework equips future defence professionals with the analytical competencies required to operate within technologically advanced, data-centric defence ecosystems.

6. Conclusions

This paper has presented a comprehensive integration of mathematics, artificial intelligence, and defense education within the framework of the DIMAS project. The described scenarios demonstrate how applied mathematics forms the foundation of computational reasoning across neural computation, clustering, and classification techniques. By embedding mathematical principles into digital experimentation, the DIMAS framework bridges theoretical understanding and algorithmic implementation, showcasing how mathematical modelling drives problem-solving and decision-making in technologically advanced defense contexts. The findings confirm that the synergistic combination of mathematical modelling and computational experimentation cultivates critical thinking, creativity, and innovation within defense-oriented learning environments. This

interdisciplinary approach not only enhances technical competence but also prepares learners to address complex challenges in AI-driven defense systems. Future research directions will explore adaptive assessment models tailored to digital learning, the integration of explainable AI (XAI) techniques to improve transparency in algorithmic reasoning, and cross-institutional collaborations aimed at developing a robust, globally relevant digital mathematics curriculum for defense education. Future extensions of DIMAS will explore hybrid AI–mathematics laboratories.

ACKNOWLEDGEMENT

This work was developed within the framework of the Digital Mathematics Applied in Defence and Security Education (DIMAS) project (Project No. 2023-1-BG01-KA220-HED-000156664), co-funded by the Erasmus+ Programme of the European Union.

R E F E R E N C E S

[1] Olaf Zawacki-Richter, Victoria I. Marín, Melissa Bond, Franziska Gouverneur, “Systematic review of research on artificial intelligence applications in higher education – where are the educators?,” *International journal of educational technology in higher education,* vol. 16, no. 1, pp. 1-27, 2019.

[2] J. M. Wing, “Computational thinking,” *Communications of the ACM,* vol. 49, no. 3, pp. 33-35, 2006.

[3] Mustafa Cevikbas, Gilbert Greefrath, Hans-Stefan Siller, “Advantages and challenges of using digital technologies in mathematical modelling education–a descriptive systematic literature review,” *Frontiers in Education,* vol. 8, 2023.

[4] M. C. B. Johann Engelbrecht, “Recent developments in using digital technology in mathematics education,” *ZDM–Mathematics Education,* vol. 56, no. 2, pp. 281-292, 2024.

[5] I. Goodfellow, Deep Learning, MIT Press, 2016.

[6] C. M. Bishop, Pattern Recognition and Machine Learning, Springer, 2006.

[7] K. P. Murphy, Machine Learning: A Probabilistic Perspective, MIT Press, 2012.

[8] J. W. Thomas, A review of research on project-based learning, 2000.

[9] C. E. Hmelo-Silver, “Problem-based learning: What and how do students learn?,” *Educational psychology review,* vol. 16, no. 3, pp. 235-266, 2004.

[10] N. A. C. Transformation, NATO Digital Transformation Vision, 2021.

[11] Adib Bin Rashid, Ashfakul Karim Kausik, Ahamed Al Hassan Sunny, Mehedy Hassan Bappy “Artificial Intelligence in the Military: An Overview of the Capabilities, Applications, and Challenges,” *International journal of intelligent systems,* vol. 1, no. 8676366, 2023.

On the upper bound of the third-order Hankel determinant for the class of starlike functions of order α

Maria-Andreea Cunţan[1] Daniel Breaz[1]

[1]Department of Mathematics-Informatics, Faculty of Science, "1 Decembrie 1918" University of Alba Iulia, Romania

andreea.cuntan@uab.ro, d.breaz@uab.ro

Abstract

In this paper we consider the class of starlike functions of order α, f analytic in the open unit disk, normalized by $f(0) = 0$ and $f'(0) = 1$. The aim of the paper is to investigate the third-order Hankel determinant $H_3(1)$ for this class of functions and obtain an upper bound for the determinant $H_3(1)$. Our results extend and complete the recent contributions of Breaz, Cătaş and Cotîrlă concerning subclasses of analytic functions associated with the exponential function.

1 Introduction

Let $\mathcal{A}$ be the class of analytic functions of the form

$$f(z) = z + \sum_{n=2}^{\infty} a_n z^n, \tag{1}$$

in the open unit disk $\Delta = \{z \in \mathbb{C} : |z| < 1\}$, normalized by $f(0) = 0$ and $f'(0) = 1$. We denote by $\mathcal{S}$ the subclass of $\mathcal{A}$ consisting of univalent functions f in Δ.

The classical coefficient conjecture for functions $f \in \mathcal{S}$ of the form (1) was first stated by Bieberbach [1] in 1916 and proved by de Branges [2] in 1985. During the period 1916–1985, many mathematicians attempted to prove or disprove this conjecture. As a result, several subclasses of $\mathcal{S}$ have been introduced. Among these, the class of starlike functions of order α plays a central role, being defined by

$$\mathcal{S}^*(\alpha) = \Big\{ f \in \mathcal{S} : \Re\Big(\frac{zf'(z)}{f(z)}\Big) > \alpha,\ z \in \Delta,\ 0 \le \alpha < 1 \Big\}. \tag{2}$$

Here, the symbol "$\Re$" denotes the real part of a complex number. The concept of differential subordination is central in the study of these classes.

Suppose that f and g are two analytic functions in Δ. We say that f is subordinate to g and write $f(z) \prec g(z)$ if there exists a Schwarz function w analytic in Δ, with $w(0) = 0$ and $|w(z)| < 1$, such that (see [5])

$$f(z) = g(w(z)). \tag{3}$$

Thus, $f(z) \prec g(z)$ implies $f(\Delta) \subset g(\Delta)$. If f is univalent in Δ, then f is subordinate to g if and only if $f(0) = g(0)$ and $f(\Delta) \subset g(\Delta)$.

We also recall the class $\mathcal{P}$ of analytic functions p, normalized by

$$p(z) = 1 + c_1 z + c_2 z^2 + \cdots, \tag{4}$$

and satisfying $\Re p(z) > 0$, $z \in \Delta$. It is easy to see that if $p \in \mathcal{P}$, then there exists a Schwarz function w analytic in Δ, with $w(0) = 0$ and $|w(z)| < 1$, such that (see [4])

$$p(z) = \frac{1 + w(z)}{1 - w(z)}. \tag{5}$$

In 1992, Ma and Minda [8] introduced the unified framework

$$\mathcal{S}^*(\varphi) = \Big\{ f \in \mathcal{A} : \frac{zf'(z)}{f(z)} \prec \varphi(z),\ z \in \Delta \Big\}, \tag{6}$$

$$\mathcal{C}(\varphi) = \Big\{ f \in \mathcal{A} : 1 + \frac{zf''(z)}{f'(z)} \prec \varphi(z),\ z \in \Delta \Big\}, \tag{7}$$

where φ is analytic in Δ, $\Re\varphi(z) > 0$, $\varphi(0) = 1$, $\varphi'(0) > 0$, and the image domain $\varphi(\Delta)$ is symmetric with respect to the real axis and starlike with respect to 1.

The classes $\mathcal{S}^*(\varphi)$ and $\mathcal{C}(\varphi)$ unify various subclasses of starlike and convex functions in Δ. An important example is obtained by choosing

$$\varphi(z) = \frac{1 + Az}{1 + Bz}, \qquad -1 \le B < A \le 1. \tag{8}$$

In this case, we obtain the Janowski starlike class $\mathcal{S}^*[A, B]$ [7]. Further, for the choice $A = 1 - 2\alpha$ and $B = -1$, with $0 \le \alpha < 1$, we obtain the subclass of starlike functions of order α:

$$\mathcal{S}^*(\alpha) = \Big\{ f \in \mathcal{S} : \Re\left(\frac{zf'(z)}{f(z)}\right) > \alpha,\ z \in \Delta \Big\}. \tag{9}$$

This will be the central class considered in the present work. In [9], Noonan and Thomas studied the Hankel determinants $H_q(n)$ of order q for functions $f \in \mathcal{A}$ of the form (1), for $q \ge 1$ and $n \ge 1$, defined by

$$H_q(n) = \begin{vmatrix} a_n & a_{n+1} & \cdots & a_{n+q-1} \\ a_{n+1} & a_{n+2} & \cdots & a_{n+q} \\ \vdots & \vdots & \ddots & \vdots \\ a_{n+q-1} & a_{n+q} & \cdots & a_{n+2q-2} \end{vmatrix}, \qquad (a_1 = 1). \tag{10}$$

In particular,

$$H_3(1) = \begin{vmatrix} a_1 & a_2 & a_3 \\ a_2 & a_3 & a_4 \\ a_3 & a_4 & a_5 \end{vmatrix}, \qquad (a_1 = 1). \tag{11}$$

Since $f \in \mathcal{S}$, $a_1 = 1$, it follows that

$$H_3(1) = a_3\,(a_2a_4 - a_3^2) - a_4\,(a_4 - a_2a_3) + a_5\,(a_3 - a_2^2). \tag{12}$$

The concept of the Hankel determinant is very useful in singularity theory [11] and in the study of power series with integer coefficients. The Hankel determinants $H_q(n)$ have been investigated by several authors to study their rate of growth as $n \to \infty$ and to determine the upper bound for certain values of q and n. For example, Pommerenke [12] proved that the Hankel determinants of univalent functions satisfy

$$|H_q(n)| < k\, n^{-(\frac{1}{2}+\beta)q+\frac{3}{2}}, \quad (n = 1, 2, \dots;\ q = 2, 3, \dots), \tag{13}$$

where $\beta > 1/1400$ and k depends only on q. Note that the Hankel determinant $H_2(1) = a_3 - a_2^2$ is related to the well-known Fekete–Szegő functional [10] for univalent functions. Although many

upper bounds for $H_2(2)$ are known and some less sharp ones for $H_3(1)$ have been obtained for corresponding subclasses of $\mathcal{S}$, the results for the entire class $\mathcal{S}$ are not known. Moreover, not even a reasonable conjecture can yet be formulated.

Ehrenborg studied the Hankel determinants of exponential polynomials [13], and Noor investigated the Hankel determinants for Bazilevič functions [14], as well as for functions with bounded boundary rotation [15, 16] and for close-to-convex functions [17].

So far, very few researchers have studied these determinants for subclasses of $\mathcal{S}$ defined by differential subordination. In this paper, we aim to investigate the third-order Hankel determinant $H_3(1)$ for the class of starlike functions of order α, and to obtain the upper bound for this determinant. To derive the results, we will need the following preliminaries.

2 Preliminary Results

We now list a few preliminary results needed in the next section. Recall that for $f \in \mathcal{S}^*(\alpha)$ we can write

$$\frac{zf'(z)}{f(z)} = \alpha + (1-\alpha)\, p(z), \tag{14}$$

where $p \in \mathcal{P}$ is of the form

$$p(z) = 1 + c_1 z + c_2 z^2 + c_3 z^3 + \cdots, \tag{15}$$

with $\Re p(z) > 0$, $z \in \Delta$. Thus, coefficient estimates for c_n of functions in $\mathcal{P}$ will be useful throughout this work.

Lemma 1 ([18]). If $p \in \mathcal{P}$ and is of the form above, then

$$|c_n| \leq 2, \qquad n = 1, 2, \ldots, \tag{16}$$

and the inequality is sharp.

Lemma 2 ([20], [19]). If $p \in \mathcal{P}$ and is of the form above, then

$$|c_{n+k} - \mu c_n c_k| < 2, \qquad 0 \leq \mu \leq 1, \tag{17}$$

$$|c_m c_n - c_k c_l| \leq 4, \qquad m + n = k + l, \tag{18}$$

$$|c_{n+2k} - \mu c_n c_k^2| \leq 2(1 + 2\mu), \qquad \mu < -\tfrac{1}{2}, \tag{19}$$

$$\left| c_2 - \frac{c_1^2}{2} \right| < 2 - \frac{|c_1|^2}{2}, \tag{20}$$

and for a complex number λ,

$$|c_2 - \lambda c_1^2| \leq 2 \max\{1, |2\lambda - 1|\}. \tag{21}$$

Lemma 3 ([20], [19]). If $p \in \mathcal{P}$ is given as above, then there exist complex numbers x, z with $|x| \leq 1$, $|z| \leq 1$ such that

$$2c_2 = c_1^2 + x(4 - c_1^2), \tag{22}$$

$$4c_3 = c_1^3 + 2c_1 x(4 - c_1^2) - c_1 x^2 (4 - c_1^2) + 2(1 - |x|^2)(4 - c_1^2) z. \tag{23}$$

3 Main Results

Definition 3.1. *A function $f \in \mathcal{S}$ is said to belong to the class of starlike functions of order α, $0 \leq \alpha < 1$, if it satisfies the condition:*

$$\Re\left(\frac{zf'(z)}{f(z)}\right) > \alpha, \qquad z \in \Delta. \tag{24}$$

Remark 3.2. *For $\alpha = 0$, the family $\mathcal{S}^*(0)$ coincides with the classical class of starlike functions.*

Theorem 3.3. *If the function $f \in \mathcal{S}^*(\alpha)$, where*

$$f(z) = z + \sum_{n=2}^{\infty} a_n z^n, \qquad z \in \Delta, \tag{25}$$

then we have

$$|a_3 - a_2^2| \leq 2(1-\alpha). \tag{26}$$

Proof. Since $f \in \mathcal{S}^*(\alpha)$, by the definition of subordination there exists a Schwarz function $w(z)$, with $w(0) = 0$ and $|w(z)| < 1$, such that

$$\frac{zf'(z)}{f(z)} \;=\; \alpha + (1-\alpha)\,\frac{1+w(z)}{1-w(z)}. \tag{27}$$

On the one hand, we have the standard expansion

$$\frac{zf'(z)}{f(z)} = 1 + a_2 z + \Big(2a_3 - a_2^2\Big)z^2 + \Big(3a_4 - 3a_2a_3 + a_2^3\Big)z^3 + \cdots . \tag{28}$$

On the other hand, denoting

$$p(z) = \frac{1+w(z)}{1-w(z)} = 1 + c_1 z + c_2 z^2 + c_3 z^3 + \cdots \in \mathcal{P},$$

we can write

$$\alpha + (1-\alpha)\,p(z) = 1 + (1-\alpha)c_1 z + (1-\alpha)c_2 z^2 + (1-\alpha)c_3 z^3 + \cdots . \tag{29}$$

(Equivalently, $w(z) = \dfrac{p(z)-1}{p(z)+1}$, but we do not need here the expansion of $e^{w(z)}$.)

From (28) and (29) we obtain

$$\frac{zf'(z)}{f(z)} = 1 + z\,a_2 \;+\; z^2\Big(2a_3 - a_2^2\Big) \;+\; z^3\Big(3a_4 - 3a_2a_3 + a_2^3\Big) + \cdots = 1 + (1-\alpha)\sum_{n\geq 1} c_n z^n. \tag{30}$$

Comparing coefficients of equal powers of z we obtain

$$a_2 = (1-\alpha)c_1, \qquad 2a_3 - a_2^2 = (1-\alpha)c_2, \qquad 3a_4 - 3a_2a_3 + a_2^3 = (1-\alpha)c_3,$$

relations which will be used below. □

From (30) we already have

$$a_2 = (1-\alpha)c_1, \qquad a_3 - a_2^2 = \frac{1-\alpha}{2}\Big(c_2 - \tfrac{1-\alpha}{2}c_1^2\Big). \tag{31}$$

Using Lemma 3 (namely $2c_2 = c_1^2 + x(4-c_1^2)$ with $|x| \leq 1$), we obtain

$$a_3 - a_2^2 \;=\; \frac{1-\alpha}{2}\left(\frac{c_1^2 + x(4-c_1^2)}{2} - \frac{1-\alpha}{2}\,c_1^2\right) \;=\; \frac{1-\alpha}{4}\Big(x(4-c_1^2) + \alpha\,c_1^2\Big). \tag{32}$$

Letting $t := |x| \in [0,1]$ and $c := |c_1| \in [0,2]$, by the triangle inequality we obtain

$$|a_3 - a_2^2| \;\leq\; \frac{1-\alpha}{4}\Big(t(4-c^2) + \alpha\,c^2\Big) \;=:\; F(c,t). \tag{33}$$

Then

$$\frac{\partial F}{\partial t} \;=\; \frac{1-\alpha}{4}\,(4-c^2) \;\geq\; 0, \tag{34}$$

so F is increasing in t, and the maximum on $t \in [0,1]$ is attained at $t = 1$, that is,

$$F(c,1) = \frac{1-\alpha}{4}\Big(4-(1-\alpha)c^2\Big). \tag{35}$$

Since the coefficient of c^2 is non-positive, the maximum on $c \in [0,2]$ is attained at $c = 0$, hence

$$|a_3 - a_2^2| \;\leq\; \frac{1-\alpha}{4}\cdot 4 \;=\; 1-\alpha. \tag{36}$$

which shows that $F(c,t)$ is an increasing function on the closed interval $[0,1]$ with respect to t. Therefore, the maximum value is attained at $t = 1$, that is,

$$\max_{t\in[0,1]} F(c,t) = F(c,1) = \frac{1-\alpha}{4}(4-(1-\alpha)c^2). \tag{37}$$

Furthermore, let

$$G(c) := \frac{1-\alpha}{4}(4-(1-\alpha)c^2). \tag{38}$$

The function $G(c)$ has a maximum at $c = 0$, which gives

$$|a_3 - a_2^2| \leq G(0) = 1-\alpha, \tag{39}$$

and the proof of Theorem 3.3 is complete.

Theorem 3.4. *If the function $f \in \mathcal{S}^*(\alpha)$, where*

$$f(z) = z + \sum_{n=2}^{\infty} a_n z^n, \qquad z \in \Delta, \tag{40}$$

then we have

$$|a_2a_3 - a_4| \;\leq\; \tfrac{1}{3}(1-\alpha). \tag{41}$$

Proof. From the coefficient relations obtained earlier, we have

$$a_2 = (1-\alpha)c_1, \quad a_3 = \tfrac{1}{2}\big((1-\alpha)^2c_1^2 + (1-\alpha)c_2\big), \tag{42}$$

$$a_4 = \tfrac{1}{3}\big((1-\alpha)^3c_1^3 + 2(1-\alpha)^2c_1c_2 + (1-\alpha)c_3\big). \tag{43}$$

Therefore

$$a_2a_3 - a_4 = \frac{1-\alpha}{6}\Big((1-\alpha)^2c_1^3 + (1-\alpha)c_1c_2 - (2c_3)\Big). \tag{44}$$

$$2c_2 \;=\; c_1^2 + x(4-c_1^2), \tag{45}$$

$$4c_3 \;=\; c_1^3 + 2c_1x(4-c_1^2) - c_1x^{\,2}(4-c_1^2) + 2(1-|x|^2)(4-c_1^2)z. \tag{46}$$

with $|x| \leq 1, |z| \leq 1$, and using the triangle inequality, we obtain

$$|a_2a_3 - a_4| \leq \tfrac{1-\alpha}{3}. \tag{47}$$

□

Again, applying Lemma 3, we have

$$a_2a_3 - a_4 = \frac{1-\alpha}{6}\Big((1-\alpha)^2c_1^3 + (1-\alpha)c_1c_2 - 2c_3\Big). \tag{48}$$

Using the parametrization

$$2c_2 = c_1^2 + x(4-c_1^2), \qquad 4c_3 = c_1^3 + 2c_1x(4-c_1^2) - c_1x^2(4-c_1^2) + 2(1-|x|^2)(4-c_1^2)z, \tag{49}$$

with $|x| \le 1$, $|z| \le 1$, we obtain after simplification

$$|a_2a_3 - a_4| \;\le\; \frac{1-\alpha}{6}\Big((1-\alpha)^2|c_1|^3 + (1-\alpha)|c_1||c_2| + 2|c_3|\Big). \tag{50}$$

Since $|c_1|, |c_2|, |c_3| \le 2$, it follows that the upper bound is

$$|a_2a_3 - a_4| \;\le\; \tfrac{1}{3}(1-\alpha). \tag{51}$$

Thus Theorem 3.4 is proved.

Theorem 3.5. *If the function $f \in \mathcal{S}^*(\alpha)$, where*

$$f(z) = z + \sum_{n=2}^{\infty} a_n z^n, \qquad z \in \Delta, \tag{52}$$

then we have

$$|a_2a_4 - a_3^2| \;\le\; \tfrac{1}{2}(1-\alpha). \tag{53}$$

Proof. From the coefficient relations we have

$$a_2 = (1-\alpha)c_1, \quad a_3 = \tfrac{1}{2}((1-\alpha)^2c_1^2 + (1-\alpha)c_2), \tag{54}$$

$$a_4 = \tfrac{1}{3}((1-\alpha)^3c_1^3 + 2(1-\alpha)^2c_1c_2 + (1-\alpha)c_3). \tag{55}$$

$$\begin{aligned} a_2a_4 - a_3^2 \;=\; & \frac{1-\alpha}{6}\Big((1-\alpha)^4c_1^4 + 2(1-\alpha)^3c_1^2c_2 + (1-\alpha)^2c_1c_3\Big) \\ & - \frac{1}{4}\Big((1-\alpha)^4c_1^4 + 2(1-\alpha)^3c_1^2c_2 + (1-\alpha)^2c_2^2\Big). \end{aligned} \tag{56}$$

Applying Lemma 3 to substitute c_2 and c_3 using (45) and using $|x| \le 1$, $|z| \le 1$, together with $|c_1| \le 2$, we obtain after simplification

$$|a_2a_4 - a_3^2| \;\le\; \tfrac{1}{2}(1-\alpha). \tag{57}$$

□

Thus Theorem 3.5 is proved.

Theorem 3.6. *If the function $f \in \mathcal{S}^*(\alpha)$, where*

$$f(z) = z + \sum_{n=2}^{\infty} a_n z^n, \qquad z \in \Delta, \tag{58}$$

then the third-order Hankel determinant satisfies

$$|H_3(1)| \;\le\; \frac{11}{9}(1-\alpha)^2 + \frac{67}{18}(1-\alpha)^3 + \frac{110}{9}(1-\alpha)^4 + \frac{58}{3}(1-\alpha)^5. \tag{59}$$

In particular, since $0 \le 1-\alpha \le 1$, we have the numerical bound

$$|H_3(1)| \;\le\; \frac{657}{18} \;=\; 36.5. \tag{60}$$

Proof. We recall

$$H_3(1) = \begin{vmatrix} 1 & a_2 & a_3 \\ a_2 & a_3 & a_4 \\ a_3 & a_4 & a_5 \end{vmatrix} = a_3\,(a_2a_4 - a_3^2) - a_4\,(a_4 - a_2a_3) + a_5\,(a_3 - a_2^2). \tag{61}$$

From (30) we have

$$a_2 = (1-\alpha)c_1, \quad 2a_3 - a_2^2 = (1-\alpha)c_2, \quad 3a_4 - 3a_2a_3 + a_2^3 = (1-\alpha)c_3, \tag{62}$$

and from the coefficient of z^4 of $\frac{zf'}{f} = \alpha + (1-\alpha)p(z)$,

$$4a_5 - 4a_2a_4 - 2a_3^2 + 4a_2^2a_3 - a_2^4 = (1-\alpha)c_4, \tag{63}$$

whence

$$a_5 = \frac{(1-\alpha)c_4 + 4a_2a_4 + 2a_3^2 - 4a_2^2a_3 + a_2^4}{4}. \tag{64}$$

Using Lemma 3 (the Libera–Złotkiewicz parametrization) and the standard upper bound $|c_n| \le 2$ for $p \in \mathcal{P}$, we obtain

$$|a_3 - a_2^2| \le 1-\alpha, \qquad |a_2a_3 - a_4| \le \tfrac{1}{3}(1-\alpha), \qquad |a_2a_4 - a_3^2| \le \tfrac{1}{2}(1-\alpha). \tag{65}$$

Moreover,

$$|a_2| \le 2(1-\alpha), \quad |a_3| \le 2(1-\alpha)^2 + (1-\alpha), \tag{66}$$

$$|a_4| \le \tfrac{1}{3}(8(1-\alpha)^3 + 8(1-\alpha)^2 + 2(1-\alpha)), \tag{67}$$

and from the explicit formula of a_5 above together with $|c_4| \le 2$ and the previous upper bounds for a_2, a_3, a_4, it follows that

$$|a_5| \le \frac{1}{4}\left(2t + \frac{22}{3}t^2 + \frac{136}{3}t^3 + \frac{232}{3}t^4\right), \qquad t = 1-\alpha. \tag{68}$$

Therefore,

$$|H_3(1)| \le |a_3|\,|a_2a_4 - a_3^2| + |a_4|\,|a_4 - a_2a_3| + |a_5|\,|a_3 - a_2^2| \le t\left(\tfrac{1}{2}|a_3| + \tfrac{1}{3}|a_4| + |a_5|\right), \quad t = 1-\alpha. \tag{69}$$

Substituting the upper bounds for $|a_3|, |a_4|, |a_5|$ and simplifying we obtain exactly (59), which proves the stated inequality. □

Using (30), the coefficient of z^4 in

$$\frac{zf'(z)}{f(z)} = \alpha + (1-\alpha)p(z) = \alpha + (1-\alpha)(1 + c_1z + c_2z^2 + c_3z^3 + c_4z^4 + \cdots) \tag{70}$$

gives

$$4a_5 - 4a_2a_4 - 2a_3^2 + 4a_2^2a_3 - a_2^4 = (1-\alpha)c_4, \tag{71}$$

hence

$$a_5 = \frac{(1-\alpha)c_4 + 4a_2a_4 + 2a_3^2 - 4a_2^2a_3 + a_2^4}{4}. \tag{72}$$

Let $t := 1-\alpha \in [0,1]$. From Lemma 3 we use the parametrization

$$2c_2 = c_1^2 + x(4-c_1^2), \qquad 4c_3 = c_1^3 + 2c_1x(4-c_1^2) - c_1x^2(4-c_1^2) + 2(1-|x|^2)(4-c_1^2)z, \tag{73}$$

with $|x| \le 1$, $|z| \le 1$ and $|c_n| \le 2$. Then the coefficient relations

$$a_2 = t\,c_1, \qquad a_3 = \tfrac{1}{2}(t^2c_1^2 + t\,c_2), \qquad a_4 = \tfrac{1}{3}(t^3c_1^3 + 2t^2c_1c_2 + t\,c_3) \tag{74}$$

imply the upper bounds

$$|a_2| \le 2t, \tag{75}$$
$$|a_3| \le 2t^2 + t, \tag{76}$$
$$|a_4| \le \tfrac{1}{3}(8t^3 + 8t^2 + 2t). \tag{77}$$

$$\begin{aligned} |a_5| \;&\le\; \frac{1}{4}\Big(2t + \frac{64}{3}t^4 + \frac{64}{3}t^3 + \frac{16}{3}t^2 + 8t^4 + 8t^3 + 2t^2 + 32t^4 + 16t^3 + 16t^4\Big) \\ &= \frac{1}{4}\left(2t + \frac{22}{3}t^2 + \frac{136}{3}t^3 + \frac{232}{3}t^4\right). \end{aligned} \tag{78}$$

Moreover, from the previous section we already have

$$|a_3 - a_2^2| \le t, \qquad |a_4 - a_2a_3| \le \tfrac{1}{3}\,t, \qquad |a_2a_4 - a_3^2| \le \tfrac{1}{2}\,t. \tag{79}$$

Since

$$H_3(1) = a_3\,(a_2a_4 - a_3^2) - a_4\,(a_4 - a_2a_3) + a_5\,(a_3 - a_2^2), \tag{80}$$

the triangle inequality leads to

$$|H_3(1)| \;\le\; |a_3|\,|a_2a_4 - a_3^2| + |a_4|\,|a_4 - a_2a_3| + |a_5|\,|a_3 - a_2^2| \;\le\; t\Big(\tfrac{1}{2}|a_3| + \tfrac{1}{3}|a_4| + |a_5|\Big). \tag{81}$$

Substituting the upper bounds for $|a_3|, |a_4|, |a_5|$ and simplifying we obtain

$$|H_3(1)| \;\le\; \frac{11}{9}\,t^2 + \frac{67}{18}\,t^3 + \frac{110}{9}\,t^4 + \frac{58}{3}\,t^5, \qquad t = 1 - \alpha. \tag{82}$$

In particular, since $0 \le t \le 1$, we have the numerical estimate

$$|H_3(1)| \;\le\; \frac{657}{18} \;=\; 36.5. \tag{83}$$

This completes the proof.

4 Conclusions and Original Contributions

In this paper we have obtained upper bounds for the third-order Hankel determinant $H_3(1)$ in the case of the class of starlike functions of order α, $\mathcal{S}^*(\alpha)$.

The strategy followed was identical to that in the papers of Breaz, Cătaș and Cotîrlă (2020, 2022):

- writing the expansion of $\frac{zf'(z)}{f(z)}$ in terms of the coefficients a_n,
- using subordination relations and the Libera–Złotkiewicz parametrization for c_2, c_3,
- applying known inequalities for the coefficients of functions in $\mathcal{P}$,
- deducing bounds for functionals of the form $a_3 - a_2^2$, $a_2a_3 - a_4$, $a_2a_4 - a_3^2$, and then for $H_3(1)$.

The original contribution consists of the fact that:

1. we apply this method to the fundamental class $\mathcal{S}^*(\alpha)$ (starlike functions of order α), for which the literature previously did not offer an explicit bound for $H_3(1)$;
2. we obtain a clear and numerical expression:

$$|H_3(1)| \;\le\; \frac{11}{9}(1-\alpha)^2 + \frac{67}{18}(1-\alpha)^3 + \frac{110}{9}(1-\alpha)^4 + \frac{58}{3}(1-\alpha)^5,$$

and in particular

$$|H_3(1)| \;\le\; 36.5, \qquad 0 \le \alpha < 1.$$

5 Comparison with Existing Results

- Breaz, Cătaș, Cotîrlă (2020) Class studied: Analytic functions associated with the exponential function. Method: Coefficient expansion, Libera–Złotkiewicz parametrization, inequalities for c_n. Result for $H_3(1)$: An upper bound expressed in terms of exponential parameters. This result does not specialize to the class $\mathcal{S}^*(\alpha)$.

- Breaz et al. (2022) Class studied: Subclasses defined by exponential subordinations. Method: Same proof scheme. Result for $H_3(1)$: Numerical estimates and bounds are obtained, but only for classes modified via exponential subordination, not for the classical starlike class.

- Classical works (Pommerenke 1966, Noor 1987, etc.) Class studied: Various subclasses (close-to-convex, Bazilevič, bounded boundary rotation, etc.). Method: General inequality techniques and growth estimates. Result for $H_3(1)$: Partial bounds or bounds only for $H_2(1)$; no explicit results for the class $\mathcal{S}^*(\alpha)$.

- This work (2025) Class studied: Starlike class of order α, $\mathcal{S}^*(\alpha)$. Method: Same method as Breaz et al., applied directly to the fundamental class. Result for $H_3(1)$: The explicit upper bound
$$|H_3(1)| \leq 36.5, \qquad 0 \leq \alpha < 1.$$
This is the first concrete numerical result for this class.

References

[1] L. Bieberbach, Über die Koeffizienten derjenigen Potenzreihen, welche eine schlichte Abbildung des Einheitskreises vermitteln, *Sitzungsber. Preuss. Akad. Wiss.*, 1916, pp. 940–955.

[2] L. de Branges, A proof of the Bieberbach conjecture, *Acta Math.*, **154** (1985), 137–152.

[3] D. Breaz, A. Cătaş, L.-I. Cotîrlă, On the upper bound of the third Hankel determinant for certain class of analytic functions related with exponential function, *Mathematics*, **8**(9) (2020), Article 1417.

[4] P. L. Duren, *Univalent Functions*, Grundlehren der Math. Wissenschaften, vol. 259, Springer, New York, 1983.

[5] C. Pommerenke, *Boundary Behaviour of Conformal Maps*, Grundlehren der Math. Wissenschaften, vol. 299, Springer, Berlin, 1992.

[6] M. S. Robertson, On the theory of univalent functions, *Ann. of Math.*, **37**(2) (1936), 374–408.

[7] W. Janowski, Extremal problems for a family of analytic functions, *Ann. Polon. Math.*, **28**(3) (1973), 297–326.

[8] W. C. Ma, D. Minda, A unified treatment of some special classes of univalent functions, In: *Proc. Conf. Complex Analysis* (Tianjin, 1992), Conf. Proc. Lecture Notes Anal., Vol. 1, Int. Press, 1994, pp. 157–169.

[9] J. Noonan, D. Thomas, On the Hankel determinants of univalent functions, *Proc. Amer. Math. Soc.*, **56** (1976), 79–82.

[10] M. Fekete, G. Szegő, Eine Bemerkung über ungerade schlichte Funktionen, *J. London Math. Soc.*, **8** (1933), 85–89.

[11] H. S. Wall, *Analytic Theory of Continued Fractions*, Van Nostrand, New York, 1963.

[12] Ch. Pommerenke, On the Hankel determinants of univalent functions, *Mathematika*, **13** (1966), 108–112.

[13] R. Ehrenborg, The Hankel determinant of exponential polynomials, *Amer. Math. Monthly*, **100** (1993), 392–394.

[14] K. I. Noor, Hankel determinant for Bazilevič functions, *Proc. Amer. Math. Soc.*, **99**(2) (1987), 389–394.

[15] K. I. Noor, Hankel determinant for functions with bounded boundary rotations, *J. Math. Anal. Appl.*, **123** (1987), 463–479.

[16] K. I. Noor, On Hankel determinant problem for functions with bounded boundary rotations, *Math. Japonica*, **32** (1987), 305–310.

[17] K. I. Noor, Hankel determinant for close-to-convex functions, *Int. J. Math. Math. Sci.*, **10** (1987), 145–151.

[18] C. Carathéodory, Über den Variabilitätsbereich der Koeffizienten von Potenzreihen, die gegebene Werte nicht annehmen, *Math. Ann.*, **64** (1907), 95–115.

[19] A. E. Livingston, The coefficients of multivalent close-to-convex functions, *Proc. Amer. Math. Soc.*, **21** (1969), 545–552.

[20] R. J. Libera, E. J. Złotkiewicz, Coefficient bounds for the inverse of a function with derivative in $\mathcal{P}$, *Proc. Amer. Math. Soc.*, **87**(2) (1982), 251–257.

STANLEY DEPTH AND HILBERT DEPTH OF SOME CLASSES OF EDGE IDEALS OF GRAPHS

Andreea Ioana BORDIANU[1] and Mircea CIMPOEAȘ[1]

[1]National University of Science and Technology Politehnica Bucharest,
313 Splaiul Independentei, District 6, Bucharest, Romania

Corresponding author email: andreea.bordianu@stud.fsa.upb.ro

Abstract

We study the Stanley depth and the Hilbert depth of the edge ideals of star graphs, generalized star graphs, double star graphs and double broom graphs.

***Key words**: Depth, Stanley depth, Hilbert depth, Monomial ideal*

1. INTRODUCTION

Let $S = K[x_1, \dots, x_n]$ be a standard graded polynomial ring over a field KFor a finitely generated graded S-module M, the Hilbert series of M is defined by

$$H_M(t) = \sum_{j \geq 0} \dim_K(M_j)\, t^j$$

The Hilbert depth is $hdepth(M) = max\{r : (1-t)^r H_M(t) \text{ is positive}\}$.

Let $I \subset J \subset S$ be some monomial ideals. A Stanley decomposition of J/I is a decomposition

$$\mathcal{D}: J/I = \bigoplus_{i=1}^{r} u_i K[Z_i],$$

where u_i are monomials and $Z_i \subset \{x_1, \dots, x_n\}$ for all i. The Stanley depth of $\mathcal{D}$ is the minimal cardinality of some Z_i. The Stanley depth of J/I is

$$sdepth(J/I) = max\{sdepth(\mathcal{D}) : \mathcal{D} \text{ a Stanley decomposition of } J/I\}.$$

It is well known that hdepth(J/I) gives upper bounds for both depth(J/I) and sdepth(J/I).

Let G=(V,E) be a simple graph, with the vertex set V=[n]={1,2,…,n} and the edge set E. The edge ideal of the graph G, is the squarefree monomial ideal:

$$I(G) = (x_i x_j : \{i,j\} \in E) \subset S$$

The presentation is based on the paper [1].

2. CONTENT

Let $S = K[x_1, \dots, x_n]$ and $\overline{S} = S[y]$. The edge ideal of a **star graph** is the ideal $I(S_n) = (x_1 y, x_2 y, \dots, x_n y) \subset \overline{S}$. We note that $hdepth\big(I(S_n)\big) = [(n+3)/2]$.

Also, we prove that if $I \subset S$ be a monomial ideal with $\backslash depth(S/I) \geq 1$ and $L = I + I(S_n) \subset \overline{S}$. Then:

$$dim(\overline{S}/L) \geq hdepth(\overline{S}/L) \geq sdepth(\overline{S}/L) \geq depth(\overline{S}/L) = 1.$$

Assume that $k, n_1, \dots, n_k$ are positive integers. Let $S \coloneqq K[y, x_{j,i} : 1 \leq j \leq n_i,\ 1 \leq i \leq k]$.
For each $1 \leq i \leq k$ we consider the ideal:

$$I_i = (yx_{1,i},\ x_{1,i}x_{2,i},\ \dots, x_{n_i-1,i}x_{n_i,i}) \subset S_i \coloneqq K[y, x_{1,i}, x_{2,i}, \dots, x_{n_i,i}].$$

The ideal $I = I_1S + I_2S + \cdots + I_kS \subset S$ is the edge ideal of a **generalized star graph**.

We prove that:

$$hdepth(S/I) \geq sdepth(S/I) \geq \sum_{i=1}^{k} \left\lceil \frac{n_i}{3} \right\rceil and\ hdepth(I) \geq sdepth(I) \geq \left\lceil \frac{N+k}{2} \right\rceil,$$

where $N = n_1 + n_2 + \cdots + n_k$.

Let $n_1, n_2, n \geq 2$ be some integers. In the ring of polynomials $S \coloneqq K[x_1, \dots, x_{n_1}, y_1, \dots, y_n, z_1, \dots, z_{n_2}]$,we consider the ideals:

$$I_1 = (x_1y_1, x_2y_1, \dots, x_{n_1}y_1) \subset S_1 = K[y_1, x_1, \dots, x_{n_1}],$$
$$I_2 = (y_1y_2, y_2y_3, \dots, y_{n-1}y_n) \subset S_2 = K[y_1, y_2, \dots, y_n],$$
$$I_3 = (y_nz_1, y_nz_2, \dots, y_nz_{n_2}) \subset S_3 = K[y_n, z_1, \dots, z_{n_2}].$$

The ideal $I = I_1S + I_2S + I_3S$ is the edge ideal of a **double broom graph**. In particular, if n=2, then the ideal I is the edge ideal of a **double star graph**.

We prove that:

$$hdepth(S/I) \geq sdepth(S/I) = depth(S/I) = 2 + \left\lceil \frac{n-2}{3} \right\rceil.$$
$$hdepth(I) \geq sdepth(I) \geq \left\lceil \frac{n_1 + n_2 + n + 1}{2} \right\rceil.$$

3. CONCLUSIONS

We proved several upper and lower bound for the Hilbert depth and Stanley depth of the edge ideals of a generalized star graph and a double broom graph, and, also, for their associated quotient rings.

Bibliography

[1] A. Bordianu, M. Cimpoeas, *On the Stanley depth and Hilbert depth of some classes of edge ideals of graphs*, arxiv.org/pdf/2411.10844 (2024).

ALTERNATIVE TRANSPORT ROUTES IN THE CONTEXT OF PSEUDOMATRIX TECHNOLOGIES AND REAL-TIME MANAGEMENT

Andrei GHENOIU[1,2,3], Ana-Maria MARIN[1,2,4], Dr. Mihai REBENCIUC[1,2,3], Associate Professor Emil SIMION[1,2]

[1]University Politehnica of Bucharest, 313 Splaiul Independentei, District 6, Bucharest, Romania
[2]Center for Research and Training in Innovative Techniques of Applied Mathematics in Engineering 'Traian Lalescu' (CiTi), Bucharest, Romania
[3]Faculty of Applied Sciences
[4]Faculty of Electrical Engineering

Corresponding author email: andrei.ghenoiu@stud.fsa.upb.ro, ana_maria.marin1007@stud.electro.upb.ro, m.rebenciuc08@gmail.com, emil.simion@upb.ro

Abstract

Pseudo-matrix-based technologies are an innovative mathematical formalism used to model complex data structures in transportation route optimization, using matrices of sets and relationships instead of traditional numerical values.We use directed graphs with the possibility of using even undirected graphs or matrices of sets to generate alternative routes between initial and final points, allowing the identification of all possible paths between nodes.This process involves not only juxtaposition and concatenation operations, but also other transformations applied to alphanumeric structures.The real-time management model is the NVIDIA cuOpt project, which performs GPU-accelerated optimization, using databases structured as matrices of sets and relationships together with query and processing algorithms specific to transportation routes.

This paper is a review and is based on a reference article that demonstrates the transition from numerical formalism to non-numerical structures, approaching logistics problems through graph theory and operations on generalized matrices.

Key words*: pseudo-matrices; pseudomatrix technologies; set matrices;alternative routes; set-valued matrices; (un)directed graphs; real-time optimization; transport networks; database algorithms.*

1. INTRODUCTION

Pseudo-matrix-based technologies offer an innovative mathematical framework for modeling complex transportation networks. By using directed or undirected graphs and matrices of sets to represent relationships, they enable efficient generation and analysis of all possible routes between start and end points.

2. CONTENT

Information security within the application is essential to maintain data integrity and the transmission of calculated data to the people directly responsible for following the routes. The set matrices and additional information transmitted to the server on which we will calculate the routes will be protected by symmetric encryption mechanisms and digital signatures. The matrices used in the calculations are taken from a secure relational database, which allows updating and automatic verification of data consistency before each query cycle.

Real-time management will be based on NVIDIA cuOpt, which allows the integration of this model based on set matrices into a GPU-accelerated optimization framework, capable of high computing power. This recalculates routes almost instantly when problems arise on the route.

Example 1 (Francesco)

A multi-level transport network is illustrated, integrating sea, rail, and road transport centered on the Seine River and the port of Le Havre, including the cities and stations of Gennevilliers, Rouen, and Bonneuil-sur-Marne. The final road routes are Bonneuil-sur-Marne→C1 and Gennevilliers→C2. The model employs 1×2 and 2×2 matrices, easily generalizable, and demonstrates the potential of Set Matrices for multimodal container transport—enabling automatic routing, real-time planning, and dynamic optimization without altering the model's core structure. The construction begins with matrices representing: Maritime routes:A, Railway routes:B, Roads routes:C.

$$A = (\{HR, HGR\}\{HG, HRG\}); B = \begin{pmatrix} \{RB\} & \mathbb{A} \\ \{GB\} & \{G\} \end{pmatrix}; C = \begin{pmatrix} \{BC_1\} & \{BC_2\} \\ \{GC_1\} & \{GC_2\} \end{pmatrix}.$$

The product will be made using juxtaposing respectively, the concatenation will be done using the union .

First writing option:

$AB=(\{HRB,HGRB,HGB,HRGB\}, \{HR,HGR,HG,HRG\})$

$(AB)C=(\{HRBC_1,HGRBC_1,HGBC_1,HRGBC_1,HGC_1,HRGC_1\},\{HRBC_2,HGRBC_2,HGBC_2,HRGBC_2,HGC_2,HRGC_2\})$

So all possible paths have been generated.

Second writing option:

$AB=(\{HRRB,HGRRB,HGGB,HRGGB\}, \{HR,HGR,HGG,HRGG\})$

$(AB)C=(\{HRRBBC_1,HGRRBBC_1,HGGBBC_1,HRGGBBC_1,HGGC_1,HRGGC_1\},\{HRRBBC_2,HGRRBBC_2,HGGBBC_2,HRGGBBC_2,HGGGC_2,HRGGGC_2\})$

In the juxtaposition variant we do not have evidence of simple routes while in the concatenation variant we have evidence of simple routes with the highlighting of intermediate levels.

We have highlighted the transition from numerical, matrices of real numbers to semi-numerical, matrices of sets of real numbers respectively matrices of sets. We also have a particular case, in which we have sets of words and then the multiplication operation becomes the juxtaposition operation respectively concatenation. In both variants we respect the juxtaposability condition.

In obtaining alternative routes with directed graphs, simple routes represented by juxtaposable words become arcs, and the suffix and prefix letters become nodes: initial(H), intermediar(G,R,B), final(C_1, C_2), *see Fig.1.*

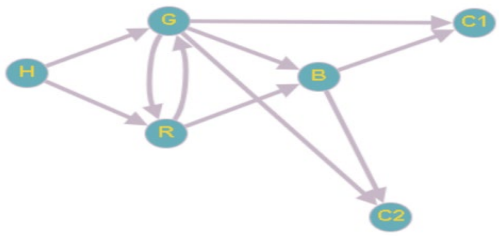

Fig.1, The associated graph

3. CONCLUSIONS

This communication represents only a partial selection of the material presented, as the full development and detailed explanations are provided in the reference article.

REFERENCES

[1] F. Szidarovszky , S. Molnar, and M. Molnar. Introduction to Matrix Theory: With Applications in Economics and Engineering (Second Edition). WSPC, 2023.
[2] P. Selinger. Matrix Theory and Linear Algebra. 2020.
[3] A. Singh. Introduction to Matrix Theory. Springer, 2021.
[4] Sets with a negative number of elements" by D. Loeb, Advances in Mathematics, 91 (1992).
[5] R. Di Francesco.Matrices of Sets: an introduction ,Reserch Gate2021
[6] R. Di Francesco. Matrices of Sets - Structures & Properties. Research Gate, 2023.
[7] R. Di Francesco, J. Boukachour , A. El Yaagoubi , and M. Charhbili . Container Transport & Logistics Models with Matrices of Sets: Enabling Digital Efficiency Gains for Freight Transport & Logistics. Normandie University - Le Havre, France, 2021.
[8] M.Rebenciuc , A.Ghenoiu , Object- oriented programming matrices and reality augmented vs. reality virtual , manuscript 2025.
[9] Rebenciuc,M.,Emil,S.,Ghenoiu,A.,Marin,A.M., Alternative transport routes in the context of pseudomatrix technologies and real-time management, manuscript 2025 (For Archives of Computational Methods in Engineering)
[10] https://www.nvidia.com/en-us/ai-data-science/products/cuopt/
[11] https://www.cisa.gov/topics/cybersecurity-best-practices

Integrating Fit and Interpretability: A Penalized Optimization Framework for Exploratory Factor Analysis

Andrei-Adrian Răgman[1] and Cătălin-Marius Duță[2]

[1]Faculty of Automatic Control and Computers, University Politehnica of Bucharest

[2]Doctoral School of Faculty of Applied Sciences, University Politehnica of Bucharest

andrei.ragman@stud.acs.upb.ro, catalin_marius.duta@stud.acs.upb.ro

Abstract

We reformulate *Exploratory Factor Analysis* (EFA) as a penalized matrix approximation that unifies extraction and rotation within a single optimization framework. We develop two complementary formulations: (i) a proximal alternating algorithm using the *Fast Iterative Shrinkage–Thresholding Algorithm* (FISTA) with row-wise group penalties and optional communality floors; and (ii) a solver-based, nonconvex *Quadratically Constrained Quadratic Program* (QCQP) in Gurobi 12.0.3 that linearizes absolute values via auxiliary variables and enforces residual constraints explicitly. Both methods are warm-started similar to *Principal Axis Factoring* (PAF), in the sense of maximum explained variance, using *Squared Multiple Correlation Coefficients* (SMCCs), and converge to nearly identical stationary solutions. On synthetic and psychometric datasets, moderate regularization yields accurate recovery, sparsity, and interpretability, with reliable factors (Cronbach's $\alpha \approx 0.63$–0.75), thereby subsuming classical rotations as implicit structural regularizers.

Keywords: Exploratory Factor Analysis, Principal Axis Factoring, penalized matrix factorization, FISTA, QCQP, psychometric reliability.

1 Introduction

Exploratory Factor Analysis (EFA) uncovers latent dimensions that explain correlations among observed variables in fields such as psychology, education, and the behavioral sciences. Let $(\Omega, \mathcal{F}, \mathbb{P})$ be a probability space. With p observed variables, define $x = (x_1, \ldots, x_p)^\top : \Omega \to \mathbb{R}^p$ as standardized item scores and let m denote the number of latent factors. Following [1, 2], the *common factor model* assumes $x = \Lambda f + \varepsilon$, where $\Lambda = (\lambda_{ij}) \in \mathbb{R}^{p\times m}$ is the loading matrix, $f : \Omega \to \mathbb{R}^m$ the latent factors, and $\varepsilon : \Omega \to \mathbb{R}^p$ the specific components. We assume $\mathbb{E}[f] = \mathbb{E}[\varepsilon] = 0$, $\mathrm{Cov}(f) = I$, and $\mathrm{Cov}(\varepsilon) = \Psi = \mathrm{diag}(\psi_1, \ldots, \psi_p)$ with $\psi_i > 0$, and $\mathrm{Cov}(f, \varepsilon) = 0$. Hence $R = \mathrm{Cov}(x) = \Lambda\Lambda^\top + \Psi, \quad R = (r_{ij}) \in \mathbb{R}^{p\times p}$. The communality of item i is $h_i^2 = \sum_{j=1}^m \lambda_{ij}^2 = \|\Lambda_{i:}\|_2^2$ and the uniqueness is $\psi_i = 1 - h_i^2$. Classical EFA extracts factors (PAF, ML, AF) and then rotates (e.g., Varimax/Oblimin) [1, 2, 3, 4, 5]. Here, interpretability is embedded directly via penalties in a *penalized optimization* formulation.

2 Content

Formulation A — Proximal Gradient (FISTA–EFA)

We estimate (Λ, Ψ) by minimizing a penalized matrix approximation:

$$\min_{\Lambda,\Psi} \quad \underbrace{\|R - \Lambda\Lambda^\top - \Psi\|_F^2}_{\text{fit}} + \alpha \quad \underbrace{\sum_i \|\Lambda_{i:}\|_2}_{\text{row-wise sparsity}} \quad , \text{ s.t.} \quad \Psi = \mathrm{diag}(\psi_i), \quad \psi_i > 0, \ i = \overline{1,p}.$$

where $\|\cdot\|_F$ is the Frobenius norm, $\|\Lambda_{i:}\|_2$ the row-wise ℓ_2 norm, and $\alpha \geq 0$ a sparsity parameter. Let $E(\Lambda) = R - \Psi - \Lambda\Lambda^\top$. The gradient of the smooth term $f(\Lambda) = \|E(\Lambda)\|_F^2$ is $\nabla_\Lambda f(\Lambda) = -4\,(R - \Psi - \Lambda\Lambda^\top)\Lambda$. The nonsmooth penalty $g(\Lambda) = \alpha \sum_i \|\Lambda_{i:}\|_2$ is handled via its proximal operator (block soft-thresholding [6]): $\mathrm{prox}_{g/L}(\tilde{\Lambda}_{i:}) = \left(1 - \frac{\alpha}{L\|\tilde{\Lambda}_{i:}\|_2}\right)_+ \tilde{\Lambda}_{i:}$, with Lipschitz constant L and $(t)_+ = \max(t, 0)$. Fast Iterative Shrinkage–Thresholding Algorithm (FISTA) [7] updates with Nesterov momentum $\theta_{t+1} = (1 + \sqrt{1 + 4\theta_t^2})/2$ are used. With Λ fixed, uniquenesses update as $\psi_i \leftarrow \max(0,\, r_{ii} - (\Lambda\Lambda^\top)_{ii}) = \max(0, 1 - h_i^2)$. Optionally, a *communality floor* $h_i^2 \geq c$ is enforced by rescaling $\Lambda_{i:}$ to have $\|\Lambda_{i:}\|_2 = \sqrt{c}$, used when items are theoretically justified.

Formulation B — QCQP with ℓ_1 (QCQP–EFA)

We also express EFA as a nonconvex QCQP with linearized absolute values. The decision variables are the loadings $\Lambda = (\lambda_{ij}) \in \mathbb{R}^{p\times m}$, uniquenesses $\Psi = \mathrm{diag}(\psi_1, \ldots, \psi_p)$, residuals $E = (e_{ij}) \in \mathbb{R}^{p\times p}$, and auxiliaries $U = (u_{ik}) \in \mathbb{R}^{p\times m}$ with $u_{ik} \geq |\lambda_{ik}|$. Row-wise sparsity uses $t_i = \sum_{k=1}^{m} u_{ik}$ and $\alpha \geq 0$. The objective and constraints are

$$\min_{\Lambda,\Psi,U} \sum_{i,j} e_{ij}^2 + \alpha \sum_i t_i,$$

$r_{ij} - \sum_k \lambda_{ik}\lambda_{jk} - \delta_{ij}\psi_i = e_{ij}$, $t_i = \sum_k u_{ik}$, $\psi_{\mathrm{lb}} \leq \psi_i \leq \psi_{\mathrm{ub}}$, $e_{ij} = e_{ji}$, with δ_{ij} the Kronecker delta. Bilinear terms $\lambda_{ik}\lambda_{jk}$ induce nonconvexity, handled via Gurobi's nonconvex QCQP mode. A communality floor $h_i^2 = \|\Lambda_{i:}\|_2^2 \geq c$ can be enforced by $\psi_{\mathrm{ub}} = 1 - c$.

Initialization

Both formulations are warm-started in Harman style, akin to PAF [1]. Initial communalities are SMCCs from R, yielding $R^\star$ with $\mathrm{diag}(R^\star) = \mathrm{SMCC}(R)$. Let (V_m, D_m) be the top m eigenpairs of $R^\star$, where $V_m \in \mathbb{R}^{p\times m}$ is a matrix containing the top m eigenvectors on its columns and $D_m \in \mathbb{R}^{m\times m}$ is a diagonal matrix whose entries are the top m eigenvalues. By Eckart–Young [8], $\Lambda^{(0)} = V_m D_m^{1/2}$ [9]. Uniquenesses use $\psi_i^{(0)} = \max(0, 1 - h_i^2)$ with $h_i^2 = \|\Lambda_{i:}^{(0)}\|_2^2$.

Results

On the synthetic data generated ($p = 12$, $m = 3$, $n = 300$), both FISTA–EFA and QCQP–EFA recovered ground truth under moderate α, outperforming PAF in RMSE and Frobenius norm error; QCQP remained stable for $\alpha > 0.6$. Applied to a 38-item psychometric dataset ($N = 259$; KMO ≈ 0.83; Bartlett $p < .001$), both produced a coherent four-factor structure—emotional strain, self-efficacy, academic satisfaction, behavioral regulation—with Cronbach's $\alpha \approx 0.63$–0.75. Penalization removed minor cross-loadings and retained *theoretically* relevant low-communality items via a communality floor. Compared to PAF with Promax rotation, the proposed methods yielded a more parsimonious and interpretable structure, with clearer factor representation and fewer ambiguous item loadings. The integration of sparsity penalties guided the model toward stable, non-overlapping patterns that align more closely with theoretical constructs. Consequently, the resulting latent dimensions exhibit stronger conceptual coherence and greater robustness across initialization and regularization settings.

Conclusion

Penalized EFA integrates fit and interpretability in a single objective. A proximal FISTA scheme with row-wise group penalties and optional communality floors, and a nonconvex QCQP in Gurobi with auxiliary variables, both warm-started akin to PAF (SMCC-based), converge to near-identical stationary solutions. Moderate regularization recovers ground-truth loadings with stable sparsity and, on psychometric data, yields a coherent four-factor structure with satisfactory reliability (Cronbach's $\alpha \approx 0.63$–0.75). This approach delivers interpretability during estimation and subsumes rotations within a transparent optimization framework, outperforming the Classical PAF.

References

[1] H. H. Harman, *Modern Factor Analysis*. University of Chicago Press, 3rd ed., 1976.

[2] K. G. Jöreskog, "Some contributions to maximum likelihood factor analysis," *Psychometrika*, vol. 32, no. 4, pp. 443–482, 1967.

[3] H. F. Kaiser and J. Caffrey, "Alpha factor analysis," *Psychometrika*, vol. 30, pp. 1–14, 1965.

[4] H. F. Kaiser, "The varimax criterion for analytic rotation in factor analysis," *Psychometrika*, vol. 23, pp. 187–200, 1958.

[5] R. I. Jennrich, "Standard errors for obliquely rotated factor loadings," *Psychometrika*, vol. 38, no. 4, pp. 593–604, 1973.

[6] N. Parikh and S. Boyd, "Proximal algorithms," *Foundations and Trends in Optimization*, vol. 1, no. 3, pp. 142–160, 2014.

[7] A. Beck and M. Teboulle, "A fast iterative shrinkage-thresholding algorithm with application to wavelet-based image deblurring," in *Proceedings of the IEEE International Conference on Acoustics, Speech and Signal Processing (ICASSP)*, pp. 693–696, 2009.

[8] C. Eckart and G. Young, "The approximation of one matrix by another of lower rank," *Psychometrika*, vol. 1, no. 3, pp. 211–218, 1936.

[9] I. T. Jolliffe, *Principal Component Analysis*. Springer Series in Statistics, Springer, 2nd ed., 2002.

PREREQUISITE CONDITIONS FOR MAINTAINING THE NUCLEAR TRANSMUTATION IN LASER-DRIVEN SUBCRITICAL REACTORS

ANTONELA TOMA, RĂZVAN MORARU, ANDREI VASILE SPOIALĂ,
ŞTEFAN-MIHAI CURPĂN, ANDREI MANTA

The Center for Research and Training in Innovative Techniques for Mathematics Applied in Engineering "Traian Lalesc" (CiTi) of **the National University of Science and Technology "Politehnica" Bucharest**

ABSTRACT

The nuclear fission of reactive isotopes typically results in the occurrence of two daughter nuclei of similar atomic number (similar atomic masses).

At their turn the daughter nuclei have to release energy by particle emission, under the form of the alpha, beta, gamma particles, but both the daughter nuclei and the emitted particles (usually designated in literature as the nuclear waste) could have very long decay time, which yields to long exposure to radioactive effects and a menace to any life form.

To prevent the occurrence of such a bio-hazard, it is desirable to decrease the decay time. A way to achieve this aim is granted by the nuclear transmutation, a method that induce a new nuclear fission cycle in the long-life fission products (LLFPs) and actinides, for which the full decay time could last from the order to tens of thousands of years to million of years.

In order to induce new fission cycle in LLFPs or actinides, laser-driven subcritical reactors are used. These reactors make use of an in-flux of accelerated particles, typically protons, by the means of which, the bombardment of a spallation target (usually consisting of Tungsten atoms) is undergone, with the release of neutrons which at their turn induce the new nuclear fission cycle into the exposed nuclear waste.

Throughout the present article, we tried to assess the performances of a subcritical reactor driven by an in-flux of protons accelerated not by a classical particle accelerator (as the synchroton for instance is), yet by a Plasma Wakefield Particle Acccelerator, due to its sensible gain in sustainability, since a Plasma Wakefield Particle Accelerator could accelerate over a distance of just 100 m a flux of particles to a similar speed obtained into a classical cyclothron or synchroton, which would instead require an installation ranging to several kilometers and a huge consumption of energy.

In order to mathematically describe and assess the performances of the designated method we considered a mathematical model based upon the juxtaposition of the Bateman chain-reaction equations and the non-homogeneous Poisson Processes and as a result we deduced that a prerequisite for sustaining the nuclear transmutation and prevent it from collapsing into a classical decay reaction (transition mathematically described in terms of the secular equilibrium and homogeneous Poisson processes), and deduce as conclusion that the entire procedure amounts to the control of the spallation-neutron flux and consequently to the ability to control and modulate the speed of the plasma-wake field accelerated particles, by making use of the plasma accelerator's properties.

Keywords: Particle Accelerators, Nuclear Fission Product, Nuclear Transmutation, Nuclear Waste Recycling, Poisson processes, Bateman Equation

1. INTRODUCTION

Particle accelerators offer the capabilities of delivering high-flux, high-energy particles and serve as intense neutron sources, therefore constituting important tools for both the theoretical physics applied technology. State of the art conventional accelerators come with downsides such as them being intrinsically large (the Geneva CERN LHC encompasses a 27-kilometre ring of superconducting magnets), expensive, energy-hungry and require massive cryogenic infrastructure. This scale/energy cost barrier restricts their deployment for distributed or common industrial applications and is a principal obstacle translating accelerator-driven systems from concept to practical, wide-scale use. [12, 15]

As an alternative, plasma wakefield accelerators (PWFA) are being explored as potentially more energy-efficient sources of high-energy proton/electron beams. An electromagnetic wave is launched ahead of the particle beam as a driver. Through its interaction with the plasma, a wakefield is generated. In an analogous way to the surfers who gain speed by following the wave, the particle bunch is accelerated by the plasma oscillations induced by the driver wave. This mechanism enables extremely high acceleration gradients, allowing particles to reach relativistic energies over propagation distances as short as a few tens of meters - less than 100 m. [12, 14, 2, 15]

The motivation for writing this paper comes from the urgent need to address the risks of long-term storage of nuclear residues. This work explores the aspects of making accelerator-driven transmutation viable from both technical and economic standpoints and aims at integrating PWFA technology into practical accelerator driven waste remediation procedures. The main methods taken into consideration are: assessing the capabilities of the PWFA as a compact neutron driver, building the plasmaspallationtransmutation model needed to estimate performance, developing methods to maximize neutron yield and avoid limiting regimes.

2. THE BASICS OF NUCLEAR PHYSICS AND THE NUCLEAR DECAY

In order to understand the entire conceptual unfolding of the present article, a preliminary inroad upon the basics of nuclear physics is necessary.

E. Rutherford's experiment in 1909 confirmed the existence of subatomic particles - quanta. [1] The experiments and theory developed by Louis de Broglie in 1924, Erwin Schrdinger in 1925-1926, and the model proposed by Max Born during the 1926 Oxford conference demonstrated the dual nature of quanta, which can simultaneously be understood as: [1]

- Elementary particles/quanta (corpuscles) - the nature indicated by the experiments of Max Planck or A. Einstein
- And waves - the nature indicated by A. Compton's experiment

The manifestation universe of quanta is described by Quantum Mechanics, or more specifically by its Relativistic formulation, called the Quantum

We must consider that unlike all of Newtonian Mechanics (including its relativistic description) - where the energy values of physical systems form a continuum (can be modeled by continuous functions), at the quantum level, energy values are organized into discrete levels.

Quantum particles are "confined" to certain infinitesimal regions of space (in a certain sense, they have limited freedom of movement; for example, a particle that is part of a nucleon has a very restricted sphere of movement, and this movement is rather transformed into oscillation. This intuition is confirmed by de Broglie's duality principle: [1] wave-particle duality, so that each particle behaves like a string - more precisely, like a quantum harmonic oscillator, oscillating at certain frequencies. Thus, each wave-particle admits a certain discrete spectrum of oscillation frequencies. Moreover, the frequency values are linked to the possible energy values by the formula: [1]

$E = \hbar\omega$, where $\hbar =$ the reduced Planck constant and $\omega =$ frequency

For any quantum system, transitioning to a different energy level can only occur through - and the enitre quantum dynamics is in fact reduced to the following two phenomena: [1]

- Absorption of particles
- Emission of particles

These absorption, emission phenomena reside at the heart of the nuclear decay, because at the quantum level, dynamics are understood in terms of changes in the state of a particle, or a system of particles, and each quantum state has an associated a certain energy level $\rightarrow$ therefore, the dynamics of states involve changing the energy level as a result of interaction (mediated by bosons), in other words, the change of state will be the result of emission or absorption phenomena of particles (in the modeling of which bosons will intervene). [1] The root of these phenomena lies in Albert Einstein's famous relation: $E = mc^2$.

- This correlates the static and dynamic characteristics of the mass of substances.
- According to this relation: any rest mass of a body must correspond to an equivalent amount of energy released or absorbed by that body. [1, 3]

  If the mass of a body decreases, then it releases energy, by emitting particles, and if its mass increases, the respective body receives energy (absorbs particles) from an energy source.

The difference between the sum of the rest masses of all nucleons in the nucleus and the rest mass of the nucleus is called the mass defect, denoted by Δm This difference, the "mass defect" is transferred into the intranuclear binding energy (that intranuclear force that binds together the nucleons) which can be calculated using Einstein's relation. [1, 3, 5, 13]

In this way, the intranuclear energy that keeps particles together in the nucleus is calculated, energy that can be released upon the nucleus splitting through nuclear fission. [3, 5, 13]

The phenomenon occurs during the formation of any nucleus, the total mass of particles will decrease correspondingly with the release of an equivalent amount of energy, which is converted into intranuclear binding energy. The ratio between this energy and the number of nucleons that interacted during the formation of the nucleus (number of particles forming the nucleus, also denoted by A) is called: *average energy per nucleon*.

(1) So that, the higher this energy, the more stable the nucleus.
(2) Empirically, for heavy metals at the end of Mendeleev's table (for which A - the number of nucleons - is very large, greater than 200 nucleons), due to the very large number of nucleons, automatically the average binding energy per nucleon will have a smaller value and thus the nucleus will be more unstable $\rightarrow$ nuclear fission will be easier to trigger). [3, 5, 13]

Nuclear reactions can occur by bombarding a target nucleus with projectile particles, which can be: [3, 5, 13]

- Nuclear particles - nucleons (protons or neutrons)
- Nuclei (generally of Helium): He^{2+}
- Photons
- Electrons, neutrinos, or mesons

Two opposite types of nuclear reactions that release energy are possible:

The obtained energy is based on mass defects, which corresponds to less than a thousandth of the total mass of the nuclei participating in the reaction. It would be ideal to obtain energy corresponding to the entire mass of the participating nuclei, however, the annihilation of the entire mass of the nuclei is not physically possible.

Nevertheless, the energy of intranuclear bonds is on the order of MeV (the energy released by the fission of one kilogram of Uranium is comparatively equal to that released by burning 250,000 tons of coal). [3, 5, 13]

The basis of Nuclear Reactions lies in the fact that the nuclei of some uranium isotopes are very close the instability limit and under the shock of collision with a particle (for example by "bombarding" with neutrons) can fission. [3, 5, 13]

For example, the nucleus of the isotope $[235][92]U$, if hit by a neutron with energy 0.025 MeV, splits into two new nuclei of smaller mass (and two or three neutrons with sufficient energy to cause further splitting of uranium nuclei and thus chain reactions are achieved, which are self-sustaining).

Therefore, the generation of nuclear energy is inherently linked through fusion and fission processes to the release of intranuclear binding energy.[3, 5, 13]

2.1. **Nuclear Decay.** The decay of a nucleus represents the transition of a nucleus from a quantum state associated with a higher energy level to a quantum state associated with a lower energy level - through the emission of particles (radiation) - of alpha, beta, or gamma type. In other words, radioactivity essentially represents the result of the phenomenon of decay of an unstable nucleus; more precisely, when a nucleus has an excess of energy, it becomes unstable, and to reach a form of equilibrium (to migrate toward the valley of beta-stability), it will release the excess energy through particle emission - via radioactive decay. [3, 5, 13]

In particular, for the case of interest, the decay of a nucleus (also called the ”parent nucleus”) from an initial state of excessive energy to a lower energy state by releasing particles (even nuclei in the case of the fission phenomenon) will be referred to as daughter nuclei; from all the particular cases of radioactive decay. [3, 5, 13]

Particular Cases of Radioactive Decay of the Nucleus.

- gamma decay
- beta decay
- alpha decay

We are going to focus just upon the alpha-decay, which could be rendered as prefiguration of the nuclear fission.

Nuclear fission represents the splitting of an unstable nucleus (as some of the Uranium isotopes are) into two daughter nuclei of approximately equal masses with release of energy (the daughter nuclei are the fission products or radioactive/nuclear wastes and represent a bio-hazard, since they still undergo (long-time) decay processes to attain beta-stability) [3, 5, 13]

2.2. **Nuclear Fission and the Radioactive Residues.** Nuclear fission products are the atomic fragments (daughter nuclei) resulting from the fission of the parent nucleus. Typically, a nucleus with a high atomic mass, such as Uranium, undergoes fission by splitting into:[3, 5, 13]

- Two daughter nuclei - with considerably smaller mass
- A few neutrons
- The release of thermal energy (derived from the kinetic energy of the nuclei)
- With the release of gamma radiation

The two daughter nuclei represent nuclear fission products, but they are also designated by the term radioactive products or radionuclides. Since the daughter nuclei are very unstable isotopes and consequently radioactive, they will emit radiation in order to transform into a more stable atom.

Due to the radiotoxicity of the radionuclides that make up the nuclear residue and the biohazard it can generate, the issue arises of storing these residues under maximum security conditions (the creation of nuclear waste repositories being a problem in itself), or finding alternative ways to ”recycle” these residues.

The shorter the lifespan, particularly the half-life, the greater the amount of emitted radioactivity and the faster the disintegration of the radionuclides occurs.

Additionally, there is also the possibility that certain reaction products may decay into other unstable radionuclides, which in turn will emit radiation, and this must be taken into account when planning the storage capacity and duration of nuclear waste. [9]

Through the process of Uranium fission, hundreds of different radionuclides can result, however, these can be classified into 5 categories based on their decay duration: [9, 6]

- Fission products with an extremely short lifespan:
  Radioactivity levels drop very quickly in the case of fission products with a short lifespan, and these are so predominant that within less than 1 month after removal/extraction from the nuclear reactor, 87% of the nuclear residue will have already disintegrated, transforming into stable isotopes.
- Fission products with a short lifespan:
  I^{131}, Ba^{140} - with a lifespan of a few weeks.
- Fission products with a medium lifespan - a few years
- Fission products with a long lifespan - several decades
- Long-lived fission products (LLFPs) - millions of years [6]

Wherefore arises the necessity to emply a method of nuclear for achieving the decrease in the half-life time for the major actinides and the LLFPs.

2.2.1. *Transmutation of LLFPs and Nuclear Reprocessing of Actinides Using Accelerator-driven Subcritical Reactors.* Neutron fluxes generated in subcritical reactors with the help of particle accelerators (particularly with the aid of accelerated proton fluxes) can be applied equally to actinides and LLFPs, to reduce their lifespan and automatically the associated radiotoxicity; but it must be mentioned from the outset that the mode of operation on actinides will differ from the mode of operation on LLFPs: [6, 10]

- LLFPs will undergo nuclear transmutation, through which they will be stabilized ”instantly”
- while actinides will be reprocessed, more precisely, they will undergo a process of nuclear fission.

3. Deriving the Mathematical Model for the Plasma Accelerated Transmutation

In order to decrease the half-life of the LLFPs and actinides, the authors of the present article proposed the use of an plasma-wake field accelerated particles influx. As it will be explained in what follows, the LLFPS's lifetime could be achieved by the means of an Accelerator Driven Systems through a process called Spallation - the entire process being driven by an influx of accelerated particles. [6, 10, 8, 7]

Accelerator Driven Systems (ADS) and the Spallation Process. The main components for a sub-critical nuclear reactor are: [6, 10]

- the particle accelerator, that generates the proton strem. The authors opted for a plasma wake-field accelerator, due to its innovative properties comparing to the classical particle accelerators.
- a target, classically made of Tungsten, on which the spallation is produced, dispatching by collision with the influx of accelerated protons, an in-flux of neutrons which will induce a transmutation chain
- into the high-level waste, located into the reactor core. [6, 10]

More precisely, the radioactive wastes is irradiated by the strong flux of neutrons produced by the spallation neutron source.

Thus the spallation process can be defined as consisting of 2-step phenomenon: [6, 10]

- the first step takes place inside the target nuclei of Tungsten. The primary particle reacts with nucleons-neutrons and protons, producing an internuclear cascade of high energy (more than 20 MeV) protons, neutrons and pions within the nucleus. During the intranuclear cascade, some of these energetic hadrons escape as secondary particles, while others deposit their kinetic energy in the nucleus, leaving it in an excited state.
  This is followed by the nuclear de-excitation. Evaporation takes place when the excited nucelus of Tungsten relaxes by emitting low-energy (less than 20 MeV) neutrons, protons, alpha particles, with the majority of the particles being neutrons. The low energy neutrons produced during the nuclear de-excitation are important in a spallation source because they can be moderated to even lower energies for use as research probes.
- Secondary high-energy particles produced during the intranuclear cascade move roughly in the same direction as that of the incident proton and can collide with other nuclei in the target. The reactions that follow are a series of secondary spallation reactions that generate more secondary particles and low energy neutrons. The so-called hadronic cascade is the accumulation of all reactions caused by primary and secondary particles in a target. [6, 10]

The most efficient neutron production, in terms of neutrons per incident proton, occurs with proton energies between 1 and 1.5 GeV, within which each proton can produce 15 to 25 neutrons; such high energy levels are required because lower energy protons (in the MeV range) are less efficient, lacking the necessary energy to trigger the multineutron cascade and evaporation process. [6] This speed could be accelerated in the in-flux of protons by the means of a plasma wakefield accelerator, wherefore, aside from its superior sustenaibility, stems the reason for proposing the use of this kind of accelerator.

Regarding the neutron flux distribution: it could be shown that the number of neutrons produced by spallation is proportional to the proton beam power $P = U \cdot I$. Nevertheless, it was experimentally shown that the neutron yield per 1W of proton beam power is almost independent on beam energy above approximately 1 GeV. [6]

Devising the Mathematical Model.

Poisson Probability Law and the Bateman Equation. Provided that the decays alter the concentration of given isotopes, these two mathematical models are inherently related as we are going to see.

A.1. The Probabilistic Model. The probabilistic model is based upon the Poisson probability law that describes the probability as at a moment t to be recorded k events of disintegration (in our case nuclear transmutation induced by neutron-nucleus fission reactions). This probability is considered to follow a Poisson distribution: [3, 6, 7]

$$P(y_t = k) = \frac{(\lambda t)^k}{k!} \cdot e^{-\lambda t}$$

Where:

y_t = the random variable that counts the number of nuclear events (involved in the general scheme of transmutation) that occur at the moment t ($t > 0$) [3]

λt = the decay constant specific to the considered nucleus

Actually, the λt, the expected average number of events, is exactly the expected value (the means) for the random variable y_t, which can be depicted under the possibility table: [3]

$$y_t \sim k, \quad p_k = \frac{(\lambda t)^k}{k!} \cdot e^{-\lambda t}$$

So that:

$$E[y_t] = \sum_{k=0}^{\infty} k \cdot \frac{(\lambda t)^k}{k!} \cdot e^{-\lambda t} = \lambda t$$

Supposing that one considers the collection of Poisson random variables y_t ($t \geq 0$) that describe the number of decay events at each moment, we obtain a Stochastic Process $(y_t)_t$, which can statistically/probabilistically describe the (long-term) evolution of the investigated physical phenomenon. [3, 6, 7]

The Deterministic Model. The deterministic model is based on the Bateman equation. This model describes the general mean of nuclide concentration in a decay chain, and it is used therefore to predict the amount of each isotope at a specific point in time. [6, 10, 3, 7, 8]

In order to quantify/evaluate the decay process several measures could be introduced:

A = the activity, the number of disintegrations per second, this value is numbered also by the random variable y_t and thus $A = y_t$ (this could be related to the phenomenon of nuclear spallation, because the number of neutrons procured by spallation yield to an enhanced number of transmutation processes in the given mass of actinides and LLFPs)

N = the number of nuclei in the sample. Considering the induced decay consists just in a first order reaction, the sample activity A is proportional to N.

λ = the proportionality constant (the decay rate). $A = \lambda N$

In addition, the activity is defined as the number of disintegrations per second:

$$A = \frac{N(t) - N(t+\Delta t)}{\Delta t} \Rightarrow A = -\frac{dN}{dt} \quad \text{for } \Delta t \to 0$$

$$-\frac{dN}{dt} = \lambda N \Rightarrow N(t) = N(0) \cdot e^{-\lambda t}$$

The decay constant λ is inherently related to the lifetime of the investigated nucleus ($\tau = \frac{1}{\lambda}$), so that the nuclear decay law can be rewritten as:

$$N(t) = N(0) \cdot e^{-t/\tau}$$

After the time $t = \tau$, the number of radioactive nuclei in the sample is reduced through the constant e:

$$N(\tau) = N(0) \cdot \frac{1}{e}$$

The half-life $T_{1/2}$ stands for the time after which the number of radioactive nuclei in a sample is reduced to half of its initial value and at $T_{1/2}$, the number of radioactive nuclei could be expressed as: [7, 3, 6]

$$N(t = T_{1/2}) = N(0) \cdot e^{-\lambda T_{1/2}} = \frac{1}{2} N(0) \Rightarrow T_{1/2} = \frac{\ln(2)}{\lambda} = \ln(2) \cdot \tau \approx 0.693 \cdot \tau$$

Variants of the Bateman Equation in Serial and Nonlinear Decay Models.
The Bateman equation is a mathematical model describing abundancy/concentration and activities a decay reaction, which can naturally be generalised for a decay chain as a function of time - based on the decay rate s and initial abundancies. It designates rather a system of differential equations, than a single differential equation. It is rather a method for setting up differential equations describing the chain of interest based on known properties. [8]

The Bateman equation for the two-decay chain

We are going to consider a two-decay chain - through the simplest case of a parent nuclei feeding (by decay/transmutation) a daughter sample of (transmuted) nuclei. [8]

The following notations will be made:

- The initial number of parent and daughter atoms: $N_1(0), N_2(0)$
- The number of parent and daughter atoms in time: $N_1(t), N_2(t)$
- The parent and daughter activities in time: $A_1(t), A_2(t)$
- The parent and daughter decay rates: λ_1, λ_2

The equation for the time evolution of the parent is the same as for a single step decay:

$$\frac{dN_1(t)}{dt} = -\lambda_1 N_1(t)$$

The equation for the time evolution of the daughter, however, includes a term describing daughter decay but also daughter feeding by the parents: [8]

$$\frac{dN_2(t)}{dt} = -\lambda_2 N_2(t) + \lambda_1 N_1(t)$$

The solution for the single step decay is:

$$N_1(t) = N_1(0) \cdot e^{-\lambda_1 t}$$

By substituting this into the second equation, we obtain: [8, 7, 3, 7]

$$\frac{dN_2(t)}{dt} = -\lambda_2 N_2(t) + \lambda_1 N_1(0) \cdot e^{-\lambda_1 t}$$

The final solution is obtained by applying Lagrange multipliers method:

$$N_2(t) = N_2(0) \cdot e^{-\lambda_2 t} - N_1(0) \cdot \frac{\lambda_1}{\lambda_2 - \lambda_1} \cdot (e^{-\lambda_2 t} - e^{-\lambda_1 t})$$

Activities of the parent and the daughter can be calculated from: [8]

$$A_1(t) = \lambda_1 N_1(t) = \lambda_1 N_1(0) \cdot e^{-\lambda_1 t}$$

$$A_2(t) = \lambda_2 N_2(t) = \lambda_2 N_2(0) \cdot e^{-\lambda_2 t} - N_1(0) \cdot \frac{\lambda_1 \lambda_2}{\lambda_2 - \lambda_1} \cdot (e^{-\lambda_2 t} - e^{-\lambda_1 t})$$

The Bateman equation for a general serial decay chain:

The time evolution of nuclide concentration undergoing a serial linear decay chain is governed by a set of first-order differential Bateman equation - which extend the anterior presented case. The Bateman equations for the radioactive decay case of nuclide series in linear chain describing nuclide concentrations appear as a system: [8]

$$\frac{dN_1(t)}{dt} = -\lambda_1 N_1(t)$$

$$\frac{dN_i(t)}{dt} = -\lambda_{i-1} N_{i-1}(t) - \lambda_i N_i(t) \quad \text{for } i \in \{2, \ldots, n\}$$

Assuming zero concentrations of all daughters at time zero: $N_1(t=0) \neq 0$, $N_i(t=0) = 0$ for all $i > 1$, the concentration of the n-th nuclide after time t was given by Bateman: [8]

$$N_n(t) = N_1(0) \cdot \lambda_n \sum_{i=1}^{n} \left(\frac{\prod_{j=1, j\neq i}^{n} \lambda_j}{\prod_{j=1, j\neq i}^{n} (\lambda_j - \lambda_i)} \cdot e^{-\lambda_i t} \right)$$

The Bateman equation for nuclear (nonlinear) transmutation chain: [8, 6, 10]

In a transmutation system, the nuclides are being transmuted also due to interactions with the particles flux (that emerges from the accelerated proton

beam collided spallation target). These particles being mainly nucleons, but in the presence of a spallation target also high energy protons or pions. The decay constants that govern Bateman equations for a decay case are then substituted by transmutation constants.

At this point, by the transmutation constants λ_{ij} we understand the probability of the i-th nuclide production per time unit from the j-th nuclide destruction, as a result of the nuclear interaction with the whole spectrum of interacting particles (particularly due to the nuclear interactions with the neutron-flux) or simply due to the induced nuclear decay.

We define:

- λ_j as the decay constant of the j-th nuclide
- b_{ij}^d as the branching ratio of the j-th nuclide decay into the i-th nuclide
- ϕ_{neutrons} as the incident neutron flux
- σ_{ij} as the cross section for production of the i-th nuclide by neutrons during interactions with j-th nuclides [6, 10]

$$\lambda_{j\to i} = \lambda_{ij} = b_{ij}^d \cdot \lambda_j + \int \phi_{\text{neutrons}}(E) \cdot \sigma_{ij}(E)\, dE$$

Where the terms: $b_{ij^d} \cdot \lambda_j$ account for the spontaneous disintegration - characterising the phenomenon of natural-occuring decay. Therefore in order to sustain the phenomenon of nuclear transmutation and prevent it from collapsing into the classical long-term decay, the decisive factor is embodied by:

$$\int \phi_{neutrons}(E) \cdot \sigma_{ij}(E) dE$$

Moreover the transmutation constants appear as the coefficients of the Bateman equations describing the general, non-linear transmutation chain for which w nuclides as follows:

$$\frac{dN_i(t)}{dt} = \sum_{j=1}^{w} \lambda_{ij} \cdot N_j(t)$$

Where: $N_j(t)$ denotes the concentration of the j-th nuclide (at time t); the constants which are not covered in the previous equations are defined using the mass flow balance and they physically represent nuclide disintegration rate $\lambda_{ij} = -\sum_{j=1, j\neq w}^{w} \lambda_{ij}$; $i \in \{1, \ldots, w\}$

The set of equations:

$$\frac{dN_i(t)}{dt} = \sum_{j=1}^{w} \lambda_{ij} \cdot N_j(t)$$

Mathematically represents a system of first-order linear differential equations, the solution of a complex case be obtained as a linear superposition of the solutions in simpler case.

RELATING THE BATEMAN EQUATION FOR THE NUCLEAR TRANSMUTATION TO THE INCOME FLUX OF NEUTRONS

This intrinsic link between the mathematical model for the transmutation reaction and the nuclear spallation - via the incident flux of neutrons (that will lead us also to a formula for embedding the plasma wake-field accelerators' parameters) resides in/revolves around the term: [4, 11, 8]

$$\int \phi(E) \cdot \sigma_{ij}(E)\, dE$$

Definition of the Differential Neutron Flux $\phi(E)$. $\phi(E)$ describes the distribution of neutron with respect to their kinetic energy, in the form of a function that illustrates the number of neutrons at each specific energy level: [4, 11, 8]

$$\phi(E) = \phi(E,\vec{r},t) = n(E,\vec{r},t) \cdot v(E)$$

Where:

$n(E,\vec{r},t)$ is the neutron density, the number of neutrons per unit volume at a specific position $\vec{r}$, with an energy E, at a time (measured in neutrons/cm^2)

$v(E)$ is the neutron velocity, directly related to its kinetic energy E by the classical equation:

$$E = \frac{1}{2} m \cdot v^2$$

The Neutron Density $n(E,\vec{r},t)$. The Neutron density is intrinsically related to the phenomenon of nuclear spallation - which actually represents the source for these neutrons. We have to understand how the parameters of the plasma wake-field accelerated proton beam influence the phenomenon of spallation and thus the term: $n(E,\vec{r},t)$ [4, 11, 8]

The physical meaning of the terms in the integral $\int \phi(E) \cdot \sigma_{ij}(E)\, dE$: [4, 11, 8]

- E (the integration constant) represents the kinetic energy of the incident neutron, since not all the neutrons in a system have the same energy (they exist over a wide spectrum of energies, from very slow thermal neutrons to fast neutrons with millions of electron volts (MeV) of energy).
- dE (the integration domain) represents the entire range of possible neutron energies present in the system, from zero to the maximum possible energy. It is not a fixed, universal range, but rather depends on the specific physical environment being modeled.
- $\phi(E)$ is the differential neutron flux, which describes the density of neutrons per unit energy at a given energy.
- $\sigma_{ij}(E)$ are the microscopic cross-sections, namely the probability of a specific transmutation reaction of the j-th nuclide into the i-th nuclide, which can occur by neutron capture or fission occurring at

a given neutron energy E (the cross-sections are highly dependent on energy with large spikes at certain energies).

The physical meaning for the entire integral within the expression of the reaction rate is that this quantity represents the macroscopic reaction rate per target nucleus. It gives the average probability per second that a single nucleus will undergo the specified reaction, considering the full energy spectrum of neutrons.

This would represent the "transmutation constant" for a neutron induced reaction. To get the total number of reactions per unit volume per second, this integral is multiplied by the number density of the target nuclei yielding to the classical-like notion of:

$$\text{Reaction Rate} = \left[\int \phi(E) \cdot \sigma_{ij}(E)\, dE\right] \cdot N_i$$

Within this context, for the nuclear transmutation reactions, the incident neutrons flux could be understood as similar to a "catalyst" in the sense that its presence hastens or favours/increases the production of new more stable nuclides, once with the consumption of the given nuclear wastes.

The physical meaning of the terms in the integral $\int \phi(E) \cdot \sigma_{ij}(E)\, dE$ is essential for understanding the efficiency and dynamics of neutron-induced transmutation processes. It connects the microscopic nuclear physics with the macroscopic engineering of spallation sources and accelerator-driven systems.

3.1. **Adapting the plasma-wake-field accelerated proton beam in order to facilitate the Nuclear Transmutation.**

We are going to witness that a collection of Poisson Random Variables, each of them depending on the same parameter: λ not only will be enough for describing the reaction chain ascribed by the Nuclear Transmutation, but it will furthermore represent a limit case, whose realization we will have to avoid.

To this end we are going to directly make use of the Reaction Rates obtained by the Bateman-Equations for the chain of reactions - embodied by the Nuclear Transmutation - and integrate into a broader mathematical model, broadening at the same time the embedding/integration of the plasma-wake-field accelerated protons beam into the mathematical model.

3.1.1. *Non-Homogeneous Poisson Processes (NHPP):.* A counting process: $\{N_t\}_{t\geq 0}$ is called a **non-homogeneous Poisson process** - with the intensity function: $\lambda(t)$, whenever the following three conditions are met: [7]

i) $N_0 = 0$

ii) $\forall) t > 0$: the random variables N_t (which constitute/make the stochastic process up) are Poisson distributed, with the average: [7]

$$m(t) = \int_0^t \lambda(s) ds = \mathbb{E}[N_t]$$

$\rightarrow$ The function $t \mapsto \lambda(t)$ being known in literature as the intensity function (generalisation of the Poisson (constant) parameter λ)

iii) For any set of temporal-indices: $0 \leq t_1 < t_2 < \cdots < t_n$:

$$N_{t_1}, N_{t_2} - N_{t_1}, \cdots, N_{t_n} - N_{t_{n-1}}$$

- Are independent random variables.

$\downarrow$

Therefore, using the definition of the random variables' independence, we obtain:

$$\begin{aligned}
&\mathbb{P}(N_{t_1} = k_1, N_{t_2} = k_2, \cdots, N_{t_n} = k_n) \\
&= \mathbb{P}\left(N_{t_1} = k_1, N_{t_2} - N_{t_1} = k_2 - k_1, \cdots, N_{t_n} - N_{t_{n-1}} = k_n - k_{n-1}\right) \\
&= \frac{e^{-m(t_1)\cdot(m(t_1))^{k_1}}}{k_1!} \cdot \frac{e^{(-(m(t_2)-m(t_1))} \cdot (m(t_2) - m(t_1))^{k_2-k_1}}{(k_2-k_1)!} \cdot \cdots \cdot \frac{e^{(-(m(t_n)-m(t_{n-1}))} \cdot (m(t_n) - m(t_{n-1}))^{k}}{(k_n-k_{n-1})!}
\end{aligned}$$

If one sets: $\lambda(t) = \lambda, \forall) t \geq 0$, in the result, it will be obtain a regular Poisson process. So that **the Poisson processes** can be rendered as a particular class of the nonhomogeneous Poisson processes. [7]

For a non-homogeneous Poisson Process, we can also mathematically describe how the counted events are situated in time: [7]

For instance we can consider S_n the time of the n^{th} occurence (event):

$\rightarrow$ S_n is an (extended) random variable (that generalizes a Poisson distribution) with values in $[0; \infty)$ an:

$$\mathbb{P}(S_n > t) = \mathbb{P}(N_t \leq n-1) = \sum_{i=0}^{n-1} \frac{e^{m(t)} \cdot (m(t))^i}{i!}$$

- If: $\lim_{t\to\infty} m(t) = \infty$, then:

$$\mathbb{P}(S_n = \infty) = \lim_{t\to\infty} \mathbb{P}(S_n > t) = 0$$

The density of S_n is

$$\rho_{S_n}(t) = \frac{e^{-m(t)} \cdot (m(t))^{n-1} \cdot m'(t)}{(n-1)!} = \frac{e^{-m(t)} \cdot (m(t))^{n-1} \cdot \lambda(t)}{(n-2)!}, t \geq 0$$

As well as the interarrival time: $T_n = S_n - S_{n-1}$ - which for a nonhomogeneous Poisson process $(T_n)_{n\in\overline{1,\infty}}$ are not necessarily indpeendent random variables (which generalizes the notion of an exponential random variable): [7]

- For $0 \leq s \leq t$:

$$\begin{aligned}\mathbb{P}(T_{n+1} > t | S_n = s) &= \mathbb{P}(S_{n+1} > s+t | S_n = t) = \mathbb{P}(N_{s+t} = n+1 | S_n = t) \\ &= \mathbb{P}(N_{s+t} - N_s = 1 | S_n = t) = \mathbb{P}(N_{s+t} - N_s = 1) \\ &= e^{-(m(s+t)-m(s))}\end{aligned}$$

Remark: notice that $S_n = t$ depends on the non-homogeneous Poisson process until time t $\Rightarrow$ hence: $\{N_{s+t} - N_s = 1\}$ and $\{S_n = t\}$ are independent.

The nonhomogeneous Poisson processes are an instance of Markov processes. [7]

The reason behind the option to work with Nonhomogeneous Processes: *One can* ***render the nuclear transmutation as a chain of reactions****, each of them being described by its own reaction rate:* $\lambda(t)$*, therefore* ***one can mathematically describe the nuclear transmutation by the means of a non-homogeneous Poisson process*** *- whose intensity functions are exactly the reaction rates* $\lambda(t)$. [7, 8, 4, 11, 6, 10, 9]

Therefore, the adequate framework for describing the evolution of the nuclear transmutation chain of reactions (in terms of counting the decay events), is embodied by the Nonhomogeneous Poisson Processes.

- The general solution for the number of atoms of nuclide N_i in a linear decay chain is:

$$N_n(t) = N_1(0) \cdot \Pi_{i=1}^{n-1} \lambda_i(t) \cdot \sum_{i=1}^{n} \frac{e^{-\lambda_i(t)}}{\Pi_{k=1, k \neq i}^{i} (\lambda_k - \lambda_i)}$$

$\Rightarrow$ The long-term behaviour of $\lambda_n(t)$ depends on the relationship between the decay constants in the chain:

- So that, supposing: $\lambda_1 << \lambda_2, \lambda_3, \cdots$ - which corresponds to the case where the parent nuclide N_1 has a much longer half-life (a much smaller decay constant), than all its daughter products, the system will eventually reach a state of **secular equilibrium** - withouth having attaining the $\beta-$stability.

$\Rightarrow$ **Nevertheless, this case should be avoided by any means, because our goal is to hasten the decay of a long-lived parent nuclide and transform it into a stable or short-lived product; in fact we are trying to extinguish the long lived parent**.

– Assuming that we describe the nuclear transmutation in terms of a non-homogeneous Poisson Process, the secular equilibrium could be understood/rendered as a limiting case - embodied by a Poisson process - obtained as a state of assymptotic stability.

⇢

This could be achieved by **Neutron bombardment** - which effectively yields the nuclear transmutatioin.

In fact, the development of the nuclear transmutation depends upon:

The high flux of neutrons - that result through the nuclear spallation phenomenon and feeds the nuclear transmutation

↓

As we have already seen the reaction rates could be expressed as functions depending on the flux of neutrons, on the other side, this functional expression also englobes the cross-section σ (the probability of nuclear interaction).

And the cross-sectionss depend on the energy of the neutron influx ⇒ therefore, achieving the goal of nuclear transmutation also depends upon **maintaining a broad spectrum of neutron energy spectrum**.

→ **Maintaining a broad spectrum of neutron energy spectrum could be achieved by controlling the proton beam energy**

⇒ The neutrons' energy inherently depends upon the speed of the incident accelerated proton beam, therefore attaining a broad neutron energy spectrum could be achieved by controlling (changing - modulating the speed of the accelerated protons).

⇒ **The arrising question resides in how could one modify the speed of the accelerated protons within the Plasma-Wakefield Accelerator?**

⇒ A series of articles propose as solution the use of plasma density perturbation as a mean of controlling the particle acceleration.

⇒ As a solution for preventing the non-Homogeneous Poisson process associated to the transmutation-Bateman chain of equations from turning into a classical Poisson process (which embody the model for the long-term decay), the authors of the article propose the speed control for the plasma wake-field accelerated proton beam, since in this way, a broader energy spectrum of spallated neutrons could be achieved, leading to a full coverage of the LLFPs fission threshold.

In order to achieve this aim the authors propose the adapting of the plasma wake-field accelerator **the authors of the present article propose the following strategy**:

- In order to prevent the transmutation chain to turn into a long-term decay for the LLFPS, the spallated neutron flux should have a maintained broad spectrum.

- Since the spallation (dislocation of the neutron from the Tungsten target) inherently depends upon the in-flux of accelerated protons, the energy of dislocated neutrons automatically inherits the momentum impressed by the colliding proton.
- Therefore the authors propose as solution the control of the proton beam energy, in the sense of inducing a broad energy spectrum for the proton beam, which could be obtained by making use of the particle wake field accelerator - by the means of the frequency modulation within the plasma wake-field accelerator.
- At this point, it is required to return at the mechanism behind the plasma wake-field accelerators, where an ultra-fast laser pulse (the witness beam or the driver beam) induce the plasma wake-fields, which accelerate the injected particles (in the present case, the accelerated protons). Given this mechanism, a frequency modulation could be indirectly induced for the accelerated proton beam by operating through the driver ultra-fast laser pulse. [12, 14, 2, 15]
- By frequency-modulating the drive ultra-fast laser pulse for the wake-field plasma accelerator, the proton beam will authomatically inherit a modulation of their frequency, which will be further transfered into the multifarious energy spectrum of the spallated neutrons.

$\Rightarrow$ **The phase or frequency modulation techniques for plasma accelerated particles are well established** [12, 14, 2, 15]**, nevertheless there was no article which to propose this technique as a solution for maintaining/feed the chain of nuclear transmutation of LLFPs.**

REFERENCES

[1] A.Belyaev, D.Ross, *The basics of Nuclear and Particle Physics*, Springer, 2021

[2] A.Cakir, O.Guzel, *A brief review of plasma wakefield acceleration*, Dept. of Phys. Eng., Istanbul Technical University, 2020

[3] W.Daucey, *High Energy Physics*, lecture nots, Imperial Colledge, 2020

[4] S.Gales, *Nuclear Energy and Waste transmutation with high power acceleration and laser systems*, ELI-NP and IPN Orsay, France, 2019

[5] N.A.Jelley, *Fundamentals of Nuclear Physics*, Cambridge University Press, 2012

[6] K.Katovsky, V.K.Verma, *Spent nuclear fuel and accelerator driven subcritical systems*, Springer, 2019

[7] Y.A.Katoyants, *Introduction to the statistics of Poisson Processes and Applications*, Springer, 2023

[8] Z.Meisel, *Nuclear Physics*, Lecture Notes, Ohio University, 2017

[9] National Research Council USA, *Nuclear Wastes: Technologies for Separation and Transmutation*, 1996

[10] H.Nifenecker, O.Meplan, S.David, *Accelerator Driven Subcritical Reactor*, CRC Press, 2023

[11] J.Sanz, R.de la Fuente, J.M.Perlado, *Impact of the neutron flux on transmutation products at fussion reactor first-walls*, Science Direct, 1988
[12] A.Seryi, E.Seraia, *Unifying Physics of Accelerators, Lasers and Plasma*, CRC Press, 2023
[13] P.Talou, R.Vogt, *Nuclear Fission*, Springer, 2023
[14] X.Xu, *Phase space dynamics in plasma based wakefield acceleration*, Springer, 2020
[15] H.Wiedemann, *Particle Accelerator Physics*, Springer, 2015

A RESEARCH ON THE POSSIBILITY TO SAFELY USE THE RAMAN SPECTROSCOPY IN-VIVO

ANTONELA TOMA, RĂZVAN MORARU, DIANA RADU,
AND ALEX-ANDRA CRISTACHE

'Traian Lalescu" Center for Research and Training in Innovative Techniques of Applied Mathematics in Engineering of the The National University of Science and Technology "Politehnica" Bucharest

ABSTRACT: The present article investigates the required conditions for the safe intra-operatory use of an alternative approach to achieve a better intra-operative conduct of the Raman spectroscopy by using optical solitons. The article briefly presents the principle of the Raman spectroscopy as well as its limitations. In order to surpass the barrier embodied by the limited amount of back-scattered photons and grant more accuracy to Raman spectroscopy, the authors proposed as alternative the use of ultra-short soliton pulsed laser instead of a classical (continuous wave) laser. This strategy does not constitute in itself an element of originality, since there exists numerous references to the conjoined use of Raman spectroscopy and the ultra-fast solitonic-pulsed laser, yet to the best of the authors' knowledge, there is still none article to assess the potential risk this method might pose to the human health when used in-vivo.

In order to attain a better insight of the ways to avoid any potential risk against the human safety, the authors, revised the theory of solitonic pulsed laser signals based at core on mode-locking in order to produce the characteristic balance between the Kerr-nonlinearity and dispersion. The article also offers a survey of the most prominent risks of laser-tissue interaction and also expresses the underlying relation between these risks and the way how they get reduced just to the interplay between the photothermal and photochemical effects.

The amount of energy released by the laser and thereafter converted by exposure into heat leading to the damaging effect of tissular overheating is described by the Pennes bioheat equation. Therefore the authors verified whether the Lyapunov stability of this could be obtained as a variation of the heat equation depending upon the laser's parameters. Nevertheless, in result, it was obtained that regardless of the initial conditions adjustment, the Lyapunov stability is impossible to be achieved. Therefore the authors had to devise a new strategy for preventing the occurrence of the photothermal and photochemical adverse side-effects. This strategy relies upon the pulsed very nature of the solitonic laser signal and the adjustment:

- interpulse duration - larger than the vibrational relaxation (which prevents the free radicals generation)
- the duration of each pulse, chosen to be less than the time required for overheating of the tissular structure.

The chosen frequency spectrum interplay with the laser's energy also plays a crucial role as the calculations undergone for a concrete study case reveal in the last section of our research.

As a conclusion, the authors found that by adapting the laser's parameters according to the above mentioned strategy could grant both scientific accuracy and the avoidance of harmful impact upon the clinically-exposed patients for the Raman spectroscopy used in-vivo.

Key-words: Raman Spectroscopy, Solitonic ultra-short pulsed lasers, laser-matter interaction side-effects and risks, Bio-heat equation's stability

1. INTRODUCTION

Raman spectroscopy grants the possibility to fully classify substances - ranging from molecules to biological tissues or crystal structures based upon their vibrational modes. [8, 6] Therefore foreboding promises of this technique in the field of cancer prevention and intra-operative guided surgery have aroused a great interest in the last 25 years, numerous medical articles record the need for further in-vivo investigation tools, particularly in the malign-tissue identification - both in clinical exams and in surgery; more precisely Raman spectroscopy was designated as a tool to respond to the need for diagnostic tools for biopsy guidance for early diagnosis of (pre-)malignant, surgery guidance, which can be used intra-operative assessment of resection margins to achieve adequate tumour resection. [7, 9]

Moreover that fibre-optic probes have enabled the use of Raman spectroscopy for in vivo clinical applications. The integration of Raman spectroscopy with other diagnostic techniques has been a major step in the de-

mechanisms.

Raman spectroscopy takes advantage of the fact that for each chemical sample is uniquely characterise by the frequency ν_{probe} of its vibrational modes. [8, 6, 12, 1]

A laser pulse is emitted towards the sample. Supposing that the laser's electromagnetic frequency ν matches the samples frequency, a phenomenon of interference or absorption takes place. [8, 6, 12, 1]

At the same time, this interactions also leads to the transformation of th sample's molecular structure into a dipole, whose oscillatory/vibrational motion can lead to the (inelastic) back-scattering of the initial laser pulse with a modified frequency: $\nu - \nu_{probe}, \nu + \nu_{probe}$.

More precisely, the detector is an interferometer that records the signals that return after contact with the sample - through the phenomenon of reflection - Raman scattering: [8, 6, 12, 1]

- $A_{modified} \cdot \cos(2\pi(\nu - \nu_i)t)$ - stands for the Stokes-shifted Raman scattering where the scattered light has a frequency lower than the incident light by ν_i
- $A_{modified} \cdot \cos(2\pi(\nu + \nu_i)t)$ - stands for the anti-Stokes shifted Raman scattering, where the Amplitude of the scattered light has a frequency higher than the the incident light by ν_i.

  Where: $A = \frac{1}{2}\frac{\partial\alpha}{\partial q^i}E_0 q_0^i$ stands for the amplitude of the spreaded Raman wave.

  Thus the received signals, once subjected to the Fourier transform: [8, 6, 12, 1]

$$\mathcal{F}[s](\nu) = \int_{-\infty}^{\infty} s(t)e^{-i2\pi\nu t}dt$$

  $\rightarrow$ grant us the frequency for any received signal: [8, 6, 12, 1]

$$S_{Stokes_Raman}(t) = \mathcal{F}[A\cos(2\pi(\nu - \nu_i)t)] = \nu - \nu_i$$
$$S_{anti-Stokes_Raman}(t) = \mathcal{F}[A\cos(2\pi(\nu + \nu_i)t)] = \nu + \nu_i$$

  - By the substracting from these terms the initial frequency ν, one obtains: $\{\nu_i\}_i$ the vibrational modes for the substance that represents the sample probe. [8, 6, 12, 1]

  Neverthless, the following problem arises: only a tiny fraction of the signal (10^{-17}) interacts with the molecular sample and becomes Raman Scattered. The information about/regarding the vibrational frequencies of the molecule is difficult to retrieve even if the detector is high-performance. [8, 6, 12, 1]

  One proposal/approach to solve this problem would be to emit the electromagnetic signal (wave/radiation) in the form of a soliton.

  To surpass the limitations of typical Raman spectroscopy (the low fidelity due to the tiny fraction of the signal that interact with the sample), the authors have investigated as alternative using as laser

beam for the Raman spectroscopy a solitonic pulse; therefore the authors had to examine the procedure for generating the ultra-short solitonic pulses within the laser cavity using the environment (gain medium) Ti:Sapphire's birefringence to achieve control between the anomalous dispersion of the group velocity and the self-phase modulation, leading to the non-linear Kerr effect.

The key role in this procedure is assigned to the self-phase modulation [13], which inherently deals with the pulse amplitude $A(z)$, solution of Schrödinger equation: [13]

$$\frac{dA}{dz} = -i\gamma|A(z)|^2A(z)$$

Where the power of the electric signal is constant (does not vary) along the axis of propagation of the electric field, the Oz axis: [10, 13, **?**] $\frac{d|A|^2}{dz} = \frac{d(A\overline{A})}{dz} = \frac{dA}{dz}\overline{A} + A\frac{d\overline{A}}{dz} = 0$, turning the Schrödinger equation exactly into a Korteweg de Vries equation (whose solution is the soliton wave).

where γ is a constant, defining the environment/gain medium within the laser cavity (resonator)
and z is the uni-dimensional laser propagation axis

Since the power is invariant (a constant), the Kerr effect manifests itself only in terms of phase (in the form of a phase rotation): in terms of polar coordinates: A=$|$A$|e^{i\varphi} \Longrightarrow \frac{d}{dz}|A|e^{i\varphi} + i|A|e^{i\varphi}\frac{d\varphi}{dz} = -i\gamma|A(z)|^3e^{i\varphi}$; where: $\frac{d\varphi}{dz}$=- $\gamma|A|^2$=¿the phase function φ calculated in the z coordinate will therefore be: $\varphi(z) = \varphi(0) - \gamma|A(0)|^2z$ the factor describing SPM (this relationship illustrates that SPM is induced by the electric field strength). [10, 13]

In the presence of an attenuation factor, the propagation equation is: $\frac{dA(z)}{dz} = -\frac{\varphi}{2}A(z) - i\gamma|A(z)|^2A(z)$ and the solution will be: A(z)=A(0)$e^{-\frac{\varphi}{2}z}e^{-i\gamma|A(0)|^2}l_{eff}$ (where $l_{eff}(z) = \int_0^z e^{-\alpha z}dz$is the effective length) - which is exactly the equation defining a soliton. [10, 13, **?**]

The generated ultra-short solitonic pulse laser beam is extremely powerful and can sustain an increased rate of anti-Stokes Raman back-scattering, making thus the procedure more efficient even when used in-vivo.

But which is the cost in terms of side-effects and human safety risks? Could this risks be avoided?

3. Human Safety Concerns

In spite of the enthusiasm granted by the academic environment to the possibility of applying in-vivo the Raman spectroscopy, there exist several issues related to it.

The first issue resides in the method's low fidelity, due to the minimal fraction of (anti-)Stokes shifted photon that are backscattered - when the method employs an usual laser. In order to enhance the method's accuracy, the authors proposed the use of a solitonic ultrafast femtosecond-pulsed laser (due to well-established properties of stability specific to the solitonic signals).

Nonetheless, there still remains a series impediments against employing in-vivo the method of Raman spectroscopy. For instance, there exist numerous articles which propose the (picosecond) solitonic lasers as a mean for surgical treatments. This means that such solitonic pulsed-lasers could exhibit harmful potential against the human health. Why do such side/adverse effects take place? Could these adverse effects be diminished or even by-passed?
Therefore the authors closely examined the potential harmful side-effects associated to the tissue-(solitonic pulsed) laser interaction:

The high-power ultrashort lasers can lead to the formation of the following adverse effects through interaction with biological tissue: [5, 11, 3, 2]

- Photochemical effect
- Photothermal effect
- Photomechanical effect
- Ionization phenomenon (plasma formation)

However, it will be shown that the photomechanical effect essentially boils down to the photothermal effect and the ionization/plasma formation phenomenon, which in turn is closely related to the photothermal effect. [5, 11, 3, 2]

Risks of in vivo use on human health:

In order to increase the accuracy of the method and favour the generation of photons scattered with the Stokes or anti-Stokes Raman frequency shift spectrum, we proposed the use of a solitonic laser signal (a much more powerful and stable signal, which, as we shall see, will favour the generation of anti-Stokes shifted Raman photons).

However, this modification also poses risks to human health due to adverse effects adverse effects on benign tissue examined in vivo.

Let us recall that the phenomenon (Raman) of laser signal scattering is a consequence of the oscillation of the molecular sample with which the incident laser beam interacts, because the electromagnetic wave modifies the oscillation polarizability.

Molecular vibration is generated by the dipole pulse: [8, 6, 13, 5, 11, 3, 2]

$$p(t) = \alpha \cdot E(t) = \alpha \cdot E_0 \cdot cos(2\pi\nu t)$$

And from Taylor's formula (applied for polarizability α viewed as a function of spatial coordinates):

$$p(t) \approx \alpha(q_0)E_0 \cdot \cos 2\pi\nu t + \frac{1}{2} \cdot \frac{\partial \alpha}{\partial q^i}|_{q^i=q_0^1} E_0 \cdot q_0^1 \cdot (\cos(2\pi(\nu - \nu_i)t) + cos(2\pi(\nu + \nu_i)t)$$

In other words, the molecular vibration of the sample depends on p and indirectly on the intensity E(t) of the incident beam.

The higher the energy of the incident laser beam, the greater the accuracy of the method, but the adverse effects will also become significant.

There are two fundamental adverse effects that can damage benign tissue (when Raman spectroscopy is used in vivo) and thus endanger human health (causing other conditions, including genetic mutations and diseases), namely: [13, 5]

Photothermal effect:

- When photons/electromagnetic waves come into contact with the molecular substrate being examined, the energy transferred by the photons changes the molecular vibration movement, and this movement releases heat.
- Furthermore, the greater the amount of energy transferred (and thus the heat released), the more pronounced the unfolding of the constituent polymers of the tissue will be, up to the level of protein aggregation; resulting in structural changes, culminating in cell lysis (death) and ultimately irreversible tissue damage. [5]

Photochemical effect:

- The energy transferred by photons leads to chemical changes - for example, changes in covalent bonds - through which oxidative products (RXs = intermediate oxidative products, e.g. free radicals) are released. [5]
- This contributes to the phenomenon of protein oxidation, and the induced changes can also lead to genetic mutations
- The photochemical effect is also due to laser irradiation (the intensity applied by the laser per unit area).
- Intuitively, the photochemical effect of photons is, on a lower energy scale, perfectly similar to the interaction between UV radiation (ionising radiation, e.g. gamma radiation), which also causes genetic mutations by breaking protein bonds in genetic material (DNA). [5, 11]

As a result, the Raman spectroscopy method can only be used in vivo to the extent that ways can be found to avoid photochemical and photothermal effects; this is precisely what we propose in this article.

But first, we need to discover how these phenomena are described mathematically:

Mathematical description of the photothermal effect:

The mathematical description of the photothermal effect is carried out on several levels: [5, 11, 3, 2] I. Firstly, the way in which the energy radiated by the laser signal incident on the tissue surface is converted into heat (by the vibration of the electronic cloud at the cell surface of the tissue) and then assimilated/absorbed into the depth of the tissue.
- The process of heat transfer at the tissue level is governed by an EDP, called **the Pennes Bioheat Equation formula** [3, 2]
- In order to derive the Pennes Bioheat Equation, it is necessary to take into account the laws of thermal/caloric energy conservation at the tissue level.
- The thermal energy balance in a volume/reflection of tissue is governed by the following conservation formula: [3, 2]

$$Q_{\text{gain}} = Q_{\text{storage}} + Q_{\text{loss}} + (\mathcal{W} = Q_B)\,, \text{ where:}$$

- Q_{gain} = rate of assimilation/accumulation (gain) of heat, by cumulating all energy phenomena.
- $Q_{storage}$ = heat stored by the tissue
- Q_{loss} = the lost at boundary heat
- $\mathcal{W} = Q_B$ = the heat generated by the metabolic processes at the level of constituent tissular cells [3, 2]

In order to model by the means of an equatioin this energetical formula, we have to divide the tissue into blocks of infinitesimal volume (actually we discretise the tissular strate exactly as in the case of an integration problem or a problem of numerical computation). [3, 2]
- The heat propagation/transfer at the level of the infinitesimal tissular volume/region - which is realized in two forms (through the following two phenomena): [3, 2]

- through **the conduction phenomenon**: which implies that at the level of the considered tissular region, the gradient of temperature (the difference in temperature) is responsible for the flow propagation from the zone where a surplus of thermal/caloric energy exists to regions where the temperature has lower values.
- And through **the convection phenomenon**: which involvees that the caloric energy (the heat) is carried further once with the passing of the blood. [3, 2]

- The conduction phenomenon of heat is deemed at the sectional level of the considered region/volume:
- And it is mathematically modeled by the **Fourier law of heat**

conduction:

$$Q = \frac{-k \cdot A \cdot (T_2 - T_1) \cdot \Delta t}{\Delta L}$$

- The flow of heat is the transfer rate of heat per area unity per the time unity, according to the formula: [3, 2]

$f = \frac{Q}{A \cdot \Delta t} \Rightarrow f(\text{ (the heat flux vector)}) = -\frac{k \cdot (T_2 - T_1)}{\Delta L} \Rightarrow f = -\frac{k \cdot \nabla T}{\Delta L}$, where:

- k is the coefficient of thermal conductivity [3, 2]
- the magnitude ∇T is equal to the change in temperature per the length/distance unity.
- ΔL is for simplicity approximated to the distance/length measurement unity: $\Delta L \simeq 1$

$\Rightarrow f \simeq -k \cdot \nabla T$

$\downarrow$

$\rho \cdot C_p \cdot \frac{\partial T}{\partial t} = \nabla \cdot (k \nabla T) + Q_{\text{heat generated by other sources at the tissular level}}$

- With: $\nabla \cdot (k \cdot \nabla T) = \nabla \cdot f$ is the heat conduction term.
- In other words, the temperature variation in time is equal to the quantity of (thermal) energy which pass through the system: $\nabla \cdot (k \nabla T)$
- at which is added the caloric energy generated by metabolic processes (Q_M) and the caloric energy carried by the blood through the tissue (Q_B) - which is due to the heat convection phenomenon: [3, 2]

$$Q_B = w_B \cdot C_B \cdot (T_B - T), \text{ where:}$$

- w_B represents the blood perfusion (the volume of blood which passes through the respective tissular region during the unity of time)
- C_B represents the blood capacity to carry/store caloric energy
- T_B, also denoted as T_a, is the blood specific temperature.

$\Rightarrow$ By gathering together all these data, we obtain the Pennes Bioheat equation - that illustrates/describe the transfer of heat through the tissue: [3, 2]

$\rho \cdot C_p \cdot \frac{dT(\vec{r},t)}{dt} = \nabla \cdot (k \nabla T(\vec{r}),t) + (Q_B = w_B \cdot C_B) \cdot (T_{\alpha - T}) + Q_M + Q_P$, where:

- C_P is the tissue's capacity to store caloric energy.
- Q_P is the volumetric rate of laser caloric energy deposition (within the tissue).

In fact, Q_P is the term that describes the photothermal effect induced by the laser pulse over the tissue.

Namely, the laser irradiance is the measure for the caloric energy transferred/deployed/deposited by the laser per the unit contact area between the laser and tissue.

$\Rightarrow$ The absorption of photons' energy generates/yields to the volumetric heat source - described by the factor Q_P; this terms could expressed as a function - that depends upon: [3, 2]

- the Irradiance
- the absorption coefficient specific to the exposed tissue, μ_a
- and the spatial distribution within the tissue (because the Q_P value decays exponentially once with the departure from the tissular surface).

$\Rightarrow$ **Therefore, it is the term: Q_P the one that embeds the laser's irradiance ("the squared amplitude") within the mathematical model.** II. Another level of assessing the photothermal effect consists in the assessment of the thermal relaxation time (the time required that once with the end of the pulsed laser action, the tissue's temperature to decrease by 37%). [3, 2, 5, 11]

- The thermal relaxation time does not explicitly appears within the Heat Bioequation.
- Nevertheless, the underlying principles are embedded into the Pennes Heat Bioequation through the presence of:
  - the conduction term: $\nabla \cdot (k \nabla T)$
  - and the volumetric capacity of heat storage $\rho \cdot C_P$.
- Once the pulse influence is stopped ($Q_P = 0$), the temperature distribution/profile within the tissue will authomatically decrease.
- The rate of decay for the temperature spatial distribution is governed by the formula:

$$\alpha = \frac{k}{\rho \cdot C_p} \text{for the thermal relaxation time}$$

- Smaller the value of this coefficient is, the smaller the required time for the exposed tissular region to get colder is, and consequently the tissue returns faster to its normal temperature.

The photothermal effect and its linkage to the Ionization Phenomenon

At the outset, we will introduce the basis of the Photothermal effect and thereafter we will defien the way how the photomechanical and ionization phenomena are related to it. [5, 11, 3, 2]

The basis of the photothermal effect resides in the fact that the energy carried by the photons of the laser signal is absorbed by *the chromophore molecules* in the tissue cells.

- For example, water, hemoglobin, and melanin absorb photons of specific wavelengths specific to each of these molecules.
- The occuring problem is that the wavelength of the signal at which absorption occurs varies depending on the chromophore -¿ the absorption spectrum is very broad -¿ which requires difficulty in determining an appropriate wavelength for the laser signal so as to avoid absorption of the laser signal by any of the chromophores present in

the tissue.
- The energy of the photons absorbed by the chromophores is converted into heat, which can lead to: [5, 11, 3, 2]
  - Coagulation: at temperatures of approximately 60°C or higher, protein denaturation and tissue contraction will occur (one can also take beneficially advantage of this effect, for instance to produce hemostasis in the case of hemorrhage).
  - Evaporation: rapid heating of water molecules in tissue to temperatures above 100°C can cause the molecules to evaporate from the tissue.
  - Carbonization: sudden heating to extreme temperatures above 100°C will burn/carbonize the affected surface of the tissue.
- On the other hand, it is precisely the evaporation, or more generally, the thermal expansion of water molecules in tissue—that generates: [5, 11, 3, 2]
  - Shock waves
  - Or even micro-explosions

  at the tissue level, which pulverize/remove portions of the tissue surface
- This phenomenon is also known as **"ablation"** and represents the main mechanism of the **photomechanical effect**.
- In fact, the ablation designates the process of photomechanically removing material from the surface of a solid medium by irradiating it with a laser signal.
- This principle serves as the basis for the laser machining. [11]

$\rightarrow$ Therefore, at a microscopic scale, there exists the risk that due to the photothermal associated to the Raman spectroscopy, photomechnical corrosion of the tissular structures to appear.

$\Rightarrow$ **Thus the photomechanical risks are themselves consequences of the photothermal effect (in particular of evaporation induced by the photothermal effect)**.
- Another contribution to the phenomenon "tissue abblation" is represented by the ionization/plasma formation.

Why does this happen? [11, 5]
- Plasma formation represents the further step beyond he photothermal evaporation.
- More precisely, if the temperature induced by exposing the tissue to the laser signal is above the temperature of 100 Celsius degrees, evaporation occurs.
- Thereafter, the resulted molecules in a gaseous state are further ionized by the laser signal (their electrostatic profile is modified). The ionized gaseous medium is plasma.

- It should be also remarked that for a sufficiently powerful laser, the intermediate evaporation step is not even necessary, as ionization (change in the electrostatic charge profile) of the liquid medium occurs directly.

- Furthermore, the generated plasma can act corrosively on tissue surface - due to the ablation.
- Because the amount of plasma produced expands rapidly and generates (due to electrostatic repulsion mechanisms) shock waves and micro-explosions/cavitation bubbles - which break/erode the tissue surface - thus leading to ablation.
- The root of both phenomena stems in the laser irradiance (the radiation flux carried by the laser per unit area of tissue surface); more precisely:
  - If the laser flux has low values, the material is only heated (the absorbed laser energy will lead to evaporation, but not necessarily to ionization).
  - on the other side, If the laser flux is very strong, then plasma will form on the exposed surface of the tissue (and automatically ablation).
- Therefore avoiding these side-effects depends on the possibility to control the laser enegy (and inherently its frequency)
- For a pulsed laser, this concerns to the laser flux, also called **fluence**, which represents the amount of energy carried/transferred by the laser pulse per unit area of the exposed surface: [5, 11, 3, 2, 10, 13]

$$I_{fluence} = \frac{E(\text{energy of the pulse})}{A(\text{area of exposed surface})} = \frac{\hbar c}{\lambda} \cdot \frac{1}{A_{laser}}$$

- In fact, when choosing the frequency value, a balance must be struck between: - The value prescribed by the fluence limitation
- and avoiding/reducing the phenomenon of absorption (photothermal) and heat generation,i.e. temperature increase.

Another issue we have to focus on is whether the amount of generated heat and the temperature values (which we have seen must be kept below the threshold of 60 degrees Celsius, ideally close to the homeostatic temperature of the human body) could be controlled solely on the basis of the fluence (and automatically the frequency) of the laser signal?

To address this issue, it is enough to return to the so-called **Pennes Bioheat equation**:

$$\rho C_p \frac{\partial T}{\partial t} = \nabla \times (k \nabla T) + w_B c_B (T_a - T) + Q_m + Q_p$$

- The contribution of the laser to heat generation (in fact the only "exogenous" factor that intervenes in the physiological processes of the human body in generating heat at the level of the exposed tissue) is encoded by the factor: Q_p - the heat per unit volume of tissue exposed to the laser signal (Q_P stands for the volumetric absorption rate of the caloric energy due to the interaction with the laser), which at its turn is dependent on the laser parameters, more precisely on the laser's irradiance: $I(\vec{r},t)$:

$$Q_p(\overrightarrow{r},t) = \mu_a(\overrightarrow{r}) \cdot I(r,t)$$

$\rightarrow$ At the tissular surface, $I(\vec{r},t)$ might be expressed in terms of the fluence in the following way:

- We consider that the pulse emission duration is τ_P and the contact area between the pulse and the tissue is $\mathcal{A}_{laser}$

  Energy of the pulse $= I_{\text{fluence}} \cdot \mathcal{A}_{laser}$

$\downarrow$

- Average laser power at the contact surface during pulse emission:

$$P_{medie} = \frac{E}{\tau_P} = \frac{I_{fluence} \cdot \mathcal{A}_{laser}}{\tau_P}$$

- The average laser intensity during contact/exposure will be:

$$I_{average} = \frac{P_{average}}{\mathcal{A}_{laser}} = \frac{I_{fluence}}{\tau_P} = \frac{1}{\tau_P} \frac{\hbar c}{\lambda \cdot \mathcal{A}_{laser}}$$

$$\Rightarrow Q_p(\vec{r},t) = \mu_a(\vec{r}) \cdot \frac{\hbar \cdot c}{\lambda \cdot \mathcal{A}_{laser}} \cdot f\left(\vec{r}_{spatial}\right) \cdot g(t_{temporal})$$

The terms $f(\vec{r}_{\text{spatial}}), g(t_{\text{spatial}})$ account for the (spatial and temporal) dissipation once with the photons' advance within the depth of the tissue.

4. Strategies for avoiding the Risks/Adverse effects for the Human Health:

In order to reduce (up to the order of avoiding) the adverse risks presented in the precedent section, we are going to employ a broader strategy, that imbines several facettes:

SI. At the outset, we are going to investigate the (Lyapunov) stability of the Pennes Bioheat equation.

- We have seen that laser's contribution to the increase of temperature in the exposed tissue could be mathematically modeled through the presence of the factor Q_P within the Pennes Bioheat Equation.

- Furthemore, this factor could be rendered also as a function of laser's frequency $Q_P(\lambda)$
- And we are going to assess the long-term evolution of the Bioheat equation by the means Lyapunov stability with respect to the Q_P factor.

SII. We will also directly make use of the defining properties for the adverse effects related to the laser-tissue interaction. Our strategy consists in adapting the laser parameters in order to reduce or even by-pass the generation of adverse effects.

SIII. Another possibility to investigate is in what conditions, the so called Raman anti-Stokes frequencies could induce a cooling effect (nevertheless due to its association with the fluorescence, this thread of research goes beyond the scope of the present article).

4.0.1. *SI. Lyapunov stability for the Pennes Bioheat equation.* At this point, we employ the Lyapunov stability results specific to the heat equation in the study of the Pennes Bioheat equation. We attain this goal simply noting that by choosing the scalar field: [2]

$$L[\cdot] = \Delta^2 \cdot = \Delta \cdot \Delta \cdot$$

we retrieve the expression of the classical heat PDE exactly under the guise of a linear system:

$$\frac{du}{dt} = L[u] \Leftrightarrow \frac{du}{dt} = \nabla \cdot \nabla u = \nabla^2 u = \Delta u$$

The only difference (particularisation) for the Pennes Bioheat equation resides in the presence of the additional positie constants: $\rho, k, C_P, Q_B = C_B \cdot w_B, Q_M, Q_P$ (which are physically relevant, yet $\rho, k, C_p, Q_B, Q_M, Q_P$), but from the mathematical point of view do not embody a barrier in employing the tools of stability theory):

$$\rho \cdot C_p \cdot \frac{dT(\vec{r},t)}{dt} = \nabla \cdot (k \nabla T(\vec{r}),t) + (Q_B = w_B \cdot C_B) \cdot (T_{\alpha - T}) + Q_M + Q_P$$

- We have to readjust the form of the Bioheat equation into a proper way, in order to make apparent the initial condition (the equilibrium point).
- To this end, we have to observe that the factor Q_P which accounts for the laser-tissue interaction represents the solely influence external to the typical tissular environment.
- In addition, the term Q_P could be rendered as a function of λ (the

solitonic pulse frequency) - and thus stands for a variable that cumulates the lasers's effect:

$$Q_P(\lambda) = \mu_a(\vec{r}) \cdot I(\vec{r},t) = \mu_a(\vec{r}) \cdot \frac{\hbar \cdot c}{\lambda \cdot \mathcal{A}_{\text{laser}}}$$

and take into account that in the absence of the external laser influence/source, the the only sources of heat-generation are $Q_B \cdot T_\alpha, Q_N$ - Thus, we can re-express the Pennes Bioheat Equation under the guise of a PDE with initial conditions:

$$\begin{aligned} \rho \cdot C_p \frac{\partial T}{\partial t} &= k \cdot \nabla^2 T + Q_B \cdot (T_\alpha - T) + Q_M + Q_P \\ T(t_0, \vec{r}) &= Q_B \cdot T_\alpha + Q_M \end{aligned}$$

$\rightarrow$ Because at the initial moment (let it be denoted as: t_0), the share/contribution of heat (the rate of heat-deposition/absorption) is due only to the intra-tissular metabolism Q_M and to the blood perfusion Q_B.

For the sake of the mathematical description and ease of the mathematical description, let us denote by:

- $C_1 = Q_B \cdot T_\alpha + QM$
- $C_2 = Q_P$

$\Rightarrow$ Thus we re-express the equation as:

$$\begin{aligned} \frac{\partial T}{\partial t} &= k \cdot \nabla^2 T + C_1 + C_2 \\ T(t_0, \vec{r}) &= C_1 \end{aligned}$$

The implementation of the stability theory tools involves the following steps:

Step1: In order to apply the classical results of the stability theory, we have to "veil" (remove) the additional constants C_1, C_2:

$\rightarrow$ By defining a new function instead of $T(\vec{r},t)$, say:

$$(\vec{r},t) = T(\vec{r},t) - C_1 \cdot t - C_1$$

$\downarrow$ This transformation is chosen specifically to make the new equation homogeneous and to simplify the initial condition:

$$\begin{aligned} \partial_t \text{ת} &= \partial_t T - C_1 \\ \nabla \text{ת} &= \nabla T \Rightarrow \nabla^2 \text{ת} = \nabla^2 T \end{aligned}$$

↓ Substituting these expressions into the modified heat equation, we obtain the new problem:

$$\partial_t \text{ת} = \nabla^2 + C_2$$
$$\text{ת}(t = t_0, \vec{r}) = 0$$

The initial condition takes this form because:

$$\text{ת}(t_0, \vec{r}) = \text{ת}(t_0, \vec{r}) + C_1 = C_1 - C_1 = 0.$$

Step 2 Investigate the stability in terms of C_2:
- The stability of the original equation for $T(t, \vec{r})$ is utterly/absolutely equivalent to the stability of the transformed equation for ת.
- The equation: $\partial_t \text{ת} = \nabla^2 \text{ת} + C_2$ is a linear PDE with the constant source term C_2
- It is obvious that there exists the trivial solution:

$$\text{ת}^0(t, \vec{r}) = 0 = \text{ the initial condition for the PDE defining ת}, \forall) t, \vec{r}$$

$\Rightarrow$ The initial condition 0 is an equilibrium point.
- Under these auspices, the stability of the PDE refers to whether over long time: $\text{ת}(t, \vec{r})$ remains close to 0 (and thus T stays close to $Q_B \cdot T_\alpha + Q_M$) so that the temperature falls back to the normal values regardless of small variations of the variable Q_P.
$\Rightarrow$ The assessment will depend upon the source term C_2.
Remark It is a simple calculation which shows us that a partiular solution for this equation is represented by: $\text{ת}_{\text{particular}} = C_2 \cdot t$
$\Rightarrow$ The full solution will be:

$$\text{ת}(\vec{r}, t) =^{heat} (\vec{r}, t) + C_2 \cdot t$$

where: $\text{ת}^{heat}(\vec{r}, t)$ is the classical heat equation's solution:

$$\partial_t \text{ת} = \nabla^2 \text{ת}$$

(which could be obtained for instance by applying the Fourier Transform Method).
- However ת^{heat} is stable, **due to the maximum principle for the Heat Equation**.
- And assuming the behaviour for: $\text{ת}(\vec{r}, t) \xrightarrow{\text{as } t \to \infty} 0$

$$\| \text{ת}(\vec{r}, t) - 0 \| = \| \text{ת}^{\text{heat}}(\vec{r}, t) + C_2 \cdot t - 0 \| \leq \| \text{ת}^{\text{heat}}(\vec{r}, t) \| + \| C_2 \cdot t \| \xrightarrow[t \to \infty]{} 0 + (\infty = \| C_2 \cdot t \|)$$

$\Rightarrow$ **The solution ת could by no means be stable.**
Remark: Supposing that $C_2 \cdot t$ would be negative, which involves: $C_2 < 0$

$\Rightarrow$ It could be shown that the source term would act as a "sink" leading to the phenomenon of dissipation and thus the PDE is stable.

– Nonetheless, we simply dismiss the case: $C_2 < 0$, since in our context, where:

$$C_2 = Q_P = \mu_a(\vec{r}) \cdot I(\vec{r},t) = \mu_a(\vec{r}) \cdot \frac{\hbar \cdot c}{\lambda \cdot \mathcal{A}_{\text{laser}}} (\geq 0)$$

→ which represents the laser energy absorbed and converted into heat by the tissue, therefore this quantity could not take negative values.

The Pennes Bioheat Equation will definitely be **unstable** *in the presence of the laser (interaction with the tissue)* **and it is not possible to find any way for stabilizing the Pennes Bioheat Equation**.
⇒ Since Q_P is a nondecaying, constant, positive source of heat in the tissue and the energy is continuously added; the only barrier is embodied by the interaction duration. → In practice $t \to \infty$, yet: $Q_P = 0$, for $t < \tau_{\text{interaction}}$ denoted as τ_p However even during a finite-temporal interaction, the PDE remains unstable, because even over any interval $[t_0; t_0 + \tau_P]$: $\| \text{ת}(\vec{r}, t - 0 \|$ could be made bigger than ε, regardless of how close is $\text{ת}(\vec{r}, t_0)$ to the initial condition 0 (so regardless of any choose of δ).

The only chance for maintining temperature as close to the normal values as possible cuts back to adapting the interaction/exposure time (due to the intervention of the dissipation of the excessive temperature).

4.0.2. *SII. Adapting the laser parameters to attain the avoidance of the adverse effects for the Raman Spectroscopy:*

In order to reduce/diminish at once both the photothermal and the photochemical effects (that can occur once with the application in-vivo of the Raman spectroscopy), we are going to take advantage of two essential properties associated to these effects, namely:

– For **the photothermal effect**, the property which we are going to use is embodied by **the thermal relaxation time of the molecules**
– For **the photochemical effect**, the property which we are going to use is embodied by **the average lifetime of the intermediate reactive/oxidative products**.

The authors propose as strategy ***to link these propertie to the discontiuous character of the solitonic pulsed signal emited by the laser*** *in the following way:*

– **If the intermediate duration (the temporal gap) between the emission of the pulses will be ”sensibly” bigger than the thermal relaxation time/duration**, *then the molecular layer will have enogh time ”to get cold by itself (without any external intervention).*

– Moreover, **if the efective duration of each pulse is comparably less than the average lifetime of the intermediate reactive/oxidative products**, *then these products will not have enough time to get formed.*
    - More precisely, by inducing energy through photons grouped in extremely short pulses (it would be adequate a solitonic laser signal formed from pulses in the order of picoseconds or even femtoseconds), then will be generated/produced intermediate reactive/oxidative products; however, if each of signal's pulses ends before the intermediate oxidate/reactive products to have had enough time to built up or to undergo further reactions - which can lead/yield to irreversible deterioration of the tissular cells, and the temporal gap between each consecutive pulses of the signal will be large enough, the reactive products can dezintegrate/decay by itself or can even get involved in "benign" reactions (for instance the intermediate oxidative/reactive products (free radicals) can get recombined or can undergo non-radiative decay) before the occurence of the next pulse.

5. Study case for parameters adjustment

Aside from the interpulse and pulse duration adjustment, another key element is represented by the optimal selection of the signal's frequency selection as the following line of reasoning illustrates.

More precisely, the photochemical effect is due to the energy transfer, which occurs once with the exposure of the biological tissue to the pulsed laser signal, that lead to the ionization of the exposed area. The ionization modifies the electronic structure of the tissular molecules, which at its turn lead to the release/generation of the reaction species – free radicals – as the mono-oxygen, superoxydes, hydroxides.

For instance the Ultra-Violet radiation, due to its high intensity/high energy (its has the highest value within the spectrum of the electromagnetic rays) leads to the free radicals generation during a contact within the range of solely several milliseconds up to a second.

The rate for radicals generation R could be quantified by using the formula:

$$R = I \cdot \sigma \cdot Phi$$

where:

I represents the laser irradiance
σ is the energy absorption probability (cross-section)
Φ stand for the efficiecy coefficients, with which the absorbed energy is transfered into the phenomenon of free radicals generation.

What happens into the case of an ultra-fast solitonic pulsed lser?

- In which case the exposure time for each pulse has the order of femtoseconds $(10^{-15}s)$

It is important to take into account that the after the contact transfer of energy, given the non-continuous exposure, due to the pulsed nature of the considered laser signal, there exists an interpulse period, when the the energetic surplus could be released preventing thus the generation of free radicals (the phenomenon of energetic balancing is also called the vibrational relaxation).
The strategy we have proposed consists in generating pulsed solitonic laser so that:

I. the interpulse period/gap has to be chosen greater then the vibrational relaxation (in order to prevent the generation of free radicals) – and thence less then the order of milliseconds.
II. the duration of each pulse to shorter enough in order to prevent the over-heating (of the order of femtoseconds).

In order to achieve both of these aims, one has to devise an ultra-fast solitonic pulsed laser - with greater values for the wave-length, situated above the safe-threshold of 700 nm (NIR – near Infrared) – we propose to opt for a pulsed laser with the wave length = 900 nm (so that the emitted electromagnetic pulsed signal will belong to the Infra-Red spectrum).

By this way the energy carried per each pulse will equal:

$$E = \hbar \cdot \frac{c}{\lambda}$$

which for the value $\lambda = 900nm$ approximately equals 1eV (a value less than even the the energy carried by the natural light). The obtained value for the carried energy assigned to the wave length $\lambda = 900nm$, together with the pulse duration: $t_p = 100fs$ (the generated solitonic pulsed laser is ultra-fast) will thus exclude the photo-thermal risk.
Moreover, expressed in terms of average power, by considering the pulse duration: $t_p = 100fs$, the average power of the laser will be approximately equal to 1.37 eV and $2.2 \cdot 10^{-19}J$ (which is an infinitesimal value compared to lasers used for surgical

purpose); notwithstanding, in order to exclude the possibility of free-radicals formation, as mentioned above, one has to obtain an interpulse duration greater than the vibrational relaxation time (greater therefore than the order of several tens of picoseconds) – which by judging the problem exclusively in terms of λ, ω would be impossible.
- In the sense that: in order to obtain the interpulse duration greater then the order of picoseconds, one should set an interpulse duration at the order of nanoseconds (which clearly would excede the vibrational relaxation duration), however such a temporal gap between pulses would require a repetition rate $\omega_{repetition}$ at the order of several tens of kHz, for instance: $\omega_{repetition} = 80kHz$. - On the other side, the frequency assigned to a wavelength of 900 nm, ω equals due to the relation:

$$E = \hbar \cdot \frac{c}{\lambda} = \hbar \cdot \omega$$

a frequency of approximately 333 THz.

Therefore, we have to make the distinction between the frequency (ω) induced by the wave-length λ and the repetition rate: $\omega_p \leftarrow$ whose values could by set by using the Mode-Locking Mechanism (which also generates the solitons pulsed laser signal); in the sense that to the classical Mode-Locking Mechanism one has to consider in addition a q-switch, which selectively "pause" the emittance of pulsed signal at certain time intervals.
Given all these considerations we propose the use of an ultrafast solitonic pulsed laser with the following setting:

* the wave-length: $\lambda = 900nm$
* the pulse duration: $t_p = 100fs = 100 \cdot 10^{-15}s$
* the pulse energy: $E_p = 2.2 \cdot 10^{-19}J$
* the repetition rate: $\omega_{repetition} = 80kHz$
  - so that the repetition period: $T = \frac{1}{\omega_p} = 1.25 \cdot 10^{-5}s = 1.25ms$ (each pulse is repeated by 1.25 micro-seconds);
  - so that the interpulse period has the order of microseconds, far beyond the required time for the vibrational relaxation to take place.
* spot diameter: $100m \rightarrow r = 50 \cdot 10^{-6}m$.

Wherefore we can compute the following exposure parameters:

* The pulse energy: $P_{avg} = E_p \cdot \omega_{rep} = 17.6 \cdot 10^{-15}J = 17.6fJ$
  $\rightarrow$ which stands for an infinitesimal value compared to surgical purposed-used laser.

- We can thereafter compute the peak power pulse:

$$P_{peak} = \frac{E_p}{t_p} = \frac{17.6 \cdot 10^{-15} J}{100 \cdot 10^{-15}} = 0.17W$$

- which, given the exposure area, computed as: $A = \pi \cdot r^2 = \pi \cdot (50 \cdot 10^{-6})^2 = 7.854 \cdot 10^{-9} m^2$,
- so that the average irradiance (equal to average power over area) could be computed as:

$$I_{avg} = \frac{P_{avg}}{A} = 2.24 \cdot 10^{-6} W/m^2$$

  - Which, again, is an infinitesimal value far from exerting any harmful influence.

We can also compute the duty cycle (the total percentage of contact considering all the emitted pulses), which is further equal to: t_p/T (the duration of each pulse divided by the repetition period), and obtain for the given pulse that this value equals:

$$\text{duty cycle} = t_p \cdot \omega_{rep} = 100 \cdot 10^{-15} \cdot 80 \cdot 10^3 = 8 \cdot 10^{-9} = 8 \cdot 10^{-9} = 8 \cdot 10^{-7}\%$$

this formula is interpreted in the following way: supposing that the pulsed laser is employed (intraoperatively to perform the Raman spectroscopy) during 1 hour = 3600 s, from 1 hour, the effectively contact between the pulse and the tissue amounts to solely: 0.0000008% of the procedure total duration.
Therefore both the irradiance value and the duty cycle have insignificant values compared to the classical surgery lasers and practically pose no risks to the human health supposed that one follows the indicated parameters setting, which could be achieved by employing an Ti:Sapphire solitonic pulsed laser.
Remark: We stress again the importance of using the modelocking mechanism, which not only plays the crucial role in generating the solitonic pulsed laser, but also grants the possibility to attach the q-switch for controlling the average irradiance and thus maintain the rate for radicals generation R far less than the threshold of radicals generation.

6. Conclusions

We can draw as conclusion from all the previous considerations, that despite the fact that for there exists no way to control the Lyapunov stability for the Pennes bioheat equation that quantify the photothermal risk induced by the Raman spectroscopy used in-vivo, by adjusting the interpulse and pulse duration for the solitonic pulsed laser signal employed by the method, one can reduce at once both the photochemical and the photothermal risks.

Moreover, the article proves that by considering a repetition rate of the order of kHz (which is in accordance with considering larger interpulse gaps) and values for the laser's frequency situated below the Near-Infra-Red spectrum, one can obtain in result an irradiance situated even below the risk of electromagnetic signals that pertains to the visible light.
At the same time due to the solitonic underlying structure of the considered laser, even at low energy, it could offer accuracy for the Raman spectroscopy, by stimulating the formation of anti-Stokes back-scattered photons.
Therefore, the solitoni pulsed lasers could offer a safe alternative for the intra-operative Raman spectroscopy.

7. Subsequent research directions

SIII. A promising direction of further research is embodied by investigating whether using the ultra-short pulsated signals could ensure the generation of anti-Stokes shifted response (phenomenon also known as CARS), which will involve two advantages:
1. It favorises the apparition of back-scattered anti-Stokes shifted photons, increasing thus the precision/accuracy of the Raman spectroscopy.
2. In addition, the anti-Stokes shifted frequency: $\nu + \nu_i$ by the end of the interaction is going to be greater than the initial value: $\nu \Rightarrow$ which implies that the surplus in terms of frequency stems from the energy surplus taken over from the interaction with the examined molecular sample $\Rightarrow$ The energy lost by molecular sample (and taken over by the anti-Stokes shifted photons) leads to the molecular cooling - which could counterbalances the photothermal effect.

References

[1] G.P.Agraval, *Nonlinear fiber optics*, Chapter 8: Stimulated Raman Scattering, sixth edition, Academic Press, 2019
[2] A.Bacciotti, L.Rosier, *Liapunov functions and stability in control theory*, Springer, 2009
[3] E.Berroral, *The Bio-heat equation. Tissue Optics*, Lecture notes, LTH - Lunds Tekniska Högskola, 2023
[4] C.Boudoux, *Fundamentals of Biomedical Optics: rom light interactions with cells to complex imaging systems*, Blurb, 2017
[5] M.L.Denton, D.Clark, G.D.Noojin, H.West, A.Stadick, T.Khan, *Unified modeling of photothermal and photochemical damage*, Frontiers, 2024
[6] G.Dent, E.Smith, *Modern Raman Spectroscopy. A practical support*, Wiley, 2005

[7] C.van Deurzen, R.van Doorn, J.von der Thüsen, R.Verdijk, *Raman spectroscopy for cancer detection and cancer surgery guidance: translation to the clinics*, Royal society for chemistry, 2017
[8] C.Hess, *Raman Spectroscopy: Basic principles and applications*, Lecture notes. Fritz Haber Institut, Max-Planck Gesellschaft, 2020
[9] T.Hollon, S.Lewis, C.Freudiger, D.Orringer, *Improving the accuracy of brain tumor surgery via Raman based technology*, Neurological focus, 2016
[10] F.Kärtner, *Lecture 5: Optical Solitons*, Ultrafast Optics and X-ray Group at CFEL, 2021
[11] G.Müller, K.Dörschel, H.Kar, *Biophysics of the photoablation process*, Springer Nature, 1995
[12] M.Okumura, *Raman Spectroscopy*, Chapter 6, physical Chemistry Laboratory, Lecture Notes, Spring quarter, Caltech, 2021
[13] K.Sabirov, M.Akramov, R.Otajanov, L.Matrasulov, *Soliton generation in optical fiber networks*, Elsevier, 2020

Center for Research and Training in Innovative Techniques of Applied Mathematics in Engineering ”Traian Lalescu”,
University Politehnica of Bucharest, Splaiul Independentei 313, 060042 Bucharest, Romania

BRIDGING CLASSICAL IMAGING AND QUANTUM INFORMATION

Antonela TOMA[1], Răzvan MORARU, Cătălina-Nicoleta MITU[3], Victor DORCA[4]

[1,2,3,4] "Traian Lalescu"" Center for Research and Training in Innovative Techniques of Applied Mathematics in Engineering of the The National University of Science and Technology "Politehnica" Bucharest

Corresponding author email: antonela.toma@upb.ro, razvan.moraru@upb.ro

***Abstract:** This paper explores the formal and conceptual analogies between computed tomography (CT) and quantum state tomography, highlighting the shared mathematical structures and reconstruction methods that create a bridge between the two. In classical CT, information about an unknown spatial density is obtained by measuring line integrals of the object's internal structure at multiple angles. Such projections are mathematically described by the Radon transform, the inverse of which – typically performed through the Fourier Slice Theorem and the Filtered Back Projection algorithm – allows the reconstruction of the original image.*

Quantum tomography shares a similar goal: to recover an unknown quantum state, represented by a density matrix, from the statistical results of multiple measurements performed in different bases. Each measurement provides an expectation value that is a linear functional of the state, providing a system of equation to be solved for the optimal estimate of the density matrix. Extending the analogy to quantum systems, by drawing parallels between spatial image reconstruction and quantum state estimation, this work illustrates the deep structural correspondence between classical frequency analysis and the set of mathematical methods used in quantum information theory.

Despite any formal difference, both procedures share the same logical sequence: indirect measurement, data transformation into a reconstruction domain, and inversion under suitable constraints. In both cases, reconstruction is faced with incompleteness experienced under the form of noise issues, requiring the use of regularization methods and optimization techniques to stabilize solutions. Thus, computed and quantum tomography have a deep structural resemblance – both decipher indirect measurement data in the form of an image or state reconstruction via the same basic mathematical tools in terms of Fourier analysis and inverse problems.

In order to highlight the correspondence, the relevance of this link between the classical and quantum tomography, the authors of this article included a brief description of the Shor's algorithm, which sheds light upon the fact that the correspondence between correspondence between the classical and quantum tomography goes even further in the sense that both of them could be understood as inverse Fourier methods that act upon the symmetry groups. The computed tomography acts upon the group of orthogonal transformations for a Euclidean space, whereas its quantum counterpart acts upon the group of unitary transforms that governs the dynamics over the Bloch's sphere. Thus, both the classical and quantum tomography procedures could furthermore be approached by the means of the algebraic theory of Hidden subgroup theory, which could embody a gateway for the transfer of classical algorithms within the realm of quantum computing and establishing of new development threads for quantum computing.

***Key words:** Fourier series image reconstruction, Classical computed tomography, Quantum Computing, Fourier transform over symmetry group*

Contents

1. Introduction

Any periodic signal can be represented as a sum of sine and cosine functions (also referred to as harmonic components) using the Fourier Series. The structure of the visual data can be shown in image processing by breaking down a picture (or, more generally, a signal) into its frequency components. In image processing, the structure of the visual data can be highlighted by breaking down a picture (or, more generally, a signal) into its frequency components. Analyzing, enhancing, and changing digital images for purposes including compression, filtering, and pattern recognition is known as image processing. Applications include computer vision, medical imaging, remote sensing, and multimedia systems, all of which heavily rely on frequency-domain methods such as the Fourier Series.

Frequency analysis is a fundamental approach in image processing that examines an image's frequency components rather than its spatial (pixel-based) representation. By transforming an image from the spatial domain to the frequency domain, it becomes possible to isolate and manipulate specific frequency bands with greater precision and efficiency. In this domain, the image is represented as a combination of sinusoidal patterns at varying frequencies. Low-frequency components correspond to gradual intensity changes across large regions (such as smooth gradients), while high-frequency components represent rapid changes (such as edges and fine details). The key advantage of working in the frequency domain lies in the ability to selectively enhance, suppress, or remove certain frequency ranges—making it especially useful for tasks like filtering, compression, and noise reduction.

Tomography is a technique for reconstructing the internal structure of an object from a series of its projections. In computed tomography (CT) in medical imaging, these projections are obtained by passing X-rays through the object at different angles and recording the resulting intensity patterns. Each projection represents a different view of the object. The process is complete when the projections are combined to recover the full spatial structure with the help of frequency analysis and Fourier methods. The Fourier Slice Theorem establishes that the one-dimensional Fourier transform of a projection corresponds to a slice of the two-dimensional Fourier transform of the object at a specific orientation. The inverse Fourier transform is then used to piece together the object’s complete Fourier representation and then obtain the spatial image. Paired with filtering techniques that control noise and enhance detail, this approach facilitates precise and efficient reconstructions.

In quantum tomography, the concept is similar but takes place in an entirely different physical context: instead of reconstructing a spatial image, the objective is to reconstruct the quantum state of a system. Measurements in quantum mechanics can be seen as projections in an abstract Hilbert space, and their outcomes contain partial information about the underlying quantum state. By gathering results from measurements in different bases—analogous to viewing an object from different angles—it is possible to reconstruct the state’s full mathematical description, such as its density matrix. Fourier-like techniques, along with statistical estimation, are used to process these measurement results, revealing the similarity between the structure of the quantum state (state estimation in quantum information theory) and the reconstruction of classical images.

2. Mathematical Concepts

2.1. Fourier Series and Fourier Transform

Fourier Series and Transform

-Purpose: Establish the mathematical foundation for image decomposition and reconstruction.[3]

-Key points:

-Fourier Series Recap

- Any periodic function $f(x)$ with period T can be expressed as:[3]

$$f(t) = a_0 + \sum_{n=1}^{\infty} \left[a_n + \cos\left(\frac{2\pi nt}{T}\right) + b_n \sin\left(\frac{2\pi nt}{T}\right) \right]$$

- Coefficients:

$$a_n = \frac{2}{T} \int_0^T f(t) \cos\left(\frac{2\pi nt}{T}\right) dt$$

$$b_n = \frac{2}{T} \int_0^T f(t) \sin\left(\frac{2\pi nt}{T}\right) dt$$

-Fourier Transform (Continuous/1D)

- For non-periodic functions:

$$F(\omega) = \int_{-\infty}^{\infty} f(t) e^{-i\omega t} dt$$

$$f(t) = \frac{1}{2\pi} \int_{-\infty}^{\infty} F(\omega) e^{i\omega t} d\omega$$

-Extension to 2D

- For images $f(x, y)$:

$$F(u, v) = \iint f(x, y) e^{-i2\pi(ux+vy)} dxdy$$

- This lets us analyze images in terms of spatial frequencies.

In tomography, instead of directly sampling an object in all spatial coordinates, we measure projections, which are linked to the object's Fourier transform in a specific way.

2.2. Fourier Slice Theorem[1]

Tomography

-Purpose: Describe how picture reconstruction from projections is based on Fourier analysis.

-Key points:

-Concept of Reconstruction from Projections

- We measure $p_\theta(s)$: the projection of the object $f(x,y)$ at angle θ.
- Radon Transform:

$$p_\theta(s) = \int_{-\infty}^{\infty} f(s\cos\theta - t\sin\theta\,, s\sin\theta + t\cos\theta)dt$$

where s is the position along the projection axis.

-Fourier Slice Theorem (central link)[1]

- The 1D Fourier transform of $p_\theta(s)$ equals a slice of the 2D Fourier transform $F(u,v)$ of $f(x,y)$ along the line at angle θ:

$$F_s\{p_\theta(s)\} = F(u = \rho\cos\theta\,, v = \rho\sin\theta)$$

- This means by collecting projections at multiple angles, we can assemble the object's full 2D Fourier transform and invert it.

-Classical Applications

- CT scans: X-ray absorption data → projections → Radon inversion.
- MRI: Measures Fourier space (k-space) directly, so reconstruction is just inverse Fourier transform.

In quantum physics, we can't "look inside" a state directly, but we can take many different projections (measurements in different bases) and reconstruct the quantum state — this is quantum tomography.

2.3. Quantum Theory

-Purpose: Show how tomography extends from spatial objects to quantum states.[2,4,6]

-Key points:

-Basics of Quantum States

- A pure state: $|\psi\rangle$
- Density matrix: $\rho = |\psi\rangle\langle\psi|$ for pure states, or more generally for mixed states.
- For qubits:

$$\rho = \frac{1}{2}(I + \vec{r} \cdot \vec{\sigma})$$

Where $\vec{r}$ is the Bloch vector and $\vec{\sigma}$ are Pauli matrices.

-Measurement and Projections

- Measurement in basis $\{|m\rangle\}$ gives probabilities:

$$p(m) = \langle m|\rho|m\rangle$$

- Each basis choice gives a different "projection" of the state.

-Quantum State Tomography[6]

- Goal: Reconstruct ρ from measurement data in many bases.
- Analogy to Radon transform: each measurement basis is like a projection of the object's structure, and the inversion process is comparable to Fourier reconstruction.
- Methods:
  - Linear inversion
  - Maximum likelihood estimation
  - Compressed sensing (for sparse states)

-Quantum Process Tomography

- Determines the action of an unknown quantum channel ε by studying how it transforms a complete set of input states.

-Applications

- Verification of quantum gates in quantum computing.
- Characterization of entanglement and decoherence.
- Quantum cryptography (checking state integrity).

2.3.1. Superposition Principle and Vector Spaces

In quantum mechanics, states are described by complex column vectors, the notations which physicists use for quantum states are $|A\rangle$ and $|B\rangle$. According to The Superposition Principle, given $|A\rangle$ and $|B\rangle$ two perfectly distinguishable quantum states, then any linear combination $\alpha|A\rangle + \beta|B\rangle$, where the complex coefficients have the property $|\alpha|^2 + |\beta|^2 = 1$, is also an allowed quantum state. Thus, quantum states are unit vectors, and vector orthiogonality precisely translates to distinguishability of states in measurement experiments.[2,4]

Qubits as Two-Dimensional Systems:

A qubit is a quantum system that can only take on two distinguishing values. Unlike classical bits, which are strictly in one of two states, a qubit exists in superpositions of two basis states. Such basis states may physically represent orthogonal properties such as polarizations of photons, spins of electrons, or directions of currents in superconducting circuits. Such multiplicity of physical implementations underlies the flexibility of quantum information processing.

Bra-Ket Notation and inner Products:

Physicists like to represent quantum states using a notation they call "kets", so a quantum state v would be represented as $|v\rangle$. In mathematics notations, kets are column vectors. Imagine light going

through polarized sunglasses. One pair of sunglasses lets through only vertically polarized light, another only horizontally polarized light. These are two distinct states: $|\leftrightarrow\rangle$ for horizontal and $|\updownarrow\rangle$ for vertical. Real light might not purely vertical or purely horizontal. It could be polarized at some angle in between. In quantum terms, this "in-between" polarization is a superposition of $|\updownarrow\rangle$ and $|\leftrightarrow\rangle$. For example, light polarized at a 45° angle is

$$|45°\rangle = \frac{1}{\sqrt{2}}(|\updownarrow\rangle + |\leftrightarrow\rangle).$$

Quantum mechanics employs the Dirac bra-ket notation to represent states and inner products. States are represented as kets $|\psi\rangle$, or column vectors, while their conjugate transposes are bras $\langle\psi|$, represented as row vectors. Their product, $\langle\varphi|\psi\rangle$, is the inner product, which contains orthogonality and overlap between states. Quantum states are typically normalized unit vectors, thus that $\langle\psi|\psi\rangle = 1$.

2.3.2. Unitary Evolution and Matrices

Evolution of a quantum system is regulated by unitary matrices, that are complex vector space rotations. When a matrix M is used to a state $|\psi\rangle$, physical realizability demands that normalization must be maintained, and this leads to the condition $M \dagger M = I$. This guarantees reversibility of quantum transformations as well as probability amplitudes conservation.

There are few other conditions a matrix U must fulfill in order to be unitary besides $U \dagger U = I$. A matrix is unitary if and only if one of the following is true:[2,4]

- $U \dagger U = I$,
- $UU \dagger = I$,
- the columns of U are orthonormal vectors,
- the rows of U are orthonormal vectors.

Pauli Matrices and the Bloch Sphere:

Study of single-qubit systems in quantum mechanics and quantum information theory is in fact built on the Pauli matrices. The three 2×2 matrices are expressed as:[2,4]

$$\sigma_x = \begin{pmatrix} 0 & 1 \\ 1 & 0 \end{pmatrix} \qquad \sigma_y = \begin{pmatrix} 0 & -i \\ i & 0 \end{pmatrix} \qquad \sigma_z = \begin{pmatrix} 1 & 0 \\ 0 & -1 \end{pmatrix}$$

In addition to the identity operator I, the Pauli matrices form a complete basis for the Hermitian operator space in one qubit. It implies that any observable or Hamiltonian of a qubit system can be written as a linear combination of the Pauli operators:

$$H = a_0 I + a_x \sigma_x + a_y \sigma_y + a_z \sigma_z \,,\; a_i \in \mathbb{R}$$

The Pauli operators possess some helpful algebraic properties. Each σ_i is both Hermitian and unitary, satisfying:

$$\sigma_i^\dagger = \sigma_i \qquad \sigma_i^2 = I$$

They obey anticommutation relations:

$$\{\sigma_i, \sigma_j\} = \sigma_i \sigma_j + \sigma_j \sigma_i = 2\delta_{ij} I$$

and commutation relations:

$$[\sigma_i, \sigma_j] = 2i \in_{ijk} \sigma_k$$

Where $\in_{ijk}$ is the Levi-Civita tensor. These commutation relations render the Pauli matrices generators of the Lie algebra su(2), which in turn generates the symmetry group SU(2). This group-theoretic connection highlights their role as the natural building blocks for all single-qubit unitary maps.

One qubit can be in the superposition of the computational basis states $|0\rangle$ and $|1\rangle$:[2,4]

$$|\psi\rangle = \alpha\,|0\rangle + \beta\,|1\rangle, \qquad |\alpha|^2 + |\beta|^2 = 1.$$

By writing the coefficients in spherical coordinates, one obtains:

$$|\psi\rangle = cos(2/\theta\,)\,|0\rangle + ei\phi sin(2/\theta\,)\,|1\rangle,$$

where $\theta \in [0, \pi]$ and $\phi \in [0,2\pi)$. This correspondence provides a point on the unit sphere in $\mathbb{R}^3$, known as the Bloch sphere, with Cartesian coordinates:

$$x = sin\theta cos\phi, \quad y = sin\theta sin\phi, \quad z = cos\theta.$$

North pole ($\theta = 0$) is the state $|0\rangle$ and south pole ($\theta = \pi$) is $|1\rangle$. The points in between are coherent superpositions of the basis states. The Bloch sphere therefore provides an intuitive geometric representation for qubit states with global phases ignored.

Pauli operators are generators of rotations on the Bloch sphere. A general rotation about an axis defined by the unit vector $\vec{n} = (n_x, n_y, n_z)$ by angle θ is expressed as:[2,4,6]

$$R_n(\theta) = e^{-\frac{i\theta}{2}(n_x\sigma_x + n_y\sigma_y + n_z\sigma_z)}$$

Special cases are rotations about the coordinate axes:

$$R_x(\theta) = e^{\frac{-i2}{\theta}}\sigma_x, \; R_y(\theta) = e^{\frac{-i2}{\theta}}\sigma_y, \; R_z(\theta) = e^{\frac{-i2}{\theta}}\sigma_z.$$

For example, the rotation about the y-axis in its explicit version is:

$$e^{-i\theta\sigma y/2} = \begin{pmatrix} \cos\frac{\theta}{2} & -\sin\frac{\theta}{2} \\ \sin\frac{\theta}{2} & \cos\frac{\theta}{2} \end{pmatrix},$$

which is a rotation of the Bloch vector through angle θ about the y-axis. These operations are the components of one-qubit quantum gates used in quantum computing.

Algebra's connection to geometry is highlighted by the analysis of operators of the form:[2,4,6]

$$M_p = p_x\sigma_x + p_y\sigma_y + p_z\sigma_z,$$

where $p = (p_x, p_y, p_z)$ is a unit vector. The matrix M_p is Hermitian with eigenvalues ±1. The eigenvector for the +1 eigenvalue is the qubit state in the direction p on the Bloch sphere, and the eigenvector for the −1 eigenvalue is the antipodal point. This establishes a direct correspondence between the eigenvalue structure of the Pauli operators and the geometric representation of qubits on the Bloch sphere.

The Pauli matrices also explicitly appear in physical Hamiltonians. For instance, the Hamiltonian of a spin -1/2 particle in a magnetic field B is:

$$H = -\gamma B \cdot \sigma = -\gamma\left(B_x\sigma_x + B_y\sigma_y + B_z\sigma_z\right),$$

where γ is the gyromagnetic ratio. The eigenvalues of this Hamiltonian are $\pm\gamma \mid B \mid$, which denote spin states parallel or anti-parallel with the magnetic field. On the Bloch sphere, this Hamiltonian induces precession of the Bloch vector about the axis specified by B, associating algebraic rotation with observable quantum dynamics.

3. Image processing

3.1. Fourier Series and Fourier Transform

Fourier Series expresses periodic signals as a sum of sinusoidal components, that is sine and cosine wave. Fourier series is concerned with the approximation of a function as sinusoids of different frequencies. These sinusoids are harmonically related, i.e., they are multiples of the fundamental frequency of the signal in consideration. The goal is to represent any periodic function as an ultimately infinite sum of sinusoids or complex exponential harmonically related. All such component functions possess a definite amplitude and phase that are exactly measured by respective coefficients. This capability to describe complicated phenomena in terms of intrinsic oscillations lays out the full power of Fourier analysis. The approach provides a canonical form to complicated systems that is usually simpler than the original specification, and this advantage goes across field boundaries.[3]

Fourier Transform is a representation of a signal—whether periodic or non-periodic—as a continuous summation of sinusoidal components of all frequencies. Unlike the Fourier Series, which characterizes signals as a summation of discrete harmonics, Fourier Transform takes into account a continuum of frequencies, providing a frequency-domain description of the signal. It seeks to represent any time-domain function as an integral of complex exponentials with coefficients that precisely capture the amplitude and phase of each frequency component. It is this transformation that reveals the underlying spectral content of signals so that complex time-domain phenomena can be described in terms of their constituent frequency ingredients. The strong point of the Fourier Transform is its ability to convert time-domain complexity into a simpler, structured frequency-domain representation, a feature that is exploited across fields such as communications, signal processing, physics, and engineering.

In Fourier-based image reconstruction, an image $f(x,y)$ is expressed as a sum of basis functions—typically complex exponentials—whose coefficients are obtained via the Fourier transform: [3]

$$\hat{f}(u,v) = \iint f(x,y)e^{-2\pi i(ux+vy)}dxdy$$

The Fourier coefficients $\hat{f}(u,v)$ tell us about how much of each spatial frequency is present in the image. Low frequency components are employed to describe smooth intensity variations such as gradual shading, and high frequency components capture fine texture and hard edges.

If the Fourier coefficients are known for all frequencies (u,v), the image can be reconstructed by the **inverse Fourier transform**:[3]

$$f(x,y) = \iint \hat{f}(u,v)e^{2\pi i(ux+vy)}dudv$$

In the digital case, the image is represented as a 2D array $f[m,n]$ and transformed using the **2D Discrete Fourier Transform (DFT)**:[3]

$$F[k,l] = \sum_{m=0}^{M-1}\sum_{n=0}^{N-1} f[m,n]e^{-2\pi i\left(\frac{km}{M}+\frac{ln}{N}\right)}$$

With the inverse given by:

$$f[m,n] = \sum_{k=0}^{M-1}\sum_{l=0}^{N-1} F[k,l]e^{2\pi i\left(\frac{km}{M}+\frac{ln}{N}\right)}$$

3.2. Reconstruction[3]

Reconstruction involves taking all of the frequency-domain coefficients and combining them with the inverse Fourier transform to get back the original spatial-domain image. Practically, direct computation of the DFT takes a computational complexity of $O(N^2)$ for a 1D signal or $O(N^4)$ for a 2D image of size N×N, which is prohibitive for large data sets. The Fast Fourier Transform (FFT) is an algorithm that reduces this cost to $O(NlogN)$ in 1D and $O(N^2logN)$ in 2D, making frequency-based image reconstruction viable in real-time applications. The FFT accomplishes this by recursively breaking the DFT into smaller pieces and exploiting symmetries in the complex exponentials. This efficiency is crucial in medical imaging, video processing, and any application requiring rapid transformation between the spatial and frequency domains.

The Fourier coefficients $\hat{f}(u,v)$ or $F[k,l]$ are complex quantities having both magnitude and phase information. The intensity spectrum $\left|\hat{f}(u,v)\right|$ is the amount of each spatial frequency, and the phase spectrum $arg(\hat{f}(u,v))$ is the location of structures in an image. Smooth transitions like gradual shading or background intensity are represented by low-frequency terms and sharp transitions like edges and fine textures by high-frequency terms. Both phase and magnitude are significant—discarding the phase information yields unrecognizable images even where the magnitudes are preserved.

Reversing an image back from its frequency-domain representation is a question of taking the inverse Fourier transform, which adds all frequency components together into the space domain. In digital systems, this is achieved by the Inverse Discrete Fourier Transform, typically computed by the IFFT algorithm in order to be efficient. If there is loss or alteration of some of the frequencies—e.g., due to limited sampling during acquisition or intentional filtering—the reconstructed image will differ from the original. Removal of high frequencies causes blurring, removal of low frequencies removes large-scale structure and contrast, and random loss of frequencies can lead to ringing or other artifacts.

Fourier-domain frequency manipulation directly affects the reconstructed image. Low-frequency removal reduces contrast and brightness variations across the image, but high-frequency removal blurs edges and fine detail. Frequency modification selectively underlies a broad array of filtering techniques—low-pass filters eliminate noise but cause blurring, high-pass filters enhance edges but can amplify noise too, and band-pass filters extract specific patterns. Understanding how each frequency range makes up the image is crucial in effective reconstruction and enhancement.

Fourier-based reconstruction formulates the problem of imaging analysis and reconstruction in the spatial space to one of the frequency domain, where mathematical methods and filtering

operations can more easily be used. The continuous Fourier transform and discrete Fourier transform provide the theoretical and practical environment for so doing, with the Fast Fourier Transform offering a method of calculation that is efficient. With knowledge of the interplay between magnitude, phase, sampling, and frequency content, it becomes possible to combine high-quality images from frequency-domain data into many applications.

4. Tomography[1]

While Fourier series decompose periodic signals into sums of sinusoidal components, enabling reconstruction in the frequency domain, tomography generalizes the idea of reconstruction from transformed data to a broader context.

Tomography focuses on learning about an object's interior without physically cutting it. It accomplishes this by reconstructing the interior structure from a series of measurements collected outside the body.

In computed tomography (CT), instead of directly analyzing an image's frequency content, we work with projections—line integrals of an unknown function $f(x, y)$ representing the interior structure of an object.

4.1. Radon Transform[1]

Each projection corresponds to the accumulated attenuation of a beam (such as an X-ray) as it passes through the object, along a certain direction. Mathematically, in parallel-beam geometry, a projection at angle θ is described by the **Radon transform**:[1]

$$Rf(\theta, s) = \int_{-\infty}^{\infty} f(s\cos\theta - t\sin\theta\,, s\sin\theta + t\cos\theta)dt,$$

where *s* is the perpendicular distance from the origin to the integration line, and *t* is the coordinate along that line. This formula describes the total accumulation of *f* along the line defined by (θ, s). In medical CT, this models how an X-ray beam records the comulative absorption along its path. The set of all such projections $Rf(\theta, s)$ for $\theta \in [0, \pi)$ forms a sinogram – the raw data representation in CT. The Radon transform is a linear operator and is invariant under translation and rotations of the object.

4.2. Fourier Slice Theorem[1,5]

The core principle of tomography is similar to Fourier-based reconstruction: partial measurements encode the object in a transformed domain, and an inversion process retrieves the spatial distribution. The **Fourier Slice Theorem** provides the bridge, showing that the 1D Fourier transform of a projection $Rf(\theta, s)$ with respect to *s* equals the restriction of the 2D Fourier transform of *f(x,y)* to the line through the origin at angle θ.

$$F_s\{Rf(\theta, s)\}(\rho, \theta) = \int_{-\infty}^{\infty} Rf(\theta, s)e^{-2\pi i\rho s}ds = \hat{f}(u = \rho\cos\theta\,, v = \rho\sin\theta),$$

where F_s denotes the 1D Fourier transform with respect to *s*.

This result means that each projection provides a slice of the object's Fourier transform along a radial line in frequency space. As more projections are collected at many angles, the Fourier domain

will be gradually filled with radial samples. If enough projections are available, one can assemble these slices into the full Fourier representation and invert it to recover $f(x, y)$. Because the data is collected in polar coordinates, interpolation to a Cartesian frequency grid is needed before applying the inverse 2D Fourier transform, a step that introduces additional numerical challenges.

4.3.Advantages and disadvantages of FST[1,3,5]

The practical application of the Fourier Slice Theorem to real tomographic data is not that simple. Tomography is not simply a matter of applying an inverse Fourier transform. In theory, if one could measure projections $Rf(\theta, s)$ for all angles $\theta \in [0, \pi)$ and for all real values of s, the Fourier domain $\hat{f}(u, v)$ would be completely determined. In practice, however, only a finite number of projection angles are measured, and along each projection the detector records data at discrete sample points rather than continuously. This means that the Fourier domain is only partially covered, leaving gaps in the radial frequency lines. This limitation means that when we try to reconstruct the object, artifacts such as streaks or blurring appear because the sampling is insufficient to perfectly approximate the continuous Fourier space. The fewer projections, the more pronounced these artifacts become.

Another challenge is represented by the interpolation from polar to Cartesian frequency grids. FST naturally provides Fourier data in polar coordinates: each projection gives a radial slice through the Fourier domain. To apply the inverse Fourier transform numerically (using FFT, for example), the data must be represented on a Cartesian frequency grid. Since polar and Cartesian nodes rarely coincide, this requires interpolation of the polar data onto a rectangular grid before performing the inverse FFT. Some interpolation techniques are not exact. Errors are introduced especially in regions where the polar sampling is sparse, typically near the outer parts of frequency space (high frequencies). These errors manifest in the final reconstruction as additional noise, ringing, or blurring.

The most elementary approach is *nearest-neighbor interpolation*, where the value at a Cartesian frequency point (u, v) is assigned from the closest polar sample. If $g(\rho, \theta)$ denotes the sampled Fourier data in polar coordinates, then nearest-neighbor interpolation amounts to

$$\hat{f}(u, v,) \approx g(\rho_k, \theta_j),$$

where (ρ_k, θ_j) is the closest polar grid point to (u, v). While computationally efficient, this piecewise constant approximation produces blocky artifacts and jagged edges, especially in regions dominated by high-frequency content.

A more accurate alternative is *linear spline interpolation*, which approximates the function between known samples using continuous, piecewise linear segments.

Suppose we know the sampled Fourier data along a radial direction, $\{g(\rho_k, \theta_j)\}_k$, where ρ_k are discrete radial frequencies for a fixed angle θ_j. For an intermediate point $\rho \in [\rho_k, \rho_{k+1}]$, linear spline interpolation defines

$$g(\rho, \theta_j) \approx \frac{\rho_{k+1} - \rho}{\rho_{k+1} - \rho_k} g(\rho_k, \theta_j) + \frac{\rho - \rho_k}{\rho_{k+1} - \rho_k} g(\rho_{k+1}, \theta_j).$$

This formula produces a continuous function along ρ, ensuring that the interpolant is piecewise linear between nodes, while still exactly matching the known sample values at the grid points ρ_k.

The main advantage of linear spline interpolation is that it is computationally efficient and provides a smoother approximation than nearest-neighbor interpolation, which is piecewise constant and prone to blocky artifacts. Linear splines guarantee continuity of the interpolated function, which helps reduce visible discontinuities in the reconstructed image. However, the method still has limitations: because the interpolant is only first-order continuous (the derivative is not continuous at the knots), the resulting approximation can still appear angular and may blur fine details or sharp edges. Additionally, when sampling density in angle θ is insufficient, linear spline interpolation alone cannot compensate, leading to streaking artifacts in reconstructions.

Noise in the data is harmful, particularly for high frequencies. A main property of the Radon transform is that it smooths the original function by integrating along lines. This effect diminishes the contribution of high-frequency details in the projection data. When the Fourier Slice Theorem is used to invert the transform, these weak high-frequency components must be amplified to restore detail. However, the noise present in measurements is not smoothed in the same way and can dominate the high frequency band. As a consequence, reconstruction procedures tend to amplify noise when attempting to restore fine detail. This instability is the main reason why tomography is an ill-posed problem: the inversion is highly sensitive to small perturbations in the data. To counteract this, filters are applied, often combined with windowing functions that suppress excessive noise amplification at the cost of losing some resolution.

4.4.Interpolation[5]

4.4.1. Piecewise Interpolation

In tomography, piecewise interpolation is preferred over global polynomial interpolation because of both practical and numerical reasons. A global interpolating polynomial, such as the Lagrange polynomial of degree n-1, would require fitting a single high-degree polynomial through all sampled Fourier data. This approach is unstable. As the number of samples increases, the polynomial oscillates strongly between points (Runge phenomenon), which introduces artificial artifacts instead of reducing them. Moreover, global methods are computationally expensive and sensitive to noise. A small error in one sample can distort the entire approximation.

By contrast, piecewise interpolation (linear, cubic spline, PCHIP, etc.) only uses local information to approximate between neighboring samples. This ensures numerical stability, lower computational cost, and better local accuracy. Each small interval is interpolated independently, so local errors remain localized instead of propagating across the whole frequency space. This is essential in tomography, where data are often noisy and incomplete, and where reconstructions depend heavily on maintaining smooth and consistent local transitions in the Fourier domain.

An overview of the algorithm that creates a piecewise linear interpolant can be found here. This algorithm's stages serve as the foundation for more complex piecewise polynomial interpolants, also known as splines.

First, the interval index k is determined such that

$$x_k \leq x \leq x_{k+1}.$$

Second, we define a local variable $s := x - x_k$.

Third, we compute the first divided difference

$$\delta_k := \frac{y_{k+1} - y_k}{x_{k+1} - x_k}.$$

Finally, we construct the interpolant

$$P(x) = y_k + \frac{y_{k+1} - y_k}{x_{k+1} - x_k}(x - x_k)$$
$$= y_k + \delta_k s.$$

This is the Newton form of the (linear) interpolating polynomial. It can be generalized to higher-degree interpolants by using higher-order divided differences; i.e., divided differences of divided differences.

So, we have constructed the straight line that passes through (x_k, y_k) and (x_{k+1}, y_{k+1}). The points x_k are sometimes called breakpoints.

Note: $P(x)$ is a continous function of x, but its first derivative $P'(x)$ is not. $P'(x) = \delta_k$ on each subinterval and jumps at the breakpoints.

4.4.2. Cubic Interpolation and Cubic Spline Interpolation[5]

A more advanced alternative is *piecewise cubic interpolation*, where each interval between neighboring data points is approximated by a cubic polynomial. Unlike linear interpolation, which guarantees only continuity of the function values, cubic interpolants can also enforce continuity of the first derivative, and in some cases even the second derivative, across interval boundaries. This extra smoothness significantly improves the visual and numerical quality of the reconstruction. Piecewise cubic interpolation requires specifying not only the function values at the nodes but also estimates of the slopes (derivatives).

For an interval $[x_k, x_{k+1}]$ with spacing $h = x_{k+1} - x_k$ and local variable $s = x - x_k$, consider the following cubic polynomial:

$$P(x) = \frac{3hs^2 - 2s^3}{h^3} y_{k+1} + \frac{h^3 - 3hs^2 + 2s^3}{h^3} y_k + \frac{s^2(s-h)}{h^2} d_{k+1} + \frac{s(s-h)^2}{h^2} d_k,$$

where y_k, y_{k+1} are the known function values and d_k, d_{k+1} are the slopes at the nodes.

Interpolants for derivatives are known as Hermite or osculatory interpolants because of the higher-order contact at the breakpoints. If we know both function values and first derivatives at a set of points, then a piecewise cubic Hermite interpolant can be fit to those data.

But if we are not given the derivative values, we need to define the slopes d_k somehow. There are different possibilities for defining these slopes. One widely used approach is the piecewise cubic Hermite interpolating polynomial (PCHIP), which selects slopes in such a way that the interpolant is shape-preserving. This means that if the data are monotone or convex in a local interval, the interpolant will not introduce spurious oscillations (artificial wiggles that appear because of smoothness prioritization) or overshoots (interpolated curve rises high/drops lower than actual data near sharp changes). While PCHIP ensures only $\mathbb{C}^1$ continuity (the first derivative is continuous but the second derivative is not), it avoids these artifacts that can occur with cubic splines. As a result, the interpolated curve follows the natural trend of the data more faithfully, even if it is not as mathematically smooth.

Another common choice is the cubic spline, which instead enforces global smoothness. In addition to continuity of the function values and first derivatives at the nodes, cubic splines also require continuity of the second derivative (curvature) across all interior knots:

$$P(x_k) = y_k, \quad P'(x_k^-) = P'(x_k^+), \quad P''(x_k^-) = P''(x_k^+), \quad for\ \ k = 2, \ldots, n-1.$$

To close the system, special boundary conditions must be imposed. One popular choice is the "not-a-knot" condition, which requires that the first two subintervals $[x_1, x_2]$ and $[x_2, x_3]$ be described by the same cubic polynomial (and similarly for the last two subintervals). This effectively reduces the number of knots by two and yields a unique spline solution without artificially fixing endpoint slopes.

4.5. Filtered Back Projection[1,3,5]

The most widely used method for reconstructing an image from projection data is Filtered Back Projection. An inversion formula for the Radon transform is given by the classical filtered back projection formula:

$$f(x,y) = \frac{1}{2} B(F^{-1}[|S|F(Rf)(S,\theta)])(x,y), \qquad \forall (x,y) \in \mathbb{R}^2$$

Proof. Let $f \in L^1(\mathbb{R}^2) \cap C(\mathbb{R}^2)$ with $F_f \in L^1(\mathbb{R}^2)$ and let $(x,y) \in \mathbb{R}^2$ be fixed. Applying the 2D Fourier inversion formula to f yields the identity

$$f(x,y) = F^{-1}(Ff)(x,y) = \frac{1}{4\pi^2} \iint Ff\,(X,Y) e^{i(xX+yY)} dXdY.$$

By changing the variables $(X,Y) \in \mathbb{R}^2$ from Cartesian coordinates to $(S,\theta) \in \mathbb{R} \times [0,\pi)$ in polar coordinates, i.e.,

$$X = S\cos(\theta) \quad \text{and} \quad Y = S\sin(\theta)$$

we get $dXdY = |S|dSd\theta$. Thus, with the Fourier slice Theorem follows that

$$f(x,y) = \tfrac{1}{4\pi^2} \int_0^\pi \int Ff(S\cos(\theta), S\sin(\theta)) e^{iS(x\cos(\theta)+y\sin(\theta))} |S| dSd\theta$$

$$\overset{FST}{\Longleftrightarrow} f(x,y) = \tfrac{1}{4\pi^2} \int_0^\pi \int F(Rf)(S,\theta) e^{iS(x\cos(\theta)+y\sin(\theta))} |S| dSd\theta$$

$$= \tfrac{1}{2\pi} \int_0^\pi F^{-1}[|S|F(Rf)(S,\theta)](x\cos(\theta) + y\sin(\theta), \theta) d\theta$$

$$= \tfrac{1}{2} B(F^{-1}[|S|F(Rf)(S,\theta)])(x,y)$$

due to the definition of the back projection.

The classical FBP formula is highly sensitive with respect to noise and it cannot be used in practice. The formula can be stabilized by incorporating a low-pass filter F_L.

Definition (Low-pass filter). *Let L>0 and let* $W \in L\infty(\mathbb{R})$ *be even and compactly supported with*

$$supp(W) \subseteq [-1,1].$$

A function $F_L: \mathbb{R} \to \mathbb{R}$ *of the form*

$$F_L(S) = |S|W(S\ /\ L) \qquad for\ S \in \mathbb{R}$$

is called low-pass filter *for the stabilization of the FBP formula, where L denotes its bandwidth and W is its window function. For the sake of brevity, we set* $F \equiv F_1$ *so that*

$$F_L(S) = LF(S\ /\ L) \qquad \forall\, S \in \mathbb{R}.$$

In the following, let F_L be a low-pass filter with bandwidth L and window W. Because of the compact support of W, we have $F_L \in L^p(\mathbb{R})$ for all $1 \leq p \leq \infty$ and

$$supp(F_L) \subseteq [-L, L].$$

Now, let the target function f satisfy $f \in L^1(\mathbb{R}^2)$. Based on the FBP formula we define the *approximate FBP reconstruction* f_L via

$$f_L(x, y) = \frac{1}{2} B(F^{-1}[F_L(S)F(Rf)(S, \theta)])(x, y), \quad \forall (x, y) \in \mathbb{R}^2.$$

This equation defines a *band-limited* approximation of the target function f. A function whose Fourier transform Ff has compact support is called a *band limited* function.

4.6. Filtered Back Projection guided by the Interpolation model

Recent research shows that filtered back-projection can be improved by tailoring the reconstruction filter to the interpolation model used for the sinogram.

By representing the projection data with B-splines and combining the ramp filter with the spline fitting process, the filtering and interpolation steps are treated as a single operation. This model-driven approach produces cleaner reconstructions and higher peak signal-to-noise ratios (PSNR), with the greatest benefits when using low-degree interpolation such as linear splines. Among the tested strategies, oblique projection and fractional spline filtering give the largest improvements (up to **2.5 dB** over the classical Shepp-Logan filter) while moving from linear ($n = 1$) to cubic ($n = 3$) splines yields a further **2-4 dB** gain regardless of the specific filter. The fractional derivative method offers a slight additional advantage by implementing the ramp filter analytically within the spline framework, ensuring a reconstruction that is fully consistent with the underlying mathematical model.

Traditionally, FBP first applies a ramp filter (such as the Ram–Lak or Shepp–Logan filter) to each projection and then performs interpolation during back-projection.

However, when the sinogram is modeled with B-spline interpolation, the filtering operator can be modified to match the spline space, yielding measurable improvements in image quality.

The approach is to merge the ramp filtering and spline fitting processes into a single operation. Let $p_\theta(t)$ be the projection data for angle θ and $g_\theta(t)$ its ramp-filtered version.
Instead of applying a standard filter and then interpolating, one represents $g_\theta(t)$ as a spline expansion

$$g_\theta(t) \approx \sum_{k \in \mathbb{Z}} c_\theta(k)\, \beta_n(t - k),$$

where β_n is a B-spline of degree n and the coefficients $c_\theta(k)$ are computed directly in the Fourier domain.
Because the ramp filter corresponds to a fractional derivative, it can be combined with the spline prefilter in a single frequency-domain operation.

Three spline-guided filtering strategies have been proposed:

- B-spline interpolating ramp filter.
  The ramp filter and B-spline prefilter are combined so that the ramp-filtered sinogram is represented directly in the spline basis.

- Oblique projection filter.
  Instead of simple interpolation, the filtered sinogram is projected obliquely onto the spline space, producing a least-squares–like approximation that better matches the band-limited nature of the data.
- Fractional spline filter.
  Using fractional B-splines, the ramp filter is applied analytically as a fractional derivative, which naturally reduces the spline degree by one and eliminates the need for a strict band-limitation assumption.

Experiments with the Shepp–Logan phantom (128×128 pixels, 256 projection angles) demonstrate the benefit of these methods.
For linear interpolation ($n = 1$), the standard Shepp–Logan filter yields a peak signal-to-noise ratio (PSNR) of 29.16 dB, while the B-spline filter achieves 30.98 dB, the oblique projection filter 32.91 dB, and the fractional spline filter 33.10 dB.
With cubic splines ($n = 3$), the PSNR improves further to about 34.7–34.9 dB, roughly two decibels higher than the classical filter.[1,3,5]

These results highlight that interpolation and filtering are inherently linked: selecting a spline model not only improves the interpolation from polar to Cartesian coordinates, but also allows the ramp filter itself to be optimized for that model, yielding sharper edges and reduced artifacts in the final tomographic reconstruction.

5. Tomography in Quantum Systems[6]

Qubit (quantum bit) is the quantum information unit, analogous to the classical bit but governed by the laws of quantum mechanics. A classical bit will be in one of two states (0 or 1), while a qubit will exist in a superposition of both states simultaneously. A qubit may be represented mathematically as a vector in a two-dimensional Hilbert space: $|\psi\rangle=\alpha|0\rangle+\beta|1\rangle$, where $|0\rangle$ and $|1\rangle$ are the computational basis states, and $\alpha, \beta \in \mathbb{C}$ are complex coefficients satisfying $|\alpha|^2 + |\beta|^2 = 1$. A more general description uses the density matrix formalism, and this can be applied to both pure states (maximally known) and mixed states (statistical mixtures). Geometrically, every pure qubit state is a point on the Bloch sphere, $|0\rangle$ and $|1\rangle$ being the poles and all other points superpositions. It is this rich structure that renders the qubit superior to the classical bit and upon which quantum computing, communication, and tomography are founded.

The most natural visualization of a qubit is the Bloch sphere, a geometric model of all pure qubit states. In this model, a qubit state is a point on a unit sphere in three dimensions. The poles of the sphere represent the basis states: $|0\rangle$ is represented by the north pole and $|1\rangle$ by the south pole. Any other point on the surface represents a superposition of the basis states as:

$$|\psi\rangle=\cos\left(\frac{\theta}{2}\right)|0\rangle+e^{i\phi}\sin\left(\frac{\theta}{2}\right)|1\rangle,$$

where θ and ϕ are spherical coordinates.[2,4,6]

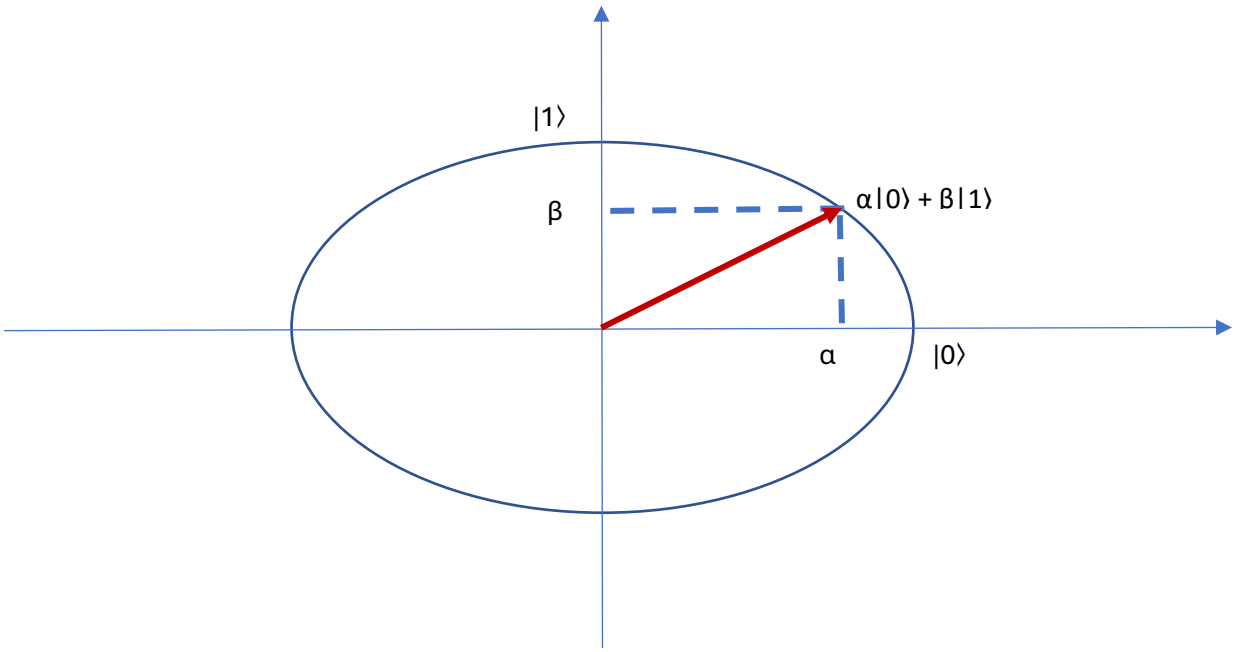

Figure 1: The representation of the qubits over the Bloch Sphere

Tomography is a general concept: one reconstructs an unknown object by combining information from many partial measurements or projections. In classical computed tomography, this is to reconstruct the spatial absorption distribution in a body from X-ray projections at many angles. In quantum tomography, the principle is the same, but the object of study is a quantum state rather than a physical cross-section. Since quantum states may not be measured directly, only probabilistically, measurement outcomes, tomography is the reconstruction of the density matrix ρ which is the full statistical description of a quantum system.

The case of a single qubit:[2,4]

A qubit state is fully described by a 2×2 density matrix, which can be expressed in terms of the Bloch vector $\overline{r} = (r_x , r_y , r_z)$:

$$\rho = \frac{1}{2}\left(I + r_x\sigma_x + r_y\sigma_y + r_z\sigma_z\right),$$

where σ_x, σ_y, σ_z are the Pauli matrices. Geometrically, this is a point on the Bloch sphere. To calculate ρ, one can compute the expectation values of such Pauli operators, $\langle\sigma_x\rangle, \langle\sigma_y\rangle, \langle\sigma_z\rangle$.This is achieved by creating many copies of the qubit and measuring them in three bases (the eigenbases of X, Y and Z). The ratio of relative frequencies of measurement outcomes provides directly estimates for components of r. Plugging these values into the formula reconstructs the density matrix.

This process is more or less like reconstruction from projections in CT. Any measurement basis is akin to a "projection" of the state to be determined on some axis of the Bloch sphere, exactly as any X-ray scan is a projection of the object along some direction. A single measurement provides incomplete information, but the collection of all measurements put together enables us to reconstruct.

The most straightforward reconstruction technique is linear inversion, whereby measured frequencies are simply inverted to yield expectation values and used in place of the Bloch-vector expansion. This will often, however, result in an unphysical density matrix (negative eigenvalues) owing to finite sampling and noise. To avoid this, current techniques employ Maximum Likelihood Estimation (MLE): one finds the physical state ρ (semipositive definite with trace = 1) that maximizes

the likelihood of obtaining the experimental data. MLE is more stable, adheres to quantum constraints, and is used widely in experimental quantum information.

Whereas qubit tomography demonstrates the underlying principle, actual quantum information tasks involve handling more extensive systems: multi-qubit registers or qubits of larger dimension. The mathematical object to be reconstructed remains the density matrix ρ but increases in size with increasing system dimension. For a system of dimension d, ρ is a $d \times d$ Hermitian, it is a positive semidefinite matrix of unit trace. It thus possesses d^2-1 real degrees of freedom. For n qubits, the dimension is $d= 2^n$ and the number of parameters becomes $4^n -1$, which grows exponentially with the number of qubits. This scaling gives very severe challenges for quantum tomography.

In order to build such a state, one has to perform an informationally complete set of measurements, i.e., a set of observables or bases whose values produce enough independent equations so that all of the unknown parameters of ρ can be solved.

5.1. Density Matrices and Quantum Measurements[2,4,6]

Up to this point we have described a qubit as a pure state

$$|\psi\rangle = \alpha|0\rangle + \beta|1\rangle, \qquad |\alpha|^2 + |\beta|^2 = 1,$$

which is adequate when we know the system is perfectly prepared. In practice, however, a qubit may be in a statistical mixture of different pure states. For example, a source might emit $|0\rangle$ with probability p and $|1\rangle$ with probability $1 - p$.

To describe such situations, we use a density matrix

$$\rho = \sum_k p_k \, |\psi_k\rangle\langle\psi_k|,$$

which is a positive-semidefinite, Hermitian 2×2 matrix with unit trace $(tr\rho = 1)$. Pure states appear as special cases where $\rho = |\psi\rangle\langle\psi|$.

Measurements in quantum mechanics are represented by observables, i.e. Hermitian operators O. When a system in state ρ is measured, the expectation value of O is

$$\langle O\rangle = tr(O\rho).$$

Tomography relies on collecting enough of these expectation values to determine all the unknown entries of ρ.

A set of observables is called tomographically complete if their expectation values uniquely specify the density matrix. For a single qubit, measurements of the Pauli operators $\sigma_x, \sigma_y, \sigma_z$ together with the identity form such a complete set.

5.2. Linear Inversion in Quantum State Tomography[2,4,6]

The goal of quantum state tomography is to reconstruct the density matrix ρ of an unknown quantum system from experimental measurements.

Each measurements outcome provides an estimate of the expectation value of some observable O_i.

If we perform a tomographically complete set of measurements—typically the three Pauli operators $\sigma_x, \sigma_y, \sigma_z$—these expectation values form a linear system

$$m = Mr,$$

where

$m = (\langle O_1 \rangle, \langle O_2 \rangle, \dots)^T$ is the vector of measured averages,
$r = \left(r_x, r_y, r_z\right)^T$ is the unknown Bloch vector,
and M is the measurement matrix whose entries are $M_{ij} = tr\left(O_i \sigma_j\right)/2$.
Linear inversion simply solves this equation for r using standard linear algebra (matrix inversion or least squares if the system is overdetermined).
The reconstructed density matrix is then

$$\hat{\rho} = \frac{1}{2}\left(I + \hat{r}_x \sigma_x + \hat{r}_y \sigma_y + \hat{r}_z \sigma_z\right).$$

This procedure is conceptually straightforward: estimate the expectation values from repeated measurements, plug them into the linear system, and compute the Bloch vector. However, experimental noise and finite sampling can yield a solution $\hat{\rho}$ that is not a valid physical state—for example, it may have a small negative eigenvalue, violating the requirement $\rho \geq 0$. Such unphysical results arise because linear inversion does not impose the positivity constraint during reconstruction.
Despite this drawback, linear inversion remains important because it provides a fast, unbiased baseline estimate of the quantum state and serves as the starting point for more refined methods, such as maximum-likelihood estimation, which enforce positivity and other physical constraints.

6. The link between classical tomography and quantum state tomography

The role of linear inversion in quantum state tomography closely mirrors its role in classical tomography. In classical imaging, the goal is to reconstruct an unknown object, such as the internal structure of the human body, from a collection of projection measurements taken at different angles. Each projection corresponds to a line integral of the object's density function, and these integrals are combined into a system of linear equations. By inverting this system—directly or approximately —one recovers the density distribution. This process is what underlies reconstruction methods such as filtered back-projection.

Quantum tomography follows the same logic, but the object being reconstructed is no longer a spatial density function—it is the quantum state of a system, encoded in the density matrix ρ. Measurements of different observables (for instance, Pauli operators) provide expectation values, which play the role of the projection data in the classical case. Here, performing a measurement in the X, Y, and Z bases is directly analogous to taking projections of a body at different angles in a CT scan: each setting gives a different "slice of information" about the unknown system. These expectation values are linearly related to the unknown parameters of ρ, just as projection data are linearly related to the unknown pixel values in an image. Linear inversion again supplies the reconstruction step: solving the linear system formed by measurement results yields the best-fit density matrix, in the same way solving the Radon transform equations yields the object's density distribution.

Linear inversion is therefore the natural link between classical and quantum tomography. In both cases, the unknown object—whether a spatial density function or a quantum density matrix—is not observed directly, but only through indirect measurements that are linearly related to it.

Reconstruction consists of inverting this linear relationship: projections in classical tomography and expectation values in quantum tomography.

The key difference is in interpretation: in classical tomography, the reconstructed image corresponds to a tangible spatial distribution, while in quantum tomography it represents the full probabilistic description of a quantum system.

6.1. Symmetry Groups

One of the most important tools in the modern physics is embodied by the symmetry group; more precisely to define a physical theory consists in:

• a differentiable manifold M

- the natural generalization of a surface
- a space, which locally (at the level of an infinitesimal neighborhood) is isomorphic to a linear space $\mathbb{R}^N$
- so that the isomorphism map is also differentiable (wherefore the name of differentiable manifold stems)

• and a group of symmetries $(G,\cdot)$ - in the sense that:

• The entire dynamics/motion over the manifold M is realised by the intercession of the transformations from the symmetry group G:

more precisely, for any $y_1, y_2 \in M$, there exists a transformation $a \in G$, so that:

$$a \cdot y - 1 = y_2$$

- So, the points over the manifold M are moved by the elements/transformations of the symmetry/transformation group G.

Some notable examples of symmetry groups are:

I. Given a finite (cyclic) group with N elements, for instance: $\mathbb{Z}_N = \frac{\mathbb{Z}}{\lambda\mathbb{Z}}$ (obtained by considering the factorization: $a\ mod\ N, \forall) a \in \mathbb{Z}$ (for instance: $16\ mod\ 3 = 1$))

$$\mathbb{Z}_N = \{0, 1, 2, \cdots, N - 1\}$$

so that the points in $\mathbb{Z}_N$ could be visually/geometrically represented as a polygon with N edges of identical edges inscribed within a circle of radius 1. So that, the composition of $\mathbb{Z}_N$ could be represented geometrically as rotations that interchange the N vertices of the respective polygon over the circle of radius 1: These rotations are of angle: $\frac{2\pi}{N}$ And could be represented mathematically as:

$$e^{\frac{2\pi iky}{N}}$$

Due to the fact that the circle of radius one could be understood as a subset of the set of complex numbers: $\mathbb{C}$ and the trigonometric rotations could be encoded via the exponential due to the Euler's formula: $e^{iy} = \cos(y) + i\sin(y)$These considerations will play a central role in establishing the link between the Fourier transform considered over groups and for instance the Shor's algorithm.

II. Considering the linear space: RN, the most prominent transformations groups are the following groups of matrices (subsets of $M_N(\mathbb{R})$):

• The general linear group, that comprises all the invertible matrices:

$$GL(N;R) = \{A \in M_N(\mathbb{R}) | \det(A) \neq 0\}$$

- This groups comprises contains all the linear transforms over $\mathbb{R}^N$(including any change of frame - coordinate/basis change in RN).

• The group of orthogonal transformations:

$$O(N) = \{A \in M_N(\mathbb{R}) | A \cdot A^t = A^t \cdot A = I_N\}$$

- mathematically, the elements of $O(N)$ stand for rotations and reflections over $\mathbb{R}^N$(with the determinant equal to 1 or −1).

- Thus $O(N)$ stands for the counterpart (generalization) of the rotation group when one replaces the finite group $\mathbb{Z}_N$ by $\mathbb{R}^N$

III. In particular, when one considers the linear space: $\mathbb{C}^N$, the role of O(N) is replaced by the group of unitary transformations:

$$U(N-1) = \{A \in M_N(\mathbb{C}) | A \cdot A^t = A^t \cdot A = I_N\}$$

The elements of $U(1)$ for instance act as rotations upon the complex plane $\mathbb{C}$ and given that the Bloch sphere could be projected over the complex plane, the elements of $U(1)$ are those transformations that act upon the qubits (embodying the quantum gates - used to define quantum circuits (as the basis for the quantum computation)).

It is important to mention that the considered group of symmetries (matrix-transformations) is the one that defines a given physical theory - for instance the Quantum Electrodynamics (and thus also the quantum computation) are defined by the group of unitary transformations: $U(1)$.

6.2.Elements of representation theory

The link between the symmetry groups and the Fourier transform is mediated/obtained through the notion of Group Representation:

• Given a group of symmetries: $(G,\square)$, to write a representation of the group G means:

- To consider a linear space V (for instance V might be chosen as: $\mathbb{R}^N$ or $\mathbb{C}^N$ (where N is the dimension of the considered representation))

- and one group homomorphism π that maps/assigns:

$$\pi : G \rightarrow GL(V)$$

and so that:

$$\pi(a \square b) = \pi(a) \cdot \pi(b), \forall) a, b \in G$$

- for instance, in case that: $V = \mathbb{R}^N$:

$$\pi: G \to GL(\mathbb{R}; N)$$

- which assigns (and thus represents) any element $a \in G$ as a matrix transformation from $GL(\mathbb{R}; N)$ that acts upon the linear space: $\mathbb{R}^N$.

• In this case it is also said that the group G acts upon the linear space of representation V.
• The set of all the possible representations of a given group $(G,\square)$ is de-noted as: $\tilde{G}$ and is also called the Pontryaghin group - denoted by: $\tilde{G}$.

There exists a theorem which states that for any locally compact group (a group, which locally is bounded/allows bounded and closed neighborhoods), the group of all the possible representations: $\tilde{G}$ is isomorphic to G.

Once one has defined the concept of representation of a group $(G,\square)$ and the Pontryaghin dual group of representations: $\tilde{G}$, one can assign the notion of character to any representation:

- More precisely, given a representation of the group: $(G,\square) : \pi \in \tilde{G}$, the character is defined as:

$$\chi_\pi(a \in G) = tr(\pi(a))$$

• for instance, supposing that one considers $\pi : G \to GL(\mathbb{C}, N)$ a representation, then:

$\pi(a) = A \in GL(C,N) \Rightarrow \xi\pi(a) = tr(A)$ the trace of the matrix A
↓
so that the character is just a function: $\chi : G \to C$.

6.3.Fourier Transform on a group

At this moment, we are in the position to generalize the Fourier transform defined over $\mathbb{R}$ to the case when it is considered over a group G.

In order to attain this aim, we have to consider:

- a group G, with a representation π over the general liniar group associated to the linear space $\mathbb{C}$ ($\pi : G \to GL(\mathbb{C})$),

- and given any function:

$$f : G \to \mathbb{C}$$

• the Fourier transform of the function f is defined as:

$$F[f] = \hat{f}_\pi = \sum_{a \in G} f(a) \cdot \pi(a)$$

• Respectively the inverse Fourier transform is defined as:

$$f(a) = \sum_{\pi \in \tilde{G}} tr(\pi(a^{-1})) \cdot \tilde{f}_\pi = \sum_{\pi \in \tilde{G}} \chi_\pi(a^{-1}) \cdot \hat{f}_\pi$$

The classical Fourier transform reconsidered:

Let us revise how this generalization reduces just to the classical definition of the Fourier transform for the particular case when: $(G,\square) = (R,+)$:

- First of all, it is important to notice that any representation of the commutative/abelian group $(R,+)$ could be obtained by the means of the exponential function:

→ The exponential function grants all the unitary and irreducible representations for the group (R, +)

- Since the group: $(R,+)$ is abelian, locally compact, the Pontryaghin duality theorem states that the dual group (the set of all the irreducible, unitary, continuous) representations: $\tilde{G}$ is also a locally-compact abelian group.

- The group $(R,+)$ is represented over: $GL(\mathbb{C},1) = U(1)$ and each representation has the form:

$$\pi_\xi : \mathbb{R} \to U(1) : \pi_\xi(y) = e^{i\xi y}$$

- so that each real number $\xi \in \mathbb{R}$ defines a representation and therefore the dual group: $\widetilde{\mathbb{R}} \simeq \mathbb{R}$ is isomorphic to $\mathbb{R}$ itself (every real number $\xi \in \mathbb{R}$ labels a representation).

$*$ At this point, based on the previous considerations related to the Fourier transform over a group G, the Fourier transform for the group $(R,+)$ will have the form:

$$F[f] = \tilde{f}(\xi) = \int_{-\infty}^{\infty} f(y)\cdot\pi_\xi(y)dy = \int_{-\infty}^{\infty} f(y)\cdot e^{-i\xi y}dy$$

- and the inverse Fourier transform rebuilds f as the continuous superposition (the integral) of these irreducible "modes" of the group action representation (frequencies):

$$f(y) = \frac{1}{2\pi}\int_{-\infty}^{\infty} \tilde{f}(\xi)\cdot e^{-i\xi y}d\xi$$

- Expressing what amount contains f of each representation.

6.4.The application of the group Fourier Transform for the Shor's algorithm as a gateway

The (discrete) Fourier transform considered upon the finite (cyclic) group: ZN is used to find the hidden period of the function used for the data encryption.

The property used is just the action of the discrete Fourier transform upon the qubits - it is used to rotate/change the state of a qubit:

$$|a\rangle = \frac{1}{\sqrt{q}}\cdot\sum_{c=0}^{q-1}\left|c\right\rangle * e^{2\pi i a\frac{c}{2}}$$

- Thus, mimicking the action of slicing the state.

- By considering this action, the Fourier transform could be perceived as a gateway by the means of which: when considering the Fourier transform over groups, one can generalize the classical reconstruction algorithms in the following way:

I. First one quantifies the classical algorithm in terms of the Fourier transforms defined upon the symmetry group for the space of the classical algorithm

II. Consider the group homomorphism between the symmetry groups assigned to the classical and quantum assigned spaces.

III. Thereafter decode/reinterpret the classical algorithm in terms of the Fourier transform considered over the quantum symmetry counterpart group in order to deduce the steps for the quantum counterpart algorithm

⇒ Thus, the gateway between the classical and quantum algorithms resides in a symmetry groups' homomorphism followed by the reenacting of the algorithm steps in terms of group Fourier Transform.

6.5. Overview of Shor's Algorithm

Peter Shor's algorithm, introduced in 1994, is one of the first quantum algorithms to demonstrate exponential speedup over its classical counterparts. Its goal is to factorize a large integer n efficiently by finding the period r of the modular exponential function

$$F(a) = x^a \ mod \ n$$

where x is an integer coprime to n. Once the period r is found, the factors of n can be obtained using simple arithmetic relations based on the properties of modular exponentiation.
F(a) is a periodic function, with period r, thus we know that $x^0 \ mod \ n = 1$, $x^r \ mod \ n = 1$, and $x^{2r} \ mod \ n = 1$ and so on. Because of this:

$$x^r \equiv 1 \ mod \ n$$

$$(x^{r/2})^2 \ = x^r \equiv 1 \ mod \ n$$

$$(x^{r/2})^2 - 1 \equiv 0 \ mod \ n$$

and if r is an even number

$$(x^{r/2} - 1)(x^{r/2} + 1) \equiv 0 \ mod \ n$$

The product $(x^{r/2} - 1)(x^{r/2} + 1)$ is an integer multiple of n. As long as $x^{r/2}$ is not equal to ± 1, then at least one of $(x^{r/2} - 1), (x^{r/2} + 1)$ must have nontrivial factor in common with n. So, by computing $\gcd(x^{r/2} - 1, n)$, and $\gcd(x^{r/2} + 1, n)$, we will obtain a factor of n, where gcd is the greatest common denominator function.

The algorithm consists of the following steps:

Step 1: Determine if n is a prime, an even number, or an integer power of a prime number. If it is, we will not use Shor's algorithm.

Step 2: Pick an integer q that is a power of 2 such that $n^2 \leq q < 2n^2$.

Step 3: Pick a random integer x that is coprime to n (two numbers are coprime when their greatest common divisor is 1).

Step 4: Create a quantum register and partition it into two parts, register 1 and register 2. Thus the state of our quantum computer can be given by: $|reg1, reg2\rangle$. Register 1 must have enough qubits to represent integers as large as $q - 1$. Register 2 must have enough qubits to represent integers as large as $n - 1$. The calculations for how many qubits are needed would be done on a classical computer.

Step 5: Load register 1 with an equally weighted superposition of all integers from 0 to $q-1$. Load register 2 with all zeros. The total state of the quantum memory register at this point is:

$$\frac{1}{\sqrt{q}}\sum_{a=0}^{q-1}|a,0\rangle$$

Step 6: Apply the transformation $x^a \ mod \ n$ for each number stored in register 1 and store the result in register 2. Due to quantum parallelism this will take only one step, as the quantum computer will only calculate $x^{|a\rangle} \ mod \ n$, where $|a\rangle$ is the superposition of states created in step 5. The state of quantum memory register at this point is:

$$\frac{1}{\sqrt{q}}\sum_{a=0}^{q-1}|a, x^a \ mod \ n\rangle$$

Step 7: Measure the second register, and observe some value k. This has the side effect of collapsing register one into an equal superposition of each value a between 0 and $q-1$ such that

$$x^a \ mod \ n = k$$

The state of the quantum memory register after this step is:

$$\frac{1}{\sqrt{\|A\|}}\sum_{a'=a'\in A}|a', k\rangle$$

Where A is the set of a's such that $x^a \ mod \ n = k$, and $\|A\|$ is the number of elements in that set.

Step 8: Compute the discrete Fourier transform on register one. The discrete Fourier transform, when applied to a state $|a\rangle$, changes it in the following manner:

$$|a\rangle = \frac{1}{\sqrt{q}}\sum_{c=0}^{q-1}|c\rangle * e^{2\pi iac/q}$$

This step is performed by the quantum computer in one step through quantum parallelism. After the discrete Fourier transform our register is in the state:

$$\frac{1}{\sqrt{\|A\|}}\sum_{a'\in A}\frac{1}{\sqrt{q}}\sum_{c=0}^{q-1}|c, k\rangle * e^{2\pi ia'c/q}$$

Step 9: Measure the state of register one (call this value m). This integer m has a very high probability of being a multiple of q/r, where r is the desired period.

Step 10: Take the value m, and on a calssical computer do some post processing which calculates r based on knowledge of m and q, in particular:

- There is a high probability that $m = \lambda * (q/r)$ where λ is an integer
- If we perform floating point division of m/q, and then calculate the best rational approximation to m/q whose denominator is less than or equal to q.
- We take this denominator to be a candidate for r.
- If our candidate r is odd, we double it if doing so leads to a value less than q.

Step 11: Once you have attained r, a factor of n can be determined by taking $\gcd(x^{r/2}-1, n)$ and $\gcd(x^{r/2}+1, n)$. If you have found a factor of n, stop, if not go back to step 4. There is the need to go back to step 4, in case Shor's algorithm failed to produce factors of n.

6.6. Shor's Algorithm and the Tomographic Perspective

The mathematical essence of Shor's algorithm can be interpreted through the concept of tomographic "sections" – slices that reveal periodic or structural properties of a function or state. In this view, Shor's quantum period-finding procedure is analogous to reconstructing a hidden structure (periodicity) by examining its projections in a transformed space.

In Shor's algorithm, this reconstruction occurs in the frequency domain through the Quantum Fourier Transform acting over the group $\mathbb{Z}_N$. In classical tomography, reconstruction occurs in spatial or projection space through the inverse Fourier transform, which inverts the projections obtained via the Radon transform.

Therefore, both approaches rely on the interplay between a function and its transformations – in one case over an abstract commutative group (quantum), and in the other over Euclidean space (classical).

6.7.Transformations as Translations and Rotations in the Euclidean Group

In classical tomography, transformations correspond to translations and rotations in the Euclidean group $E(n)$ associated with $\mathbb{R}^2$ or $\mathbb{R}^3$. These operations describe the movement of the projection plane through different spatial orientations. The inverse Fourier transform then reconstructs the original object by summing over all such projections.

Analogously, in Shor's algorithm, the QFT acts as a transformation that **rotates** and **translates** the quantum state within its Hilbert space representation. Although the domain is abstract and unitary rather than geometric, the algebraic structure is similar: both processes explore the invariances and symmetries of their associated transformation groups.

6.8.Tomography and the Hidden Subgroup Problem

From an algebraic perspective, both classical and quantum tomography can be described in terms of inverse transformations applied to symmetry groups:

In classical tomography, the relevant symmetry group is the Euclidean or orthogonal group $E(n)$ or $O(n)$, whose elements represent spatial rotations and translations. In quantum tomography, the transformations belong to the unitary group $U(N)$, which acts on the Hilbert space of quantum states. These unitary operations "move" states across the Bloch sphere, effectively changing the measurement basis or the informational projection of the quantum system.

In both contexts, reconstruction corresponds to the inversion of a group action — that is, to retrieving hidden information (structure, symmetry, or periodicity) from observed projections.

From this algebraic point of view, all tomographic techniques — classical and quantum — can be unified within the framework of Hidden Subgroup Problems (HSPs). In Shor's algorithm, the hidden subgroup corresponds to the set of integers forming the periodicity r of the modular exponential function. The QFT reveals this subgroup by transforming the problem into a frequency-domain pattern recognition task.

Similarly, in classical tomography, one reconstructs an object (a "hidden structure") by analyzing its projections, effectively solving an inverse problem where the underlying symmetry (e.g., rotational invariance) defines the subgroup structure.

This algebraic viewpoint provides a foundation for generalizing classical reconstruction methods to the quantum level, suggesting that algorithms developed for classical tomography or Fourier image reconstruction can be reinterpreted as instances of quantum hidden subgroup algorithms.

6.9.The inverse Fourier Transform and the Hidden Subgroup Problem framework

The Hidden Subgroup Problem (HSP) provides a unifying algebraic structure that connects Fourier analysis, tomographic reconstruction, and quantum algorithms. In its general form, the HSP can be stated as follows: given a group G and a function $f: G \to S$ that is constant on the cosets of a hidden subgroup $H \subseteq G$ and distinct on different cosets, the task is to determine H.

This abstract formulation includes both classical signal reconstruction problems and quantum period-finding algorithms. In Shor's algorithm, $G = \mathbb{Z}_n$ and $H = r\mathbb{Z}_n$ (the subgroup of integers modulo n generated by the period r); the Quantum Fourier Transform (QFT) is used to identify H by revealing the frequency components corresponding to its periodic structure.

From the perspective of classical tomography, the same mathematical mechanism appears under a different form: the Inverse Fourier Transform is applied to reconstruct an unknown spatial or functional structure from its projections — effectively retrieving the hidden symmetry or distribution underlying the measurement data.

Thus, the Inverse Fourier Transform serves as the conceptual and operational bridge between the two domains: In classical algorithms, it reconstructs images or densities by inverting the Radon or projection transforms; In quantum algorithms, it inverts the encoding of periodicity or symmetry to reveal the hidden subgroup.

This correspondence highlights a deep algebraic unity: both the tomographic inversion and the quantum period-finding procedure are instances of the same group-theoretic inversion principle — the recovery of hidden structural information through Fourier duality. The realization of this connection through the framework of Hidden Subgroup Problems establishes a bridge between classical Fourier-based reconstruction methods and quantum algorithms such as Shor's, suggesting that many classical inverse problems can be generalized to the quantum domain via this shared transformational foundation.

6.10.Proposal for a Transcription algorithm

In order to effectively bridge the quantum computing and the classical reconstruction techniques, one need to take into account:

- The fact that symmetry groups used by the classical image reconstruction algorithms are obtained on the basis of the rotations groups: as SO(2), SO(3) – as well as in the most general case: SO(2N) or SO(2N+1)
- While the quantum computing constructs quantum circuits on the basis of quantum gates – which, in the most general case, are mathematically described in terms of groups of unitary transformations: U(N)

Therefore, in order to effectively construct the link between image reconstruction techniques and the quantum computing, one need to relate the groups of unitary transformations U(N) to the orthogonal groups SO(2N).
Thus we are led towards a problem of representation for the group of unitary transformations that act upon the complex linear space: C^N:

$$U(N) = \{U \in \mathcal{M}_{\mathcal{N}}(C) \big| U^{\dagger}U = I\_N\}$$

Whose elements are all the invertible matrices with the determinant equal to 1 in the general linear group $GL(C,N)$ – with the property that: $U^{-1} = U^{\dagger}$ and $det(U) = 1$; the determinant being 1 means that the transform is unitary and thus a natural to the complex case of the transformation subgroup $SO(N) \leq GL(R,N)$.

$$U(N) \simeq \left\{ \begin{pmatrix} A & -B \\ B & A \end{pmatrix} \in \mathcal{O}(2N) | A,B \in \mathcal{M}(\mathbb{R}), A^T B = B^T A \right\}$$

Moreover the group of complex unitary transformations could be represented by the means of the special orthogonal group of transformations in the following way:

- Consider at the outset the fact that any complex matrix could be described as the sum of two real matrices:

  $U = A + iB$, with $A, B \in \mathcal{M}_{\mathcal{N}}(R)$, for any complex matrix: $U \in \mathcal{M}_{\mathcal{N}}(C)$

- And therefore could be represented as a matrix with real entries by the means of a map $\pi: \mathcal{M}_{\mathcal{N}}(C) \to \mathcal{M}_{2\mathcal{N}}(R)$ – defined by the association rule:

  $$\pi(U) = \begin{pmatrix} A & -B \\ B & A \end{pmatrix} \in \mathcal{M}_{2\mathcal{N}}(R), \forall U \in \mathcal{M}_{\mathcal{N}}(\mathrm{C})$$

- If furthermore: $U \in U(N) \leq \mathcal{M}_{\mathcal{N}}(C)$, with: $U = A + i\,B$ and $U^{\dagger}U = I_N$
  By computing the transpose between U and its Hermitian transpose, one obtains:

  $$U^{\dagger}U = I_N \Leftrightarrow (A+iB)^T \cdot (A+iB) = I_N \Leftrightarrow (A^T - iB^T)(A+iB) = I_N$$

  so that: $A^T A + B^T B = I_N$ and $A^T B = B^T A$

  whence it follows that:

  $$\pi(U)^T \cdot \pi(U) = \begin{pmatrix} A^T & B^T \\ -B^T & A^T \end{pmatrix} \cdot \begin{pmatrix} A & -B \\ B & A \end{pmatrix}$$
  $$= \begin{pmatrix} A^A + B^T B & -A^T B + B^T A \\ -B^T A + A^T B & B^B + A^T A \end{pmatrix}$$
  $$= \begin{pmatrix} I_N & O_N \\ O_N & I_N \end{pmatrix}$$

- Which means that the matrix assigned by the representation π to any complex unitary transformation: $U \in U(N)$ is just an orthogonal matrix:

  $$\pi(U) \in \mathcal{O}(2N) \leq GL(2N, \mathrm{R}), \forall)\, U \in U(N)$$

- Thus there could be evinced an injective groups homomorphism by the means of which: $U(N)$ could be identified with a subgroup of $\mathcal{O}(2N)$; more precisely, since one can describe the group of unitary complex transformations:

- To this adds the fact that for any: $U \in U(N) \Rightarrow det(U) = 1 \Rightarrow det\big(\pi(U)\big) = 1$

Whence it follows that: $\pi(U) \in SO(2N) \leq \mathcal{O}(2N)$, which yields that the representations π maps:

$$\pi: U(N) \to SO(2N) \leq \mathcal{O}(2N\} \leq GL(2N, R)$$

The effective link with the classical tomography revolves around the fact that the classical tomography could be described in terms of the Fourier Transform defined over the symmetry groups $SO(2N)$; for instance considering a problem of planar tomography, one is naturally led towards the group $SO(2)$:

- The matrices in the group $SO(2)$ (orthogonal transforms with the determinant equal to 1) describe all the possible rotations in the plan:

$$SO(2) = \left\{ R_\theta = \begin{pmatrix} cos(\theta) & -sin(\theta) \\ sin(\theta) & cos(\theta) \end{pmatrix} \middle| \theta \in [0; 2\pi) \right\} \simeq U(1)$$

An abelian compact group that is isomorphic to the circle group:

$$(U(1),\cdot) \simeq \left(S^1 = \{e^{i\theta}\},\cdot\right)$$

The Fourier transform upon this group will therefore be described in terms of the representations for the group: $(U(1),\cdot) \simeq \left(S^1 = e^{i\theta},\cdot\right) : e^{i \cdot n \cdot \theta}, n \in Z$, so that for any function: $f \in L^2\left(SO(2)\right)$, the Fourier coefficients are obtained by the means of discrete Frequencies: $\left\{e^{-i \cdot n \cdot \theta}\right\}$:

$$f(n) = \frac{1}{2\pi} \cdot \int_0^{2\pi} f(\theta) \cdot e^{-i \cdot n \cdot \theta} d\theta$$

So that the function f could be retrieved by applying the inverse Fourier transform:

$$f(\theta) = \sum_{n \in Z} f(n) \cdot e^{i \cdot n \cdot \theta}$$

(where the one dimensional Fourier series could be understood as the Fourier transform over the group $SO(2)$)

- We are going to make use of the Fourier transform over the group $SO(2)$ and relate it to the classical tomography:

- The classical bidimensional (planar) tomography makes use of the attenuation coefficient $(f(x, y))$ of the X-ray at each point of the exposed area in order to build the image
- and measures the line-integrals of $f(x, y)$ along line
  - of angle θ
  - and offset s (illustrating the distance between the intercept and the origin)
- The set of all the line integrals for $f(x, y)$ alongside such lines is parametrized by the Radon transform:

$$Rf(\theta, s) = \int_{x\, cos(\theta) + y\, sin(\theta) = s} f(x, y) dl$$

Where: $\theta \in [0; 2\pi)$ is the line's rotation angle

$s \in R_+$ intercept-origin distance

- Therefore the Radon transform $Rf(\cdot,\cdot)$ could be rendered as a function defined over the space:

$$(\theta, s) \in SO(2) \times R$$

- with the Fourier slice theorem illustrating the inherent identity between the Fourier transform of the Radon transform and the Fourier transform of the attenuation's coefficient (relation that proves the possibility to retrieve the image from sections):

$$\mathcal{F}_s[Rf(\theta, s)](\omega) = \hat{f}(\omega\, cos(\theta)\,, \omega\, sin(\theta))$$

The 1-dimensional Fourier transform for each for each projection describes a section of the Fourier Transform for the bidimensional image, so that:

$$\widehat{Rf}(n, \omega) = \frac{1}{2\pi} \cdot \int_0^{2\pi} \int_{-\infty}^{+\infty} Rf(\theta, s) \cdot e^{i(n\theta + \omega s)} ds d\theta = 2\pi i^{-n} \hat{f}(\omega\, cos(\theta)\,, \omega\, sin(\theta))$$

- Therefore the inversion of the Radon transform (that actually reconstructs the image out of the attenuation coefficient of the X-rays by back-projection) could be equated to considering the inverse Fourier transform over the group: $SO(2) \times R$, which exhibits the Fourier transform over the group $SO(2)$ *as* foundation of the classical tomography.

Taking advantage of the fact that $SO(2)$ is just the representation group of $U(1)$; and more generally: $SO(2 \cdot N)$ is just the representation group of $U(N)$, it means that any operation involving the Fourier transform over the special orthogonal group has a direct correspondent within the unitary group, which amounts has a direct correspondent in term of a quantum operation upon a qubit, or more generally a system of N qubits, unveiling thus a bidirectional intrinsic gateway for the algorithm transcription between the classical image reconstruction methods and the quantum algorithms.

The scheme of this transcription algorithm is based upon the representation as:

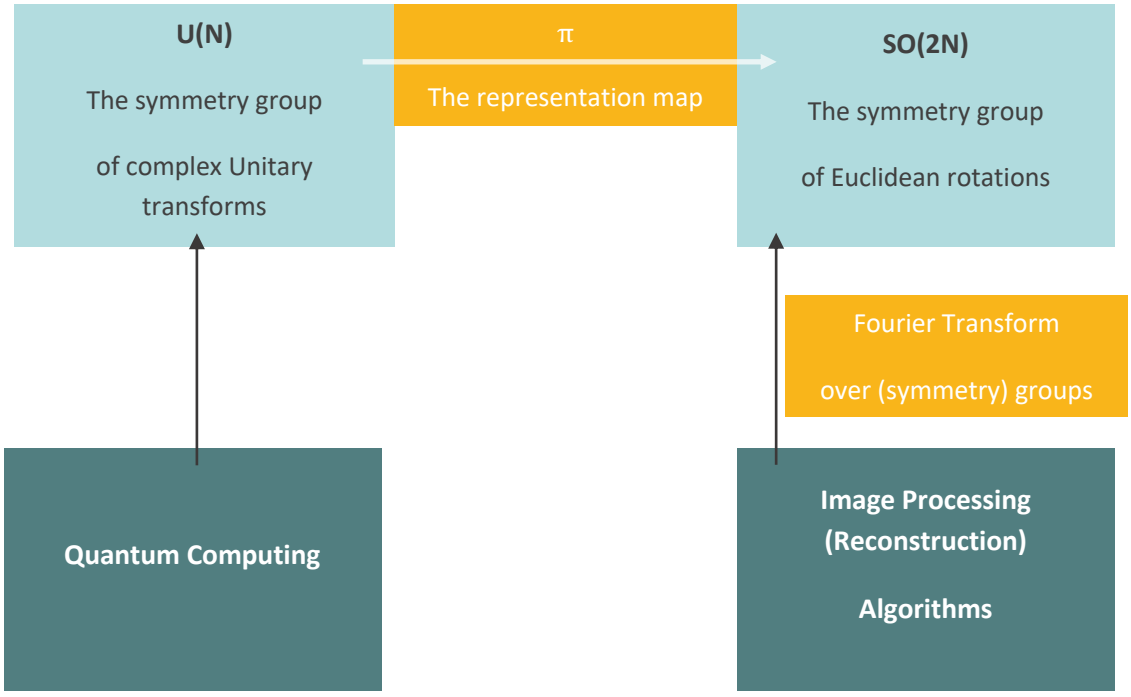

Figure 2: The logical foundation for a transcription algorithm

Bibliography;

1. M.Beckmann, *Computer Tomography*, Lecture Notes, Dec.2023
2. A.Dawar, *Quantum Computing. Bits and qubits*, Lecture notes, Cambridge Univ., 2019
3. L.Grafatos, *Classical Fourier Analysis*, Springer, IInd Ed., 2010

4. A.Ekert, T.Hosgood, A.Kay, C.Macchiavello, *Introduction to Quantum Information* Science, 2025
5. S.Holbert, M.Liebling, M.Unser*, Filter Design for Filtered backprojection guided by the interpolation model*, Swiss Federal Institute of Technology, 2015
6. R.Schmiec, *Quantum State Tomography of a single qubit: comparison of methods*, Dept. of Physics, Basel Univ., Lecture Notes, 2016

ADAPTIVE COMMUNICATION SECURITY USING AI-DRIVEN CRYPTO-AGILITY

Emil SIMION[1], Bianca-Maria COLAN[1], Andrei-Ionuț DĂNESCU[1]

[1]University Politehnica of Bucharest, 313 Splaiul Independentei, District 6, Bucharest, Romania

Corresponding author email: andrei.danescu0901@stud.etti.upb.ro

Abstract

Today, most communication systems still use fixed security protocols and static setups that do not react well when the context changes or when new threats appear, especially with the progress of quantum computing. In this paper, we suggest an adaptive approach to communication security that combines artificial intelligence with mathematical optimization. The main idea is crypto-agility, meaning the system can switch automatically between cryptographic protocols depending on the threat level, available resources, and latency needs. Unlike costly solutions such as quantum key distribution or specialized hardware, our design relies on existing standards like TLS 1.3 and IPSec, supported by software-based HSM modules. To guide the AI in decision making, we define a utility function that balances security, computing cost, and performance impact. We also discuss how techniques such as fractional calculus and wavelet analysis can be used for anomaly detection, while evolutionary algorithms can help improve switching strategies. A simple block diagram shows how telemetry data is processed by the AI engine, which calculates the utility score and applies the selected protocol at the gateway. The aim is to create a security solution that is scalable, adaptable, and ready for post-quantum challenges, while still being practical for research institutions and critical infrastructures.

Key words: *crypto-agility; anomaly detection; AI in security; post-quantum cryptography; optimization algorithms*

1. INTRODUCTION

As quantum computing continues to advance, many of the cryptographic methods we rely on today may no longer be secure [1] [2]. This creates an urgent need for systems that can adjust their security settings whenever conditions change. In this paper, we introduce an adaptive security model that brings together AI-based decision engines and mathematical optimization to tackle this problem. To keep the work clear and consistent, all symbols and abbreviations follow the same rules, and measurements are expressed using the International System of Units.

2. CONTENT

The proposed model employs an AI Policy Engine that evaluates network telemetry (latency, CPU usage, threat indicators) and applies a utility function:

$$U(p) = \alpha \cdot S(p) - \beta \cdot C(p) - \gamma \cdot P(p) \quad [2]$$

Our utility function model is inspired by the multi-criteria decision approach discussed in [3], where AI dynamically selects post-quantum algorithms based on contextual factors. In our case, we adapt this idea to balance security gain, computational cost, and performance penalty in communication networks.

Here, S(p) denotes security gain, C(p) computational cost, and P(p) performance penalty for a given policy p. The AI engine selects among policies such as AES-128, AES-256, or hybrid post-quantum schemes [3] [2].

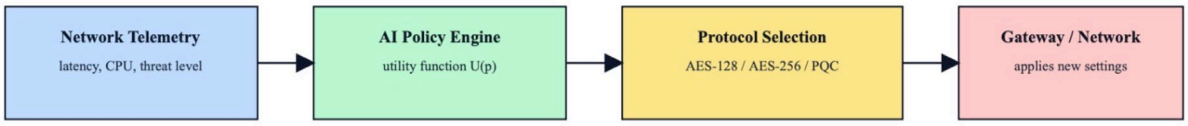

Figure 1: Minimal block diagram of the AI-driven crypto-agility system.

Figure 2 presents the block diagram of the proposed system. Telemetry data are processed by the AI engine, which computes the utility function U(p), selects the optimal cryptographic protocol, and enforces it at the gateway.

In the future, this project could be improved in a few ways. One is to test if fractional calculus and wavelet analysis can help find anomalies in encrypted traffic. Another is to use evolutionary algorithms so the system can switch protocols better when the network changes. It would also be good to try the system in red/blue team simulations to check how it works in more realistic attack situations.

3. CONCLUSIONS

In this paper we presented an adaptive security system that can react to changes in network conditions and different kinds of threats. By putting together AI decision-making, some mathematical methods, and well-known cryptographic standards, the system can give a good level of protection. At the same time, it can serve as a base for future communication infrastructures that should be ready to face post-quantum challenges.

4. REFERENCES

[1] M. T. R. D. G. e. a. Marchesi, "Reviewing Crypto-Agility and Quantum Resistance in the Light of Agile Practices," in Agile Processes in Software Engineering and Extreme Programming, Springer, 2023.

[2] J. Näther, D. Nachtigall, C. Rechberger and D. Slamanig, "Toward a Common Understanding of Cryptographic Agility: A Systematic Review," arXiv, 2024.

[3] A. K. S. e. a. Ali, "AI-Driven Dynamic Selection of Post-Quantum Algorithms for Mobile Application Security," ResearchGate Preprint, 2025.

A DOUBLY NONLINEAR PARABOLIC PROBLEM WITH VARIABLE EXPONENTS, HOMOGENEOUS NEUMANN CONDITIONS AND GENERALIZED LOGISTIC SOURCE

Bogdan MAXIM[1]

[1]University of Craiova, 13 Alexandru Ioan Cuza Street, Craiova, Romania

Corresponding author email: maxim.bogdan.n6h@student.ucv.ro

Abstract: ***The aim of this talk is to present new qualitative results—namely existence, uniqueness, boundedness, and asymptotic behavior—for a general class of doubly nonlinear parabolic problems with variable exponents and homogeneous Neumann boundary conditions. These problems arise naturally in various image processing applications, such as image denoising. Our analysis is conducted in the framework of weak solutions under minimal assumptions. The main analytical tools employed are a generalized weak maximum principle for doubly nonlinear parabolic equations in divergence form (utilized within the monotone method) and Rothe's method for time discretization.***

Key words*: Quasilinear parabolic equations; PDE's with variable exponents; weak solutions to PDEs; image processing.*

1. INTRODUCTION

In this talk, we study the weak solutions of the following **doubly nonlinear parabolic problem** with **Neumann boundary conditions**:

$$\begin{cases} \frac{\partial b(x,u(t,x))}{\partial t} - div\, a(x,\nabla u) = f(x,u(t,x)), & (t,x) \in (0,\infty) \times \Omega \\ a(x,\nabla u) \cdot \nu = 0, & (t,x) \in (0,\infty) \times \partial\Omega \\ u(0,x) = u_0(x), & x \in \Omega \end{cases} \tag{1}$$

where $\operatorname{div} a(x,\nabla u)$ denotes a general differential operator that may include, for example, a finite sum of $p(x)$-Laplacians with different variable exponents.

The use of **variable exponent diffusion operators** is well known in image processing, particularly for image denoising while preserving edges, and has demonstrated significant effectiveness in practice.

2. CONTENT

We introduce a nonlinear operator $K(u) = v$, where v is the solution of the auxiliary problem:

$$\begin{cases} \frac{\partial b(x,v(t,x))}{\partial t} - div\, a(x,\nabla v) + \lambda b(x,v) = f\big(x,u(t,x)\big) + \lambda b\big(x,u(t,x)\big), & (t,x) \in (0,\infty) \times \Omega \\ a(x,\nabla v) \cdot \nu = 0, & (t,x) \in (0,\infty) \times \partial\Omega \\ v(0,x) = u_0(x), & x \in \Omega \end{cases} \tag{2}$$

for some fixed $\lambda > 0$. Using **monotone operator techniques** — based on the **weak comparison principle** for doubly nonlinear parabolic problems — together with **variational methods**, we prove that the mapping K is well-defined and possesses at least one **fixed point**.

The existence of a solution for problem (2) is established via a **time discretization scheme (Rothe's method)**, combined with analytical tools developed by the author in a recent work (see Bogdan Maxim - A doubly nonlinear elliptic problem with variable exponents, homogeneous Neumann conditions and generalized logistic source, https://arxiv.org/abs/2506.23660) for the following quasilinear elliptic problem:

$$\begin{cases} -div\, a(x,\nabla U) + \lambda b(x,U) = g(x), & x \in \Omega \\ a(x,\nabla U)\cdot \nu = 0, & x \in \partial\Omega \end{cases} \quad (3)$$

Particular care is required in selecting **convergent subsequences** in suitable function spaces during the discretization procedure.

From the constructive approach used to obtain the solution of (1), we derive **upper and lower bounds** as well as insights into its **asymptotic behavior**.
In particular, as $t \to \infty$, the function $u(t,\cdot)$ converges to a **steady state** of (1) in the L^2 – norm.

3. CONCLUSIONS

We establish existence and uniqueness results for the Neumann problem (1), which, to the best of our knowledge, are new contributions to the literature, as most existing works focus on the Dirichlet case. Future work will address regularity properties of the solutions and further qualitative analysis of their long-time behavior.

COMPARISON OF ELEMENT-FREE GALERKIN AND INDICATOR KRIGING APPROACHES IN UPDATING FACIES PROBABILITY FIELDS

Bogdan SEBACHER[1], Silvia MARZAVAN[1], Roxana DOBRE[1],

[1]Military Technical Academy "Ferdinand I" of Bucharest, 39-49, BLV. George Coşbuc, Bucharest, Romania

Corresponding author email: bogdan.sebacher@mta.ro

Abstract

The exploration phase of a reservoir involves integrating geological information from multiple and often uncertain sources. Seismic inversion techniques generate facies probability fields, while core data provide discrete lithological observations at well locations. These two types of information are typically uncorrelated and characterized by different levels of uncertainty. This study presents a comparative analysis of two approaches for conditioning facies probability fields to hard geological observations: the Element-Free Galerkin (EFG) method and Indicator Kriging (IK). Both methods incorporate spatial anisotropy to account for the directional continuity of geological structures. The EFG formulation utilizes anisotropic kernel functions within a regularized moving least squares framework, enabling smooth probabilistic updates informed by seismic-derived prior fields. In contrast, the IK method relies on an anisotropic covariance model to interpolate indicator variables, explicitly capturing spatial correlation and topology. The performance of both methods is evaluated using quantitative and spatial metrics, including prediction accuracy, uncertainty reduction, and structural consistency of the updated facies maps. Comparative results demonstrate how EFG and IK differ in their ability to represent anisotropy, reproduce hard data, and preserve the geological realism of the facies architecture, providing practical insights for their application in reservoir characterization workflows.

Keywords*: Element-free Galerkin; Indicator Kriging; Facies probability field; Facies data; Regularization;*

1. INTRODUCTION

The reliable estimation of facies distribution within a reservoir is essential for effective field development and management planning. During the exploration phase, geologists and geophysicists collect complementary data describing subsurface rock types, their contacts, dimensions, and orientations, obtained from core analyses, outcrop studies, and seismic inversion. One of the key elements in geological modeling is the facies probability field, which must be conditioned to the facies observations obtained from wells. This study presents a comparative analysis between two conditioning approaches: a regularized Element-Free Galerkin (EFG) method and the Soft Indicator Kriging (SIK) in its blended form. Both methods aim to update prior facies probability fields derived from seismic inversion using well-based facies data. In the EFG formulation, the conditioning is achieved through a regularized mesh-free framework that integrates soft geological observations via a penalty term defined by the seismic-derived probability field, allowing for flexible anisotropy representation. In contrast, the SIK blended approach combines indicator kriging estimates with prior probabilities through a spatially adaptive weighting function, providing a Bayesian-like update.The comparative evaluation investigates the performance, stability, and interpretability of both methods in reproducing spatial facies patterns and balancing the influence between seismic information and well observations.

2. CONTENT

The implementation of the EFG and SIK methods is carried out on a two-dimensional reservoir model. For a selected facies type, a prior probability field is available, and facies occurrence has been observed at thirteen spatial locations. The main objective is to condition these discrete facies observations to the prior probability field and generate a consistent, spatially coherent update of the facies probability distribution. In this study, the facies probability field is denoted by p, while the facies observation at location u is represented by $obs(u) \in \{0,1\}$ depending on whether the facies type is present (1) or absent (0) at that location. Figure 1 (left) illustrates the prior probability field of the considered facies. The facies observations, expressed in probabilistic form, include five locations where the facies type is present and nine locations where it is absent. The methodologies were applied under anisotropic properties of the facies distribution.

Regularized Element-Free Galerkin

Within the Element-Free Galerkin (EFG) framework, for each unsampled location $u = (x, y)$ the updated probability is computed as, as $p^u(u) = X^T a$, where the vector $X^T = [1\ x\ y]$ corresponds to the coordinates of the estimation location, and $X_i^T = [1\ x_i\ y_i]$ represents the coordinates of all locations $u_i = (x_i, y_i)$ with known facies observations. The parameter vector $a^T = [a_0\ a_1\ a_2]$ is determined by minimizing the following cost function:

$$J(a) = \sum_i w_i \left(X_i^T a - obs(u_i)\right)^2 + \lambda\left(X^T a - p(u)\right)^2$$

where w_i are spatial weighting coefficients controlling the local influence of each observation, and λ is a regularization parameter that balances the contribution of the observed facies data and the prior probability field.

Soft Indicator Kriging (SIK) in blended form

In the classical indicator kriging framework, the indicator variable for facies is defined as:

$$I(\boldsymbol{u}) = \begin{cases} 1, \text{ if facies occurs at location } u \\ 0, \qquad\qquad \text{otherwise.} \end{cases}$$

For a given unsampled location u, the kriged estimate of the facies probability is:

$$p_{SIK}(u) = \sum_i \lambda_i\ I(u_i) + \lambda_u\, p(u)$$

In Soft Indicator Kriging (SIK), the estimation parameters λ_i, λ_u are derived by minimizing the estimation variance under the unbiasedness constraint.

$$minimize\ Var\left(p_{SIK}(u) - I(u)\right)\ subject\ to \sum_i \lambda_i + \lambda_u = 1.$$

A practical and widely adopted variant of SIK is the blended form, which linearly combines the indicator kriging estimate with the prior probability according to a spatially variable weighting factor $\alpha(u)$:

$$p^u(\boldsymbol{u}) = \alpha(\boldsymbol{u}) p_{SIK}(u) + [1 - \alpha(\boldsymbol{u})] p(u),$$

where $\alpha(u)$ is often expressed as a decreasing function of the kriging variance $\sigma^2(u)$, for example:

$$\alpha(\boldsymbol{u}) = exp\ (-\frac{\sigma^2(\boldsymbol{u})}{\sigma_0^2}).$$

This blending approach provides a Bayesian-like update of the probability field: areas with low uncertainty (close to hard data) are dominated by the kriging estimate, while regions of high uncertainty revert toward the soft prior.

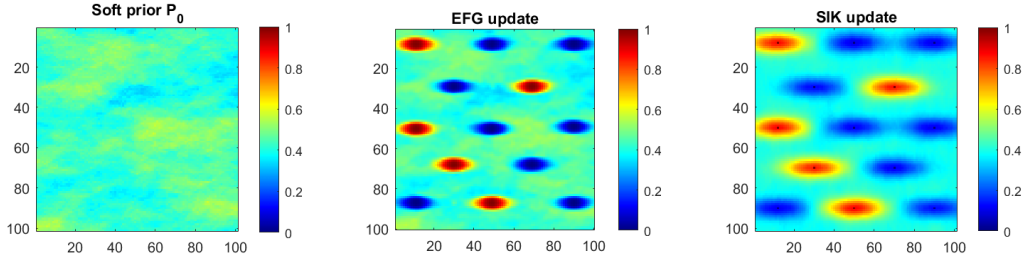

Figure 1 Facies probability fields; right-prior; middle EFG update; left SIK update

Figure 1 illustrates the updated facies probability fields obtained using the EFG method (middle) and the SIK method (right). It can be observed that the EFG approach better preserves the prior probability distribution outside the influence zone of the facies observations. In contrast, the linear interpolation inherent to the SIK formulation tends to distort the prior information, assigning excessive weight to the kriging update beyond the regions constrained by data.

3. CONCLUSIONS

Overall, the comparison highlights that the EFG method offers greater stability and better preservation of prior geological information, whereas the SIK approach provides stronger conditioning near observation points but may oversmooth or distort the prior away from data constraints.

MATHEMATICAL MODELLING OF INSTABILITIES IN COUNTER-ROTATING VORTEX PAIRS

Cristian-Emil MOLDOVEANU[1,*], Andrada-Livia CIRNEANU[1,]

This paper presents a comprehensive analytical investigation of the main instability mechanisms governing the evolution and decay of longitudinal vortices, with emphasis on configurations relevant to aerodynamic wakes and vortex–pair interactions. Building on classical filament and Lamb-Oseen vortex models, the study addresses both long-wavelength and short-wavelength instability phenomena. The long-wave behaviour is examined through the stability of an isolated straight filament and the Crow instability in counter-rotating vortex pairs, highlighting the mutual induction processes that generate sinusoidal deformations and vortex reconnection. The analysis focuses on the internal vortex-core dynamics, demonstrating the neutral stability of Rankine-type cores and detailing the onset of elliptic instability under pure strain fields. The theoretical framework integrates linear perturbation approaches, Bessel-function-based solutions, and known desingularisation techniques for realistic core structures. The results provide a coherent foundation for understanding the mechanisms of vortex persistence, deformation, and decay, which are essential for numerical simulations, aircraft wake modelling, and broader fluid-dynamics applications.

Keywords: Vortex dynamics; Crow instability; Elliptic instability; Vortex core stability; Longitudinal vortices.

1. Introduction

Longitudinal vortices generated in the wake of an aircraft are among the most persistent and influential structures in aerodynamics. Originating from the pressure imbalance between the lower and upper wing surfaces, these vortices form intense, coherent counter-rotating pairs that can survive over large downstream distances [1]. Their evolution is central not only to the aerodynamics of lift-induced drag and energy dissipation but also to operational safety, since wake vortices represent a well-known hazard for following aircraft during take-off, landing, or carrier-based operations [2]. The long-lived coherence of these structures, especially in low-turbulence atmospheric conditions, has motivated decades of research involving experimental campaigns, numerical simulations, and analytical studies [3].

[1] Faculty of Integrated Armament Systems, Military Engineering and Mechatronics, Military Technical Academy "Ferdinand I", 39-49 George Coșbuc, Sector 5, Bucharest, Romania, cristian.moldoveanu@mta.ro, andrada.cirneanu@mta.ro

A defining feature of these longitudinal vortices is their susceptibility to a rich variety of **vortex instabilities** that govern their deformation, interactions, and ultimate decay. The stability of a vortex system is not governed by a single mechanism but by the interplay between several classes of perturbations, each acting at different spatial and temporal scales. At large wavelengths, counter-rotating vortex pairs may experience **Crow instability**, a long-wave symmetric deformation driven by mutual induction. This mechanism causes the vortices to develop sinusoidal displacements out of phase, eventually leading to reconnection events that accelerate wake decay. At the opposite scale, **short-wavelength perturbations** act on the internal vortex-core structure and may interact with the local strain and rotation fields. One of the most important among these mechanisms is the **elliptic instability**, which arises when a vortex core subjected to an external strain field exhibits a resonant amplification of three-dimensional perturbations. The elliptic instability plays a critical role in the internal destabilisation and subsequent collapse of vortex tubes. It is widely recognised as a generic mechanism in fluid dynamics, with implications ranging from jets and wakes to rotorcraft aerodynamics and atmospheric flows [2].

These instabilities do not develop in isolation. The presence of **external turbulence** modifies the stability landscape by introducing additional perturbations, altering the effective strain rate, and facilitating vortex interaction and annihilation. While moderate levels of turbulence can accelerate wake destruction and mitigate the hazard posed to following aircraft, low-turbulence conditions allow the vortices to retain coherence over long distances, making the understanding of instability mechanisms even more critical. Moreover, operational constraints at major airports, combined with the introduction of large transport aircraft such as the Airbus A380, have intensified the need to refine wake separation standards based on accurate modelling of vortex instability and decay [2].

2. Mathematical model for the stability of a vortex filament

The stability of an isolated longitudinal vortex can be examined by modelling the vortex core as a thin filament of circulation $\boldsymbol{\Gamma}$, whose centreline is described by the curve $\vec{\boldsymbol{X}}(\boldsymbol{s},\boldsymbol{t})$, parametrised by the arclength $\boldsymbol{s}$and evolving in time $\boldsymbol{t}$. With the local induction approximation, filament motion is determined by its self-induced velocity along the binormal direction (figure 1):

$$\dot{\vec{X}}(s,t) = \gamma \frac{\vec{b}(s,t)}{R(s,t)}, \gamma = -\frac{\Gamma}{4\pi} ln \frac{a}{L}, \qquad (1)$$

where $R(s,t)$ is the local radius of curvature of the filament, $\vec{b}(s,t)$ is the local binormal vector, a is the radius of the vortex core, and L is a characteristic length scale of the flow under consideration ($a / L << 1$).

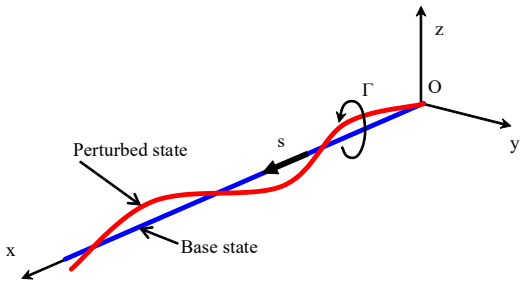

Figure 1. Perturbed vortex filament

For the base flow, we consider a straight vortex filament of constant circulation Γ, described by the equation:

$$\vec{X}(s,t) = s\vec{e}_x \tag{2}$$

where $s \in R$ (Figure 1). Since the curvature radius of a straight filament is infinite, its self-induced velocity is zero (the straight filament therefore remains motionless).

An infinitesimal perturbation is added to the base flow (see Figure 1).

$$\vec{X}(s,t) = s\vec{e}_x + Y(s,t)\vec{e}_y + Z(s,t)\vec{e}_z \tag{3}$$

where $|Y| << 1, |Z| << 1$. The study of the evolution of the perturbed filament can therefore be reduced to analysing the geometric deformation of the curve $\vec{X}(s,t)$.

Thus, we do not consider the evolution of the vortex filament in the tangential direction along the curve $\vec{X}(s,t)$. Taking into consideration $\vec{\tau}(s,t)$, as the local tangent vector to the curve, after several developments of Eq. (1), we obtain:

$$\dot{\vec{X}}(s,t) \times \vec{\tau}(s,t) = \gamma \frac{\vec{b}(s,t)}{R(s,t)} \times \vec{\tau}(s,t) \tag{4}$$

$$\dot{\vec{X}}(s,t) = \dot{Y}(s,t)\vec{e}_y + \dot{Z}(s,t)\vec{e}_z \tag{5}$$

$$\vec{\tau}(s,t) = \frac{\vec{X}'(s,t)}{\left|\vec{X}'(s,t)\right|} \tag{6}$$

$$\frac{\vec{b}(s,t)}{R(s,t)} = \frac{\vec{X}'(s,t) \times \vec{X}"(s,t)}{\left|\vec{X}'(s,t)\right|^3} \tag{7}$$

$$\vec{X}' = \vec{e}_x + Y'\vec{e}_y + Z'\vec{e}_z;\ \vec{X}" = Y"\vec{e}_y + Z"\vec{e}_z;\ \vec{\tau} = \vec{e}_x + Y'\vec{e}_y + Z'\vec{e}_z \tag{8}$$

$$\frac{\vec{b}}{R} = -Z"\vec{e}_y + Y"\vec{e}_z, \quad \dot{\vec{X}} \times \vec{\tau} = \dot{Z}\vec{e}_y - \dot{Y}\vec{e}_z \tag{9}$$

$$\gamma \frac{\vec{b}}{R} \times \vec{\tau} = \gamma\left(Y"\vec{e}_y + Z"\vec{e}_z\right), \tag{10}$$

where the products of infinitesimal terms have been neglected.

We therefore obtain the linearised system:

$$\dot{Y}(s,t) = -\gamma Z"(s,t)\ ,\ \dot{Z}(s,t) = \gamma Y"(s,t)\ . \tag{11}$$

For the linear system (11), we seek a solution of the form:

$$Y(s,t) = \hat{y}e^{i(ks-\omega_k t)}, Z(s,t) = \hat{z}e^{i(ks-\omega_k t)} \tag{12}$$

where k is the wavenumber of the perturbation

For the existence of a non-trivial solution, the following condition must be imposed:

$$\omega_k^2 - \gamma^2 k^4 = 0, \tag{13}$$

$$\omega_k(k) = \pm\gamma k^2 = \pm\frac{\Gamma k^2}{4\pi} ln\, k\, a,\ \omega_k(ka) = \mp\frac{\Gamma(ka)^2}{4\pi a^2} ln(ka). \tag{14}$$

We have chosen $1/k$ as the characteristic length scale of the flow. In Figure 2, the oscillation frequency of the modes is plotted as a function of ka, a vortex filament with $\Gamma = 1$ and $a = 0.2$.

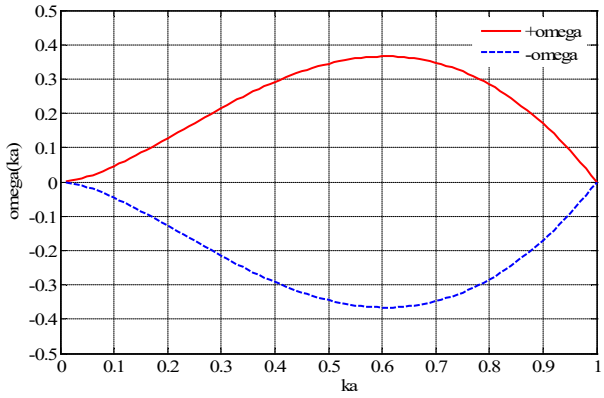

Figure 2. Oscillation frequency of the modes of the vortex filament

3. Mathematical model for the Crow instability mechanism

In the previous section, we saw that a vortex subjected to a shear flow can become unstable with respect to long-wavelength perturbations. In the case of a pair of counter-rotating vortices, the flow induced by each vortex on the other locally corresponds to a pure shear. Therefore, the system is unstable [5]. Crow instability can develop under the action of natural external perturbations, providing a possible mechanism for the premature breakdown of aircraft wakes.

We consider a pair of counter-rotating longitudinal vortices (see Figure 3) with circulations $\Gamma_1 = -\Gamma_0$ and $\Gamma_2 = \Gamma_0$, separated by a distance b. If this vortex pair is represented by two vortex filaments, the equations of the unperturbed filaments are:

$$\vec{X}_1(s,t) = s\vec{e}_x - \frac{b}{2}\vec{e}_y - U_d t\vec{e}_z,\ \vec{X}_2(s,t) = s\vec{e}_x + \frac{b}{2}\vec{e}_y - U_d t\vec{e}_z. \tag{15}$$

where $U_d = \frac{\Gamma_0}{2\pi b}$ is the descent velocity of the counter-rotating vortex pair in the unperturbed state, and s is the longitudinal coordinate (along the $\vec{e}_x$- axis).

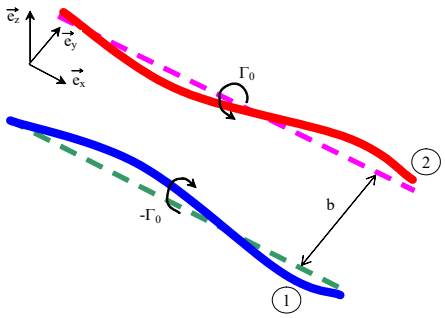

Figure 3. Crow instability in a pair of counter-rotating vortices

We now consider the vortex pair to be perturbed, in which case the equations of the vortex filaments become:

$$\vec{X}_1(s,t) = s\vec{e}_x - \frac{b}{2}\vec{e}_y - U_d t\vec{e}_z + \vec{r}_1(s,t),$$
$$\vec{X}_2(s,t) = s\vec{e}_x + \frac{b}{2}\vec{e}_y - U_d t\vec{e}_z + \vec{r}_2(s,t). \quad (16)$$

where the radial displacements $\vec{r}_1$ and $\vec{r}_2$ are functions of time t and of the longitudinal coordinate s, and represent the displacements of the vortex cores from their initial unperturbed positions

$$\vec{r}_1(s,t) = y_1(s,t)\vec{e}_y + z_1(s,t)\vec{e}_z,$$
$$\vec{r}_2(s,t) = y_2(s,t)\vec{e}_y + z_2(s,t)\vec{e}_z. \quad (17)$$

This system admits solutions of the exponential form

$$y_1(s,t) = \hat{y}_1 e^{at+iks},\ y_2(s,t) = \hat{y}_2 e^{at+iks},$$
$$z_1(s,t) = \hat{z}_1 e^{at+iks}, z_2(s,t) = \hat{z}_2 e^{at+iks}. \quad (18)$$

The expressions for $\hat{y}_1$, $\hat{y}_2$, $\hat{z}_1$ and $\hat{z}_2$ are given by the following algebraic system:

$$\sigma\hat{y}_1 = -\hat{z}_1[1+\omega_d(kb)] + \hat{z}_2\psi(kb),$$
$$\sigma\hat{z}_1 = -\hat{y}_1[1-\omega_d(kb)] + \hat{y}_2\chi(kb),$$
$$\sigma\hat{y}_2 = \hat{z}_2[1+\omega_d(kb)] - \hat{z}_1\psi(kb),$$
$$\sigma\hat{z}_2 = \hat{y}_2[1-\omega_d(kb)] - \hat{y}_1\chi(kb). \quad (19)$$

In the system of equations (19), the first mutual-induction function $\chi(kb)$, the second mutual-induction function $\psi(kb)$ (Figure 4), as well as the self-induction function $\omega_d(kb)$ (Figure 5) [6] have been used.

These functions are integrals that can be expressed analytically in terms of modified Bessel functions of the second kind [7]:

$$\chi(\beta) = \int_0^\infty \frac{\cos\beta x}{[x^2+1]^{3/2}}dx = \beta K_1(\beta), \quad (20)$$

$$\psi(\beta) = \int_0^\infty \frac{\cos\beta x+\beta x\sin\beta x}{[x^2+1]^{3/2}}dx = \beta^2 K_0(\beta) + \beta K_1(\beta), \quad (21)$$

$$\omega_d(\beta) = \int_d^\infty \frac{\cos\beta x+\beta x\sin\beta x-1}{x^3}dx = \frac{\beta^2}{2}\left(\frac{\cos\beta d+\beta d\sin\beta d-1}{(\beta d)^2} - Ci(\beta d)\right), \quad (22)$$

$$Ci(\beta) = \int_0^\beta \frac{\cos x}{x}dx. \quad (23)$$

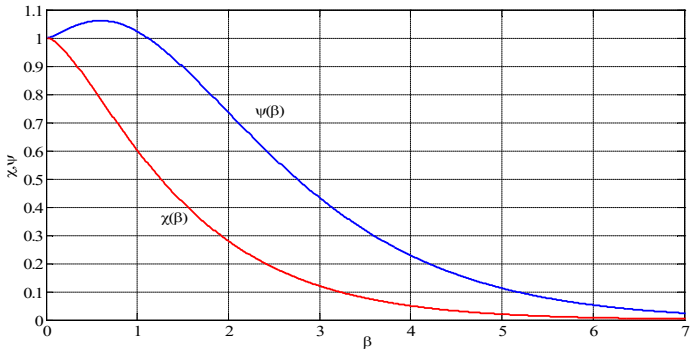

Figure 4. Mutual induction functions

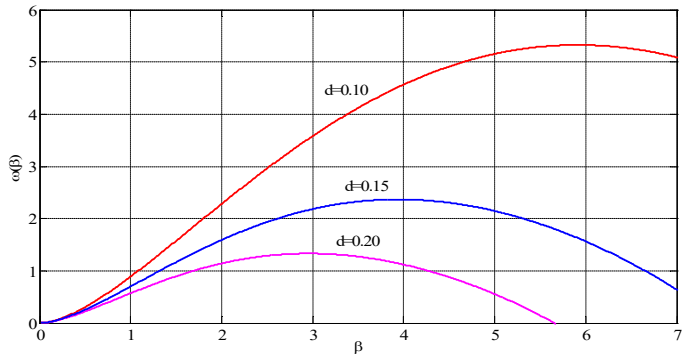

Figure 5. Self-induction function

In the preceding integrals, some terms are not defined for $\xi \to 0$, which corresponds to a point located on the vortex filament itself. This issue arises from the non-physical nature of the vortex-filament approximation.

To address this problem, the vortex's internal structure must therefore be taken into account. Several 'desingularisation' methods have been proposed. Most of these methods, however, have the drawback of being applicable only at wavelengths much longer than the vortex-core dimensions [8], [9]. The most common technique is the '*cutoff*' method [5], which consists of removing a small segment of the filament on either side of the point where the calculation is performed. The optimal value for the cutoff parameter is $0.642\frac{r}{b}$ [5], where r is the vortex-core radius and b is the separation distance between the two vortices.

Figures 6-7 show the stability curves $\sigma(kb)$ for different values of the ratio c/b. We observe that for $c/b = 0.10$, only the symmetric modes are present. In this case (Figure 6), the wavelength corresponding to the maximum amplification rate $0.810(\Gamma_0/2\pi b^2)$, and the corresponding wavenumber $\lambda = \frac{2\pi}{k} = 7.39b$ and $\mathrm{kb} = 0.85$.

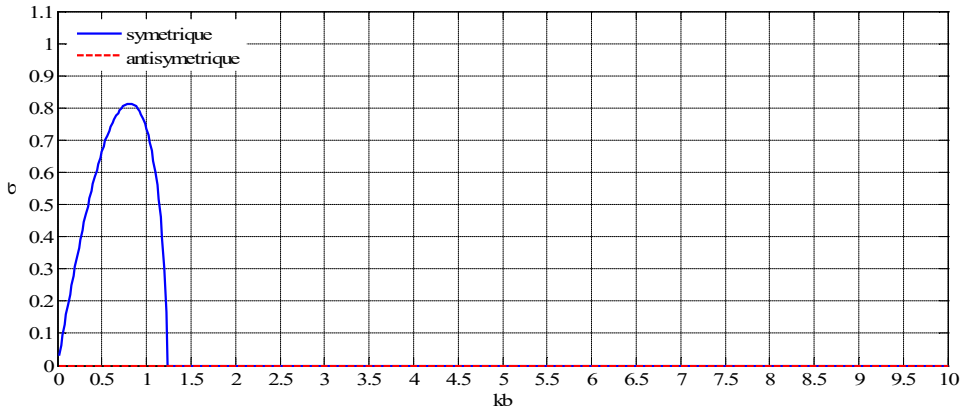

Figure 6. Stability curves for $c/b = 0.10$

For $c/b = 0.20$ (Figure 7), the maximum amplification rate is $0.787(\Gamma_0/2\pi b^2)$, and the associated wavelength is $\lambda = 2\pi/k = 6.28b$ and $kb = 1$.

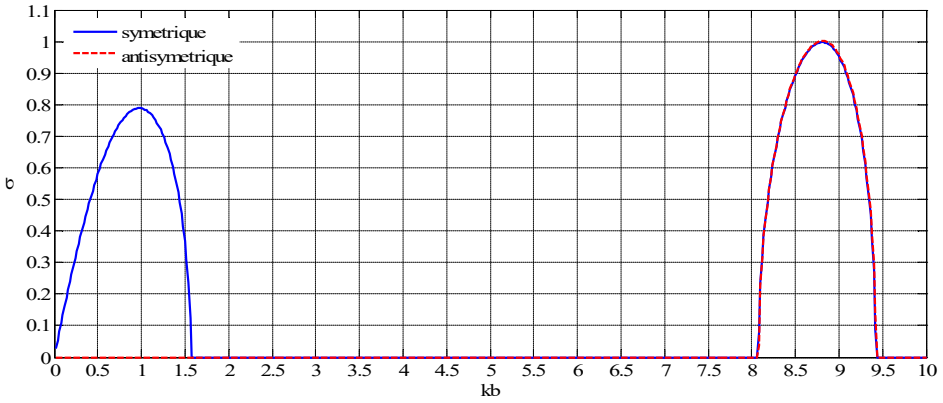

Figure 7. Stability curves for $c/b = 0.20$

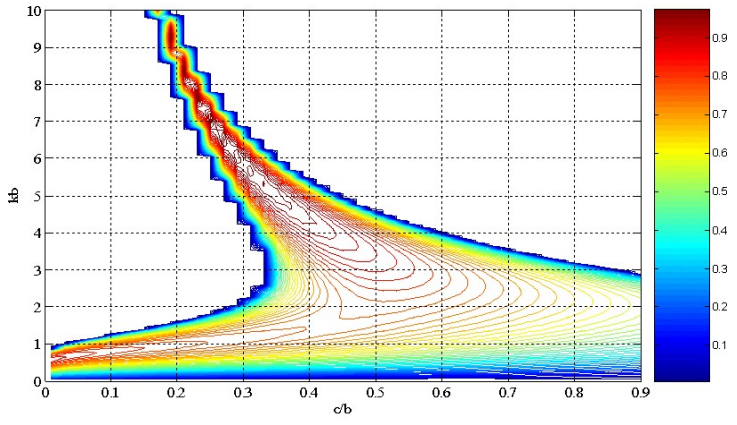

Figure 8. Stability domain for the symmetric modes of the Crow instability

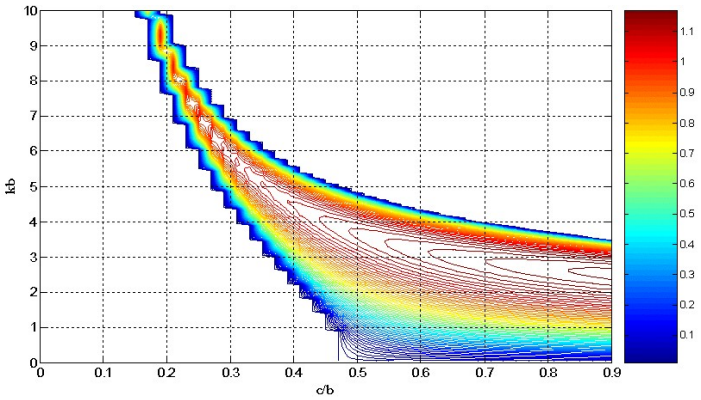

Figure 9. Stability domain for the antisymmetric modes of the Crow instability

It is observed that long-wavelength perturbations (which are fully consistent with the assumptions made in the derivation of the Crow-instability model) occur for the symmetric modes over the entire range of c/b values considered for the vortex core. In contrast, the antisymmetric modes can produce long-wavelength instabilities only for vortices with larger values of c/b.

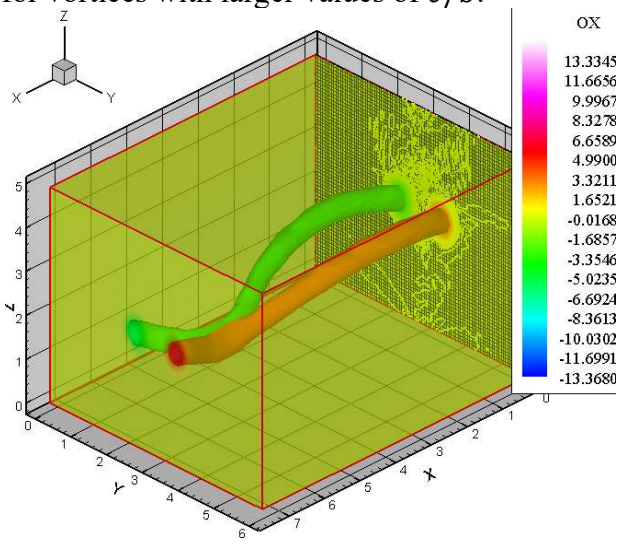

Figure 10. Example of Crow instability obtained in a counter-rotating vortex pair

Figure 10 presents the results obtained from the numerical simulation of the evolution of a counter-rotating vortex pair for which the external conditions, including predominant atmospheric turbulence, allowed the development of a long-wavelength Crow-type instability mechanism.

4. Mathematical model for the short-wavelength instabilities and for elliptic instability

We consider as the base flow an isolated axisymmetric vortex, expressed in a polar coordinate system whose origin is located at the vortex core:

$$\vec{U}_0 = U_\theta(r,t)\vec{e}_\theta,\ P(r,t) = \rho \int \frac{U_\theta^2(r,t)}{r} dr \tag{24}$$

Small perturbations are added to the base flow

$$\begin{gathered} u_\theta^*(r,t) = u_\theta(r,t) + U_\theta(r,t);\ u_r^*(r,t) = u_r(r,t), \\ u_x^*(r,t) = u_x(r,t);\ p^*(r,t) = p(r,t) + P(r,t). \end{gathered} \tag{25}$$

Since the system of equations governing the perturbations is a linear system of differential equations, the general solution can be sought as a linear combination of normal modes:

$$[u_x; u_r; u_\theta; p/\rho] = [\hat{u}_x(r); \hat{u}_r(r); \hat{u}_\theta(r); \hat{p}(r)] \cdot e^{i(kx+m\theta-\omega_k t)} \tag{26}$$

For the interior of the vortex core ($\boldsymbol{r < c}$), after several intermediate steps, the following equations are obtained:

$$r^2 D^2 \hat{u}_x + rD\hat{u}_x + (\beta^2 r^2 - m^2)\hat{u}_x = 0. \tag{27}$$

The differential equation (27) is a Bessel equation whose independent solutions are the Bessel functions $J_m(\beta r)$ and $Y_m(\beta r)$. Since the solution is not limited for $r \to 0$, the solution of equation (27) is:

$$\hat{u}_x(r) = AJ_m(\beta r), \tag{28}$$

where A is an arbitrary constant. We then obtain the pressure:

$$\hat{p} = A\frac{\gamma}{k} J_m(\beta r). \tag{29}$$

Experimental observations show that instabilities exist in the vortex core. This is the case for a pair of counter-rotating vortices, which, in addition to the long-wavelength Crow instability, also exhibit a short-wavelength instability affecting the internal structure of the vortices. We can see that the vortex cores are affected and that the vortex-core lines exhibit oscillatory distributions. It therefore appears that the pure shear field induced here by a neighbouring vortex is at the origin of a new instability mechanism: the elliptical instability. Historically, the elliptical instability was identified by [10] in the 1970s for vortex rings. In that case, the shear field is induced by the vortex ring on itself.

To analyse the elliptical instability analytically, the base flow is considered to be a solid-body rotating vortex subjected to a pure shear deformation field in the plane perpendicular to the vortex axis:

$$\begin{gathered} U_x = \varepsilon x, U_y = \varepsilon y,\ U_r = \varepsilon r \sin 2\theta, \\ U_\theta = r + \varepsilon r \cos 2\theta,\ P = (1-\varepsilon^2)\frac{r^2}{2}. \end{gathered} \tag{30}$$

We consider the case of an inviscid flow with perturbations small compared to the velocity of the base flow.

The system of equations governing the perturbations is a linear system with coefficients independent of the variables $\boldsymbol{x}$ and $\boldsymbol{t}$, therefore the general solution can be written as a linear combination of normal modes:

$$[u_x; u_r; u_\theta; p/\rho] = q \cdot e^{ikx+\omega t}, \tag{31}$$

with $q = [\hat{u}_x(r,\theta); \hat{u}_r(r,\theta); \hat{u}_\theta(r,\theta); \hat{p}(r,\theta)]$.

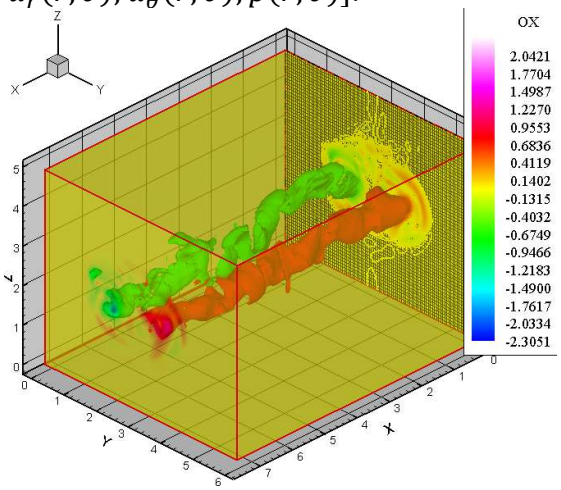

Figure 11. Example of elliptic instability obtained in a counter-rotating vortex pair

Figure 11 presents the results obtained from the numerical simulation of the evolution of a counter-rotating vortex pair for which the external conditions, including predominant atmospheric turbulence, allowed the development of a short-wavelength elliptic-type instability mechanism.

5. Conclusions

The present study provides a comprehensive analytical framework for understanding the main instability mechanisms governing counter-rotating vortex pairs, with emphasis on both large and small-scale processes that dictate their evolution, deformation, and eventual decay. By combining classical vortex filament theory, linear perturbation methods, and detailed modelling of vortex-core dynamics, the work clarifies how distinct classes of perturbations interact with the base flow to shape the stability characteristics of aircraft wake vortices and analogous aerodynamic configurations.

At large spatial scales, the Crow instability emerges as the dominant mechanism controlling the mutual deformation of counter-rotating longitudinal vortices. This long-wavelength symmetric mode, driven by mutual induction between the two vortices, leads to sinusoidal displacements of their centrelines and culminates in reconnection events and accelerated wake decay. The analytical results obtained, supported by the evaluation of mutual and self-induction functions expressed in terms of modified Bessel functions, confirm the sensitivity of the instability growth rate to the vortex-core size, thus providing a quantitative

foundation for predicting the operational behaviour of wake vortices in flight conditions.

In contrast, the short-wavelength regime is governed by mechanisms that act within the vortex core itself. The analysis of an axisymmetric vortex subjected to external shear reveals that local perturbations satisfy Bessel-type differential equations, indicating the presence of characteristic oscillatory solutions within the core. When the vortex is exposed to a pure strain field, such as that induced by a neighbouring vortex, these internal perturbations may resonate with the base flow, leading to the emergence of elliptic instability. Historically identified in vortex rings, this instability mechanism is shown to play an equally significant role in the dynamics of longitudinal vortices. The present formulation highlights how the coupling between solid-body rotation and external strain yields a three-dimensional amplification mechanism that destabilises the vortex core and promotes a transition to turbulence.

Taken together, the long-wavelength Crow instability and the short-wavelength elliptic instability provide a unified explanation for the multi-scale degradation of counter-rotating vortex pairs. Their complementary effects illustrate that wake-vortex decay is not driven by a single process but by a cascade of instability phenomena acting at different spatial scales, from global sinusoidal deformation to local core oscillations. The analytical results obtained in this paper thus offer a coherent theoretical foundation applicable to aircraft-wake modelling, rotorcraft aerodynamics, numerical simulation of trailing vortices, and the broader study of coherent structures in turbulent flows. In practical terms, a rigorous understanding of these instability mechanisms is essential for improving wake-vortex prediction models, refining airport-separation standards, and developing future strategies for active or passive vortex-attenuation technologies.

R E F E R E N C E S

[1]. Marchall, J.S., Brancher, P., Giovannini, A. (2001) - *Interaction of unequal anti-parallel vortex tubes,* Journal Fluid Mech 446(Cambridge University Press), 229-252.

[2]. Leweke, T., Williamson, H.K. (1998) - *Cooperative elliptic instability of a vortex pair*, Journal of Fluid Mechanics Vol. 360, Pag. 85-119.

[3]. Loiseleux, T., Chomaz, J.M., Huerre, P. (1998) - *The effect of swirl on jets and wakes: Linear instability of the Rankine vortex with axial flow,* Physics of Fluids Vol. 10 (5), Pag. 1120-1134.

[4]. Kalogirou, I.D.; Romeos, A.; Giannadakis, A.; Mihalakakou, G.; Panidis, T. *Vortex Dynamics Effects on the Development of a Confined Turbulent Wake*. *Fluids* **2025**, *10*, 283. https://doi.org/10.3390/fluids10110283

[5] Crow, S.C. (1970) - *Stability theory for a pair of trailing vortices*, AIAA Journal 8, Pag. 2172-2179.

[6] Jahnke, E.J., Emde, F. (1945) - *Tables of Functions*: Dover, New York.

[7] Gradshteyn, I.S., Ryzhik, I.M. (1965) - *Table of integrals, series and products*: Academic Press, New York.

[8] Margerit, D. (1997) - *Mouvement et dynamique des filaments et des anneaux tourbillons de faible épaisseur*: Thèse de doctorat de l'Institut National Polytechnique de Lorraine.

[9] Margerit, D., Brancher, P., Giovannini, A. (2004) - *Implementation and validation of a slender vortex filament code: its application to the study of a four-vortex wake model*, International Journal for Numerical Methods in Fluids Vol. 44, Pag. 175-196.

[10] Moore, D.W., Saffman, P.G. (1974) - *A note on the stability of a vortex ring of small cross-section*, Proc. Royal Society Vol. A, 338, Pag. 535.

SOME REMARKS ON ALMOST HERMITIAN METALLIC MANIFOLDS AND THEIR SUBMANIFOLDS

Cristina Elena HRETCANU[1]

[1] Stefan cel Mare University, Suceava, Romania
Corresponding author email: cristina.hretcanu @ fia.usv.ro

Abstract

In this paper, we consider an almost complex metallic structure associated with an almost complex structure, referred to as almost Hermitian metallic manifolds, and investigate certain properties of their submanifolds. We focus on the structures induced on these submanifolds and examine their characteristics in this context. Furthermore, several illustrative examples of such submanifolds within almost Hermitian metallic manifolds are provided.

Key words*: Riemannian manifold; almost complex metallic structure; almost Hermitian metallic manifolds; sectional curvature; submanifold.*

1. INTRODUCTION

The real metallic number, denoted by $_{p\ ,q}$, is the positive solution of the equation $x^{2} =$ $+ q$, where
$\boldsymbol{p}$ and $\boldsymbol{q}$ are positive integers and $\Delta = p^2 + 4q > 0$. These $\sigma_{p,q}$ numbers belong to the family of metallic means, introduced by Spinadel (2002), and represent a natural generalization of the golden number $\varphi = \frac{1+\sqrt{5}}{2}$.

Golden and metallic structures are examples of polynomial structures on manifolds, as originally defined by Goldberg and Yano (1971). The almost complex golden structure was first introduced by Crasmareanu and Hretcanu (2008). Since then, the geometry of metric manifolds endowed with these types of polynomial structures has been the subject of extensive study.

The investigation of metallic structures on Riemannian manifolds was initiated in the work of Hretcanu and Crasmareanu (Hretcanu C.E.; Crasmareanu M, 2013). Subsequently, the study of submanifolds within metallic Riemannian manifolds was further developed in several papers, including Hretcanu and Blaga (Hretcanu C.E., Blaga A.M., 2018 & 2021).

A more recent contribution introduced a generalization of the golden structure, referred to as the almost (α, p)-golden structure, and explored the geometry of Riemannian manifolds endowed with this structure (Hretcanu and Crasmareanu, 2023). The study of the corresponding submanifolds was later continued in (Hreţcanu C.E., Druţă-Romaniuc S.L, 2024).

2. CONTENT

The complex analogue of the real metallic number, known as the complex metallic number, arises as a solution to the equation $x^2 = px + q$, where p and q are real numbers satisfying $p^2 + 4q < 0$.
Let M be a smooth manifold. An endomorphism Φ of the tangent bundle TM is called an almost complex metallic structure on M if it satisfies $\Phi^2 = p\Phi + qI$, where I denotes the identity endomorphism. The pair (M, Φ) is then referred to as an almost Hermitian metallic manifold (Hretcanu & Blaga, 2025). In the special case $p = q = 1$, one obtains an almost Hermitian golden

manifold, and some properties of the almost complex golden structure were recently investigated by Hreţcanu and Cirlan (2025).

In this paper, we explore various frameworks in which almost complex metallic structures are expressed through the language of almost complex geometry. We derive several properties of isometrically immersed submanifolds within almost Hermitian metallic manifolds and examine the characteristics of holomorphic and totally real submanifolds in this setting. Furthermore, we focus on the characterization of semi-invariant submanifolds in almost Hermitian metallic manifolds and provide illustrative examples. Finally, we introduce the notions of Φ-holomorphic sectional curvature and Φ-holomorphic bisectional curvature for such manifolds and investigate their fundamental properties.

3. CONCLUSIONS

The study of quadratic endomorphisms on a given manifold has recently been broadened through the introduction of a new class. If a Riemannian metric is incorporated under an appropriate compatibility condition, it gives rise to a novel geometric framework. The submanifolds of such manifolds also inherit noteworthy structures, opening new avenues for research and further enriching the field of differential geometry.

4. REFERENCES

1. Crâşmăreanu M., Hretcanu C.E., *Golden differential geometry*, Chaos Solitons & Fractals, volume 38, issue 5: 1229 – 1238, **2008.**
2. Goldberg, S.I.; Yano, K., *Polynomial structures on manifolds*, Kodai Math. Sem. Rep., 22, 199 – 218, **1970**.
3. Hretcanu C.E., Crasmareanu M, *Metallic structures on Riemannian manifolds,* Revista De La Union Matematica Argentina Volume: 54 Issue: 2 Pages: 15-27**, 2013**.
4. Hretcanu C.E., Blaga A.M., *Submanifolds in metallic Riemannian manifolds*, Differential Geometry - Dynamical Systems, Vol.20, 83-97, **2018.**
5. Hretcanu C.E., Blaga A.M., *Types of Submanifolds in Metallic Riemannian Manifolds: A Short Survey,* Mathematics, 9(19), 2467*,* **2021.**
6. Hretcanu C.E., *Crasmareanu M., The (α,p)-Golden Metric Manifolds and Their submanifolds,* Mathematics, vol. 11, issue 14, 1-13, **2023.**
7. Hreţcanu C.E., Druţă-Romaniuc S.L., *On the Geometry of Semi-Invariant Submanifolds in (α, p)-Golden Riemannian Manifolds*, Mathematics, 12(23), 3735, **2024.**
8. Hreţcanu C.E.,, Cirlan V*., On the Geometry of the Kähler Golden Manifold*, Axioms, 14(8), 564, **2025.**
9. Hreţcanu, C.E., Blaga, A.M. *On the Geometry of Slant Submanifolds in Almost Hermitian Metallic Manifolds*. Mediterr. J. Math. 22, 193, **2025.**
10. Spinadel, V.W., *The metallic means family and forbidden symmetries*, Int. Math. J., 2, 279--288. **2002.**

Development of a Self-Hosted Personal Cloud Server with IoT Integration and Remote Access Capabilities

David-Theodor IONITA[1], Ioana Corina BOGDAN[1,2], Horia Alexandru MODRAN[1]

[1]Transilvania University of Brasov, Faculty of Electrical Engineering and Computers Science, Department of Electronics and Computers, Romania
[2]Traian Lalescu Research and Training Center for Innovative Techniques in Applied Mathematics in Engineering (CiTi), Bucharest, Romania

Corresponding author email: david.ionita@student.unitbv.ro, {corina.bogdan, horia.modran}@unitbv.ro

Abstract

Nowadays, data privacy and commercial cloud services are major concerns for technology users. In this context, users are open to adopt self-hosted cloud solutions, investing in equipment and facilities, which ensure direct control over data, enhanced security and economic advantages thorough scalable setups using budget-friendly hardware. As a solution, the personal cloud storage centre integrates a Raspberry PI 5 with an 8TB running Nextcloud in a Docker container. The system replicates essential functions encountered in commercial cloud services maintaining date property and security through user accounts and two-factor authentication. For remote control, two methods are analysed, one method based on VPN, and the second one based on Zero Trust Access (ZTNA). This analysis allows to evaluate complexity, performance and security trade-offs commercial cloud service. Obtained results prove that a self-hosted cloud based on Zero Trust access is a more reliable and secure alternatives to VPNs services.

Key words*: VPN, Zero Trust, Network-Attached Storage (NAS). Raspberry Pi 5.*

1. INTRODUCTION

Concerns about data privacy in mainstream cloud storage services have led to growing interest in self-hosted cloud servers. Users are increasingly aware that major providers may analyse or deduplicate their files to optimize services [1]. Therefore, many are steering towards personal cloud solutions that keep data under their own control [1]. A private, self-hosted cloud offers improved security, as data remain in a controlled environment not shared with third-party servers [2]. It also provides cost and scalability benefits such as an inexpensive hardware (e.g., a Raspberry Pi) can serve as a low-power server with terabytes of storage, in this way allowing avoiding fees and capacity limits imposed by commercial services [2]. In addition, self-hosted solutions based on open-source platforms like Nextcloud or ownCloud offer customized options and full control over the server, and a reliable synchronization and remote control. This approach enhances privacy and strongly ensures energy efficiency when comparing with large-scale commercial data centres.

2. CONTENT

We present a stable personal cloud storage system built on a Raspberry Pi 5 with an 8 TB HDD NAS (Network-Attached Storage) drive, running Nextcloud in a Docker container as the core platform (see software and hardware perspectives in Fig. 1 and Fig. 2). The system replicates the file synchronization and sharing functionality of traditional cloud storage services while preserving full data ownership and control [2]. Key features such as user accounts and two-factor authentication (2FA) are implemented to fortify access to the server. To enable secure remote access to this private cloud (addressing a key challenge of personal clouds [1]), we evaluate two connectivity methods: a VPN-based solution and a Zero Trust Network Access (ZTNA) approach. A traditional VPN creates an encrypted tunnel for remote users but typically grants broad network access once connected, increasing the attack surface [3]. In contrast, a Zero Trust model follows a

"never trust, always verify" principle, granting access only to specific services after verifying user identity [3]. We examine both approaches in terms of complexity, performance, and security [4].

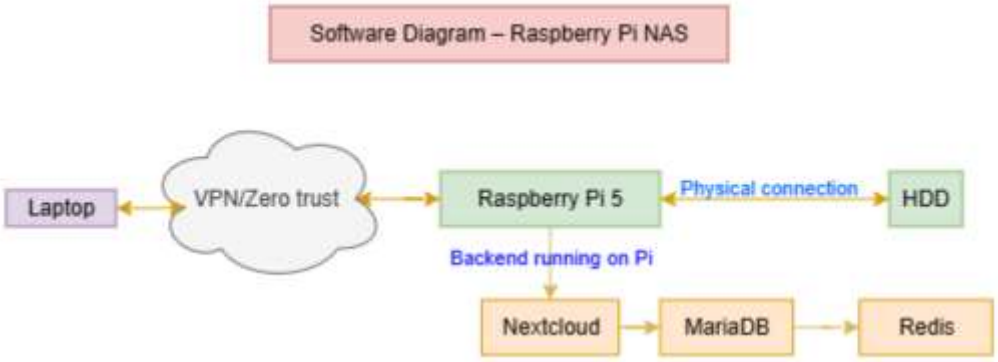

Fig. 1: NAS Software Diagram.

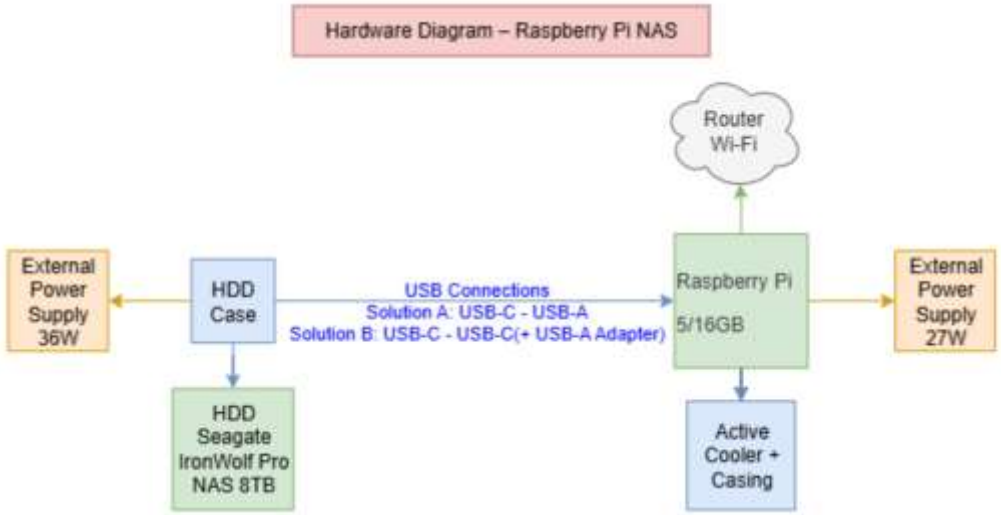

Fig. 2: NAS Hardware Diagram.

3. CONCLUSIONS

Our findings indicate that a self-hosted cloud can achieve functionality comparable to public cloud services while significantly improving data privacy and control. In particular, Zero Trust access minimizes implicit trust and exposure, offering a robust alternative to VPN tunnels for personal cloud storage.

References:

[1] Wickramarachchi A., Mallawaarachchi V., Remote access for personal cloud devices, Int. Research, Conf on Smart Computing and Systems Engineering, 2018.

[2] Fairuz R., Maalik I., Zuraidy A., Personal Cloud Storage using Raspberry Pi, International Journal of Computer Applications (0975 – 8887) Volume 180 – No.22, 2018.

[3] Zohaib, S.M.; Sajjad, S.M.; Iqbal, Z.; Yousaf, M.; Haseeb, M.; Muhammad, Z. Zero Trust VPN (ZT-VPN): A Systematic Literature Review and Cybersecurity Framework for Hybrid and Remote Work. Information 2024, 15, 734. https://doi.org/10.3390/info15110734.

[4] I.C. Bogdan, E. Simion, Cybersecurity, assessment and certification of critical infrastructures, Polytechnic University of Bucharest, Sci Bull, Series C, Vol. 86, Iss. 4, 2024.

Predicting a player's performance in Electronic Sports

Codreanu Denis-Gabriel[1]

[1]National University of Science and Technology Politehnica Bucuresti, Faculty of Automatic Control and Computer Science, 313 Splaiul Independentei, District 6, Bucharest, Romania
denis.codreanu2005@yahoo.com

Abstract

The world of Electronic Sports is rapidly evolving around us. Player development, audience engagement, and team strategy have reached a level higher than ever before. In this study, an Extreme Gradient Boosting (XGBoost) regressor was employed on basic observable data such as kills/deaths ratios in order to predict a player's kill count in upcoming Counter-Strike matches, based on their historical performance. The model, when evaluated using data computed from the exploratory analysis, demonstrated a precision of 78% in predictions within a range of 5 kills. The classification metrics, used in tracking the player's performance, presented an average accuracy of 67%, a recall of 69%, a precision of 65% and an F1 score of 66%. These findings were obtained from data collected during an amateur game and did not include personal or psychological information about the player that could significantly improve the classification.
Key words*: Player Performance Prediction; Machine Learning; XGBoost; Regression; Classification Metrics; Kill/Death Ratio; Performance Analytics; Predictive Modeling; Data Analysis.*

1. INTRODUCTION

Counter-Strike is a free-to-play first-person shooter game developed by Valve that involves two teams, each of five players. Over time, the game has transitioned from small-scale local environments to major professional tournaments, currently attracting audiences of up to almost three million concurrent viewers.

This paper investigates the application of a machine learning model for predicting a player's future kill count in Counter-Strike, a key metric frequently used to quantify individual in-game performance relative to peers. The data set will be composed of other statistics that can also project the player's performance, such as damage per round, deaths, map, time, and others.

2. CONTEXT

2.1. Data and Features

Counter-strike is played on servers provided by the game, but there is also the possibility of creating your own server. One such platform that provides community servers is *Faceit*. It serves as a platform for players to meet online and create pre-made teams with which they can play against others. *Faceit* has an application programmable interface (API), available for everyone with an account on the platform, that can provide us with important match data in the form of JSON files.

The following data has been extracted through the API: kills, the enemy team's average elo, the time at which the game was played, the rounds of a game, deaths, the average damage per round and the player's elo as numerical values. We also extract the map as a categorical value and the won or lost status of the match as a binary value. These have been used to compute the variables necessary for the model's predictions.

2.1.1. Elo difference

The elo rating system is a method of calculating a player's skill level. It is mainly used in the chess rating system, but also in other sports. Since *Faceit* already provides us with a functioning elo system, we will make use of it. To capture the differences between matches in which the player has been paired against opponents of a larger skill gap, we will consider the absolute value of the difference between the mean of the enemy team's elo and the player's elo.

2.1.2. Time

Human activity patterns commonly exhibit periodicity, which may indirectly influence gameplay performance depending on the time of day. Therefore, we try to capture the moments that the player

most often starts a match on *Faceit*. To better express the distances between time intervals we model a *sine* function which in turn represents a clock.

2.1.3. Moving Average and slope

The "Hot Hand" effect suggests that recent successful actions may increase the likelihood of continued high performance. Since the analysis relies exclusively on historical performance indicators, derived features are designed to capture potential temporal trends associated with changing form. To achieve this, we will be using two different methods of transforming our data: moving average and moving slope.

The moving average transforms our data in windows measuring averages across slices of five to twenty matches. An exponentially weighted moving average (EWMA) will be used.

A player's form will be constant across a specific timeline, because of factors like mental state, decision making and underlying skill. To transpose it into matches and kills, we know that the current form of a player has a noticeable correlation with its recent form; therefore, the most weight will be attributed to the most recent match. EWMA will be used regarding the kills, deaths and average damage per round. Since the EWMA cannot indicate changing trends, we will use the regression line of the last five played matches. The sign of the slope serves as an idea of the current trend, a change in the sign indicating a change in performance. We call this a *moving slope*.

2.1.4. Winrate and winstreak

Besides the base performance that a player can only change through rigorous training and preparation, there are also several psychological factors that can affect the way he plays. One of them is how he reacts to a win or loss and how he manages to get over the result of a match. Because of that, we will implement an EWMA-based winrate. Another variable we want to add is the current streak our player is on. We will split this streak into 2 new variables: the sign of the streak and the number of streaks. This is done to differentiate losing from winning streaks.

2.1.5. The map

Maps can easily be correlated in today's sports with playing on a different football field or basketball court, or different tennis courts where you could play on grass or clay. For our model, the best way to present this data is through one-hot encoding.

2.2. The model

The chosen model for this analysis is *Extreme Gradient Boosting for regression*, since it can easily capture nonlinear relations between the variables. Due to the volatility of the match rounds, we predicted a player's kills per round rather than kills, then we multiplied by the number of rounds for that match, a variable not used in the analysis. This metric allows for a more stable prediction.

2.3. Predictions

For results, a categorical way of making our predictions is adopted. Performance has been modelled based on the player's ability to surpass his mean of kills in a match: yes, for above the mean and no for below; therefore, the results will be judged based on classification metrics. Results are as follows: **67%** accuracy, a recall of **69%**, a precision of **65%**, an F1 score of **66%**. We will also model a custom accuracy as a variable that quantifies a prediction that is within the five kills range from the actual kills since the match results can be very volatile, achieving a **78%** accuracy.

3. CONCLUSIONS

The study demonstrated that player performance can be predicted using basic in-game statistics through an XGBoost model. The approach achieved 78% accuracy within a ±5-kill range and a 67% overall classification accuracy, proving that observable data can still be proven useful despite the absence of psychological or contextual variables, which strongly influence human performance. The model achieved stronger predictive capability for amateur-level data, likely due to higher inter-match variability. In contrast, performance was more difficult to predict for advanced players, whose actions are generally more consistent.

DOUBLE COUNTING – THE SECRET KEY IN THE ARCHITECTURE OF MATHEMATICAL PROBLEM SOLVING

Dumitrescu Dan-Ștefan
International Informatics High School,9 Balta Albina, District 3, Bucharest, Romania
dlrici234@gmail.com

Abstract: Double counting is an elegant and highly effective mathematical method used to solve problems across various fields of mathematics. The core idea involves identifying a single quantity and counting it in two distinct ways. This approach leads to clever and unexpected relationships between different mathematical objects or structures. The main challenge lies in determining what exactly should be counted. In this paper, we aim to explore how double counting can offer original, efficient, and creative solutions to a wide range of problems. We will examine applications of this method in contexts such as permutations, grids, student sets, and geometry, drawing on problems featured in international mathematical competitions.

Key words: Double counting; Combinatorial methods; Mathematical relationships; Competition problems; Enumerative combinatorics; Problem-solving strategies

1. Introduction

Double counting is based on identifying a quantity that can be counted in two different ways. Throughout this presentation, we will examine how this method can be applied to four problems taken from different areas of mathematics. We will explore double counting in the context of permutations, enumerative combinatorics, grid-based problems, and geometric problems, each illustrating a distinct perspective on the power and versatility of this technique.

2. Content

1. Double Counting in Permutations(IMO 1987)

Let $p_n(k)$ be the number of permutations of $\{1,2,\dots,n\}$ that have exactly k fixed points.

$$\text{Prove that } \sum_{k=0}^{n} k\, p_n(k) = n!$$

Solution. Count ordered pairs $(x,\sigma)$where σ is a permutation of $\{1,\dots,n\}$ and x is a fixed point of σ. Fix x and the number of permutations fixing x is $(n-1)!$, hence in total n!

On the other hand, if σ has exactly k fixed points, then there are k choices for x. Summing over all permutations gives $\sum_{k=0}^{n} k\, p_n(k)$. Equating the two counts yields the identity.

2. Double Counting in Class–Student Incidence(Iran 2010)

A school has n students. Each class has at least two students, and if two distinct classes share at least two students, then their sizes are different. Prove that the total number of classes is at most $(n-1)^2$.

Solution. For each class of size x, it contributes $\binom{x}{2}$ unordered student pairs; by hypothesis no pair is counted in two different classes. Let X_x be number of classes of size, $X_x \binom{x}{2} \le \binom{n}{2}$.

$$\sum_{x=2}^{n} X_x \le \binom{n}{2} \sum_{x=2}^{n} \frac{1}{\binom{x}{2}} = \frac{n(n-1)}{2} \sum_{x=2}^{n} \frac{2}{x(x-1)} = \frac{n(n-1)}{2} \cdot 2\left(1 - \frac{1}{n}\right) = (n-1)^2.$$

So the number of classes is at most $(n-1)^2$.

3. Double Counting in Grid Colorings(Romania TST 2009)

Let $N = n^2 + 1$. An $N \times N$ grid of unit squares is colored with N colors, each color appearing exactly N times. Show that there exists a row or a column that contains unit squares of at least $n + 1$ colors.

Solution. Let c_i be the number of colors in column i and l_i the number of colors in row i. For a color t, let a_t be the number of columns and b_t the number of rows on which color t appears. Since color t covers N cells, we have $a_t b_t \ge N$.Double counting color–column and color–row incidences yields$\sum_{i=1}^{N} c_i = \sum_{t=1}^{N} a_t$ and $\sum_{i=1}^{N} l_i = \sum_{t=1}^{N} b_t$.
Assume for contradiction that every row and column uses at most n colors, i.e. $c_i, l_i \le n$. Then

$$(nN)^2 \ge \left(\sum_{i=1}^{N} c_i\right)\left(\sum_{i=1}^{N} l_i\right) = \left(\sum_{t=1}^{N} a_t\right)\left(\sum_{t=1}^{N} b_t\right) \ge \left(\sum_{t=1}^{N} \sqrt{a_t b_t}\right)^2 \ge N^2(n^2+1).$$

a contradiction. Thus some row or column contains at least $n + 1$ colors.

4. Double Counting in Plane Geometry(IMO 1989)

Let S be a set of n points in the plane with no three collinear. For every $P \in S$ there are at least k points of Sequidistant from P. Prove that $k < \frac{1}{2} + \sqrt{2n}$.

Solution. Count triples $(A_i, \{A_j, A_\ell\})$ with i, j, ℓ distinct and $A_iA_j = A_iA_\ell$. Lower bound: for each $A_i$there are at least $\binom{k}{2}$ unordered pairs $\{A_j, A_\ell\}$, so the total is Triples $\ge n\binom{k}{2}$
Upper bound: for each unordered pair $\{A_j, A_\ell\}$ there are at most two choices of A_i, since no three points are collinear (at most two points can lie on the perpendicular bisector of A_jA_ℓ). Hence Triples $\le 2\binom{n}{2} = n(n-1)$. Combining gives $n(n-1) \ge \frac{n\,k(k-1)}{2} \Rightarrow 2(n-1) \ge k(k-1)$. Solving the quadratic inequality in k yields $k < \frac{1}{2} + \sqrt{2n}$.

3.Conclusion Double counting offers elegant and unexpected solutions across multiple areas of mathematics. Its flexibility and simplicity make it a fundamental tool in both problem solving and mathematical enrichment.

References

[1] Mathematical Excalibur

[2] IMO Compendium

[3] AOPS

Vector Calculus and Signal Theory with Applications in Engineering

Eduard Roland KECS [1], Robert Alfred KECS [1]

[1] Faculty of Electronics, Telecommunications and Information Technology, National University of Science and Technology POLITEHNICA Bucharest, 313 Splaiul Independentei, District 6, Bucharest, Romania

Corresponding author email:

eduard_roland.kecs@stud.fils.upb.ro

robert_alfred.kecs@stud.fils.upb.ro

Abstract

Vector calculus, vector space theory, and signal analysis represent interconnected mathematical pillars underlying modern engineering systems. Vector calculus provides a geometric framework for describing multidimensional fields, while signal and system theory offers analytic tools for processing and interpreting time- and space-dependent information. The inclusion of vector space and matrix methods further enables efficient representation, transformation, and computation of signals in both continuous and discrete domains. This paper explores the synthesis of these concepts and demonstrates their role in modeling electromagnetic wave propagation, highlighting the synergy between differential operators, vector spaces, and matrix-based system analysis.

Key words: *Vector Calculus, Signal Theory, Vector space methods*

1. Introduction

The interplay between vector calculus and signal theory forms the foundation for modeling physical processes and engineering systems. Vector calculus focuses on the study of continuous vector fields that describe how quantities vary spatially, while signal theory emphasizes temporal and frequency-domain representations.[1],[2] The combination of these two allows engineers to analyze systems where both spatial and temporal variations are essential—such as electromagnetic fields, sound propagation, and fluid flow.[3]

In addition, vector space and matrix methods provide the algebraic structure needed to model and manipulate multidimensional signals and systems. Many engineering problems—filter design, system identification, and control—can be expressed as linear transformations in vector spaces, where matrices serve as operators acting on signal vectors.[4]

This paper outlines the theoretical framework connecting vector calculus, vector spaces, and signal theory, and illustrates their integration through an electromagnetic field application.

2. Content

A key engineering example uniting these theories is electromagnetic wave propagation. Maxwell's equations describe electric E and magnetic B fields as coupled vector signals in space and time. Combining them yields the vector wave equation, representing multidimensional signal propagation. Discretizing this system through finite element or matrix methods links continuous field theory to numerical computation.[3],[6]

In addition to electromagnetics, vector calculus finds extensive use in other engineering domains:

- **Fluid dynamics and climate modeling:** the divergence and curl operators quantify ocean currents, atmospheric vortices, and energy transfer.[3]

- **Structural mechanics:** gradients of displacement fields yield strain tensors, while divergence of stress tensors governs equilibrium conditions.[6]

- **Heat transfer:** Fourier's law uses the gradient operator to describe thermal flow, with divergence representing heat accumulation or loss.[1][2]

These applications demonstrate how vector calculus, combined with matrix and signal-space methods, enables engineers to model and simulate real-world systems that vary across both space and time.

3. Conclusion

Vector calculus, signal theory, and vector space methods together form a unified framework for understanding and designing engineering systems governed by multidimensional signals and fields. Vector calculus captures spatial variations, signal theory describes temporal and spectral properties, and matrix methods provide computational efficiency. Their integration drives advances in electromagnetics, fluid mechanics, thermodynamics, and structural analysis—fields where mathematical operators translate directly into physical meaning and engineering innovation.

4. References

[1]. Bracewell, R. N. *The Fourier Transform and Its Applications.* McGraw-Hill, 2000.

[2]. Haykin, S., & Van Veen, B. *Signals and Systems.* Wiley, 2014.

[3]. Jackson, J. D. *Classical Electrodynamics.* Wiley, 1999.

[4]. Kailath, T. *Linear Systems.* Prentice Hall, 1980.

[5]. Oppenheim, A. V., & Schafer, R. W. *Discrete-Time Signal Processing.* Pearson, 2010.

[6]. Strang, G. *Linear Algebra and Its Applications.* Cengage, 2016.

FROM VULNERABILITY TO RESILIENCE IN THE NECESSITY OF MULTI-FACTOR APPROACHES IN SIGNATURE VERIFICATION

Eduard-Ștefan SANDU[1]

[1]National University of Science and Technology POLITEHNICA, 313 Independence Square, District 6, Bucharest, Romania

Corresponding author e-mail: edy.eminem@yahoo.com

Abstract

The rapid evolution of malware, specifically spyware, and credential harvesting techniques has revealed critical vulnerabilities in single-factor digital signature mechanisms. This scientific paper investigates the necessity of employing multi-factor authentication as a central element in achieving cryptographic resilience and maintaining data integrity within digital signature systems. The focus is placed on the interplay between cryptographic key management, secure channel establishment and dynamic identity verification. The analysis incorporates threat modeling and security assurance processes to assess the impact of layered authentication on overall system robustness. The results demonstrate that integrating multi-factor authentication into digital signature verification not only strengthens non-repudiation guarantees but also enhances resistance to data exfiltration facilitated by spyware.

Key words*: spyware; authentication; cybersecurity; digital signature; identification.*

1. INTRODUCTION

Authentication represents a fundamental component of cybersecurity, serving as the process through which systems verify the legitimacy of users, devices or external entities attempting to access protected resources and information. Traditionally, authentication has relied on a single-factor authentication, which has been the most commonly used method worldwide. However, in modern threat landscapes, such single-factor systems have proven increasingly inadequate.

Passwords, although the most widespread form of authentication, are highly susceptible to compromise. Attackers can easily obtain them through methods such as deploying spyware capable of capturing keystrokes and extracting stored authentication data from browsers or memory.

2. CONTENT

This chapter situates the experimental simulation within the present scientific work and presents a simplified technical analysis of how multi-factor authentication constrains attackers who steal a victim's credentials. The objective is to evaluate the effectiveness of a four-factor authenticator, consisting of an account identifier, a static password, a time-based one-time password generated by a third-party authenticator application and a user PIN, against an assumed adversary who has deployed spyware and is attempting to exfiltrate digital signing credentials for use in cyberattacks. The emphasis is explicitly defensive and evaluative, no operational methods for delivering or developing malware are provided and the precise infection vector used by the adversary in the simulation is intentionally omitted, because exploitation techniques fall outside the scope and ethical remit of this research.

The adversary is modeled as a remote actor in possession of a generic spyware payload capable of capturing input data from the victim host like keystrokes and in-memory strings, saving the collected data to a local file. The proposed model assumes that the time-based one-time password generator

runs on a separate device, therefore, the attacker cannot steal these codes via the spyware deployed to the host as in Figure 1.

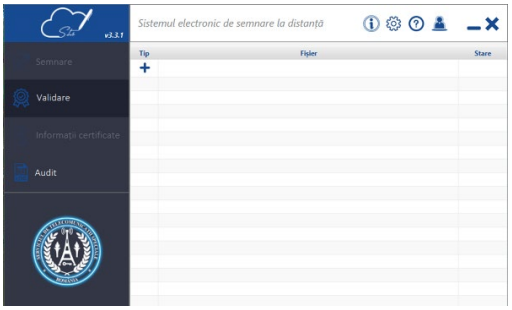

Figure 1. Remote digital signature application interface

Treating spyware as an already-present capability allows the analysis to concentrate on how multi-factor constructions prevent compromise of the signing authority once an attempt is made to capture credentials using the method described above.
To make the analysis concrete, the simulation follows the real user steps outlined earlier. After the attacker captures the account ID and static password via host instrumentation, the remote digital signing application requests a time-based one-time password as in Figure 2. The attacker therefore fails because the time-based one-time password is generated by an independent authenticator application and requires physical possession of that device.

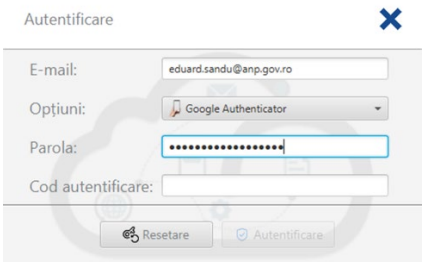

Figure 2. Time-based one-time-password request

The account's subsequent PIN, an additional knowledge factor entered only after successful multi-factor authentication, provides a final barrier, which was not previously entered and was not exfiltrated by the spyware, would prevent access to the operation that releases the signing key as in Figure 3. Thus, layered checks create a compound mode of failure for the attacker.

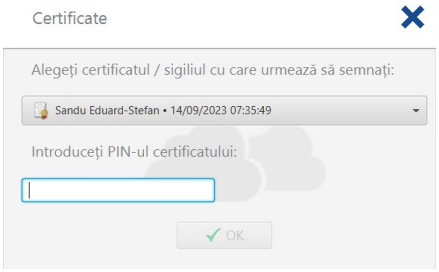

Figure 3. Request account PIN

3. CONCLUSIONS

The simulated exercise demonstrates that, under the assumptions of device separation and sequential multi-factor control, a spyware agent is substantially constrained and unable to replicate digital signature credentials despite capturing static authentication data. This result provides empirical support for the central thesis of this work, namely, the migration of digital signature systems from single-factor architectures to multi-factor architectures that significantly enhance resilience.

PARAMETER ANALYSIS IN ELECTROSPININING PROCESS

Ruxandra Ioana CIPU[1,2], Teodor Andrei CIPU[1,2], Elena Corina CIPU[1,2]

[1]University Politehnica of Bucharest, 313 Splaiul Independentei, District 6, Bucharest, Romania

[2]CiTi, 313 Splaiul Independentei, District 6, Bucharest, Romania

Abstract:

This study examines the electrospinning process mathematically and physically in order to discover important variables that affect fiber morphology, jet stability, and production efficiency. Electrospinning is an important technique in biomedical engineering because of its capacity to produce very thin fibers with high surface-area-to-volume ratios and variable porosity. It has applications in wound healing, tissue engineering, drug delivery, and implant coatings. However, the technology has limitations in process control, scalability, and consistency of fiber qualities. The effects of voltage, flow rate, spinneret-to-collector distance, and fluid viscosity on jet formation and fiber diameter using known theoretical models are analyzed. Fluid dynamics equations are utilized to investigate the relationship between electric field strength, jet thinning, and instabilities. Novel design improvements for electrospinning setups are proposed, such as a vertically moving spinneret, as well as the utilization of external magnetic fields to control fiber spatial deposition. These advancements aim to improve control over fiber architecture, functional grading, and scalability in medical and industrial applications. This project underlines the need to understand the physical principles underpinning electrospinning in order to guide process innovation by integrating mathematical modeling with practical design recommendations.

Key words: *electrospinning; nanomaterials; biomedical application; mathematical modeling; fiber morphology*

1. INTRODUCTION

Electrospinning is an electrodynamic process that enables the fabrication of ultrafine polymer fibers. This paper is meant to study this complex method of producing nanofibers with various applications, especially in the medical field. The study underlines the physical principles underpinning electrospinning in order to guide process innovation by integrating mathematical modeling with practical design recommendations.

2. CONTENT

The setup used to form thin fibers mainly contains a syringe, a power source and a grounded collector. The electrospinning process functions by applying high voltage (10-30kV) to the metal, conducting needle of a syringe that is loaded with a polymer solution, which contains polymer dispersed in solvent. As the current travels through the needle and reaches the solution, the electric force overpowers the capillary force formed at the tip of the syringe, thus creating the Taylor's cone from the droplet of polymer. The spherical geometry of the droplet, dictated by the surface tension of the solvent, becomes conic, forming a jet that is of a micrometric to nanometric order (Guo et al., 2021). This happens due to the electrostatic repulsion of ions in the solution that create the highest charge density in the apex of the Taylor's cone. As the jet continues to travel towards the grounded collector that closes the circuit, the solvent evaporates, leaving only a mesh of ultrathin fibers formed on the collector. During this time, different instabilities start to form, such as the whipping instability observed in Figure 1, which takes place because of the Coulomb repulsion. Other instabilities can appear as well, such as Rayleigh instability, where the resistance of the surface tension breaks up the jet and the asymmetric one, that due to mutual force repulsion and non-uniform charge distribution along the jet (Baghchi et al., 2015). This process is very sensitive to changes in parameter values, the most important of them all being the polymer concentration, the applied voltage, the type of solvent used, the flow rate and other process parameters such as humidity and the distance between the tip and the collector. This paper highlights the importance of parameter control and uses MATLAB simulations to evaluate the influence of process variations. Mathematical models such as the discrete Reneker bead–spring model and the continuous Lagrangian fluid model have been used to describe the complex electrohydrodynamic physics behind electrospinning (Rafiei et al., 2013). Additionally,

analytical scaling laws proposed by Fridrikh et al. (2003) and Ismail et al. (2017) were applied to correlate fiber diameter with the key parameters mentioned.

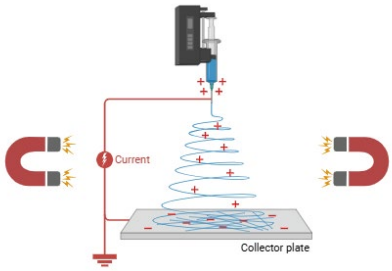

Figure 1. Illustration of electrospinning method with external permanent magnets, created in BioRender

$$d = C^{0,5}\left(\frac{\gamma\varepsilon Q^2}{I^2} * \frac{2}{\pi \ln \chi - 3}\right)^{1/3} \quad (1)$$

In this study we analyzed how the final fiber diameter changes when fluctuating different values for the process parameters. The influence of two different solvents that are commonly used in electrospinning (DMF – dimethylformamide and DCM – dichloromethane) were observed and compared with water from a point of view of the surface tension. In the first MATLAB programme, which was based on Fridrikh's formula for fiber diameter, the parameters varied were the flow rate, the current which was derived from the voltage. Ismail's more complex formula for fiber diameter (Eq. 1) was used for further analysis which also included the electric permitivity of the solution and the polymer concentration. The values were chosen to match intervals found in scientific literature, as were the other fixed variables. It was observed that the flow rate has the most influence on final fiber diameter, being directly proportional to it, as seen in Figure 2. Superficial tension does not necessarily influence the result in the beginning, however it can play a role in the Taylor cone formation, because of polymer chain entanglement and its resistance to thinning, as well as its influence on the evaporation rate.

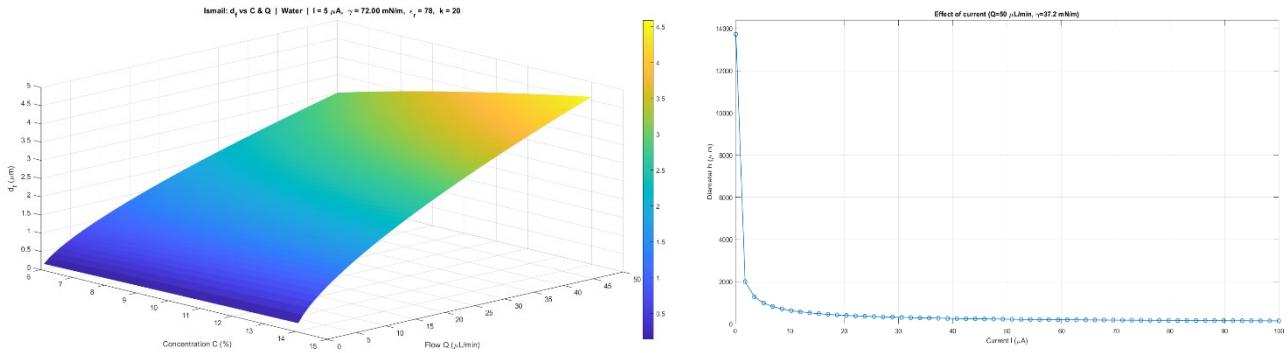

Figure 2. MATLAB simulations for parameter analysis (Ismail left, Fridrikh right)

Different methods for manipulating the fiber alignment and diameter were proposed for creating sensors or artificial muscle fibers or neurons. First, a magnetic field created by placing two permanent magnets could influence a parallel allignment of the fibers, as seen in Figure 1. – Secondly, an idea arose to change the distance between needle tip and collector during the process, in order to form a mesh with different fiber diameters, which could serve as an artificial cell matrix.

3. CONCLUSION

This study focuses on the mathematical modeling that can be used in order to achieve the wanted fiber morphology, which is of high importance in many fields, epecially in medicine. The formation of such thin fibers is very sensitive to parameter change and mathematical predictions optimizes production accuracy of these fibers and their properties. The study demonstrates the implementation of the mathematical models and adaptation to different electrospinning setups.

NUMERICAL METHODS FOR SDES WITH ECONOMIC APPLICATIONS

Elena Corina CIPU[1,2], Vasile Nicolae STĂNCIULESCU[1], Vasile PREDA[3,4,5]

[1]University Politehnica of Bucharest, Centre for Research and Training in Innovative Techniques of Applied Mathematics in Engineering "Traian Lalescu" (CiTi), Bucharest, Romania
[2]Department of Applied Mathematics, Faculty of Applied Sciences, University Politehnica of Bucharest
[3]"Gheorghe Mihoc – Caius Iacob" Institute of Mathematical Statistics and Applied Mathematics of the Romanian Academy (ISMMA)
[4]V. Trebici" Center for Demographic Research, "Costin C. Kiritescu" National Institute of Economic Research of Romanian Academy, Romania
[5]Faculty of Mathematics, University of Bucharest, Romania

Corresponding author email: corina.cipu@upb.ro

Abstract:

Stochastic differential equations have become a particularly useful tool in modeling systems influenced by random fluctuations, especially in demography, economics, and finance, where uncertainty also plays a role. This paper presents an overview of numerical methods for solving SDEs, emphasizing their stability, convergence, and efficiency. Among the classical schemes presented are the Euler-Maruyama and Milstein methods, which are examined alongside the higher-order stochastic Runge-Kutta approaches.

The analysis examines the interplay between discretization error and computational cost in the numerical approximation of stochastic integrals with respect to Wiener processes.

Applications are discussed in the context of economic growth models, stochastic interest rate dynamics, and volatility modeling, illustrating how numerical simulation provides insights into the propagation of uncertainty and risk assessment.

The study continues with the analysis of the role of the discretization step size, the properties of strong and weak convergence, and the use of Monte Carlo techniques for expected value estimation.The results emphasize the importance of selecting appropriate numerical schemes for reliable stochastic modeling in modern economic analysis.

Key words*:* SDE, numerical methods, stability, Wiener process, estimation parameters

1. INTRODUCTION

Stochastic Differential Equations provide a mathematical foundation for modeling dynamic systems under uncertainty. In economics, randomness arises naturally from market fluctuations, policy shocks, and behavioral variability, making SDE-based models essential for realistic analysis. Because most SDEs lack closed-form solutions, numerical methods such as the *Euler–Maruyama, Milstein*, and *stochastic Runge–Kutta* schemes are used to approximate their trajectories and estimate key statistical properties.

Recent advances combine SDE simulation with *Hybrid Statistical Models* to enhance the realism and security of economic data generation. HSMs integrate probabilistic modeling and computational techniques—such as *mixture models, Bayesian networks, Gaussian processes*, and *Sequential Monte Carlo methods*—to reproduce complex dependencies and temporal structures. In secure economic applications, these approaches are reinforced by cryptographic mechanisms, including *True Random Number Generators, Cryptographically Secure Pseudo-Random Number Generators and machine-learning-based entropy sources*, ensuring both stochastic validity and data integrity.

This study outlines numerical schemes for solving SDEs and demonstrates how hybrid statistical modeling can complement stochastic simulations in economic analysis, supporting uncertainty quantification, risk evaluation, and synthetic data generation.

2. CONTENT

The *stochastic exponential growth model* provides a foundational framework for analysing economic dynamics under uncertainty. It extends the classical Malthusian growth model by introducing a stochastic component that captures random shocks affecting production, population, or capital accumulation. The model is formulated as a stochastic differential equation (SDE):

$$dX_t = rX_t dt + \sigma X_t dW_t$$

where X_t denotes the economic variable of interest at time t, r expressing the deterministic growth rate and σ measures the intensity of random fluctuations with W_t a Wiener process.

The analytical solution is: $X_t = X_0 \exp\left[\left(r - \frac{1}{2}\sigma^2\right)t + \sigma W_t\right]$, implying that X_t follows a lognormal distribution. This formulation captures both the expected exponential growth and the uncertainty associated with random perturbations.

In economic applications, this model describes phenomena such as: output and capital growth in stochastic environments where technological or policy shocks occur, population dynamics under migration or fertility uncertainty or asset price evolution, forming the basis of geometric Brownian motion used in financial modelling.

Numerical implementation employs the Euler-Maruyama method, which discretizes the continuous process:$X_{t+\Delta t} = X_t + rX_t\Delta t + \sigma X_t \Delta W_t$, where $\Delta W_t \sim \mathcal{N}(0, \Delta t)$. This scheme allows simulation of multiple stochastic trajectories, providing insight into expected trends, volatility effects, and the probability of extreme economic outcomes.

Let's consider the stochastic logistic-type growth model: $dX_t = rX_t\left(1 - \frac{X_t}{K}\right)dt + \sigma X_t dW_t$, with $r =$ intrinsic growth rate, $K =$ carrying capacity, $\sigma =$ noise intensity, that is a stochastic growth model $dX_t = a(X_t, t)dt + b(X_t, t)dW_t$, where X_t is the state variable that can be population or capital, $a(X_t) = rX_t(1 - X_t/K)$ is the drift term and $b(X_t) = \sigma X_t$ is the diffusion term.

Applying Milstein's scheme: $X_{n+1} = X_n + rX_n(1 - X_n/K)\Delta t + \sigma X_n \Delta W_n + \frac{1}{2}\sigma^2 X_n[(\Delta W_n)^2 - \Delta t]$

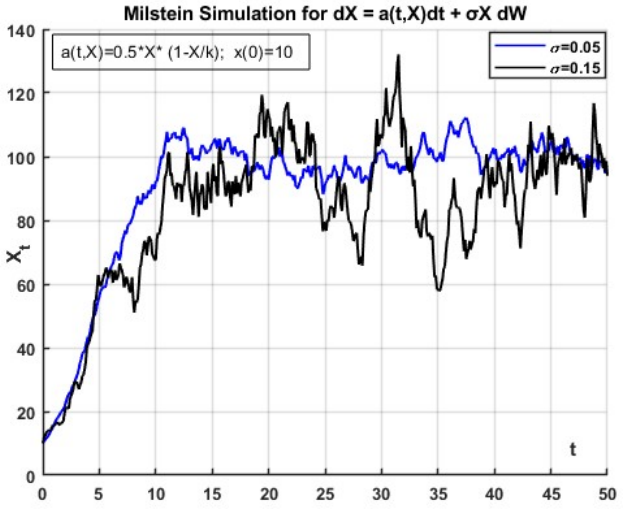

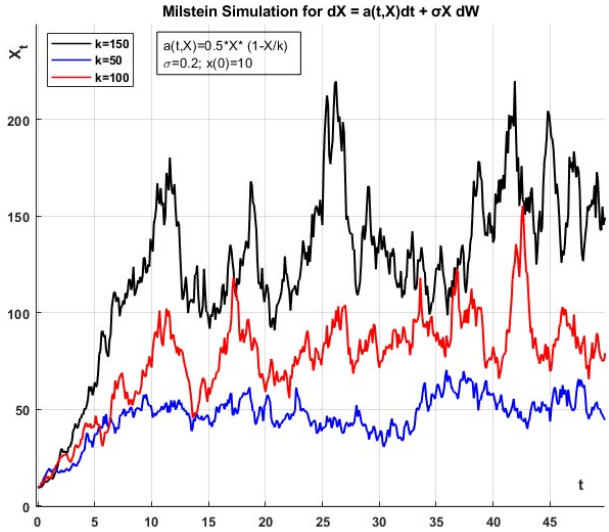

3. CONCLUSION

This study focuses on the mathematical modeling of SDEs with numerical solutions using Euler-Maruyama method and Milstein's scheme. The applicability of the stochastic exponential growth model lies in its ability to integrate deterministic economic theory with real-world randomness. It supports risk assessment, forecasting, and policy evaluation by quantifying how uncertainty propagates through economic systems. When combined with Hybrid Statistical Models (HSMs) for data generation, it also enables realistic scenario simulation and enhances robustness in empirical economic studies.

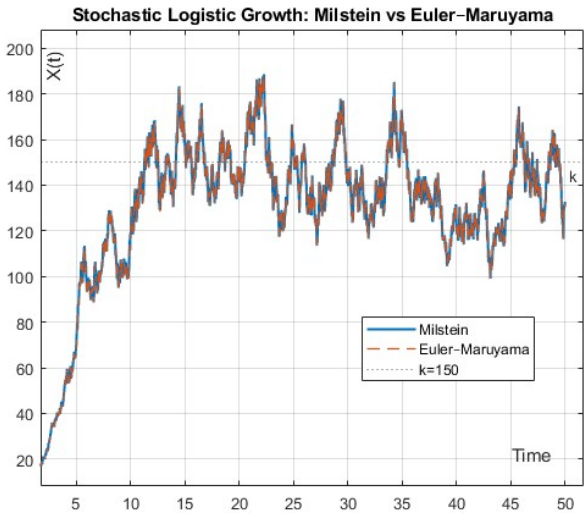

REFERENCES

[1] Timothy Sauer, *Computational solution of stochastic differential equations*. Vol 5, pag. 362-371, 2013 Wiley Periodicals, Inc.

[2] Simo Sarkka; Arno Solin, *Applied Stochastic Differential Equations*, Cambridge University Press, Institute of Mathematical Statistics Textbooks, ISBN 978-1-316-51008-7, 2019

[3] David G. Kendall, Stochastic Process and population growth, 1949, pag 230-264

ALGORITHMIC OPTIMIZATION OF LOW-VOLTAGE ELECTRICAL NETWORK

Elvis-Costin ȚUCĂ[1,2], Sorin-Teodor CHICUȘ[1,2], Elena Corina CIPU[1,3]

[1]University Politehnica of Bucharest, Centre for Research and Training in Innovative Techniques of Applied Mathematics in Engineering "Traian Lalescu" (CiTi), Bucharest, Romania
[2] Power Engineering Faculty, University Politehnica of Bucharest
[3]Department of Applied Mathematics, Faculty of Applied Sciences, University Politehnica of Bucharest

Corresponding author email: elviscostin2005@gmail.com

ABSTRACT
The paper starts with the goal to analyse models of modern electricity networks as graphs. We aim to create a modular C++ program that, for each node, handles generation or consumption, and, for edges, models real transmission lines with values such as resistance and capacity, using well-known algorithms, such as Dijkstra and Ford-Fulkerson, to analyse signals, optimise power flow, and identify potential overloads in grids with increasing penetration of renewable sources.
This program gives engineers and students a flexible platform to explore how energy moves through distributed networks, and to test scenarios where generation, consumption or network topology change. Users may customise inputs - network size, power-output profiles, line characteristics - thus enabling experimentation from small microgrids to larger distribution networks and supporting both educational and applied engineering investigations. Initial experiments indicate that the combined use of graph-based modelling and signal transformations such as Fourier and Laplace is effective in detecting issues like sudden power changes, frequency problems, or line overloads. These findings suggest the platform's potential to enhance resilience and efficiency of electricity networks in a renewable-rich environment.
Keywords: Electrical Grids, Applied Mathematics, C++, Graph Algorithms, Fourier, Laplace, AutoCAD

1. INTRODUCTION

The purpose of this work is to explore how modern electricity networks can be represented and analysed using graphs. Each point of energy generation or consumption can be seen as a node, while the transmission lines that connect them form the edges. By looking at networks this way, we can better understand how energy flows through a system and what problems might appear when renewable sources become more common.

2. CONTENT

The project is buit as a modular program in C++ that allows users to model and test different network configurations. Each edge in the graph has properties such as resistance and capacity, and the program uses algorithms like Dijkstra and Ford-Fulkerson to simulate energy flow and detect possible overloads. Users can experiment with different input values — for example, the number of nodes, power generation profiles, or line parameters — to observe how the system reacts to changes in structure or demand.

Discrete Fourier Transform (DFT):

$$X[k] = \sum_{n=0}^{N-1} x[n] * e^{-j\frac{2\pi kn}{N}}, k = \overline{1, N-1} \quad (1)$$

where a discrete signal x[n] is converted into its frequency components X[k] which helps identify oscillations, harmonics, or anomalies in power flow and being implemented numerically using the Fast Fourier Transform (FFT) for efficiency.

Numerical Laplace Transform:

$$F(s) \approx \sum_{n=0}^{N-1} f(n\Delta t)e^{-sn\Delta t} \quad (2)$$

where F(s) is the discrete approximation of the Laplace Transform for sampled signals, which allows evaluation of system transient response and network stability and is used to analyze rapid changes in power or current.

Pseudocode with examples of initial choices:

The example pseudocode shows the program's main menu, where the user can select different operations. Each choice calls a specific function as shown. This structure makes the program modular and easy to use for its purpose.

```
START
DISPLAY "1: Load Network"
DISPLAY "2: Run Simulation"
DISPLAY "3: Detect Overloads"
DISPLAY "4: Fourier Analysis"
DISPLAY "5: Laplace Analysis"
DISPLAY "6: Exit"
IF choice == 1
LoadNetworkData()
ELSE IF choice == 2
RunPowerFlowSimulation()
ELSE IF choice == 3
DetectOverloads()
ELSE IF choice == 4
FourierAnalysis()
ELSE IF choice == 5
LaplaceAnalysis()
ELSE EXIT
END
```

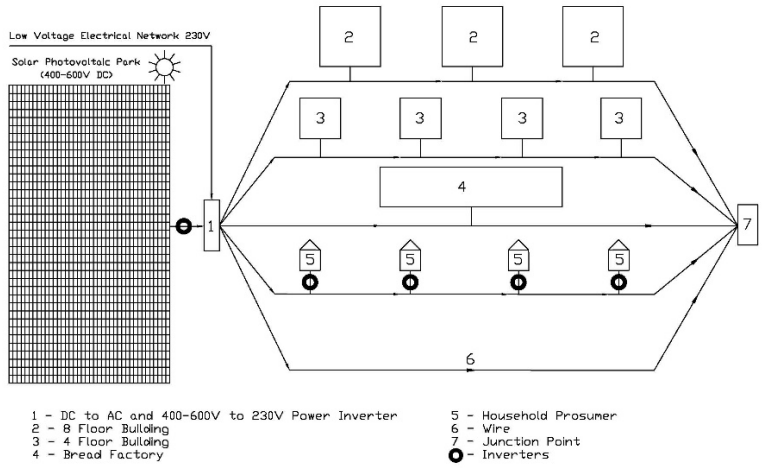

Fig. 1: Visual Representation in AutoCAD of our Electrical Network Example

3. CONCLUSIONS

This combination of energetical engineering and C++ programming is possible. These graph models and signal transformations, such as Fourier and Laplace, helps detect power variations and stability problems in the network. The project has potential not only as a learning tool for students but also as a base for future energetical engineers. It will be further developed and we will progress until it reaches the point where it could be released to the market.

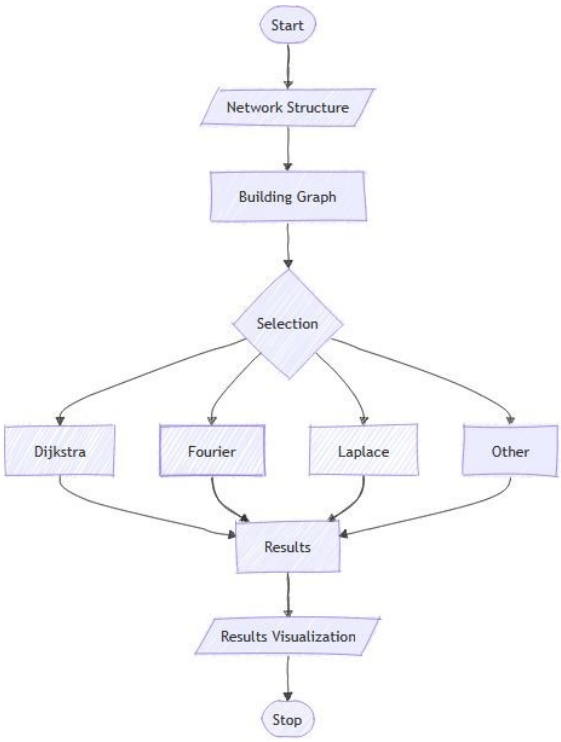

Fig. 2: Visual Representation for the Algorithm in C++

REFERENCES

[1] Sarina Adhikari, *Laplace Transforms and its Applications*. Department of Electrical Engineering and Computer Science, University of Tennessee, 2008 (semantic schilar Corpus ID: 8550540)

[2] Y.H. Gangadharaiah and N. Sandeep, *Engineering Applications of the Laplace Transform*, Cambridge Scholar Publishing, ISBN (13): 978-1-5275-7373-4, 2021

[3] Ofem, Ofem & Moses, Agana & E., Ejogobe. (2021). *Optimal power flow-path determination for voltage control in electricity distribution using the modified dijkstra's algorithm*. International Journal of Engineering & Technology. 10. 108. DOI: 10.14419/ijet.v10i2.31554.

[4] Merve Bulut, Evrencan Özcan, *Optimization of electricity transmission by Ford–Fulkerson algorithm*, Sustainable Energy, Grids and Networks, Volume 28, 2021, 100544, ISSN 2352-4677, DOI: 10.1016/j.segan.2021.100544.

STATISTICAL EVALUATION OF ENTROPY GENERATORS: ANALYSIS OF SECOND-ORDER ERRORS IN NIST SP 800-22 TESTS

Emil SIMION[1,2], Bogdan Costel MOCANU[1,2], Florin NĂSTASE[1,2]

[1]National University of Science and Technology *POLITEHNNICA* Bucharest, Bucharest - 313 Splaiul Independentei, District 6, Bucharest, Romania

[2] BlueSpace TECHNOLOGY – Ilfov, Bragadiru, st. Alexandriei, no. 82

Corresponding author email: emil.simion@upb.ro

Abstract *The robustness of entropy generators is essential for ensuring the security of cryptographic systems, particularly within the context of the EU cybersecurity framework (NIS2 Directive and the Cybersecurity Act). A critical component of their evaluation lies in the statistical validation of randomness through standardized test suites, such as NIST SP 800-22. This paper addresses open issues related to the statistical reliability of such tests, with a focus on second-order errors (type II errors), test interdependencies, and sample size requirements. We present results on the estimation of type II errors for selected tests, namely the frequency monobit test, the frequency test within a block, and the runs test. Furthermore, we highlight the mathematical challenges encountered in extending this evaluation to the other 12 statistical tests included in NIST SP 800-22. Finally, we also propose a method for estimating test independence by simulation.*

Key words*: entropy generator; randomness tests; NIST SP 800-22; statistical evaluation; type II error; test independence; cybersecurity certification; EU regulation*

1. INTRODUCTION

According to the NIS2 Directive (EU) 2022/2555 [1] on measures for a high common level of cybersecurity across the Union state, all member states should be able to take all necessary measures to ensure the protection of the essential interests of national security, to safeguard public policy and public security, and to allow for the prevention, investigation, detection, and prosecution of criminal offenses. For this purpose, member states ought to possess the ability to grant exemptions to private entities engaged in endeavours of national security, public safety, defence, or law enforcement, encompassing the prevention, investigation, detection, and prosecution of criminal offenses. According to Regulation (EU) 2019/881 [2], a European cybersecurity certification system can establish one or more of the following assurance levels for ICT products, ICT services, and ICT processes: “basic”, “substantial”, or “high”. The “basic” assurance level signifies a foundational level of cybersecurity measures, providing a minimum level of security and risk mitigation, the “substantial” assurance level indicates a higher degree of security and resilience, incorporating more robust cybersecurity measures and risk management practices, finally the “high” assurance level represents the most stringent level of cybersecurity assurance, with comprehensive and advanced security measures in place to mitigate risks effectively and ensure the highest level of protection against cyber threats. These assurance levels enable stakeholders to make informed decisions when selecting ICT products, services, and processes, fostering trust and confidence in the digital ecosystem while enhancing cybersecurity across the European Union. For the “substantial” or “high” levels, evaluation and certification are carried out by the competent authorities and specialized laboratories, respectively.

A critical element of IT systems and applications is the entropy generator, which must be analysed on several levels: statistical characteristics (measured using randomness tests), entropy source (based on physical phenomena), entropy evaluation, robustness and security (resistance to attacks in the implementation environment, self-testing mechanisms, cryptographic measures to eliminate bias), as well as compliance with reference standards.

2. CONTENT

In this paper, we address the issue of statistical characteristics of these devices. One of the statistical evaluation standards is the NIST SP 800-22 standard. This standard is a battery of 15 statistical tests, all statistical tests being performed at a level of error of order 1 (the probability of rejecting a true hypothesis) of 1%. A number of open issues regarding statistical tests in this standard ([4], [5]) are represented by:

a) the evaluation of the order 2 error (the probability of accepting a false hypothesis) of each of the 15 tests;

b) the interdependence of the 15 statistical tests;

c) the evaluation of the order 2 error for the entire battery of statistical tests

d) the minimum sample size for each statistical test necessary to reach a certain threshold of the order 1 error;

The 15 statistical tests follow three main categories of statistical distributions (half normal, norm, and χ^2), as follows:

Test	Distribution
Frequency (Monobit) Random Excursions Variant	half normal
Runs Discrete Fourier Transform Maurer's "Universal Statistical" Cumulative Sums (Cusum)	normal
The Longest Run of Ones in a Block Frequency within a Block Non-overlapping Template Matching Overlapping Template Matching Linear Complexity A Approximate Entropy	χ^2
Binary Matrix Rank	$\chi^2(2)$
Random Excursions	$\chi^2(5)$
Serial	$\chi^2(2^{m-1}) + \chi^2(2^{m-2})$

When implementing these statistical testing procedures, it involves a series of issues that are not specified in the NIST methodology, such as: the complexity of implementing the tests, the minimum sample size to reach a certain level of confidence, the confidence level of the entire statistical test suite, the calculation of the probability of accepting a false hypothesis (order 2 error) for each statistical test, respectively the entire test battery and last but not least, the independence of the tests.

In our work, we present a series of results obtained regarding the level of 2nd order error for the following tests: frequency monobit test, frequency test within a block, runs test, as well as the difficulties encountered in performing mathematical calculations for the other 12 statistical tests from the NIST SP800-22 package. We also propose a method for estimating test independence by simulation using a validated random bit generator Standard certified USB Quantum Random Number Generation module [6] and NIST SP 800-22 reference implementation [7]. Another important use case where the proposed method could be used is in the process of randomness evaluation of cryptographic algorithms. The authors of [8] propose a framework for randomness evaluation of TEA, Camellia and LEX cryptographic algorithms using statistical teste such as monobit tests, block frequency and run tests.

3. CONCLUSIONS

These results contribute to the theoretical foundation of the project MERISD3C-QKD (PN-IV-P7-7.1-PTE-2024-0735), on transmission-reception modules for integration into quantum key distribution (QKD) systems.

4. REFERENCES

[1] *Directive (EU) 2022/2555 of the EU P&C and of the Council of 14/12/2022 on measures for a high common level of cybersecurity across the Union*. Available: https://eur-lex.europa.eu/eli/dir/2022/2555/oj - *last accessed 02.10.2025*.

[2] *Regulation (EU) 2019/881 of the EU P&C of 17.04.2019 on ENISA and on information and communications technology cybersecurity certification*. Available: http://data.europa.eu/eli/reg/2019/881/oj - *last accessed 02.10.2025*.

[3] EU Cybersecurity Certification Scheme on Common Criteria (EUCC),. Available, https://certification.enisa.europa.eu/certification-library/eucc-certification-scheme_en

[4] Georgescu, C. and Simion, E., 2017. *New results concerning the power of NIST randomness tests.* Proceedings of the Romanian academy, Series A, 18, pp.381-388.

[5] E. Simion, *Entropy And Randomness: From Analogic To Quantum World*, IEEE Access, April 2020, vol. 8, pp. 74553 – 74561.

[6] https://www.idquantique.com/random-number-generation/products/quantis-random-number-generator/ - *last accessed 02.10.2025*

[7] https://csrc.nist.rip/Projects/Random-Bit-Generation/Documentation-and-Software - *last accessed 02.10.2025*

[8] Duta, C. L., Mocanu, B. C., Vladescu, F. A., & Gheorghe, L. (2014). Randomness evaluation framework of cryptographic algorithms. International Journal on Cryptography and Information Security, 4(1), 31-49.

GENERALIZATION OF SOME RECURRENCE RELATIONS FOR SEQUENCES

Magnolia Anda TILCA[1], Florin BOJOR[2]

[1] "Gheorghe Șincai" National College, 25 Gheorghe Șincai, Baia Mare, Romania
[2] "Vasile Goldiș" Western University of Arad, 94 B-dul Revoluției Arad, Romania
Corresponding author email: f_bojor@yahoo.com

Abstract

This article presents some properties of groups and some applications of noncommutative groups.

Key words*: abstract groups, subgroups, order of elements, automorphisms, Lagrange Theorem*

1. INTRODUCTION

In the following we will present without proof some basic results from group theory.

1. Let $(G,\cdot)$ be a group $a,b\in G$. If $a\cdot b=b\cdot a$ then $a^n\cdot b^m=b^m\cdot a^n,\forall m,n\in\square$.
2. Let $(G,\cdot)$ be a group, then $Z(G)=\{a\in G\,|\,a\cdot x=x\cdot a\}$ is a subgroup of G.
3. Let $(G,\cdot)$ be a group and $a\in G$, then $C(a)=\{x\in G\,|\,a\cdot x=x\cdot a\}$ is a subgroup of G and $Z(G)$ is a subgroup of $C(a)$.
4. If $(G,\cdot)$ is a group and $|G|=p^k$ where p is a prime number, then $|Z(G)|\neq 1$.
5. Let $(G,\cdot)$ be a group, then $\operatorname{ord}(x\cdot a\cdot x^{-1})=\operatorname{ord}(a)$.
6. If H is a subgroup of G then the relation $\rho_H\subseteq G\times G$ defined by $x\rho_H y\Leftrightarrow xy^{-1}\in H$ is an equivalence relation on G.
7. If $(G,\cdot)$ is a finite group and H is a subgroup of G then $\left|G/\rho_H\right|=\dfrac{|G|}{|H|}$ and is called the index of H in G. (Lagrange's Theorem).
8. A subgroup H of $(G,\cdot)$ is called a normal subgroup if
   $\forall y\in G,\forall x\in H\Rightarrow yxy^{-1}\in H$.
9. If $(G,\cdot)$ is an abelian group then any subgroup of it is normal
10. If H is a normal subgroup of $(G,\cdot)$ then $(G/H,\cdot)$ is a group.

2. CONTENT

1. Let $(G,\cdot)$ be a group and $Z(G)=\{a\in G\,|\,a\cdot x=x\cdot a\}$ the center of the group.
   a. If G is a noncommutative group with n elements, $n\in\square^*$ then $|Z(G)|\leq\dfrac{n}{4}$.
   b. Give an example of group with n elements for which $Z(G)=\dfrac{n}{4}$.

   M. Andronache G.M.10/2012
2. Let $(G,\cdot)$ and denote by F the set of finite order elements of G. If F is a finite set, prove that $\forall x\in G$ and $y\in F$ there exists $p\in\square^*$ such that $x^p\cdot y=y\cdot x^p$.

   OJM 2005

3. Let $(G,\cdot)$ be a group with m elements and $a \in G$ be an element of order n with property $a \cdot x = x \cdot a \Leftrightarrow x \in \{e, a, a^2, ..., a^{n-1}\}$. Prove that the group G contains at least $\frac{m}{n}$ elements of order n.

4. THE BIBLIOGRAPHY

1. I. Purdea, C. Pelea, *Probleme de algebră,* Ed. Fundației pentru Studii Europene, 2005.
2. Colecția Gazeta Matematică.
3. www.mategl.com.
4. D. Brânzei & col. Matematică olimpiade și concursuri școlare, Ed. Paralela 45, 2010.

Algebraic Identities as Sources of Problems

Gheorghe BOROICA[1]

[1]National College Gheorghe Șincai, 25 Gheorghe Șincai, Baia Mare, România

Corresponding author email:ghitaboroica64@gmail.com

Abstract

Algebraic identities represent one of the most fundamental and versatile tools in mathematics. From classical formulas of decomposition and factorization to complex relationships between polynomials and matrices, they provide elegant means for simplifying expressions, proving properties, and uncovering unexpected connections between seemingly different concepts. Essentially, an algebraic identity expresses an equality that holds true for all values of the involved variables, offering a general framework upon which solid mathematical reasoning can be built.

The use of algebraic identities is not limited to elementary calculations: they play an essential role in **number theory**, where they enable the transformation and analysis of complex arithmetic expressions; in **linear algebra**, where they help deduce properties of matrices, determinants, or vector spaces; as well as in the study of **inequalities**, where they can lead to elegant proofs through inspired factorizations and substitutions.

.

Key words*: Algebraic identities*

1.INTRODUCTION

The use of algebraic identities is not limited to elementary calculations: they play an essential role in **number theory**, where they enable the transformation and analysis of complex arithmetic expressions; in **linear algebra**, where they help deduce properties of matrices, determinants, or vector spaces; as well as in the study of **inequalities**, where they can lead to elegant proofs through inspired factorizations and substitutions.

2. CONTENT

The starting point in this endeavor is the following problem:

Problem 2.1. Prove that there exists an infinite number of quadruples of natural numbers (x,y,z,t), all pairwise relatively prime, such that $x^3+y^3+z^2=t^4$.

Baraj, 2000

Problem 2.2. If a,b,c are the lengths of the sides of a triangle, then prove that

$$\left|\frac{a-b}{a+b}+\frac{b-c}{b+c}+\frac{c-a}{c+a}\right|<\frac{1}{8}.$$

Problem 2.3. Show that if the natural number n can be written in the form $n = x^2 - 3y^2, x, y \in \square$, then n can be expressed in this form in infinitely many ways.

Problem 2.4. Prove that for any natural number n, the number $f(n) = 2^{2^n} + 2^{2^{n-1}} + 1$ has at least n distinct prime divisors.

Problem 2.5. Let $A, B, C \in M_{2019}(\square)$ be a matrix with the property that

$A^2 + B^2 + C^2 = AB + BC + CA$.

Prove that $\det([A,B]+[B,C]+[C,A]) \le 0$, where $[X,Y] = XY - YX$.

Problem 2.6. Consider two different sets of distinct natural numbers $\{a_1, a_2, ..., a_n\}$ and $\{b_1, b_2, ..., b_n\}$, such that the sums $\frac{n(n-1)}{2}$ of the form $a_i + a_j$ coincide with the sums $\frac{n(n-1)}{2}$ of the form $b_i + b_j$. Prove that N is a power of 2.

3. CONCLUSIONS

The purpose of this article is to highlight how algebraic identities can be effectively applied in these areas, illustrating through concrete examples their unifying power and their ability to reveal deep structures hidden behind seemingly diverse mathematical problems.

REFERENCES

[1] Titu Andreescu, Dorin Andrica, O introducere în studiul ecuațiilor diofantiene, Ed.Gil, Zalău, 2002

[2] Titu Andreescu, Dorin Andrica, 360 probleme de matematică pentru concursuri, Ed.Gil, Zalău, 2002

[3] Arthur Engel, Probleme de matematică-strategii de rezolvare, Ed,Gil, Zalău, 2006

[4] Mihai Onucu Dribe, Inegalități idei și metode, Ed.Gil, Zalău, 2003

[5] Valentin Vornicu, Olimpiada de Matematică de la provocare la experiență, Ed.Gil, Zalău,2003

MINIMUM ENERGY CONTROL PROBLEM FOR A SINGULAR TWO-DIMENSIONAL CONTINUOUS-DISCRETE TIME LINEAR SYSTEMS

Mohammed Amine GHEZZAR[1], Djillali BOUAGADA [2] , Kamel BENYETTOU[3]

[1]National $National Higher School of Mathematics, Scientific and Technology Hub of Sidi Abdellah, ACSY Team-Laboratory of Pure and Applied Mathematics (UMAB), P.O. Box 75, Algiers 16093, Algeria

[2,3]Abdelhamid Ibn Badis University Mostaganem, Department of Mathematics and Computer Science, ACSY Team-Laboratory of Pure and Applied Mathematics, Faculty SEI-BP 227/118 Mostaganem 27000, Algeria.

Corresponding author email: amine.ghezzar@nhsm.edu.dz[1] , djillali.bouagada@univ-mosta.dz[2] , kamel.benyettou@ univ-mosta.dz[3]

Abstract

The goal of this paper is to propose a contribution to the controllability and the minimum energy control problem of singular two-dimensional linear systems. The concept of controllability has a variety of applications in advanced control theory and systems research, as well as industrial and chemical process control, systems and filters, 2D image processing random fields and space-time processing, 2D feedback design techniques. Many researchers have studied and developed the problems of minimum energy control of singular two-dimensional systems. In this paper, we had interested to a new class of two-dimensional hybrid systems which is the class of singular continuous-discrete time models..

Key words: *Two dimensional systems, Continuous-discrete systems, Singular systems, Minimum energy, Controllability conditions.*

1. INTRODUCTION

Two-dimensional (2D) systems have emerged as an important extension of traditional one-dimensional models, providing a powerful framework for representing dynamic processes that evolve along two independent directions, such as space and time. Continuous-discrete systems, a specific class of 2D models, combine continuous dynamics with discrete updates, offering flexibility in modeling hybrid processes encountered in engineering and signal processing. Singular systems, characterized by the presence of algebraic constraints alongside differential or difference equations, pose additional challenges in analysis and control design. Within this context, achieving minimum energy control plays a crucial role in optimizing system performance while minimizing control effort. Furthermore, controllability conditions are fundamental for determining whether a system's state can be driven to a desired configuration. The study of these properties in 2D singular continuous-discrete systems provides valuable insights for both theoretical development and practical applications.

2. CONTENT

The proposed approach is based on the application of the Gramian matrix. It is shown that if the system is controllable, then there exists an optimum control input that steers the state from the initial state to the final state. We propose a necessary and sufficient condition of controllability criteria to

formulate and solve the minimum energy control problem. Some illustrated examples and simulations are introduced to illustrate the applicability and accuracy of the proposed method.

Let us consider the singular two-dimensional (2D) continuous-discrete time linear systems defined by the following equation:

$$E\,X'(t,i) \;=\; A\,X(t,i) \;+\; B\,u(t,i)$$

where $X'(t,i) = \partial X(t,i)/\partial t, X(t,i) \in \mathbb{R}^{n}$, and $u(t,i) \in \mathbb{R}^{m}$ are the state and input vectors, respectively. The matrices $A \in \mathbb{R}^{nxn}, B \in \mathbb{R}^{nxm}$ (with $n \geq m$) represent the system and input matrices. The variable t $\in \mathbb{R}^{+}$ is the continuous variable (usually representing time), and $i \in \mathbb{Z}^{+} = \{0, 1, 2, \dots\}$ is the discrete variable.

3. CONCLUSIONS

This study addressed the controllability analysis and minimum energy control of singular two-dimensional continuous-discrete linear systems. The controllability of such systems was investigated using the Gramian matrix approach, which provides a fundamental criterion to determine whether the system states can be driven to desired configurations through admissible control inputs. Based on this controllability framework, the minimum energy control problem was formulated and solved, ensuring that the required state transfer is achieved with the least possible control effort. The obtained results highlight the importance of the Gramian matrix in characterizing system behavior and optimizing control performance for singular 2D continuous-discrete models.

DIFFERENTIAL WRAPPER HIERARCHICAL QPSK UNDER ATMOSPHERIC IMPAIRMENTS FOR CUBESAT COMMUNICATIONS

Ion-Nicholas-Anthony BERECHET[1,3], Andrei-Valentin NAE[1,3], Edward-Mircea STIOP[1,3], Simona Mihaela BIBIC[2,3], Diana Rodica RADNEF-CONSTANTIN[4]

[1] Faculty of Electrical Engineering, National University of Science and Technology POLITEHNICA Bucharest, 313 Splaiul Independentei, District 6, Bucharest, Romania

[2] Department of Applied Mathematics, National University of Science and Technology POLITEHNICA Bucharest, 313 Splaiul Independentei, District 6, Bucharest, Romania

[3] Center for Research and Training in Innovative Techniques of Applied Mathematics in Engineering, National University of Science and Technology POLITEHNICA Bucharest, 313 Splaiul Independentei, District 6, Bucharest, Romania

[4] Astronomical Institute of the Romanian Academy, Department of Astrophysics, Cutitul de Argint 5, Bucharest, 040557, Romania

Corresponding author email: ion.berechet@stud.electro.upb.ro, andrei_valentin.nae@stud.electro.upb.ro, edward_mircea.stiop@stud.electro.upb.ro, simona.bibic@upb.ro, ghe12constantin@yahoo.com

Abstract

This paper extends the differential-wrapper hierarchical QPSK concept by incorporating realistic atmospheric constraints to better simulate CubeSat communication links through weather-affected paths. The scheme, which encodes two differential QPSK core bits and one wrapper bit via a controlled $\pm\phi$ phase offset, is simulated under diverse attenuation and phase noise profiles emulating clear, light rain, and moderate rain conditions. Each weather case introduces combined amplitude fading, Doppler prediction error, and phase jitter representative of real-world LEO satellite passes. Results demonstrate that while increased attenuation and jitter reduce effective SNR, optimized ϕ selections can maintain throughput at moderate E_b/N_0 levels. The proposed approach improves realism in evaluating differential hierarchical modulations for small satellites.

Key words: *CubeSat communication, doppler prediction, weather constraints, differential QPSK, spectral efficiency*

1. INTRODUCTION

As CubeSat missions mature toward high-data-rate applications, robustness to environmental channel variability becomes increasingly important. Previous work introduced differential-wrapper hierarchical QPSK as a constant-envelope 3-bits/symbol technique robust to large Doppler shifts without requiring phase-locked loops [1]. However, that earlier study assumed mildly impaired channels. This paper refines the model by adding statistically grounded representations of weather-dependent attenuation, amplitude fading, and phase jitter. The new simulations evaluate how these factors influence throughput and optimal ϕ values across operational signal-to-noise ratios.

2. CONTENT

To approximate realistic downlinks, the channel combines several weather dependent elements:

- Mean attenuation in dB representing long term power loss due to rain or cloud cover;
- Log-normal amplitude fading (standard deviation in dB) modeling short-term scintillation;
- Gaussian phase jitter capturing local turbulence and tropospheric irregularities.

These parameters vary per weather class: clear, light rain, and moderate rain and are applied together with the sinusoidal Doppler

Each transmitted symbol builds on its predecessor as

$$x[k] = x[k-1]e^{j(\Delta_{core}+s_k\,\phi)}, \tag{1}$$

where $\Delta_{core} \in \{\pm\pi/4, \pm 3\pi/4\}$ encodes two Gray-mapped core bits, and the wrapper bit modifies the step by $\pm\phi$. The receiver derotates by the predicted cumulative Doppler phase and extracts the phase difference between successive samples. Decision logic selects the closest among eight candidate increments.

Monte Carlo simulations sweep ϕ from 0°–40° and E_b/N_0 from 0–18 dB across multiple weather cases [2]. For each combination, bit error rates for core and wrapper bits are computed, and throughput is defined as

$$T = 2(1 - BER_{core}) + (1 - BER_{wrap}). \quad (2)$$

The analysis further identifies best ϕ values maximizing throughput both per E_b/N_0 and on average. Throughput curves and mean throughput versus ϕ plots are generated for clear, light rain, and moderate rain, showing the modulation's adaptability to environmental degradation.

Simulation results confirm that under mild to moderate weather attenuation, throughput degradation remains limited if ϕ is optimized. Light rain conditions cause minor SNR loss (<1 dB) compared to clear weather, while moderate rain induces higher phase jitter and amplitude fading, reducing mean throughput by ≈10% at low E_b/N_0. However, differential detection maintains stability without requiring carrier recovery. The dependence of best ϕ on environmental severity suggests the potential for adaptive ϕ control in future CubeSat systems.

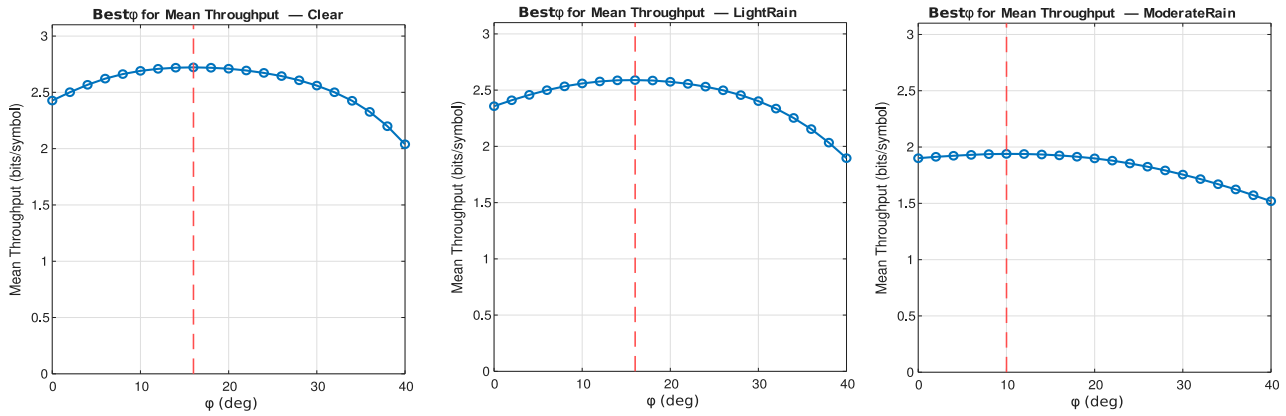

Figure 1. Best ϕ for Mean Throughput for clear weather, light rain and moderate rain for $E_b/N_0 = 8$ db.

3. CONCLUSIONS

Incorporating atmospheric impairment modelling into differential wrapper hierarchical QPSK provides a more accurate picture of its practical performance for CubeSat links.

The results emphasize that the proposed scheme not only enhances spectral efficiency but also demonstrates robustness under realistic conditions. Future research will extend this model to hardware in the loop tests and investigate adaptive ϕ selection strategies guided by real time channel estimation.

REFERENCES

[1] Ion-Nicholas-Anthony, Andrei-Valentin Nae, Edward-Mircea Stiop, Simona Mihaela Bibic (2025). Differential Wrapper Hierarchical QPSK for CubeSat Communications. StuFoTech Kiel 2025 Conference.

[2] P Series: Radiowave propagation (2023). Propagation data and prediction methods required for the design of Earth-space telecommunication systems. *Recommendation ITU-R*, 618-14.

DEPLOYING A LIGHT MODEL FOR ANALYSING THYROID TUMORS. A MATHEMATICAL APPROACH

Iulian-Nicolae PETRIIA[1,2,3], Antonela TOMA[1,3], Octavian POSTAVARU[1,3]

[1]National University of Science and Technology POLITEHNICA Bucharest, 313 Splaiul Independentei, District 6, Bucharest, Romania,

[2]Faculty of Electronics, Telecommunications and Information Technology, Bucharest

[3]Center for Research and Training in Innovative Techniques of Applied Mathematics in Engineering, 'Traian Lalescu' (CiTi), Bucharest, Romania

Corresponding author email: iulian.petriia@stud.etti.upb.ro

Abstract: *This paper investigates the role of early diagnostic of thyroid nodules and proposes a minimum machine learning–assisted model, more specifically a mathematical tool that can be further develop into a more efficient one on a microcontroller, for example a Raspberry Pi 5. One of the big problem that was encountered during the building of the model was the fact that although it seems to be a simple model to be build, GPU (Graphical Processing Units) were required and the dataset was also another key aspect to take into consideration, due to the fact that a dataset that has lacunas can present a big problem for our final results. This paper also was started from a course that Iulian-Nicolae has studied this summer related to how Python programming language can help start a tiny Machine Learning script from scratch.*

Key words*: thyroid nodule, Machine Learning, tumour, malign, benign.*

1. INTRODUCTION

The accurate evaluation of thyroid nodules remains a clinical challenge due to their high prevalence and variable risk of malignancy. While the majority of nodules are benign, the correct identification of suspicious features is essential for guiding biopsy recommendations and treatment strategies for patients even when the cancer is in an incipient status. Starting from this observation, the present study attempts to present a small mathematical tool for analysing a dataset from the internet with photos taken from patients that has malign, or benign thyroid cancer, with the ultimate goal of identifying a framework that can be reliably implemented in clinical practice. We hope that through this study we can be able, in the end to increase the efficiency of detecting the true positive cases and to have a low as possible rate of detecting false negative cases.

2. CONTENT

First of all, we used the dataset 'TN5000: An Ultrasound Image Dataset for Thyroid Nodule Detection and Classification'[1] published on 16 August 2025 which presents images that were taken from different patients that presents thyroid cancer identified and certified by doctors. We choose for implementation the software Google Colab which offers standardized NVIDIA T4 GPU. We imported all the images and the labels attached to each of the image and we used the bounding boxes that were provided for each image to identify where the tumour is exactly situated. These pieces of information were stored in '.xml' format and each image provided using the standard '.jpg'. After that, a very important step was dealing with the size of the images because there were 5000 images with different sizes and we chose to resize all the images at the most common size, being 718x500 pixels in order not to lose information for most of the images. We can assume that although 1026 images will be resized, we will have a big number of them that are at their original size. Finally, for the pre-processing data we cropped those images using that bounding box that was defined previously taking into account that we are interested in just the way a tumour look like both for malign and for

[1] The dataset is available on https://www.nature.com/articles/s41597-025-05757-4 (hyperlink accessed on 15.10.2025)

benign and also we split our data for the training, validation and testing phases that are part of the mathematical model that we have used during the testing of the algorithm.
The method utilised is mainly used nowadays for image classification with ResNet18. First, the images are stored as 3D tensors (by means of storing the height, width and finally the channels for colours). We must mention from the very beginning that we applied to all the images a filter to assign to each image just one colour in order to avoid filling the memory with unnecessary elements. We have applied convolution, normalisation and matrix multiplication on these tensors, by using the generalised formulae:

$$y = Wx + b \tag{1}$$

where 'W' is a weight matrix, 'x' is the input tensor and 'b' is a bias vector.
For the ResNet18, which is a CNN with residuals connections, in the algorithm there were defined some kernels or filters that were applied over the images to extract features that will be necessarily for identifying a new image and classified it.
We can define a convolution kernel in the following:

$$(f * x)_{i,j} = \sum_{m} \sum_{n} f(m,n) \cdot x(i+m, j+n) \tag{2}$$

And the residuals blocks:

$$y = F(x) + x, \tag{3}$$

where 'F(x)' is a transformation (usually it is a convolution, or a normalisation). In the end of the training, we would be interested in just a binary classification (e.g. benign or malign). We also defined and calculated using the algorithm the multiclass cross entropy loss since we previously said that we are just interested in a binary classification of the cancer and this model is suitable for our application:

$$Multiclass\ cross\ entropy\ loss = -\frac{1}{N} \sum_{i=1}^{N} \sum_{j=1}^{M} (y_{i,j} \cdot \log (p_{i,j}) \tag{4}$$

Where 'N' is the number of samples, 'C' is the number of classes, $y_{i,j}$ is 1 if class 'j' is correct for a random sample 'i' and 0 in the rest. Finally, $p_{i,j}$ is model-predicted probability of the same sample 'i' being in class j. The two final steps involved are the calculation of model outputs logits that are passed thought 'softmax' and the maximum probability.
We have chosen a number of 20 epochs to train the model, and we have obtained a test loss varying between 0.53 (at the first epoch) and reaching 0.42 (at the final epoch) and an accuracy of 84.40% for detecting a tumour and classify it being either benign or malign.

3. CONCLUSIONS

This study presented in short, a lightweight machine learning model for the classification of thyroid nodules. By applying preprocessing steps such as resizing, cropping and bounding-box selection, followed by the actual training with ResNet18, the model achieved an accuracy of 84.40% in distinguishing between benign and malignant cases. Although this study is at a very beginning stage it highlights both the potential (e.g. a compact mathematical model) but also the limitation (e.g. the dependence of GPU resources), but in the future we want to transfer this solution on a limited microcontroller to test its capabilities and observe the evolution of the accuracy.

Neural Network-based Feedback Linearization for non-smooth tracking

Iustin Markiș[1], Vlad Mihaly[1]

[1]Technical University of Cluj-Napoca, G. Baritiu 26-28, Cluj, Romania

Corresponding author email: iustinmarkis23@gmail.com

Abstract

This paper highlights the mathematical tools that were used to bring relevant additions to the field of control engineering, where dynamic models are described using nonlinear differential equations. In many practical situations, such mathematical models are partially or completely unknown; this work focuses on a class of dynamic systems described by nonlinear differential equations that are affine with respect to the input signal. Given that these nonlinear functions exist, their behavior can be sufficiently well approximated using a neural network with a single hidden layer with enough number of neurons. Within this context, this work extends the available working solutions by effectively handling the case of non-smooth reference tracking, under certain key assumptions. Moreover, this result comes with theoretical guarantees and proofs along with a case study in which theoretical aspects are numerically validated.

Key words*: nonlinear differential equations; universal approximation; convex optimization; Lyapunov stability.*

1. INTRODUCTION

Control engineering is a field that blends multiple mathematical concepts such as differential geometry, complex analysis, convex optimization, differential equations and linear algebra, concepts that were directly needed to formulate the results proposed by this work. Given the mathematical context, this paper focuses on extending the classic feedback linearization technique that has highly important results in control engineering, by handling its main drawback, namely that it requires a precise mathematical model of a dynamic system, which is unlikely in practice. To handle such practical scenarios neural networks are used as universal function approximators to learn unmodeled dynamics. The objective is to design a closed loop control system that can maintain good tracking performance for a given reference trajectory. In addition to current results, the solution proposed by this work allows the use of a non-smooth reference trajectory.

2. CONTENT

This work consists in some introductory content to familiarize the reader to control theory concepts highlining the mathematic tools need to understand the analysis and synthesis conducted to establish the main result of the paper. Background on the classic feedback linearization approach is also presented and acts as a conceptual basis for defining the control problem, followed by the proposed solution that is supported by theoretical guarantees and formal proofs along with numeric validation.

2.1 PROBLEM FORMULATION

Considering a class of single-input-single-output (SISO) nonlinear dynamical systems described by the following set of first order nonlinear differential equations:

$$\sum_n : \begin{cases} \dot{\eta}(t) = f_0(\eta, \xi) \\ \dot{\xi}(t) = A_n \xi(t) + B_n\big(\alpha(x) + \beta(x)u(t)\big) \\ y(t) = C_n \xi(t) \end{cases}$$

where $x = \Phi(\xi, \eta) \in \mathbb{R}^n$ denotes the original states of the system, for which Φ is a diffeomorphism with n being the order of the system, $\xi: \mathbb{R}^+ \to \mathbb{R}^r$ is the linearizable part of the system, $\eta: \mathbb{R}^+ \to \mathbb{R}^{n-r}$ the internal dynamics with f_0 a nonlinear mapping, $u: \mathbb{R}^+ \to \mathbb{R}$ describes the input function, followed by the measured output $y: \mathbb{R}^+ \to \mathbb{R}$ along with $A_n \in \mathbb{R}^{r \times r}$ being the state matric, $B_n \in \mathbb{R}^r$ the input matrix and $C_n^T \in \mathbb{R}^r$ the output matrix. The system is said to have a *relative degree* r that represents

the number of times the output $y(t)$ needs to be differentiated until the input $u(t)$ appears explicitly. Considering a feedback interconnection:

$$u^*(t) = \frac{1}{L_g L_f^{r-1} h(x)} \left[-L_f^r h(x) + v(t) \right]$$

where $L_f\, h(x)$ is the directional (Lie) derivative of h along f that admits the recursive definition $L_f^m h(x) = L_f\, L_f^{m-1} h(x)$ for any $m \in \mathbb{Z}^+$, and $v: \mathbb{R}^+ \to \mathbb{R}$ is a function that describes a reference trajectory. Considering the following assumptions:

1) The new states $\xi(t)$ are obtained through a unity transformation.
2) The sign of $L_g L_f^{r-1} h(x)$ is considered known and constant throughout its domain.

The goal is to design a closed loop control system that can maintain tracking performance for a non-smooth reference trajectory, while ensuring asymptotic stability of the equilibrium. Towards this end, based in the Universal Approximation Theorem, the ideal control signal $u^*(t)$ is approximated by a neural network with a single hidden layer:

$$\hat{u}(t) = \widehat{W} \sigma(\hat{V} x_{NN})$$

where $\widehat{W}$, $\hat{V}$ are the weights of the neural network that must be numerically found by solving a convex optimization problem, σ is a discriminatory (activation) function and finally x_{NN} the input of the neural network. In order to correctly formulate the optimization problem, an objective function must be properly chosen and the main contribution of this paper consists in how such a function is constructed. The main idea is to quantify the difference between the actual states and the state of an ideal liner system $\| \xi(t) - z(t) \|^2$, where $\|\cdot\|$ is the Euclidian norm and $z(t)$ are the ideal states of the ideally linearized system. Using this objective function allows the use of non-smooth reference trajectories.

2.2 THEOREM (STABILITY OF THE CLOSED LOOP SYSTEM):

Considering the described class of nonlinear dynamic systems that may eighter have complete or partial relative degree, under the mentioned assumptions, the approximation of the input function using a neural network with a single hidden layer, under convergence conditions, ensures asymptotic stability of the closed loop system for any reference. The result is established based on the universal approximation theorem of neural networks and Lyapunov stability theory. The proof consists in showing that the derivative of a Lyapunov function is negative definite, which directly translates to a dissipative behavior of the system, thus ensuring asimptotic stability.

$$V = \frac{1}{2} * e^T P e + \widetilde{W} \cdot \widetilde{W}^T$$

where $P = P^T$ is a symmetric and positive definite matrix that satisfies $A_c^T P + P A_c = -Q$, with Q being a positive definite matric and A_c a matrix with all its eigen values having negative real parts. The presented theorem formally ilustrates the main result of this work that extends current literature by providing a working solution that does not require full relative degree and alows the use of non-smooth functions that describe the reference trajectory for the closed loop system. The theoretical aspects were validated againts a case study on banchmarking systems for both complete and partial relative degree cases.

3. CONCLUSIONS

This work manages to underline the mathematical concepts used to provide a working solution of intelligent feedback linearization, that adds value to the current available approaches. To make the method more widely available, a relevant possible research direction would be searching for ways in which the assumption that the system must already be in the normal form, can be relaxed. Other relevant improvement would be represented by augmenting the neural networks in order to be able t0 learn non-smooth function, making the solution be feasible to a wider range of applications.

From fixed points to fractal maps: a mathematical modeling for early pathological identification in medical imaging

Kaan NASURLA[1], Mircea OLTEANU[2]

[1,2]University Politehnica of Bucharest, 313 Splaiul Independentei, District 6, Bucharest, Romania

Corresponding author email: nasurla.kaan@gmail.com

Abstract

The continuous advancement of medical imaging technologies such as MRI, CT, PET, and ultrasound has led to an unprecedented increase in the amount and resolution of clinical data. Interpreting these complex images requires analytical frameworks capable of describing irregular, heterogeneous, and self-similar structures. Traditional Euclidean geometry, based on regular forms and smooth contours, has reached its limits in modeling the complexity of natural and biological structures. To overcome these limitations, this study explores the mathematical and computational applications of fractal geometry for early tumor detection and visualization from medical imaging data. Fractal geometry, introduced by Benoît Mandelbrot in The Fractal Geometry of Nature (1982), provides the mathematical tools needed to describe objects that are self-similar across multiple scales. These structures, which appear disordered or fragmented from an Euclidean perspective, can exhibit a high degree of internal organization when analyzed using fractal principles. The concept of self-similarity relies on the principle of contraction mappings in metric spaces: a transformation that reduces distances between points by a fixed factor less than one. According to Banach's Fixed-Point Theorem, every contraction mapping in a complete metric space admits a unique fixed point. This theoretical result is fundamental to the generation of fractals and to the iterative decomposition of complex geometries encountered in biological tissues. Another important mathematical tool used in this research is the Hausdorff distance, which measures the geometric difference between two compact sets. It provides a quantitative basis for evaluating the similarity between two shapes or regions, such as comparing a segmented tumor boundary with a healthy tissue region.

Key words*: Fractal Geometry, Fractal Dimension, Box-Counting Method, Hausdorff Distance, Metric Contraction, Fixed-Point Theorem, Medical Image Analysis, Tumor Detection, Early Diagnosis, Mathematical Modeling*

1. INTRODUCTION

Euclidean geometry, based on lines, planes, and regular shapes, has long been the main tool for describing natural objects and phenomena. However, it reached a performance limit when it came to characterizing atypical, complex, and irregular shapes—such as cloud edges, rib structures, blood vessels, or tumor contours. Euclidean models, built on symmetry and regularity, cannot capture the degree of fragmentation and discontinuity that defines real structures in nature and biology.

To overcome these limitations, Benoît Mandelbrot introduced the concept of fractal geometry in his seminal work "The Fractal Geometry of Nature" (1982). This new mathematical paradigm proposes an alternative view of space and form, based on self-similarity, hierarchical complexity, and scale invariance. According to it, a fractal object exhibits a repetitive structure at different scales of observation, each level preserving the global characteristics of the ensemble. Thus, apparently chaotic phenomena can be described by coherent mathematical models, which manage to capture the hidden internal organization of natural complexity.

In the field of medical imaging, this approach has proven to be extremely relevant. Biological tissues, especially pathological ones, often exhibit a high degree of structural irregularity and spatial heterogeneity. Tumors, for example, do not have regular contours and exhibit growth patterns that repeat at different scales — a typical fractal behavior. For this reason, fractal analysis provides a powerful mathematical tool for quantifying complexity and identifying subtle differences between healthy and diseased tissues.

2. BANACH CONTRACTION PRINCIPLE

Let (X, d) be a metric space. Then a map $T: X \to X$ is called a contraction mapping on X, if there exist $k \in [0, 1)$ such that:

$$d\big(T(x), T(y)\big) \leq kd(x, y) \text{ for all } x, y \in X$$

The number k will be called contraction factor.

Let (X, d) be a complete metric space with a contraction mapping $T: X \to X$ with contraction factor k. Then T admits a unique fixed point ξ so that $T(\xi) = \xi$. The point ξ will be called the fixed point of T.

3. SELF-SIMILARITY

This is one of the fundamental properties of fractal structures and describes the ability of an object to repeat its shape or structure at different scales of observation. In other words, a self-similar system contains substructures that reproduce, in whole or in part, the shape of the initial ensemble. This characteristic reflects a type of internal order in the apparent chaos of nature and allows the mathematical modeling of complex shapes that cannot be described by traditional Euclidean geometry.

In the context of medical imaging, self-similarity is manifested by the structural repeatability of biological tissues at the macro, micro and subcellular levels. For example, vascular networks, neuronal arborizations or tumor edges present similar hierarchical patterns at various scales, which justifies the use of fractal analysis in their characterization. By quantifying the degree of self-similarity, subtle variations in tissue architecture can be identified, relevant for the early diagnosis of tumor formations and for the differentiation between normal and pathological tissues.

4. FRACTAL DIMENSION

Fractal dimension is an extension of the concept of Euclidean dimension, providing a quantitative tool for describing the geometric complexity of an object. In classical geometry, the dimension of a point is 0, of a line is 1, of a plane is 2, and of a volume is 3. However, many natural forms – such as the edges of clouds, the contours of ribs, vascular networks, or the edges of tumors – cannot be strictly confined to one of these integer dimensions. They partially occupy space, lying between two successive Euclidean dimensions, which requires the introduction of a fractional dimension.

Thus, the fractal dimension D quantifies how an object fills space depending on the scale of observation. In the case of self-similar objects, it can be defined by the general relation:

$$N(r) = k \cdot r^{-D}$$

where $N(r)$ represents the number of similar parts needed to describe the object at a scale r, k is a proportionality constant, and D is the fractal dimension.

By applying the logarithm to both sides of the relationship, the practical calculation expression is obtained:

$$D = -\frac{log\, N(r)}{log\, r} \Leftrightarrow D = \frac{log\, N(r)}{log\, (1/r)}$$

In other words, the size of an object is:

$$D = \frac{log(number\ of\ self-similar\ copies)}{log\ (scaling\ factor)}$$

5. BOX-COUNTING METHOD

The Box-Counting method is one of the most widely used and efficient techniques for estimating the fractal dimension of digital objects. Its major advantage lies in its simplicity, robustness, and universal

applicability — it can be implemented directly on two-dimensional (2D) or three-dimensional (3D) images, without requiring explicit analytical formulas of the studied object.

The basic principle of the method consists in covering the object (or the region of interest in an image) with a grid of squares (in 2D) or cubes (in 3D), each having a dimension r. It is then counted how many of these coverage units contain at least part of the object. As the dimension r decreases, an increasing number of occupied units are obtained, and the relationship between them provides an estimate of the spatial complexity of the object.

$$D = \lim_{r \longrightarrow 0} \frac{log\ N(r)}{log(\ 1/r)}$$

6. BOX-COUNTING ALGORITHM

Step 1. Structure coverage

The analyzed structure is placed in a grid of squares of equal side, denoted by r. Then the number of squares containing at least part of the object (pixels belonging to the structure) is counted. This number is denoted by $N(r)$.

Step 2. Progressive change of scale

The size of the square r changes progressively, decreasing at each step (for example, by half). For each value of r, the corresponding $N(r)$ is determined. This results in a series of pairs $(r_i, N(r_i))$, with $i = 0, 1, 2, .. k$

Step 3. Graph representation

The diagram (graph) is constructed in logarithmic coordinates, in which it is represented: $log\ N(r) = f(log(\ 1/r))$

If the object has a fractal structure, the experimental points align approximately on a straight line. The slope of this straight line is determined by linear regression and represents the Box-Counting dimension.

7. FRACTALS IN MEDICINE

Throughout history, the structures and functions of the human body have been studied through various empirical and experimental techniques, designed to confirm the proper functioning of the body or to identify the presence of certain diseases. Currently, with the development of information technology and computerized imaging, these analysis processes have transformed into a complex field, based on the digital processing of medical images (MRI, CT, PET, ultrasound).

The anatomical components and biological systems of the body can be described by mathematical models that capture their internal organization, the degree of complexity and the evolution over time. In this context, fractal analysis provides a unified framework for the mathematical modeling of irregular biological forms and processes, such as blood vessels, neuronal arborizations or tumor cell proliferations.

The fractal properties of these structures — self-similarity, controlled irregularity and hierarchical complexity — can be quantified through the fractal dimension, which reflects the level of spatial organization of tissues. Thus, fractal analysis allows not only the static characterization of an anatomical formation, but also the realization of predictions regarding the evolution of the disease based on the observed changes in the fractal dimension over time.

By applying fractal algorithms to medical images, maps of tissue complexity can be constructed, useful for:

- identifying areas with pathological potential,
- differentiating between healthy and affected tissues,
- monitoring the evolution of a tumor under treatment,
- estimating the degree of malignancy or invasiveness.

In particular, methods based on the Box-Counting algorithm have proven extremely effective in the analysis of tumor contours, vascular networks and cellular textures. They can transform complex visual information from medical images into a precise numerical representation, which can be subsequently integrated into machine learning models for computer-assisted diagnosis.

8. FRACTAL DIMENSION MAP

It is a method for spatial visualization and analysis of the complexity of a medical image. The concept derives directly from the local calculation of the fractal dimension, extended to the pixel or voxel level, to obtain a two-dimensional or three-dimensional distribution of fractal values over the entire analyzed region.

Unlike the global estimate of the fractal dimension – which provides a single value for the entire structure, the fractal dimension map allows highlighting local variations in complexity. This becomes a valuable tool in the analysis of biological tissues, as it allows the identification of areas with abnormal behavior from a structural point of view, even before the changes are visible at the macroscopic level.

For a digital medical image $I(x, y)$, the process of constructing the fractal dimension map is carried out in several steps:

1. Image segmentation
   The region of interest corresponding to the analyzed tissue is extracted. Segmentation can be manual, semi-automatic or automatic, depending on the type of data.
2. Calculating the local fractal dimension
   For each pixel (x, y)in the region of interest, a local window $W(x, y)$ of fixed size is defined.
   The Box-Counting method is applied to this window to estimate the local fractal dimension.
3. Fractal map construction
   A matrix $D(x, y)$ is formed containing the local fractal values for each position in the image. This can be visualized as a color map, where the shades encode the level of complexity.
4. Statistical analysis and clinical interpretation
   Global and local descriptors, such as mean, standard deviation, fractal entropy or spatial distribution of $D(x, y)$values, can be extracted from the fractal map. These parameters can be used for automatic tissue classification or for monitoring tumor progression.

9. CONCLUSIONS

The study presented herein demonstrates the strong connection between mathematical theory and medical imaging, highlighting how fractal geometry can serve as a powerful framework for modeling, quantifying, and interpreting the complex structures of biological tissues. Classical Euclidean geometry, limited to regular and smooth shapes, is inadequate for describing the irregular and self-similar morphologies found in nature and, in particular, within pathological tissues such as tumors.

By introducing the principles of self-similarity, metric contraction, and fixed-point theory, fractal geometry provides a rigorous mathematical foundation for analyzing natural complexity. The fractal dimension, as a quantitative descriptor of irregularity, enables the transformation of visual structural information into measurable data. Using the Box-Counting algorithm, this dimension can be efficiently estimated from digital medical images, revealing underlying morphological differences between healthy and tumorous regions.

Furthermore, the development of Fractal Dimension Maps (FDMs) allows for a local assessment of spatial complexity, producing detailed visualizations that highlight structural heterogeneity within tissues. These maps not only facilitate the early detection of pathological changes but also enable longitudinal monitoring of disease progression or therapeutic response. In clinical applications, higher fractal dimension values have been correlated with increased tissue disorganization, a hallmark of malignancy, thus offering an additional, objective biomarker for diagnostic systems.

10. BIBLIOGRAPHY

[1] Mircea Olteanu, FRACTALI

[2] Mihai-Virgil Nichita, Haos determinist și fractali în modelarea rețelelor complexe

[3] Maier, T., Kulichova, D., Schotten, K., Astrid, R., Ruzicka, T., Berking, C., & Udrea, A. (2015). Accuracy of a smartphone application using fractal image analysis of pigmented moles compared to clinical diagnosis and histological result. *Journal of the European Academy of Dermatology and Venereology : JEADV*, *29*(4), 663–667. https://doi.org/10.1111/jdv.12648

[4] Michallek, F., Nakamura, S., Ota, H. *et al.* Fractal analysis of 4D dynamic myocardial stress-CT perfusion imaging differentiates micro- and macrovascular ischemia in a multi-center proof-of-concept study. *Sci Rep* **12**, 5085 (2022). https://doi.org/10.1038/s41598-022-09144-6

[5] Michallek, F., Haouari, M.A., Dana, O. *et al.* Fractal analysis improves tumour size measurement on computed tomography in pancreatic ductal adenocarcinoma: comparison with gross pathology and multi-parametric MRI. *Eur Radiol* **32**, 5053–5063 (2022). https://doi.org/10.1007/s00330-022-08631-8

Design and mathematical modeling of a device for detecting and locating potentially dangerous sounds in the forest

Student: Kaan Nasurla
Scientific coordinator: PhD. Tania-Luminița Costache
Faculty of Automatic Control and Computer Science, University „POLITEHNICA” of Bucharest

Abstract

Annually, approximately 400 million cubic meters of wood are extracted from European forests (see Fig. 1), of which 30 million are from illegal actions. The objective of this paper is to find a solution for the rapid identification and localization of the position of a potentially dangerous object, using the Discrete Fourier Transform algorithm with time decimation, which plays a role in the frequency decomposition of sound, but also in geographic triangulation in order to locate the sound source in the forest with the best possible accuracy and precision. The work is developed from the point of view of both efficiency and redundancy. The complexity of the implementation was decisive in choosing the algorithm, and from an energy point of view, the device has a backup for extreme situations in which weather conditions in the area may affect the functionality in the optimal parameters. In addition, the device can also be used to monitor flora and fauna.

Keywords:

Discrete Fourier transform, triangulation, energy efficiency, solar panel, optimization, redundancy, discretization, bandpass filter, Newton-Raphson algorithm, Kalman filter;

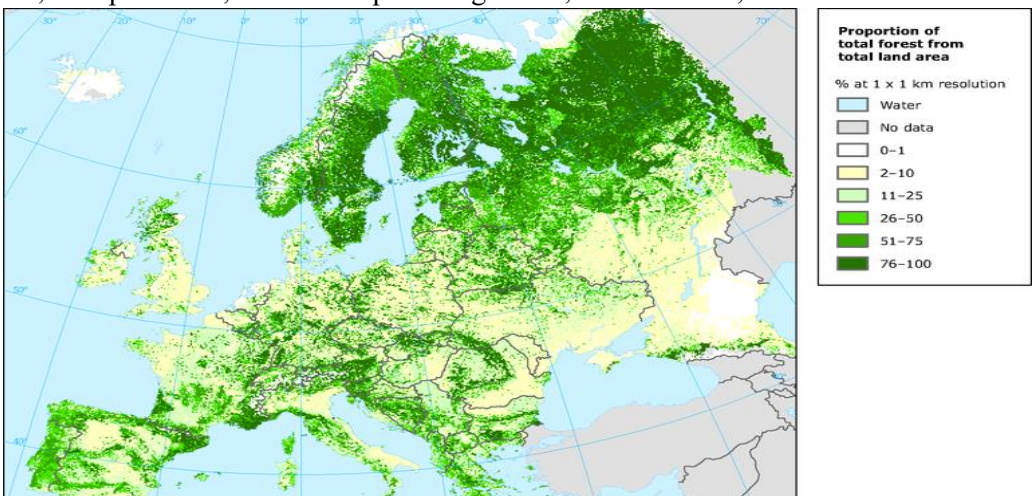

Fig 1. Forest map of Europe (~40% of Europe’s surface is forested)

Introduction

This paper aims to find a solution for the "cry for help" of forests, by modeling a device that can detect and locate potential outbreaks of illegal logging. In addition, with this device we can monitor flora and fauna in the forest, or other hard-to-reach areas.

Problem analyzed and objectives

Sinusoidal signals are the only ones that propagate undistorted through linear systems. But, in a case from everyday life, we are not faced with ideal cases, but continuous and periodic signals are not sinusoidal. In this case, the Fourier series expansion is applied, which decomposes the signal into a sum of sinusoidal signals, which have the following properties: they can be amplified, attenuated, phase-shifted. Thus, any continuous and periodic signal, of period T, for example $A\ sin(\omega t + \varphi)$, where $\omega = \frac{2\pi}{T}$ is the frequency, can be expanded in Fourier series:

$$f(t) = A_0 + \sum_{n=1}^{\infty} A_n\ sin(n\omega t + \varphi_n)$$

where A_0 is the continuous component, A_n is the amplitude of the sinusoid of order n, φ_n is the initial phase of the sinusoid of order n. Following the development of terms according to the formula $sin(a + b)$, results:

$$f(t) = a_0 + \sum_{n=1}^{\infty} a_n\ cos(n\omega t)\ +\ b_n\ sin(n\omega t)$$

where $a_0 = \frac{1}{2\pi}\int_{-\pi}^{\pi} f(t)\ dt$, $a_n = \frac{1}{\pi}\int_{-\pi}^{\pi} f(t)cos(nt)\ dt$ and $b_n = \frac{1}{\pi}\int_{-\pi}^{\pi} f(t)sin(nt)\ dt$ are called Euler-Fourier formulas.

The signal $f(t)$ is composed of several harmonics that have a frequency that is an integer multiple of the fundamental frequency. Fundamental frequency is $\omega_0 = \frac{1}{T_0}$, and the frequency of the k-order sinusoid is $\omega_k = k \cdot \omega_0$, so the signal can be decomposed:

$$f(t) = A_0 + \underbrace{A_1 sin\ (\omega_0 t + \varphi_1)}_{\text{Fundamental harmonic}} + \underbrace{A_2 sin\ (2\omega_0 t + \varphi_2)}_{\text{2nd harmonic}} + \cdots + \underbrace{A_n sin\ (n\omega_0 t + \varphi_n)}_{\text{Harmonic of order n}}$$

My solution

The device has a compact shape, which can be easily placed on the crown of trees. Being an autonomous device, connections with the control center are made via radio waves, via the telecommunications network, since the central board has a SIM card. As shown in figure 2, during transmitter → receiver we will use both the Fourier transform to move to the frequency domain, and the Fourier inversion formula to return to the time domain, at the moment of receiving the signal.

Denoting by $\mathcal{L}^1(\mathbb{R})$ the set of functions $f: \mathbb{R} \to \mathbb{R}$ for which $\int_{-\infty}^{\infty} |f(t)|\, dt < \infty$, Fourier transform of the function $f \in \mathcal{L}^1(\mathbb{R})$ is a function $\mathcal{F}[f]: \mathbb{R} \to \mathbb{C}$, where:

$$\mathcal{F}[f(t)](\omega) = \int_{-\infty}^{\infty} f(t) e^{-i\omega t} dt$$

Let $f: \mathbb{R} \to \mathbb{R}$ and $f \in \mathcal{L}^1(\mathbb{R})$ and noting with $\mathcal{F}[f(t)](\omega)$ the Fourier transform of f and assuming that $\int_{-\infty}^{\infty} |\mathcal{F}[f(t)](\omega)|\, d\omega < \infty$, the Fourier inversion formula results:

$$f(t) = \frac{1}{2\pi} \int_{-\infty}^{\infty} \mathcal{F}[f(t)](\omega) e^{i\omega t}\, d\omega;\ for\ \forall\, t \in \mathbb{R}$$

Fig 2. Using the Fourier transform and inversion formula on the transmitter-receiver path

Audio signal processing methods

Any signal is made up of sinusoids, and the set of these is the signal spectrum. The latter is determined using the Fourier series expansion for periodic signals (waveform of sin(x) in Fig. 3) and the Fourier Transform for non-periodic ones (waveform of sa(x) in Fig. 3). Signals are determined by their representation in the time domain, as a waveform, but also in the frequency domain, as a spectrum. The result is fundamental in signal and systems theory, because it is a method of representing analog signals, by knowing only a discrete number of its values, like Fig. 4.

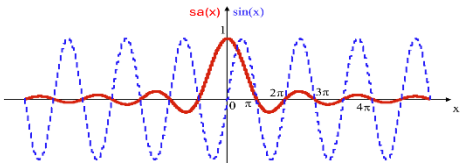

Fig 3. Waveforms of the sa(x) and sin(x) signals for comparision

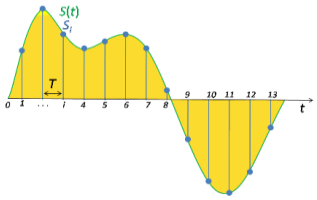

Fig 4. T-step sampled signal

In the context of detecting and locating potentially dangerous sounds in the forest environment, one of the essential steps in signal processing is its filtering to eliminate unwanted components and highlight relevant features. An effective filter used in such applications is the band-pass filter (see Fig. 5), which allows frequencies from a specific range to pass and attenuates the rest of the spectrum. In the case of forests, where the environment is rich in background sounds, the band-pass filter contributes significantly to improving the signal-to-noise ratio.

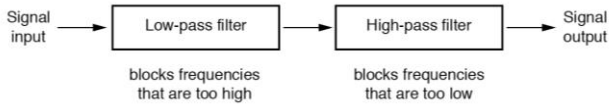

Fig 5. Bandpass filter block diagram

Discrete Fourier Transform

The signals captured by the device are non-periodic, being the composition of several signals. (see Fig. 6) Therefore, for the spectral analysis of the signal, the Fourier transform will be used, which allows us to move from the time domain to the frequency domain. This process will need to be implemented on the computer, so we must use a method that is as efficient as possible (which consumes as few computer resources as possible). Therefore, for the above calculation, we will write $x[n]$ the finite signal to which we will apply the discrete Fourier transform, and $X[n]$ is the sample of the spectrum $x[n]$ at frequency k, it results (see Fig. 7):

$$X[n] = \sum_{n=0}^{N-1} x[n] \cdot e^{-i\frac{2\pi nk}{N}};\ n = \overline{0, N-1}$$

The formula can also be written in matrix form $W \cdot x = X$, in this way:

$$\begin{pmatrix} 1 & 1 & 1 & \cdots & \cdots & 1 \\ 1 & \omega & \omega^2 & \cdots & \cdots & \omega^{N-1} \\ 1 & \omega^2 & \omega^4 & \cdots & \cdots & \omega^{2(N-1)} \\ \vdots & \vdots & \vdots & \ddots & & \vdots \\ \vdots & \vdots & \vdots & & \ddots & \vdots \\ 1 & \omega^{N-1} & \omega^{2(N-1)} & \cdots & \cdots & \omega^{(N-1)^2} \end{pmatrix} \cdot \begin{pmatrix} x[0] \\ x[1] \\ x[2] \\ \vdots \\ x[N-1] \end{pmatrix} = \begin{pmatrix} X[0] \\ X[1] \\ X[2] \\ \vdots \\ X[N-1] \end{pmatrix}$$

where $\omega = e^{-i\frac{2\pi}{N}}$, so $|\omega| = 1$ and $\overline{\omega} = \frac{1}{\omega}$. From here, results $W \cdot \overline{W} = \overline{W} \cdot W = \frac{1}{N} \cdot I_N$, where I_N is the identity matrix of order *N,* and $\overline{W}$ is the matrix with the conjugate elements of W. Then, W is an invertible matrix with $W^{-1} = \frac{1}{N} \cdot \overline{W}$.

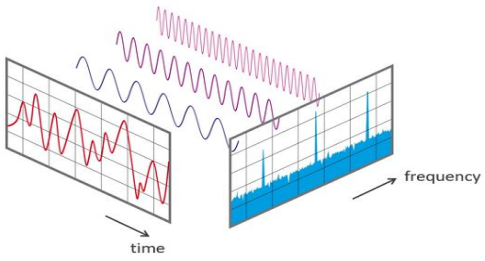

Fig 6. Decomposition of a time-domain sinusoid into multiple frequency-domain sinusoids

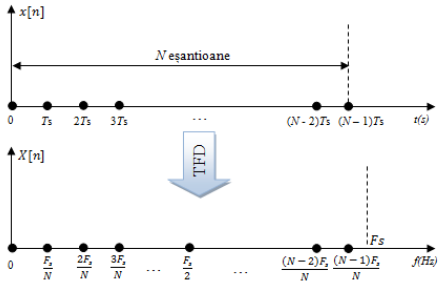

Fig 7. Fourier transform of a signal x[n]

Fast Fourier Transform (FFT) Algorithm

When we talk about the Fast Fourier Transform algorithm, we distinguish two implementation modes: time decimation and frequency decimation. This process involves reducing the sampling rate of a digital signal (see Fig. 8).

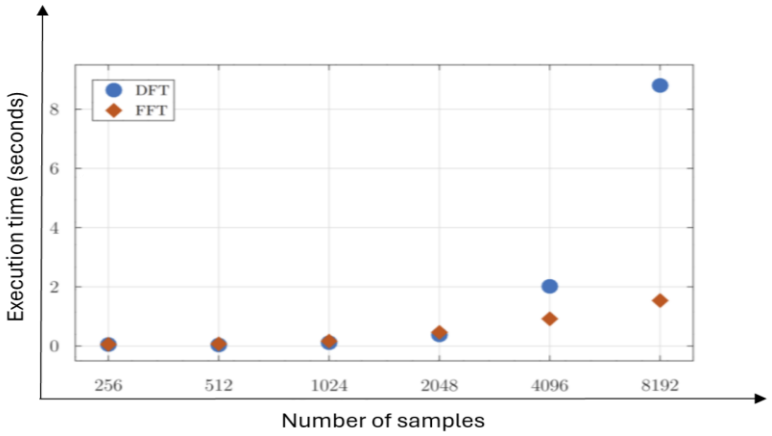

Fig 8. Difference between execution time of the FFT algorithm compared to the DFT algorithm if the number of samples increases

In the first case (see Fig. 10), to achieve time decimation, the first half of the spectrum and the second half of the spectrum are calculated separately. For each spectral sample, the calculations are performed on the signal represented in time decimated in two, thus separating the even and odd elements:

$$X(k) = \sum_{n=0}^{N-1} x(n) \cdot e^{-i\frac{2\pi}{N}kn}, \qquad k = \overline{0, \frac{N}{2} - 1}$$

$$X(k) = \sum_{n=0}^{\frac{N}{2}-1} x(2n) \cdot e^{-i\frac{2\pi}{N}k2n} + \sum_{n=0}^{\frac{N}{2}-1} x(2n+1) \cdot e^{-i\frac{2\pi}{N}k(2n+1)}$$

By grouping the coefficients, we can see that the equation simplifies to a Fourier transform operation on a half-sequence:

$$X(k) = \sum_{n=0}^{\frac{N}{2}-1} x(2n) \cdot e^{-i\frac{2\pi}{N}2kn} + \sum_{n=0}^{\frac{N}{2}-1} x(2n+1) \cdot e^{-i\frac{2\pi}{N}2kn} \cdot e^{-i\frac{2\pi}{N}k}$$

$$X(k) = \underbrace{\sum_{n=0}^{\frac{N}{2}-1} x(2n) \cdot e^{-i\frac{2\pi}{\frac{N}{2}}kn}}_{X_{even}(k)} + \underbrace{\sum_{n=0}^{\frac{N}{2}-1} x(2n+1) \cdot e^{-i\frac{2\pi}{\frac{N}{2}}kn}}_{X_{odd}(k)} \cdot e^{-i\frac{2\pi}{N}k}$$

I noted with $X_{even}(k)$ discrete Fourier transform of the even components of the sequence $x(n)$, and with $X_{odd}(k)$ on the one corresponding to the odd components. Therefore, to determine the first half of the Fourier transform of the signal x, it is necessary to calculate the transforms of the even and odd samples separately and to sum them.

$$X(k) = X_{even}(k) + X_{odd}(k) \cdot e^{-i\frac{2\pi}{N}k}, \qquad k = \overline{0, \frac{N}{2} - 1}$$

Now, we will apply the same decimation for the upper half of the spectrum, but modifying the range of k to have a formula compatible with the calculated half:

$$X(k) = \sum_{n=0}^{N-1} x(n) \cdot e^{-i\frac{2\pi}{N}kn}, \qquad k = \overline{0, \frac{N}{2} - 1}$$

$$X(k + \frac{N}{2}) = \sum_{n=0}^{N-1} x(n) \cdot e^{-i\frac{2\pi}{N}(k+\frac{N}{2})n}, \qquad k = \overline{0, \frac{N}{2} - 1}$$

Then, we rearrange the coefficients similarly to the first part:

$$X\left(k + \frac{N}{2}\right) = \sum_{n=0}^{\frac{N}{2}-1} x(2n) \cdot e^{-i\frac{2\pi}{N}\left(k+\frac{N}{2}\right)2n} + \sum_{n=0}^{\frac{N}{2}-1} x(2n+1) \cdot e^{-i\frac{2\pi}{N}\left(k+\frac{N}{2}\right)(2n+1)}$$

$$= \sum_{n=0}^{\frac{N}{2}-1} x(2n) \cdot e^{-i\frac{2\pi}{N}2kn} \cdot e^{-i\frac{2\pi}{N}\frac{N}{2}2n} + \sum_{n=0}^{\frac{N}{2}-1} x(2n+1) \cdot e^{-i\frac{2\pi}{N}2kn} \cdot e^{-i\frac{2\pi}{N}\frac{N}{2}2n} \cdot e^{-i\frac{2\pi}{N}k} e^{-i\frac{2\pi}{N}\frac{N}{2}}$$

$$= \sum_{n=0}^{\frac{N}{2}-1} x(2n) \cdot \underbrace{e^{-i2\pi n}}_{1} + \sum_{n=0}^{\frac{N}{2}-1} x(2n+1) \cdot e^{-i\frac{2\pi}{\frac{N}{2}}kn} \cdot \underbrace{e^{-i2\pi n}}_{1} \cdot e^{-i\frac{2\pi}{N}k} \cdot \underbrace{e^{-i\pi}}_{-1}$$

$$X\left(k + \frac{N}{2}\right) = \underbrace{\sum_{n=0}^{\frac{N}{2}-1} x(2n) \cdot e^{-i\frac{2\pi}{\frac{N}{2}}kn}}_{X_{even}(k)} - \underbrace{\sum_{n=0}^{\frac{N}{2}-1} x(2n+1) \cdot e^{-i\frac{2\pi}{\frac{N}{2}}kn}}_{X_{odd}(k)} \cdot e^{-i\frac{2\pi}{N}k}$$

Thus, the discrete Fourier transform of a signal can be rewritten by the following formula, where ω_N^k are the *N*-th order roots of unity:

$$\begin{cases} X(k) = X_{even}(k) + \omega_N^k \cdot X_{odd}(k) \\ X\left(k + \frac{N}{2}\right) = X_{even}(k) - \omega_N^k \cdot X_{odd}(k) \end{cases}; \quad k = \overline{0, \frac{N}{2} - 1}$$

This formula can be represented graphically as "butterfly wings":

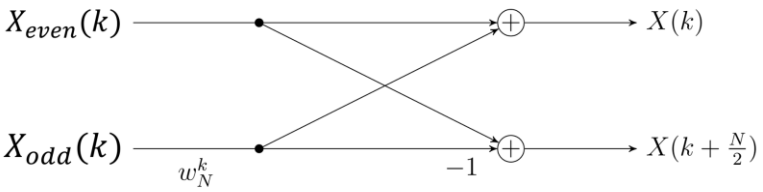

Fig 9. ,,Butterfly" graph in case of time decimation

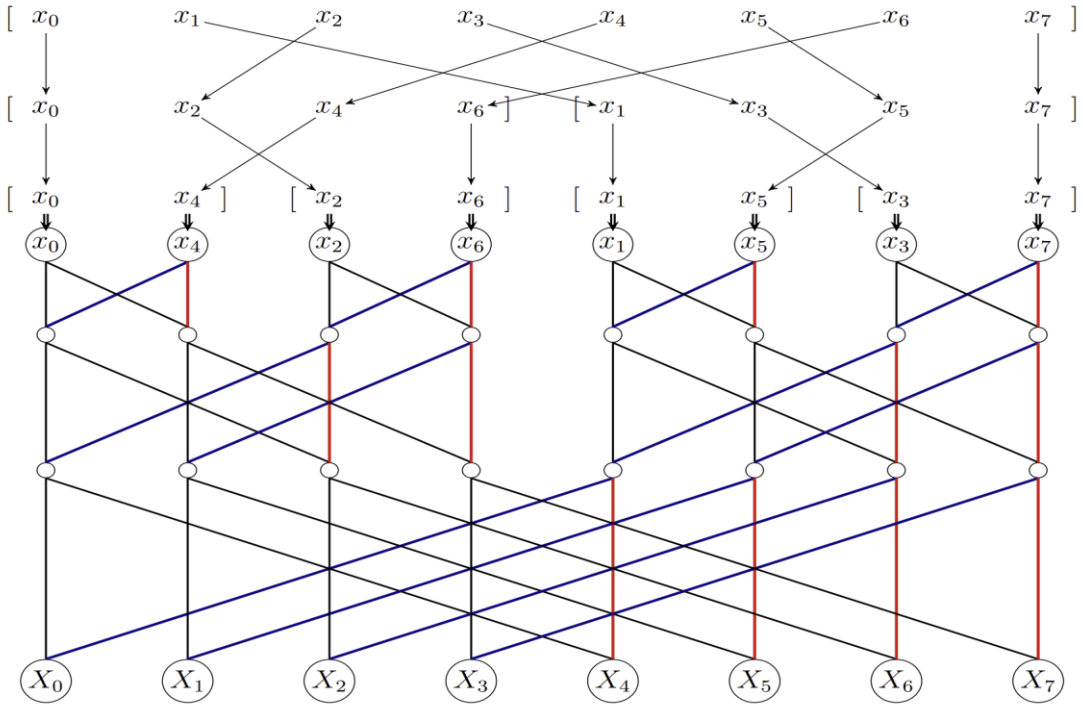

Fig 10. Calculation graph of FFT with time decimation for 8 samples

In the second case, to reduce the execution time of the Discrete Fourier Transform, decimation is performed in the transformed domain. Thus, we will develop the even and odd terms separately.

$$\begin{cases} X(2k) = \sum_{n=0}^{N-1} x(n) \cdot e^{-i\frac{2\pi}{N}2kn} \\ X(2k+1) = \sum_{n=0}^{N-1} x(n) \cdot e^{-i\frac{2\pi}{N}(2k+1)n} \end{cases} ; \; k = \overline{0, \frac{N}{2} - 1}$$

Next, we proceed similarly to the decimation in time, only this time we expand the equations into lower halves and upper halves. For the even terms we will have:

$$X(2k) = \sum_{n=0}^{\frac{N}{2}-1} x(n) \cdot e^{-i\frac{2\pi}{N}2kn} + \sum_{n=\frac{N}{2}}^{N-1} x(n) \cdot e^{-i\frac{2\pi}{N}2kn}$$

$$= \sum_{n=0}^{\frac{N}{2}-1} x(n) \cdot e^{-i\frac{2\pi}{N}2kn} + \sum_{n=0}^{\frac{N}{2}-1} x(n+\frac{N}{2}) \cdot e^{-i\frac{2\pi}{N}2k(n+\frac{N}{2})}$$

$$= \sum_{n=0}^{\frac{N}{2}-1} x(n) \cdot e^{-i\frac{2\pi}{N}2kn} + \sum_{n=0}^{\frac{N}{2}-1} x(n+\frac{N}{2}) \cdot e^{-i\frac{2\pi}{N}2kn} \cdot e^{-i\frac{2\pi}{N}2k\frac{N}{2}}$$

$$= \sum_{n=0}^{\frac{N}{2}-1} x(n) \cdot e^{-i\frac{2\pi}{N}2kn} + \sum_{n=0}^{\frac{N}{2}-1} x(n+\frac{N}{2}) \cdot e^{-i\frac{2\pi}{N}2kn} \cdot e^{-i2\pi k}$$

$$= \underbrace{\sum_{n=0}^{\frac{N}{2}-1} x(n) \cdot e^{-i\frac{2\pi}{\frac{N}{2}}kn}}_{X_{inf}(k)} + \underbrace{\sum_{n=0}^{\frac{N}{2}-1} x(n+\frac{N}{2}) \cdot e^{-i\frac{2\pi}{\frac{N}{2}}kn}}_{X_{sup}(k)}$$

It can be seen that, practically, the even terms of a Fourier transform can be calculated as the simple sum of the Fourier transform of the first half of the vector with the Fourier transform of the second half of the vector.

$$X(2k+1) = \sum_{n=0}^{\frac{N}{2}-1} x(n) \cdot e^{-i\frac{2\pi}{N}(2k+1)n} + \sum_{n=\frac{N}{2}}^{N-1} x(n) \cdot e^{-i\frac{2\pi}{N}(2k+1)n}$$

$$= \sum_{n=0}^{\frac{N}{2}-1} x(n) \cdot e^{-i\frac{2\pi}{N}(2k+1)n} + \sum_{n=0}^{\frac{N}{2}-1} x(n+\frac{N}{2}) \cdot e^{-i\frac{2\pi}{N}(2k+1)(n+\frac{N}{2})}$$

$$= \sum_{n=0}^{\frac{N}{2}-1} x(n) \cdot e^{-i\frac{2\pi}{N}2kn} \cdot e^{-i\frac{2\pi}{N}n} + \sum_{n=0}^{\frac{N}{2}-1} x(n+\frac{N}{2}) \cdot e^{-i\frac{2\pi}{N}2kn} \cdot e^{-i\frac{2\pi}{N}2k\frac{N}{2}} \cdot e^{-i\frac{2\pi}{N}n} \cdot e^{-i\frac{2\pi}{N}\frac{N}{2}}$$

$$= \sum_{n=0}^{\frac{N}{2}-1} x(n) \cdot e^{-i\frac{2\pi}{N}2kn} \cdot e^{-i\frac{2\pi}{N}n} + \sum_{n=0}^{\frac{N}{2}-1} x(n+\frac{N}{2}) \cdot e^{-i\frac{2\pi}{N}2kn} \cdot e^{-i2\pi k} \cdot e^{-i\frac{2\pi}{N}n} \cdot e^{-i\pi}$$

$$= \underbrace{\sum_{n=0}^{\frac{N}{2}-1} x(n) \cdot e^{-i\frac{2\pi}{\frac{N}{2}}kn} \cdot e^{-i\frac{2\pi}{N}n}}_{X_{inf}(k)} - \underbrace{\sum_{n=0}^{\frac{N}{2}-1} x(n+\frac{N}{2}) \cdot e^{-i\frac{2\pi}{\frac{N}{2}}kn} \cdot e^{-i\frac{2\pi}{N}n}}_{X_{sup}(k)}$$

Thus, the discrete Fourier transform of a signal can be rewritten by the following formula, where ω_N^k are the N-th order roots of unity:

$$\begin{cases} X(2k) = X_{inf}(k) + X_{sup}(k) \\ X(2k+1) = X_{inf}(k) \cdot \omega_N^k - X_{sup}(k) \cdot \omega_N^k \end{cases}$$

In order to apply this formula we must multiply by the coefficients ω_N^k during the calculation of the half-sequences and not after these calculations have been made. This means that we will have to approach an iterative calculation, starting from sequences consisting of a single element and at each step moving to a sequence of double length. This iterative approach can be followed on the following butterfly (see Fig. 11).

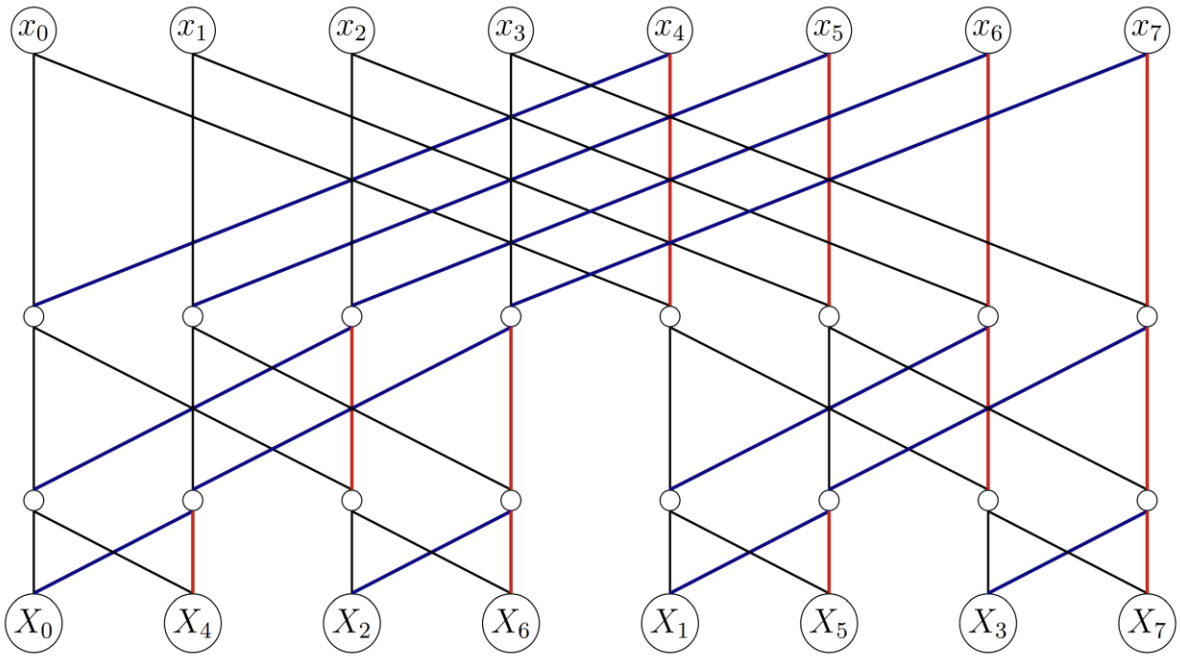

Fig 11. Calculation graph of FFT with frequency decimation for 8 samples

Localization concepts and methods

In general, for locating a stationary sound source, the Time Difference of Arrival (TDOA) method tends to be the most efficient and stable method in most practical applications.

If we consider three-dimensional space, the 3 sensors S_1, S_2 și S_3 with the coordinates (x_1, y_1, z_1), (x_2, y_2, z_2), respectively (x_3, y_3, z_3) and the unknown position of the sound source P given by (x_p, y_p, z_p), we can measure arrival time differences (see Fig. 12):

$$\begin{cases} \Delta t_{21} = t_2 - t_1;\ of\ S_2 \text{ relative to } S_1 \\ \Delta t_{31} = t_3 - t_1;\ \text{of } S_3 \text{ relative to } S_1 \end{cases}$$

Let c the speed of sound propagation in air (considered constant), then the corresponding distance differences are $c \cdot \Delta t_{21} = d_2 - d_1$ and $c \cdot \Delta t_{31} = d_3 - d_1$, where d_i is the distance between the sound source $P\ (x_p,\ y_p,\ z_p)$ and the sensor $S_i\ (x_i,\ y_i,\ z_i)$:

$$\begin{cases} d_1 = \sqrt{(x_p - x_1)^2 + (y_p - y_1)^2 + (z_p - z_1)^2} \\ d_2 = \sqrt{(x_p - x_2)^2 + (y_p - y_2)^2 + (z_p - z_2)^2} \\ d_3 = \sqrt{(x_p - x_3)^2 + (y_p - y_3)^2 + (z_p - z_3)^2} \end{cases}$$

After substituting the expressions for d_i in the distance difference equations, we obtain a system of two nonlinear equations with three unknowns $x_p,\ y_p,\ z_p$:

$$\begin{cases} \sqrt{(x_p - x_2)^2 + (y_p - y_2)^2 + (z_p - z_2)^2} - \sqrt{(x_p - x_1)^2 + (y_p - y_1)^2 + (z_p - z_1)^2} = c \cdot \Delta t_{21} \\ \sqrt{(x_p - x_3)^2 + (y_p - y_3)^2 + (z_p - z_3)^2} - \sqrt{(x_p - x_1)^2 + (y_p - y_1)^2 + (z_p - z_1)^2} = c \cdot \Delta t_{31} \end{cases}$$

This system generally has an infinite number of solutions, which in this case form a curve in three-dimensional space, being the intersection of two hyperboloids. However, to obtain a unique solution, a third equation, independent of the two, would be needed.

To address this issue, we will introduce a fourth sensor $S_4\ (x_4,\ y_4,\ z_4)$, with which we will measure a third time difference $\Delta t_{41} = t_4 - t_1$, which leads us to $c \cdot \Delta t_{41} = d_4 - d_1$ and the appearance of the third equation. By doing so, the system of three nonlinear equations with three unknowns $x_p,\ y_p,\ z_p$ is:

$$\begin{cases} \sqrt{(x_p - x_2)^2 + (y_p - y_2)^2 + (z_p - z_2)^2} - \sqrt{(x_p - x_1)^2 + (y_p - y_1)^2 + (z_p - z_1)^2} = c \cdot \Delta t_{21} \\ \sqrt{(x_p - x_3)^2 + (y_p - y_3)^2 + (z_p - z_3)^2} - \sqrt{(x_p - x_1)^2 + (y_p - y_1)^2 + (z_p - z_1)^2} = c \cdot \Delta t_{31} \\ \sqrt{(x_p - x_4)^2 + (y_p - y_4)^2 + (z_p - z_4)^2} - \sqrt{(x_p - x_1)^2 + (y_p - y_1)^2 + (z_p - z_1)^2} = c \cdot \Delta t_{41} \end{cases}$$

The analytical solution of this system is complex and we will use numerical optimization methods, such as the Newton-Raphson method, to find an approximation of the solution of the system $(x_p,\ y_p,\ z_p)$. The system can be written in the form: $F(X) = 0$, where $X = \begin{bmatrix} x_p \\ y_p \\ z_p \end{bmatrix}$ is the vector of unknowns, and $F(X) = \begin{bmatrix} f_1(x,y,z) \\ f_2(x,y,z) \\ f_3(x,y,z) \end{bmatrix}$, where:

$$f_1(x,y,z) = \sqrt{(x_p - x_2)^2 + (y_p - y_2)^2 + (z_p - z_2)^2} - \sqrt{(x_p - x_1)^2 + (y_p - y_1)^2 + (z_p - z_1)^2} - c \cdot \Delta t_{21}$$

$$f_2(x,y,z) = \sqrt{(x_p - x_3)^2 + (y_p - y_3)^2 + (z_p - z_3)^2} - \sqrt{(x_p - x_1)^2 + (y_p - y_1)^2 + (z_p - z_1)^2} - c \cdot \Delta t_{31}$$

$$\begin{cases} f_3(x,y,z) = \sqrt{(x_p - x_4)^2 + (y_p - y_4)^2 + (z_p - z_4)^2} - \sqrt{(x_p - x_1)^2 + (y_p - y_1)^2 + (z_p - z_1)^2} - c \cdot \Delta t_{41} \end{cases}$$

Next, we will calculate the Jacobian defined as $J(X) = \begin{bmatrix} \frac{\partial f_1}{\partial x} & \frac{\partial f_1}{\partial y} & \frac{\partial f_1}{\partial z} \\ \frac{\partial f_2}{\partial x} & \frac{\partial f_2}{\partial y} & \frac{\partial f_2}{\partial z} \\ \frac{\partial f_3}{\partial x} & \frac{\partial f_3}{\partial y} & \frac{\partial f_3}{\partial z} \end{bmatrix}$.

Next, we will apply the iterative algorithm for solving systems of nonlinear Newton-Raphson equations: $X_{k+1} = X_k - [J(X_k)]^{-1} \cdot F(X_k)$, where X_k is the estimate of the solution at iteration k, X_{k+1} is the estimate of the solution at iteration $k+1$, $[J(X_k)]^{-1}$is the inverse of the Jacobian matrix evaluated in X_k, and $F(X_k)$ is the function evaluated in X_k. To begin with, it is necessary to choose an initial approximation X_0. A good choice of the initial estimate can help the algorithm converge quickly, thus improving computational efficiency. Since in the present situation we cannot indicate an ideal initial approximation, we will use the centroid of the sensor locations, $x_0 = \frac{x_1+x_2+x_3+x_4}{4}$, $y_0 = \frac{y_1+y_2+y_3+y_4}{4}$, $z_0 = \frac{z_1+z_2+z_3+z_4}{4}$. We will iterate through a loop: the calculation of $F(X_k)$, Jacobian calculation $J(X_k)$ followed by a check if it is invertible. Otherwise, we will choose another initial approximation. If it is invertible, we will calculate the inverse $[J(X_k)]^{-1}$ and we will update the solution estimate according to the formula $X_{k+1} = X_k - [J(X_k)]^{-1} \cdot F(X_k)$. A stop condition will be set $\| X_{k+1} - X_k \| < \varepsilon$.

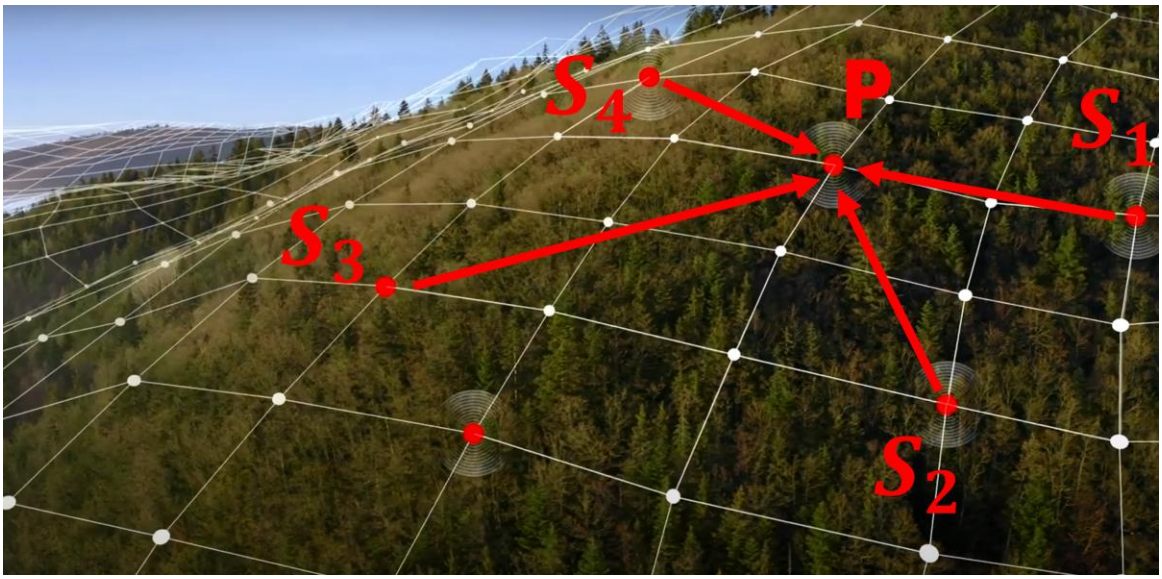

Fig 12. Localization method of the P (source of the sound) using 4 devices (S_1, S_2, S_3, S_4)

Design of the device

The device consists of two main components: the sound signal processing unit and the power source (see Fig.13). From an energetic point of view, the device is powered by solar panels that capture sunlight and store it in batteries, which are subsequently consumed by the system. On the other hand, the accumulators are designed for a high charge-discharge rate, and a full charge cycle is exhausted in about a week. The positioning at the top of the trees plays a special role, maximizing the rate of solar energy capture. The sound processing unit is sealed in a capsule, being protected from the weather and adverse weather conditions.

Fig 13. Design of the device: power source and sound signal processing unit

Improvements and future ideas

This paper aims to bring about a change in society, through its way of combating and minimizing illegal deforestation. In this sense, the system (see Fig. 14) is guided by the motto Lifelong learning, through which it wants to improve itself over time, keeping up with new technologies. Therefore, an album will be created with as many fingerprints of dangerous sounds as possible, in order to have a larger database, which allows the device to better identify dangerous sound sources.

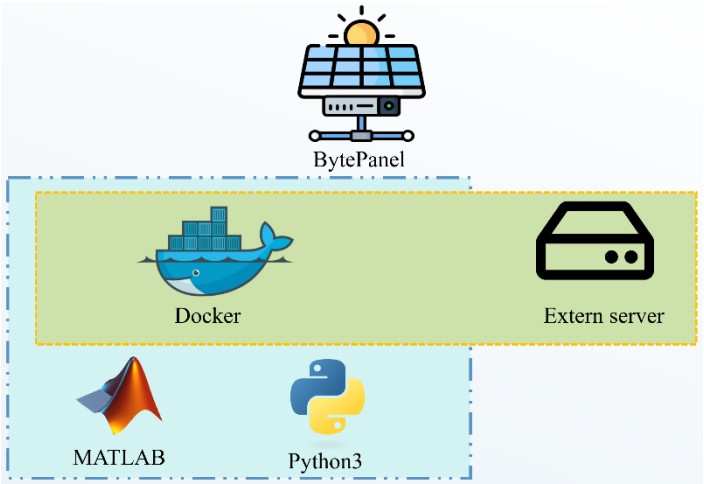

Fig 14. Organigram of the project and the software applications (MATLAB, Python3 and Docker)

Conclusion

This paper presented the design and implementation of a system for detecting and locating dangerous sounds in the forest environment, based on a network of devices that record and process sounds to classify them using the Fast Fourier Transform Algorithm, in illegal logging activities. For localization, an algorithm will be implemented that will detect the sound source based on the difference in time of arrival of the sound at at least four microphones, since a localization in three-dimensional space is desired. In order to find the geographical coordinates with the smallest possible error, the iterative Newton-Raphson algorithm for solving systems of nonlinear equations will be used, which, after a few iterations, will provide us with the position of the sound source with a moderate error.

Summarizing, we can conclude that the proposed system can reduce illegal logging activities by using computer resources effectively. During the research, several algorithms were presented in parallel, explaining their advantages, disadvantages, complexity and execution time of the calculations, the latter

being the decisive factor in the choice made. The project is also being developed to reduce measurement errors and to achieve identification with greater accuracy in the future.

Bibliography

[1] V. Branzanescu, O. Stanasila, Matematici speciale. Teorie, exemple, aplicatii, ALL, 1994

[2] T. L. Costache, Lectii de matematici speciale, Politehnica Press, 2017

[2] I. P. Mihu, C. Neghină, Prelucrarea Digitală a Semnalelor. Aplicații didactice în Matlab

[3] K. Csaba-Zoltán, Lucrarea de laborator 3, UNITBV

[4] E. Kreyszig, Advanced Engineering Mathematics, 10th edition

[5] Y. Kim, H. Ban, Introduction to Kalman Filter and Its Applications, 2019

[6] S. Ciochina, Prelucrarea numerică a semnalelor, UPB, 1996

[6] A. Mateescu, N. Dumitriu, L. Stanciu, Semnale și sisteme. Aplicații în filtrarea semnalelor, Teora, 2001

A Novel Approach to Solving Conformable Fractional 2D State Space Continuous-Time Linear Systems

Kamel BENYETTOU[1], Djillali BOUAGADA [2] and Mohammed Amine GHEZZAR[3]

[3]National $National Higher School of Mathematics, Scientific and Technology Hub of Sidi Abdellah, ACSY Team-Laboratory of Pure and Applied Mathematics (UMAB), P.O. Box 75, Algiers 16093, Algeria

[1,2]Abdelhamid Ibn Badis University Mostaganem, Department of Mathematics and Computer Science, ACSY Team-Laboratory of Pure and Applied Mathematics, Faculty SEI-BP 227/118 Mostaganem 27000, Algeria.

Corresponding author email: , kamel.benyettou@ univ-mosta.dz[1]

djillali.bouagada@univ-mosta.dz[2] amine.ghezzar@nhsm.edu.dz [3] ,

Abstract

This study addresses the solvability of two-dimensional (2D) dynamical models by introducing advanced tools based on fractional calculus and integral transforms. In particular, we investigate the application of newly defined fractional derivatives together with extended transform techniques tailored for a specific class of 2D systems. The proposed approach leverages both the two-dimensional Sumudu and Laplace transforms to obtain analytical solutions of continuous Fornasini–Marchesini models within the framework of conformable derivatives. Beyond solving the models, the work also establishes a novel formulation of the 2D Sumudu transform and explores its fundamental properties, thereby extending its applicability to multidimensional systems analysis. To illustrate the effectiveness and accuracy of the proposed methodology, a representative example is provided, highlighting not only the theoretical precision but also the practical feasibility of the developed techniques in handling complex 2D models.

Key words: *Two dimensional systems, Continuous systems Fractional Calculus, Conformable derivative, Fornasini-Marchesini Models*

1. INTRODUCTION

Two dimensional (2D) models appear and play a key role in several areas, more particularly in engineering, control theory and also in digital and image processing, fluid dynamics, mechanics and physics. Note that 2D models propagate the information in two independent directions and they have received considerable reaserch attention.

Fractional calculus can be defined as the generalization of a classical calculus of integration and differentiation not necessarily integer. It was a matter of almost exclusive interest for few mathematicians and theoretical physicist in several applications and domains. Many efforts have been done to develop fractional dynamical systems in finite and infinite dimensions, originated with the fundamental papers and monographs. However, considerable attention has, recently, been paid to the two dimensional fractional systems by the development of a mathematical framework to generalize a number of research works.

In recent years there has been a growing interest to develop this class of models where the considered derivatives is called a conformable fractional derivatives. Many efforts have been done to develop some properties of the considered derivatives and are presented in by Khalil and Abdeljawed in 2014 and 2015.

For this purpose, the main aim of this study is to propose a new method to solve the problem of the solvability for the $2D$ Fornasini- Marchesini models. The partial fractional order derivatives of a 2D continuous functions based on the conformable derivative is given.

The 2D conformable Laplace transform and some properties are used to solve the class of the first form of Fornasini-Marchesini models.

Indeed, in the beginning, throught some properties and new definitions of the 2D conformable Sumudu transform, three theorems and lemma are proposed with proofs.

2. CONTENT

Let us consider the continuous 2D Fornasini-Marchesini fractional (α, β) -order model described by the state-space equations :

$$\mathrm{T}_{t_1,t_2}^{\alpha,\beta}\mathrm{x}(t_1,t_2) = \mathrm{A}_0\mathrm{x}(t_1,t_2) + \mathrm{A}_1\mathrm{T}_{t_1}^{\alpha}\mathrm{x}(t_1,t_2) + \mathrm{A}_2\mathrm{T}_{t_2}^{\beta}\mathrm{x}(t_1,t_2) + \mathrm{Bu}(t_1,t_2)$$

where $\$x(t_1,t_2) \in R^n\$$ is the state vector, $\$u(t_1,t_2) \in R^m\$$ is the input vector and $A_i \in R^{n\times n}, i = 0.1.2, B \in R^{n\times m}$, the boundary conditions $\mathrm{x}(0,t_2)$ and $x(t_1,0)$ are given.

3. CONCLUSIONS

In this work, we investigated the interesting problem of the computation of the solution of the continuous Fornasini-Marchesini type model in its first and second forms containing partial fractional-order derivatives described by the conformable derivative. First, The solution has been derived using 2D Laplace transform and in the second part, the conformable double Sumudu transform has been defined with some properties to solve the considered class of model. It must be emphasized that the presented methods are exhaustive study of the calculation of the solutions of a 2D fractional class. An illustrative example has been given to show the accuracy and the applicability of the proposed approach.

The Convergence of the JN Relaxed Algorithm for Convection-Diffusion Cauchy Problems

Khalifa BOUMZOUGH[1], Adnane AZZOUZI[2], Abdeljalil NACHAOUI[3]

[1]Engineering of Sciences Laboratory, Faculty of Sciences Agadir, Ibn Zohr University, B.P 8106, Agadir, 80000, Souss-Massa, Morocco.

[2]Laboratory of Modeling, Applied Mathematics and Intelligent Systems (L2MASI), Faculty of Sciences Dhar El Mahraz, Sidi Mohmed ben Abdellah University, B.P 1796 Atlas, Fez, 30 000, Fez-Meknes, Morocco.

[3]Jean Leray Mathematics Laboratory, Nantes University, Nantes, France.

Corresponding author email: khalifa.miasi@gmail.com

Abstract

We introduce the JN relaxed algorithm to solve the Cauchy problem for convection-diffusion equations in a bounded domain. The algorithm iteratively updates mixed boundary conditions using a relaxation parameter to improve convergence. We establish theoretical convergence criteria and show that optimal parameter choices accelerate the algorithm compared to standard methods like the KMF algorithm. This approach offers a robust solution for applications in fluid dynamics and heat transfer.

Key words*: Inverse Cauchy Problem; convection-diffusion equation; JN relaxed algorithm; convergence analysis; KMF algorithm; iterative methods.*

UNDERSTANDING XYLELLA FASTIDIOSA SPREAD IN OLIVE TREES THROUGH DELAY DIFFERENTIAL MODELING

Mohammed El Amine KISSI[1], Abdelkader LAKMECHE[1], Andrei HALANAY[2], Bedreddine AINSEBA[3], Mohammed BOUIZEM[4], Mohamed HELAL[1]

[1]Biomathematics Laboratory, Univ. Sidi Bel Abbes, 22000, Algeria.
[2]University Politehnica of Bucharest, 313 Splaiul Independentei, District 6, Bucharest, Romania. [3]
Univ. Bordeaux IMB, UMR CNRS 5251 33076, France.
[4]University Abou Bekr Belkaid, Tlemcen, 13000, Algeria
Corresponding author email: aminekissi3@gmail.com

***Abstract:** In this work, we study the dynamics of a mathematical model describing the spread of Xylella fastidiosa disease in an olive orchard. We begin by introducing an age-structured model composed of two equations: an ordinary differential equation (ODE) describing the evolution of healthy olive trees, and a partial differential equation (PDE) modeling infected olive trees according to their age of infection. Referring to the work of P. Magal ([1]), this system is reduced to a delay differential equations model, where a delay term appears on the infected olive trees variable. We show that this model is well-posed and establish the existence of two equilibrium points: the disease-free equilibrium and the endemic equilibrium. An analysis of local stability is carried out, and for the disease-free equilibrium, a global stability analysis is performed using a Lyapunov-Krasovskii functional, using the basic reproduction number R0 depending on the delay τ . This number depends also in particular on the implantation rate Λ as well as on the mortality rates of healthy, infected and uprooted olive trees. Finally, numerical simulations illustrate the theoretical results obtained, followed by a conclusion.*

***Key words**: Xylella Fastidiosa, Hybrid mathematical model, Partial differential equation, Ordinary differential equation, Steady states, Local and global stability, Numerical simulations.*

1. INTRODUCTION

Xylella Fastidiosa is a Gram-negative bacterium that can cause diseases in a wide range of plants, including grapevines, citrus, and olive trees. This bacterium is considered a major threat to forestry and agricultural industries worldwide, as it can cause significant economic losses by damaging crops and trees. The transmission of Xylella Fastidiosa is caused by the insects such as sharpshooters and spittlebugs. Once inside the plant, the bacterium colonizes the xylem vessels, which are responsible for transporting water and nutrients throughout the plant. We are interested by the study of a hybrid mathematical model that describes the dynamic of the Xylella Fastidiosa disease. We consider, at first that the disease is transmitted from olive tree to an other one

2. CONTENT

We consider a population of olive trees, otherwise in good health, of size N(t) at time t.
The main variables in our description are:
S(t) : the size of sensitive olive trees at the time t.
i (t,a): the size of infected olive trees over time t and age a.
The initial conditions of sensitive and infected olive trees are given by S_{0} and i_{0}(a) respectively.
The variable a denote the age of the disease (age of infection), i.e. the time that has elapsed since the infected olive trees became infected.
After introducing a structured age model, we proceed to reduce it to a delay model.

3. CONCLUSIONS

In conclusion, our study began with the formulation of a model to describe the spread of Xylella Fastidiosa disease, a biological phenomenon crucial to understand. It models the evolution of susceptible and infected olive trees.
After that, we perform our study by reducing it to a delayed model, which captures the essential epidemic mechanisms
In addition, we studied the conditions for the existence of equilibrium points, their local stability, and also the global stability of the disease-free equilibrium.
Finally, using numerical simulations, we illustrated different cases and scenarios.
This work could make a significant contribution to the mathematical modeling of the spread of Xylella Fastidiosa, opening up new perspectives for the research, prevention, and control of this biological threat.

QUANTUM COMMUNICATIONS AT IMT BUCHAREST AND BLUESPACE TECHNOLOGY

Cristin KUSKO[1] and Emil SIMION[2,3]

[1]National Institute for Research and Development in Microtechnologies – IMT Bucharest, 126A Erou Iancu Nicolae, Voluntari, Romania

[2]University Politehnica of Bucharest, 313 Splaiul Independentei, District 6, Bucharest, Romania
[3] BlueSpace Technology SRL, 82 Alexandriei, Bragadiru, Romania

Corresponding author email: cristian.kusko@imt.ro

Abstract

Here, in the broad context of quantum communications, we present the design and the fabrication aspects of a Quantum Key Distribution (QKD) system based on the protocol BB84 with decoys. The goal is to realize a system comprising the Tx - Alice and Rx – Bob modules based on low cost and of the shelf optical fiber components such that the hardware is robust, secure, easy to implement and maintain ready to be deployed in free space optical communication for both terrestrial and space scenarios. We will present the design of the system as well as various characterization techniques for the components.

Key words*: Quantum Key Distribution; BB84; Fiber Optics; Fiber Optics Components; Free Space Optical Communications*

1. INTRODUCTION

The accelerated development of quantum computing both theoretically and experimentally [1] leads to the possibility of realizing in the future a scalable quantum computer with a sufficiently large number of qubits that has the capability to successfully implement the Shor algorithm for factoring large numbers into prime factors in polynomial time [2,3]. This automatically leads to the vulnerability of the asymmetric cryptosystems currently used to transmit information through the existing telecommunications infrastructure, in which their secure nature is given by their mathematical complexity. A solution to maintain the secure nature of the transmitted information is to use symmetric, disposable encryption keys – one pad key – distributed using the existing telecommunications networks, keys that from a theoretical and practical point of view prove to be invulnerable to quantum attacks. In this case, the secrecy of information is ensured by the principles of quantum mechanics, the superposition principle, the entanglement property, respectively the impossibility of copying or cloning a quantum state - no cloning theorem.

2. CONTENT

The first quantum key distribution (QKD) protocol between two parties, the transmitter - Alice and the receiver - Bob was proposed by Bennet and Brassard in 1984 [4] and experimentally implemented in 1992 [5]. This protocol is based on “prepare and measure” method in the sense that Alice prepares single photons in two polarization bases right and diagonal transmit them over a quantum channel to Bob which measure their polarization state of the detected. By exchanging information about the single photon bases over a standard classical communication channel they are able to share a cryptographic one pad key.

Currently, there are a multitude of QKD protocols that use either the BB84 “prepare and measure” method described above, BB84 with decoy states [6-8] or SARG 04 [9]. Protocols such as E91[10] or BBM92 [11] have also been proposed that use the entanglement property of photons generated by the interaction of a pump beam with a nonlinear optical element.

This work will present an overview of the aforementioned QKD protocols and sysstems from both the theoretical and experimental point of view. We will discuss the implementation of QKD in various terrestrial and space scenarios at national and international level as well as several use cases in industry, academia, etc.

Finally, we will describe the approach taken by BlueSpace technology and IMT Bucharest for design and fabrication of the hardware components of a QKD system based on the protocol BB84 with decoys in the framework of the technology transfer project MERISD3C-QKD. Here we will consider a system based on fiber optics components and we will present the design aspects, the components characterization methods such as polarization control of the single photons, entropy generation, preparation of the single photons, their detection as well as the synchronization methods between Alice and Bob. In the end we will present the security issues associated with this type of QKD system.

3. CONCLUSIONS

The design and the fabrication aspects of the transceiver modules for a quantum cryptographic system employing the BB84 with decoys protocol were presented and analysed. The focus was put on utilization of the low cost, of the shelf optical fiber components aiming the robustness of the hardware, its low cost and the ease of implementation in QKD complete systems for free space optical communications.

4. ACKNOWLEDGEMENT

This work is supported by the the Ministry of Research, Innovation and Digitization, CNCS-UEFISCDI via project MERISD3C-QKD Grant PN-IV-P7-7.1-PTE-2024-0735 Transmission-reception modules for integration into quantum cryptographic key distribution systems (QKD-Quantum Key Distribution).

4. REFERENCES

1) Editorial 40 years of quantum computing. Nat Rev Phys **4**, 1 (2022)
2) *P. W.* Shor "Algorithms for quantum computation: Discrete logarithms and factoring". Proceedings 35th Annual Symposium on Foundations of Computer Science. IEEE Comput. Soc. Press. pp. 124–134 (1994).
3) *P. W.* Shor, "Polynomial-Time Algorithms for Prime Factorization and Discrete Logarithms on a Quantum Computer". SIAM Journal on Computing. **26** ,1484–1509, (1997)
4) C. H. Bennett and G. Brassard. "Quantum cryptography: Public key distribution and coin tossing". In Proceedings of IEEE International Conference on Computers, Systems and Signal Processing, volume **175**, page 8. New York, 1984
5) Bennett, C.H., Bessette, F., Brassard, G. *et al.* Experimental quantum cryptography. *J. Cryptology* 5, 3–28 (1992).
6) Won-Young Hwang „Quantum Key Distribution with High Loss: Toward Global Secure Communication" Phys. Rev. Lett. **91**, 057901 (2003)
7) Lo, Hoi-Kwong; Ma, Xiongfeng; Chen, Kai "Decoy State Quantum Key Distribution". Phys. Rev. Lett. **94**, 230504 (2005).
8) Peng, Cheng-Zhi, et al "Experimental Long-Distance Decoy-State Quantum Key Distribution Based on Polarization Encoding". Phys. Rev. Lett. **98**, 010505 (2007).
9) Valerio Scarani, et al "Quantum Cryptography Protocols Robust against Photon Number Splitting Attacks for Weak Laser Pulse Implementations". Phys. Rev. Lett. **92**, 057901, (2004).
10) Artur K. Ekert, "Quantum cryptography based on Bell's theorem". Phys. Rev. Lett. 67, 661-663 (1991).
11) Charles. H. Bennett, Gilles Brassard, N. David Mermin, "Quantum cryptography without Bell's theorem". *Physical Review Letters*. **68**, 557 (1992).

On a Model of Rumors Spreading Through Social Media

Laurance Fakih[1]*, Andrei Halanay[1], Florin Avram[2]

[1]Department of Mathematics and Informatics, University Politehnica of Bucharest, 060042 Bucharest, Romania
[2]Laboratoire de Mathématiques Appliquées, Université de Pau, 64012 Pau, France

laurance.fakih@upb.ro (L.F.), andrei.halanay@upb.ro (A.H.), florin.avram@univ-pau.fr (F.A.)

Abstract

Rumors have become a serious issue in today's modern era, particularly in view of increased activity in social and online platforms. False information can go viral almost instantaneously through social networks that immediately affect society and people's minds. The form of rumor it develops within, whether fabricated intentionally or not, impacts public perspectives through manipulation of emotion and cognition. We propose and analyze a mathematical model describing how rumors can spread through an online social media (OSM) platform. Our model focuses on two coexisting rumors (two strains), The results provide some conditions under which rumors die out or become persistent, and they show the influence of delays, skepticism levels, and incidence rates on the dynamics of information spread.

1 Introduction

Rumors have always been a fundamental aspect of human communication for centuries, having a deep impact on perception, public opinion, and frequently playing an important role in social and political life. However, with improvements in digital technology and social media platforms, the speed at which rumors spread has reached unprecedented levels. The explosion of social networks has changed the way information is shared, making it possible for real and false information to reach large groups of people. This development raises serious concerns about the accuracy of online content and the potential dangers of misinformation.
Rumors can come from a variety of sources, including false information, unverified press releases, and individuals seeking attention.
While not all of them cause immediate harm, many have the potential to cause panic, distort public perception, and destroy one's reputation. There is a critical necessity to investigate how rumors spread in order to develop effective strategies for fighting disinformation and creating an informed society.
Rumor spreading in social networks and communities has long been a subject of interest in both sociology and mathematics. Understanding how information, whether true or false, spreads within a population can help to devise some strategies to control misinformation and improve communication channels. Mathematical models have proved to be an important tool in describing and predicting rumor dynamics.
Based on this work, researchers have introduced more complex models by including various realistic factors. Time delays, for example, represent the time a person takes to change states, such as from hearing a rumor to spreading or becoming skeptical.
In this work, we extend the current models by considering several types of rumors that are spreading at the same time, each with its own skepticism and recovery rates. We introduce an eight-variable delay differential system representing different states of individuals and analyze the stability of its equilibria for various conditions of parameters. Our goal is to understand the propagation of multistrain rumors and the variables that affect stability.

*Corresponding authors: laurance.fakih@upb.ro, andrei.halanay@upb.ro

Two rumors spreading in an OSM

In this model, we assume there are two rumors (rumor 1 and rumor 2) spreading among the users of a social media platform. We track the following 8 state variables:

- x_1: **Potential users of OSM** (individuals who could join but have not yet joined).
- x_2: **Active users of OSM** (currently using the platform, susceptible to rumors).
- x_3: **Non-users (disconnected)** from OSM who have abandoned and never joined the platform again, after a delay.
- x_4: **Considering rumor 1** (they heard rumor 1 and are thinking about it).
- x_5: **Considering rumor 2**.
- x_6: **Believers of rumor 1** (those actively spreading or convinced by rumor 1).
- x_7: **Believers of rumor 2**.
- x_8: **Skeptics for either rumor** (individuals who do not believe either rumor).

The system of equations is:

$$\begin{cases} \dot{x}_1 = \Lambda - \alpha x_1 x_2 - \mu x_1, & (1) \\ \dot{x}_2 = \alpha x_1 x_2 - \eta x_2\, x_3(t-\tau) - \mu x_2, & (2) \\ \dot{x}_3 = \eta x_2\, x_3(t-\tau) - \mu x_3 + \omega x_8, & (3) \\ \dot{x}_4 = \dfrac{\beta_1 x_2 x_6}{1 + \alpha_1 x_2 + \epsilon_1 x_6} - \gamma_1 x_4, & (4) \\ \dot{x}_5 = \dfrac{\beta_2 x_2 x_7}{1 + \alpha_2 x_2 + \epsilon_2 x_7} - \gamma_2 x_5, & (5) \\ \dot{x}_6 = \gamma_1 x_4 - \mu_1 x_6, & (6) \\ \dot{x}_7 = \gamma_2 x_5 - \mu_2 x_7, & (7) \\ \dot{x}_8 = \mu_1 x_6 + \mu_2 x_7 - \omega x_8. & (8) \end{cases}$$

All parameters are nonnegative, and $\tau > 0$ is a delay. We write the delay explicitly as $x_3(t-\tau)$ throughout. Our goals are to prove first that the solutions are essentially positive, then to identify the equilibria of this system and study their stability by looking at the linear approximation.

2 Matlab's Simulations

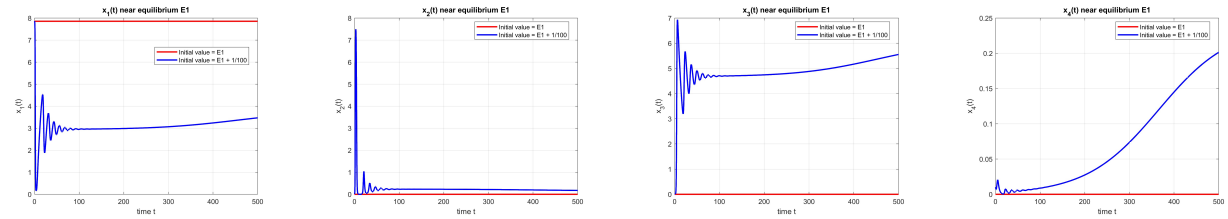

(a) $x_1(t)$ (b) $x_2(t)$ (c) $x_3(t)$ (d) $x_4(t)$

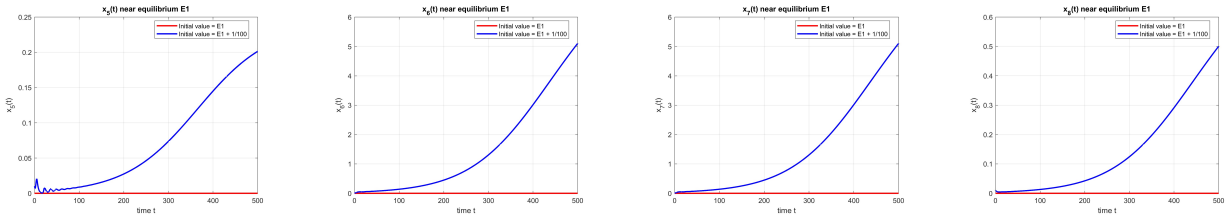

(e) $x_5(t)$ (f) $x_6(t)$ (g) $x_7(t)$ (h) $x_8(t)$

Figure 1: Equilibrium point E_1 at $\tau = 0$ with and without perturbation. E_1 is unstable.

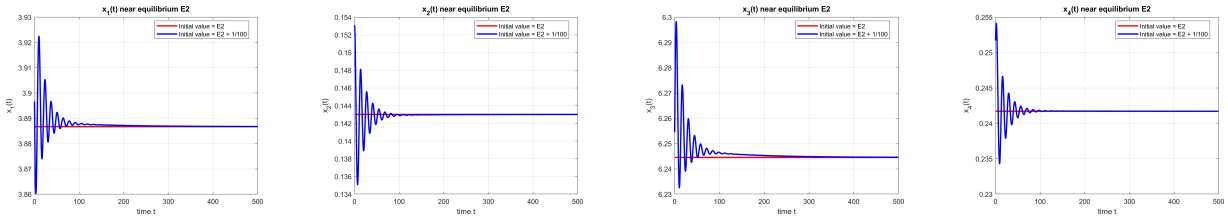

(a) $x_1(t)$ (b) $x_2(t)$ (c) $x_3(t)$ (d) $x_4(t)$

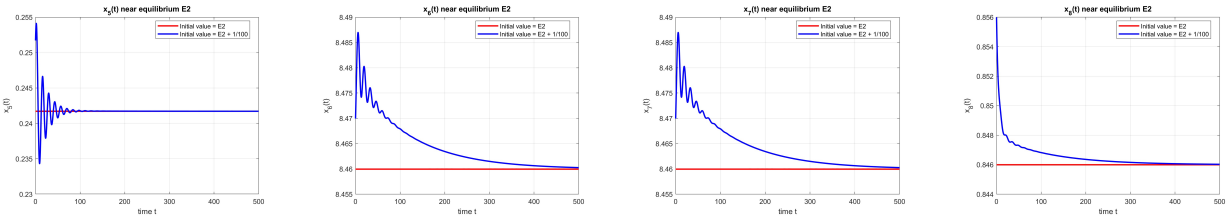

(e) $x_5(t)$ (f) $x_6(t)$ (g) $x_7(t)$ (h) $x_8(t)$

Figure 2: Equilibrium point E_2 at $\tau = 0$, with and without perturbation. E_2 is stable. *Note:* with $\tau = 0$ there is no delay-induced mechanism; accordingly, no delay-induced sustained oscillations appear, and trajectories converge to the equilibrium.

3 Conclusions

In this study, we analyzed a mathematical model of rumor spread on social media, highlighting the impact of delays, rumor incidence rates, and user skepticism on rumor propagation dynamics. Our results, supported by numerical simulations and stability analyses, align with similar research, confirming and expanding previous insights.

We have developed and analyzed a delay differential model to explore the dynamics of two coexisting rumors

spreading through an online social media (OSM) platform.
The existence and stability of the rumor present equilibrium (E_2) depends on certain critical boundary conditions that control rumor persistence, similar to the basic reproduction number in epidemic models. Just like how diseases spread if the infection rate crosses a certain limit. In simple terms, our model shows that if enough people start sharing a rumor, it won't just disappear; instead, it will keep spreading continuously throughout the network.[10]
Our research show that time delays play an important role in how rumors spread. Similar to previous research [8], we found that delays, such as hesitation periods or time before users respond to misinformation, can create complex behaviors including oscillations or periodic rumor outbreaks (Hopf bifurcations), which make it harder to stop rumors once they appear.

References

[1] Daley, D. J., & Kendall, D. G. (1965). Stochastic rumours. *Journal of the Institute of Mathematics and Its Applications*, 1, 42–55.

[2] Laarabi, H., et al. (2015). Delay differential equations in rumor spreading models. *Nonlinear Dynamics*.

[3] Ghosh, S., et al. (2021). Control strategies in rumor propagation. *Applied Mathematical Modelling*.

[4] Vosoughi, S., Roy, D., & Aral, S. (2018). The spread of true and false news online. *Science*, 359(6380), 1146–1151.

[5] Cooke, K., & Grossman, Z. (1982). Discrete delay, distributed delay and stability switches. *Journal of Mathematical Analysis and Applications*, 86, 592–627.

[6] Bellman, R., & Cooke, K. L. (1963). *Differential-Difference Equations*. Academic Press.

[7] Hale, J. K., & Verduyn Lunel, S. M. (1993). *Introduction to Functional Differential Equations*. Springer-Verlag.

[8] Li, X.; Ma, Z. Rumor Propagation with Delay: Global Stability and Optimal Control Strategies. *Appl. Math. Comput.* **2022**.

[9] Vosoughi, S.; Roy, D.; Aral, S. The Spread of True and False News Online. *Science* **2018**, *359*(6380), 1146–1151.

[10] Zhou, Y.; et al. SHIDR Rumor Model with Nonlinear Incidence and Impulsive Vaccination. *Entropy* **2023**.

[11] Beretta, E.; Kuang, Y. Geometric Stability Switch Criteria in Delay Differential Systems with Delay-Dependent Parameters. *SIAM J. Math. Anal.* **2002**, *33*(5), 1144–1165.

[12] Hale, J. K.; Verduyn Lunel, S. M. *Introduction to Functional Differential Equations*; Springer-Verlag: New York, NY, USA, 1993.

APPROXIMATIONS OF THE BEST CONSTANTS

Liviu IGNAT

[1]Simion Stoilow Institute of Mathematics
Calea Grivitei 21, Bucharest

Corresponding author email: liviu.ignat@gmail.com

Abstract

In this talk we consider some well-known quotients related with either eigenvalue problems, Sobolev or Hardy's inequality. We consider the infimum of these quotients and their discrete analogous in a finite element subspace. We estimate the difference between the best constants above as the discretization parameter goes to zero and obtain sharp convergence rates. This is joint work with Enrique Zuazua.

Key words *Sobolev / Hardy inequalities, Finite element approximation.*

1. INTRODUCTION

The determination and approximation of **best constants** in functional inequalities, such as those related to eigenvalues of elliptic operators (e.g., the Laplacian) or classical inequalities (Sobolev, Hardy), are fundamental problems in analysis and numerical mathematics. Best constants are generally defined by a minimization procedure for a Rayleigh quotient, $C_{A,B,X} = \inf_{u\in X} \frac{\|u\|_A}{\|u\|_B}$. Key questions surrounding these constants include the attainment of the infimum, the structure of the set of minimizers ($\mathcal{M}$), and, crucially for applications, their exact computation or efficient numerical approximation. The core focus of this work is to establish the optimal convergence rates for the **Finite Element Method (FEM)** approximation of some best constants.

2. CONTENT: ANALYSIS OF APPROXIMATION RATES

2.1. Standard Elliptic Eigenvalue Problems

For the 1D Laplace problem using piecewise linear finite elements (P_1), the approximation rate is known to be $\lambda_{1h} = \lambda_1 + \frac{h^2}{12} + O(h^4)$, where h is the mesh size. General theory, as found in Babuška & Osborn and Chatelin, suggests that for general operators and Hilbert spaces, the approximation difference is controlled by the distance between the continuous minimizer u_1 and the approximation space V_h:

$$\lambda_{1h}(V_h) - \lambda_1(V) \simeq \text{dist}_V(u_1, V_h)^2 = \min_{v_h\in V_h} \int_\Omega |\nabla u_1 - \nabla v_h|^2 dx$$

Since the best approximation error is typically bounded by $\text{dist}_V(u_1, V_h) \lesssim h \parallel u_1 \parallel_{H^2}$, this suggests a rate of $O(h^2)$. The challenge lies in proving a lower bound, $\text{dist}_V(u_1, V_h) \gtrsim h$, which requires knowing the non-flatness or convexity properties of the minimizer. For instance, in 1D, the lower bound is proved using the convexity of u_1 by estimating $\min_{v_h\in P_1^h} \int |u'_1 - v_{h'}|^2$ from below by $c^2h^2/12$.

2.2. Sobolev Inequality

For the Sobolev constant $S(p, N)$ defined on $\dot{W}^{1,p}(\mathbb{R}^N)$ in $\mathbb{R}^N$, the minimizers $\mathcal{M}$ are the explicit Talenti functions. The approximation rate $S_h - S$ is derived by linking the approximation error to

the **Sobolev deficit**, $\delta(u) = \frac{\|Du\|_{L^p(\mathbb{R}^N)}}{\|u\|_{L^{p^*}(\mathbb{R}^N)}} - S$. Using estimates by Figalli and Zhang that relate the deficit to the distance to the manifold of minimizers $\mathcal{M}$, we showed that the approximation rate is bounded by the distance of the discrete minimizer w_h and the space V_h to $\mathcal{M}$:

$$\inf_{U\in\mathcal{M}} \text{dist}_V^2(U, w_h) \lesssim S_h - S \lesssim \inf_{U\in\mathcal{M}} \text{dist}_V^2(U, V_h).$$

For $p = 2$, $N \geq 3$, we established the final optimal rate:

$$S_h(2, N) - S(2, N) \simeq h^{\frac{2(N-2)}{N}},$$

which is superior to standard estimates (e.g., $h^{1/3}$ for $N = 3$). The critical improvement came from adapting the analysis using **quasi-norms** (inspired by p-Laplacian literature) to optimally estimate the Sobolev deficit.

2.3. Hardy Inequality

The **Hardy constant** $S_2(N, \Omega) = \frac{(N-2)^2}{4}$ is a singular case, as the infimum is not attained in the standard $H^1(\Omega)$ space. This requires specialized numerical techniques for the discrete constant S_{2h}. We establish the optimal rate of convergence for $N \geq 3$ as:

$$S_{2h} - S_2 \simeq \frac{1}{|\log h|^2}.$$

This rate is proven using a combination of a lower bound based on the Hardy inequality with logarithmic reminders and an upper bound based on approximating a regularized pseudo-minimizer with P_h^1 functions.

3. CONCLUSIONS

This research provides a rigorous framework for determining the **optimal convergence rates** for the approximation of best constants in crucial functional inequalities using standard finite element methods. By moving beyond classical approximation theory and incorporating recent developments in non-linear analysis (Sobolev deficit estimates) and numerical analysis (quasi-norms), we derived sharp, structure-dependent rates for both the Sobolev and Hardy constants. The results highlight that the convergence behavior is highly dependent on the regularity and structure of the continuous minimizers, often leading to better convergence rates than those predicted by general, worst-case scenario numerical estimates.

Future work will explore the applications of **machine learning models** (such as those using ReLU activation functions) for approximating these constants, and investigate if a discrete deficit analysis can provide alternative optimal bounds. Furthermore, many open questions remain in the "hard analysis" of these problems concerning the concentration, regularity, and multiplicity of the minimizers.

Analysis of Solutions for Higher Order Linear Difference Equations with Finite φ- Order Coefficients

Mansouria SAIDANI
Department of Mathematics
Laboratory of Pure and Applied Mathematics
University of Mostaganem (UMAB)
B. P. 227 Mostaganem-(Algeria)
mansouria.saidani@univ-mosta.dz

Abstract. This paper examined the growth of meromorphic solutions to higher-order linear equations of the form:

$$A_n(z)f(z+h_n) + A_{n-1}(z)f(z+h_{n-1}) + \cdots + A_1(z)f(z+h_1) + A_0(z)f(z) = A_{n+1}(z) \qquad (1)$$

where $(A_{n+1}(z), \ldots, A_0(z))$ are entire or meromorphic functions and (h_i) (for $j = 1, \ldots, n$) are non-zero distinct complex numbers. Our search extends some earlier results proved by Luo and Zheng, Belaïdi and Bellaama, using the notion of φ-order.

2010 *Mathematics Subject Classification*: 30D35, 39B32, 39A10.
Key words: Meromorphic function; growth order; linear difference equation.

1 Introduction and main results

Throughout this article we assume that the reader is familiar with the basic results and standard notation of Nevanlinna's value distribution theory (see (refer to [8], [9], [10]). In this section we quote the main concepts and definitions used in the realization of this work.

Definition 1.1 ([3, 6]). The φ- (respectively, lower-) order ρ (respectively, μ) of a given meromorphic function f is represented as $\rho(f,\varphi)$ (respectively, $\mu(f,\varphi)$) and corresponds to the value given by

$$\rho(f,\varphi) = \limsup_{r\to+\infty} \frac{\log T(r,f)}{\log \varphi(r)}, (resp, \mu(f,\varphi) = \liminf_{r\to+\infty} \frac{\log T(r,f)}{\log \varphi(r)}).$$

When f is entire, then

$$\rho(f,\varphi) = \limsup_{r\to+\infty} \frac{\log\log M(f,r)}{\log \varphi(r)}, (resp, \mu(f,\varphi) = \liminf_{r\to+\infty} \frac{\log\log M(f,r)}{\log \varphi(r)}).$$

Remark 1.2. ([6]) It is important to note that in this paper, we assume that $\varphi : [0,+\infty) \to (0,+\infty)$ is a non-decreasing unbounded function that always satisfies the following two conditions:

(i). $\lim_{r\to+\infty} \frac{\log_{p+1} r}{\log_q \varphi(r)} = 0$.

(ii). $\lim_{r\to+\infty} \frac{\log_q \varphi(\alpha_1 r)}{\log_q \varphi(r)} = 1$ for some $\alpha_1 > 1$.

Definition 1.3 ([2,3]). Assume that f is a meromorphic function such that $0 < \rho(f,\varphi) = \rho < +\infty$. Then the φ-type of f is represented as $\tau(f,\varphi)$ and corresponds to the value defined as

$$\tau(f,\varphi) = \limsup_{r\to\infty} \frac{T(r,f)}{\varphi(r)^\rho}.$$

If f is entire, then

$$\tau(f,\varphi) = \limsup_{r\to\infty} \frac{\log M(r,f)}{\varphi(r)^\rho}.$$

Similarly, if $0 < \mu(f,\varphi) = \mu < +\infty$, the corresponding φ-lower types are represented and defined by

$$\underline{\tau}(f,\varphi) = \liminf_{r\to\infty} \frac{T(r,f)}{\varphi(r)^\mu} \quad (\text{respectively, } \underline{\tau}(f,\varphi) = \liminf_{r\to\infty} \frac{\log M(r,f)}{\varphi(r)^\mu}).$$

Definition 1.0.1. ([6]) *Given $a \in \overline{\mathbb{C}} = \mathbb{C} \cup \{\infty\}$, we define the* deficiency *of a with respect to a given meromorphic function f, denoted by $\delta(a, f)$, as follows:*

$$\delta(a,f) = \liminf_{r\to+\infty} \frac{m\left(r, \frac{1}{f-a}\right)}{T(r,f)} = 1 - \limsup_{r\to+\infty} \frac{N\left(r, \frac{1}{f-a}\right)}{T(r,f)}, \quad a \neq \infty,$$

$$\delta(\infty,f) = \liminf_{r\to+\infty} \frac{m(r,f)}{T(r,f)} = 1 - \limsup_{r\to+\infty} \frac{N(r,f)}{T(r,f)}.$$

Definition 1.0.2. ([13]) *Let f be a meromorphic function. Then, the φ- exponent of convergence of zero-sequence of f is defined by*

$$\lambda(f,\varphi) = \limsup_{r\to+\infty} \frac{\log N(r, \frac{1}{f})}{\log \varphi(r)}.$$

Definition 1.0.3. ([13]) *Let $\varphi : [0, +\infty) \to (0, +\infty)$ be a non-decreasing unbounded function, and p, q be positive integers that satisfy $p \geqslant q \geqslant 1$. Then the $[p, q] - \varphi$ order of a meromorphic function f are respectively defined by*

$$\rho_{[p,q]}(f,\varphi) = \limsup_{r\to+\infty} \frac{\log T(r,f)}{\log \varphi(r)}.$$

The purpose of this paper is to extend the previous results by employing the concept of $(p, q) - \varphi$ order. Indeed, we will prove the following results.

Theorem 1.1 Let $A_j(z)$ (for $j = 0, \ldots, n+1$) be entire functions of φ-order and let $k, l \in \{0, 1, 2, \ldots, n+1\}$ with $A_{n+1} \not\equiv 0$ such that $\max\{\mu(A_k, \varphi), \rho(A_j, \varphi), j \neq k, l\} = \rho \leqslant \mu(A_l, \varphi) < \infty, \mu(A_l, \varphi) > 0$. If the following assumptions hold simultaneously:

1. $\underline{\tau}(A_l, \varphi) > \underline{\tau}(A_k, \varphi)$, when $\mu(A_l, \varphi) = \mu(A_k, \varphi)$
2. $\max\{\tau(A_j, \varphi) : \rho(A_j, \varphi) = \mu(A_l, \varphi), j \neq k, l\} = \tau_1 < \underline{\tau}(A_l, \varphi)$, when $\mu(A_l, \varphi) = \max\{\rho(A_j, \varphi); j \neq k, l\}$,

then every meromorphic solution f of equation (1) satisfies $\rho(f, \varphi) \geqslant \mu(A_l, \varphi)$.

Theorem 1.2 Let $A_j(z)$ (for $j = 0, \ldots, n+1$) be meromorphic functions of φ-order and let $k, l \in \{0, 1, 2, \ldots, n+1\}$ with $A_{n+1} \not\equiv 0$ such that $\max\{\mu(A_k, \varphi), \rho(A_j, \varphi), j \neq k, l\} = \rho \leqslant \mu(A_l, \varphi) < \infty, \mu(A_l, \varphi) > 0$. If the following assumptions hold simultaneously:

1. $\underline{\tau}(A_l, \varphi) > \underline{\tau}(A_k, \varphi)$, when $\mu(A_l, \varphi) = \mu(A_k, \varphi)$;
2. $$\sum_{\rho(A_j,\varphi)=\mu(A_l,\varphi)>0, \quad j\neq k,l} \tau(A_j, \varphi) < \underline{\tau}(A_l, \varphi) < +\infty$$
$$\text{when} \quad \mu(A_l, \varphi) = \max\{\rho(A_j, \varphi), j \neq k, l\};$$

3. $$\sum_{\rho(A_j,\varphi)=\mu(A_l,\varphi)>0, \quad j\neq k,l} \tau(A_j, \varphi) + \underline{\tau}(A_k, \varphi) < \underline{\tau}(A_l, \varphi) < +\infty$$
$$\text{when } \mu(A_l, \varphi) = \mu(A_k, \varphi) = \max\{\rho(A_j, \varphi), j \neq k, l\};$$

4. $\lambda\left(\frac{1}{A_l}, \varphi\right) < \mu(A_l, \varphi) < \infty$.

Then every meromorphic solution f of equation (1) satisfies $\rho(f, \varphi) \geqslant \mu(A_l, \varphi)$.

2 AUXILIARY LEMMAS

With a view to to prove our theorems, we need the following proposition and lemmas. The Lebesgue linear measure of a set $E \subset [0, +\infty)$ is $m(E) = \lim \int_E dt$, and the logarithmic measure of a set $F \subset (1, +\infty)$ is $m_l(F) = \lim \int_F \frac{dt}{t}$.

Lemma 2.1 ([8]) Let f be a meromorphic function, and h be a non-zero complex constant. Then we have that for $r \to +\infty$.

$$(1 + o(1)) T(r - |h|, f(z)) \leqslant T(r, f(z + h)) \leqslant (1 + o(1)) T(r + |h|, f(z)).$$

Lemma 2.2 ([11]) Let p, q be positive integers and satisfy $p \geqslant q \geqslant 1$. Suppose that f is a meromorphic function such that $\rho_{[p,q]}(f, \varphi) < +\infty$. then, for any given $\varepsilon > 0$, we have

$$\begin{aligned} &\exp\left\{-\exp_p\left\{(\rho_{[p,q]}(f, \varphi) + \varepsilon) \log_q \varphi(r)\right\}\right\} \leq |f(z)| \\ &\leq \exp_{p+1}\left\{(\rho_{[p,q]}(f, \varphi) + \varepsilon) \log_q \varphi(r)\right\} \quad (r \notin E_1), \end{aligned}$$

where $E_1 \subset (1, +\infty)$ is a set of r of finite linear measure.

Lemma 2.3 ([12]) Let f be a meromorphic function of finite φ-order $\rho := \rho(f, \varphi)$. Then, for any pair of distinct complex numbers η_1, η_2, $\beta > 1$ and any given $\varepsilon > 0$, there exists a subset $E_2 \subset (1, \infty)$ of finite logarithmic measure such that, for all $|z| \notin E_2$, we have

$$\exp\left\{-\frac{(\varphi(r))^{\rho+\beta+\varepsilon}}{r}\right\} \leqslant \left|\frac{f(z + \eta_1)}{f(z + \eta_2)}\right| \leqslant \exp\left\{\frac{(\varphi(r))^{\rho+\beta+\varepsilon}}{r}\right\}.$$

Lemma 2.4 Let f be an entire function with $\mu(f, \varphi) < \infty$, then for any given $\varepsilon > 0$, there exists a set $E_3 \subset (1, +\infty)$ having infinite logarithmic measure such that for all $r \in E_3$, we have

$$\mu(f, \varphi) = \lim_{r \to +\infty, r \in E_3} \frac{\log T(r, f)}{\log \varphi(r)} = \lim_{r \to +\infty, r \in E_3} \frac{\log_2 M(r, f)}{\log \varphi(r)},$$

and

$$M(r, f) < \exp\{\{\varphi(r)\}^{\mu(f,\varphi)+\varepsilon}\}.$$

Proof. From the definition of the lower φ-order, there exists a sequence $\{r_m\}_{m=1}^{\infty}$ tending to $+\infty$ satisfying $(1 + \frac{1}{m}) r_m < r_{m+1}$, and

$$\lim_{r_m \to +\infty} \frac{\log_2 M(r_m, f)}{\log \varphi(r_m)} = \mu(f, \varphi).$$

Hence, for any given $\varepsilon > 0$, there exists an m_1 such that for $m \geqslant m_1$ and any $r \in [r_m, (1 + \frac{1}{m}) r_m]$, we obtain

$$\frac{\log_2 M(r_m, f)}{\log(1 + \frac{1}{m}) r_m} \leqslant \frac{\log_2 M(r, f)}{\log \varphi(r)} \leqslant \frac{\log_2 M((1 + \frac{1}{m}) r_m, f)}{\log \varphi(r_m)}.$$

Let $E_3 = \bigcup_{m=m_1}^{+\infty} [r_m, (1 + \frac{1}{m}) r_m]$, then for any $r \in E_3$, we have

$$\lim_{r \to +\infty, r \in E_3} \frac{\log_2 M(r, f)}{\log \varphi(r)} = \lim_{r_m \to +\infty} \frac{\log_2 M(r_m, f)}{\log \varphi(r_m)} = \mu(f, \varphi),$$

and

$$m_l(E) = \sum_{m=m_1}^{\infty} \int_{r_m}^{(1+\frac{1}{m}) r_m} \frac{dt}{t} = \sum_{m=m_1}^{\infty} \log(1 + \frac{1}{m}) = \infty.$$

The proof is complete.

Lemma 2.5 ([7]) Let f be a meromorphic function of finite φ-order $\rho(f, \varphi)$, and let η_1, η_2 be two distinct complex numbers. Then, for each $\varepsilon > 0$, we have

$$m\left(r, \frac{f(z + \eta_1)}{f(z + \eta_2)}\right) = O\left(\varphi(r)^{\rho(f,\varphi)-1+\varepsilon}\right).$$

Lemma 2.6 ([1]) Let $p \geqslant 1$ and f be a meromorphic function with with $1 \leqslant \mu_p(f,\varphi) < +\infty$ and nonzero finite iterated lower $p-\varphi$ type, $\underline{\tau}_p(f,\varphi)$. Then there exists some $E_4 \subset (1,+\infty)$ with $m_l(E_4) = +\infty$, such that, for $|z| = r \in E_4$,

$$\log_{p-1} T(r,f) < (\underline{\tau}_p(f,\varphi)+\varepsilon)\{\varphi(r)\}^{\mu_p(f,\varphi)}$$

where

$$\mu_p(f,\varphi) = \liminf_{r\to\infty} \frac{\log_p T(r,f)}{\log \varphi(r)},$$

and

$$\underline{\tau}_p(f,\varphi) = \liminf_{r\to\infty} \frac{\log_{p-1} T(r,f)}{\varphi(r)^{\mu_p(f,\varphi)}}.$$

Lemma 2.7 ([12]) If f is a meromorphic function with $1 \leqslant \mu(f,\varphi) < +\infty$, then there exists some $E_5 \subset (1,+\infty)$ with $m_l(E_5) = +\infty$, so that, for $|z| = r \in E_5$,

$$T(r,f) < (\varphi(r))^{\mu(f,\varphi)+\varepsilon}.$$

Lemma 2.8 ([5]) Let f be an entire function with $0 < \mu(f,\varphi) = \mu < \infty$. Then, there exists a set $E_6 \subset (1,\infty)$ of infinite logarithmic measure such that, for all $r \in E_6$, we have

$$\tau = \tau(f,\varphi) = \lim_{r\to\infty, r\in E_6} \frac{\log M(r,f)}{(\varphi(r))^{\mu}}.$$

3 Proof of Theorem 1.1

If the solution $\rho(f,\varphi) = \infty$, the result is valid.
Now we assume that $\rho(f,\varphi)$ is finite. Using equation (1), we obtain

$$|A_l(z)| \leq \sum_{\substack{j=1 \\ j\neq k,l}}^{n} |A_j(z)| \left|\frac{f(z+c_j)}{f(z+c_l)}\right| + |A_k(z)| \left|\frac{f(z+c_k)}{f(z+c_l)}\right| + |A_0(z)| \left|\frac{f(z)}{f(z+c_l)}\right| + \left|\frac{A_{n+1}(z)}{f(z+c_l)}\right|. \quad (2)$$

From Lemma 2.1, we get

$$\rho(f(z+c_l),\varphi) = \rho\left(\frac{1}{f(z+c_l)},\varphi\right) = \rho(f,\varphi). \quad (3)$$

Then, by using Lemma 2.2, (in the case $p = q = 1$) for any given $\varepsilon > 0$, we can find a subset $E_1 \subset (1,+\infty)$, satisfying $m_l(E_1) < \infty$ such that for all z satisfying $|z| = r \notin [0,1] \cup E_1$ and sufficiently large r, we have

$$\left|\frac{1}{f(z+c_l)}\right| \leqslant \exp\left\{(\varphi(r))^{(\rho(f,\varphi)+\varepsilon)}\right\}. \quad (4)$$

Therefore, from Lemma 2.3 that for any $\varepsilon > 0$ and $\beta > 1$, there exists a subset $E_2 \subset (1,+\infty)$ with finite logarithmic measure such that for all $|z| = r \notin [0,1] \cup E_2$, we have

$$\left|\frac{f(z)}{f(z+c_l)}\right| \leqslant \exp\left\{\frac{(\varphi(r))^{\rho(f,\varphi)+\beta+\varepsilon}}{r}\right\}, \quad \left|\frac{f(z+c_j)}{f(z+c_l)}\right| \leqslant \exp\left\{\frac{(\varphi(r))^{\rho(f,\varphi)+\beta+\varepsilon}}{r}\right\}. \quad (5)$$

We divide our proof into three cases.
Case 1. If $\max\{\rho(A_j,\varphi), j \neq k,l\} = \beta_1 < \mu(A_k,\varphi) = \mu(A_l,\varphi)$, $\underline{\tau}(A_l,\varphi) > \underline{\tau}(A_k,\varphi)$. Through the use of the definition of $\underline{\tau}(A_k,\varphi)$ and Lemma 2.8, for any $\varepsilon(>0)$, there exists a subset $E_6 \subset (1,+\infty)$ having infinite logarithmic measure such that for all $r \in E_6$, we have

$$|A_k(z)| \leqslant \exp\{(\underline{\tau}(A_k,\varphi)+\varepsilon)\varphi(r)^{\mu(A_k,\varphi)}\} = \exp\{(\underline{\tau}(A_k,\varphi)+\varepsilon)(\varphi(r))^{\mu(A_l,\varphi)}\}. \quad (6)$$

From the definition of $\underline{\tau}(A_l,\varphi)$, for sufficiently small $\varepsilon>0$ and sufficiently large r, we have

$$|A_l(z)|\geqslant \exp\{(\underline{\tau}(A_l,\varphi)-\varepsilon)(\varphi(r))^{\mu(A_l,\varphi)}\}. \tag{7}$$

On the other hand, by making use of the definition of $\rho(A_j,\varphi)$, for all given $\varepsilon(>0)$ and sufficiently large r, we can write

$$|A_j(z)|\leqslant \exp\{(\varphi(r))^{\rho(A_j,\varphi)+\varepsilon}\}\leqslant \exp\{(\varphi(r))^{\beta_1+\varepsilon}\},\quad j\neq k,l. \tag{8}$$

By replacing (4), (5), (6), (7) and (8) in (2), for all given $\varepsilon(>0)$ and sufficiently large $r\in E_6\backslash([0,1]\cup E_1\cup E_2)$

$$\exp\{(\underline{\tau}(A_l,\varphi)-\varepsilon)(\varphi(r))^{\mu(A_l,\varphi)}\}\leqslant (n-1)\exp\{(\varphi(r))^{\beta_1+\varepsilon}\}\exp\left\{\frac{(\varphi(r))^{\rho(f,\varphi)+\beta+\varepsilon}}{r}\right\}$$

$$+\exp\{(\underline{\tau}(A_k,\varphi)+\varepsilon)(\varphi(r))^{\mu(A_l,\varphi)}\}\exp\left\{\frac{(\varphi(r))^{\rho(f,\varphi)+\beta+\varepsilon}}{r}\right\}+\exp\{(\varphi(r))^{\beta_1+\varepsilon}\}\exp\left\{(\varphi(r))^{(\rho(f,\varphi)+\varepsilon)}\right\}. \tag{9}$$

Let us pick some ε small enough to satisfy

$$0<2\varepsilon<\min\{\mu(A_l,\varphi)-\beta_1,\underline{\tau}(A_l,\varphi)-\underline{\tau}(A_k,\varphi)\},$$

therefore, for sufficiently large $r\in E_6\backslash([0,1]\cup E_1\cup E_2)$, the formula (9) becomes

$$\exp\{(\underline{\tau}(A_l,\varphi)-\underline{\tau}(A_k,\varphi)-2\varepsilon)(\varphi(r))^{\mu(A_l,\varphi)-\varepsilon}\}\leqslant \exp\left\{(\varphi(r))^{(\rho(f,\varphi)+\varepsilon)}\right\},$$

Then, by making use of Lemma 2.3, Definition 1.1, we get $\mu(A_l,\varphi)-2\varepsilon\leqslant(\rho(f,\varphi)$. Using the fact that ε is arbitrary, we obtain $\rho(f,\varphi)\geqslant\mu(A_l,\varphi)$.

Case 2. Assume that $\mu(A_k,,\varphi)<\max\{\rho(A_j,\varphi),j\neq k,l\}=\mu(A_l,\varphi)$ and $\max\{\tau(A_j,\varphi):\rho(A_j,\varphi)=\mu(A_l,\varphi),j\neq k,l\}=\tau_1<\tau(A_l,\varphi)$.

Using the definition of $\mu(A_k,\varphi)$ and Lemma 2.4, for any given $\varepsilon(>0)$, there exists a subset $E_3\subset(1,+\infty)$ satisfying $m_l(E_3)$ such that for all $r\in E_3$, we have

$$|A_k(z)|\leqslant\exp\{(\varphi(r))^{\mu(A_k,\varphi)+\varepsilon}\}. \tag{10}$$

Using the definitions of $\tau(A_j,\varphi)$ and $\rho(A_j,\varphi)$, for any given $\varepsilon>0$ and sufficiently large r, we get

$$|A_j(z)|\leqslant\begin{cases}\exp\left((\tau_1+\varepsilon)\varphi(r)^{\mu(A_l,\varphi)}\right), & \text{if } \rho(A_j,\varphi)=\mu(A_l,\varphi),j\neq k,l,\\ \exp\left(\varphi(r)^{\rho(A_j,\varphi)+\varepsilon}\right)\leqslant\exp\left(\varphi(r)^{\mu(A_l,\varphi)-\varepsilon}\right), & \text{if } \rho(A_j,\varphi)<\mu(A_l,\varphi),j\neq k,l.\end{cases} \tag{11}$$

Therefore, by replacing (4), (5), (7), (10) and (11) into (2), for $\beta>1$ and all z satisfying $r\in E_3\backslash([0,1]\cup E_1\cup E_2)$ sufficiently large, we obtain

$$\exp\{(\underline{\tau}(A_l,\varphi)-\varepsilon)(\varphi(r))^{\mu(A_l,\varphi)}\}\leqslant O\left(\exp\left((\tau_1+\varepsilon)\varphi(r)^{\mu(A_l,\varphi)}\right)\exp\left\{\frac{(\varphi(r))^{\rho(f,\varphi)+\beta+\varepsilon}}{r}\right\}\right)$$

$$+O\left(\exp\left(\varphi(r)^{\mu(A_l,\varphi)-\varepsilon}\right)\exp\left\{\frac{(\varphi(r))^{\rho(f,\varphi)+\beta+\varepsilon}}{r}\right\}\right)$$

$$+\exp\{(\varphi(r))^{\mu(A_k,\varphi)+\varepsilon}\}\exp\left\{\frac{(\varphi(r))^{\rho(f,\varphi)+\beta+\varepsilon}}{r}\right\}+\exp\left((\tau_1+\varepsilon)\varphi(r)^{\mu(A_l,\varphi)}\right)\exp\left\{(\varphi(r))^{(\rho(f,\varphi)+\varepsilon)}\right\}. \tag{12}$$

We can now select a sufficiently small ε that satisfies

$$0 < 2\varepsilon < \min\{\mu(A_l,\varphi) - \mu(A_k,\varphi), \underline{\tau}(A_l,\varphi) - \tau_1\},$$

then from (12), for sufficiently large ($r \in E_3 \setminus ([0,1] \cup E_1 \cup E_2)$), we can write

$$\exp\{(\underline{\tau}(A_l,\varphi) - \tau_1 - 2\varepsilon)(\varphi(r))^{\mu(A_l,\varphi)-\varepsilon}\} \leqslant \exp\left\{(\varphi(r))^{(\rho(f,\varphi)+\varepsilon)}\right\}.$$

Then, by making use of Lemma 2.3, Definition 1.1, we get $\mu(A_l,\varphi) - \varepsilon \leqslant \rho(f,\varphi) + \varepsilon)$. Since $\varepsilon > 0$ is arbitrary, we conclude that $\rho(f,\varphi) \geqslant \mu(A_l,\varphi)$.

Case 3. Assume that $\max\{\rho(A_j,\varphi), j \neq k,l\} = \mu(A_k,\varphi) = \mu(A_l,\varphi)$ and $\max\{\tau(A_k,\varphi), \underline{\tau}(A_j,\varphi) : \rho(A_j,\varphi) = \mu(A_l,\varphi), j \neq k,l\} = \tau_2 < \underline{\tau}(A_l,\varphi)$.

Therefore, by replacing (4), (5), (6),(7) and (11) into (2), for $\beta > 1$ and all z satisfying $r \in E_6 \setminus ([0,1] \cup E_1 \cup E_2)$ sufficiently large, we get

$$\exp\{(\underline{\tau}(A_l,\varphi) - \varepsilon)(\varphi(r))^{\mu(A_l,\varphi)}\} \leqslant O\left(\exp\left((\tau_2+\varepsilon)\varphi(r)^{\mu(A_l,\varphi)}\right)\exp\left\{\frac{(\varphi(r))^{\rho(f,\varphi)+\beta+\varepsilon}}{r}\right\}\right)$$

$$+O\left(\exp\left(\varphi(r)^{\mu(A_l,\varphi)-\varepsilon}\right)\exp\left\{\frac{(\varphi(r))^{\rho(f,\varphi)+\beta+\varepsilon}}{r}\right\}\right)$$

$$+\exp\{(\underline{\tau}(A_k,\varphi)+\varepsilon)(\varphi(r))^{\mu(A_l,\varphi)}\}\exp\left\{\frac{(\varphi(r))^{\rho(f,\varphi)+\beta+\varepsilon}}{r}\right\}+\exp\left((\tau_2+\varepsilon)\varphi(r)^{\mu(A_l,\varphi)}\right)\exp\left\{(\varphi(r))^{(\rho(f,\varphi)+\varepsilon)}\right\}. \tag{13}$$

We can now select a sufficiently small ε that satisfies $0 < 2\varepsilon < \underline{\tau}(A_l,\varphi) - \tau_2$, then from (13), for sufficiently large ($r \in E_6 \setminus ([0,1] \cup E_1 \cup E_2)$), we can write

$$\exp\{(\underline{\tau}(A_l,\varphi) - \tau_2 - 2\varepsilon)(\varphi(r))^{\mu(A_l,\varphi)-\varepsilon}\} \leqslant \exp\left\{(\varphi(r))^{(\rho(f,\varphi)+\varepsilon)}\right\}.$$

Then, by making use of Lemma 2.3, Definition 1.1, we get $\mu(A_l,\varphi) - \varepsilon \leqslant \rho(f,\varphi) + \varepsilon)$. Since $\varepsilon > 0$ is arbitrary, we conclude that $\rho(f,\varphi) \geqslant \mu(A_l,\varphi)$.

4 Proof of Theorem 1.2

When the solution f satisfies $\rho(f,\varphi) = \infty$, the result is valid.

Suppose now that $\rho(f,\varphi)$ is finite. From equation (1) and Lemma 2.1, we get

$$\begin{aligned} T(r,A_l(z)) &= m(r,A_l(z)) + N(r,A_l(z)) \\ &\leqslant \sum_{\substack{j=0 \\ j\neq k,l}}^{n+1} T(r,A_j(z)) + T(r,A_k(z)) + N(r,A_l(z)) \\ &+ T\left(r,\frac{1}{f(z+c_l)}\right) + \sum_{\substack{j=1 \\ j\neq l}}^{n} m\left(r,\frac{f(z+c_j)}{f(z+c_l)}\right) + m\left(r,\frac{f(z)}{f(z+c_l)}\right) + O(1) \end{aligned}$$

$$\leqslant \sum_{\substack{j=0 \\ j\neq k,l}}^{n+1} T(r,A_j(z))+T(r,A_k(z))+N(r,A_l(z))+2T(2r,f)+\sum_{\substack{j=1 \\ j\neq l}}^{n} m\left(r,\frac{f(z+c_j)}{f(z+c_l)}\right)+m\left(r,\frac{f(z)}{f(z+c_l)}\right)+O(1). \tag{14}$$

From the definition of the φ- exponent of convergence of pole-sequence of A_l, for any $\varepsilon > 0$ and sufficiently large r, we can write

$$N(r,A_l) \leqslant (\varphi(r))^{\lambda(\frac{1}{A_l},\varphi)+\varepsilon}. \tag{15}$$

From Lemma 2.5, for the above ε, we get

$$m\left(r,\frac{f(z)}{f(z+c_l)}\right)=O(r^{\rho(f,\varphi)-1+\varepsilon}),m\left(r,\frac{f(z+c_i)}{f(z+c_l)}\right)=O(r^{\rho(f,\varphi)-1+\varepsilon}),\ j\neq l. \tag{16}$$

Case 1. If $\max\{\rho(A_j,\varphi),j\neq k,l\}=\beta<\mu(A_k,\varphi)=\mu(A_l,\varphi),\underline{\tau}(A_l,\varphi)>\underline{\tau}(A_k,\varphi)$. Using the definition of the lower type of A_k and Lemma 2.6, for $p=1$ and any given $\varepsilon(>0)$, there exists a subset $E_4\subset(1,+\infty)$ with infinite logarithmic measure such that for all $r\in E_4$, we have

$$T(r,A_k)<(\underline{\tau}(A_k,\varphi)+\varepsilon)\{\varphi(r)\}^{\mu(A_k,\varphi)}=(\underline{\tau}(A_k,\varphi)+\varepsilon)\{\varphi(r)\}^{\mu(A_l,\varphi)}, \tag{17}$$

and from the definitions of the φ-order of A_j , f and the φ-lower type of A_l, for any given ε defined above and sufficiently large r, we have

$$T(r,A_j)\leqslant(\varphi(r))^{\rho(A_j,\varphi)+\varepsilon}\leqslant(\varphi(r))^{\beta+\varepsilon},\quad T(r,f)\leqslant(\varphi(r))^{\rho(f,\varphi)+\varepsilon} \tag{18}$$

and

$$T(r,A_l)\geqslant(\underline{\tau}(A_l,\varphi)-\varepsilon)(\varphi(r))^{\mu(A_l,\varphi)}. \tag{19}$$

By replacing (15), (16), (17), (18) and (19) into (14), for sufficiently large $r\in E_4$, we get

$$\begin{aligned}(\underline{\tau}(A_l,\varphi)-\varepsilon)(\varphi(r))^{\mu(A_l,\varphi)}&\leqslant n(\varphi(r))^{\beta+\varepsilon}+(\underline{\tau}(A_k,\varphi)+\varepsilon)\{\varphi(r)\}^{\mu(A_l,\varphi)}\\&+(\varphi(r))^{\lambda(\frac{1}{A_l},\varphi)+\varepsilon)}+2(\varphi(2r))^{\rho(f,\varphi)+\varepsilon}+O(r^{\rho(f,\varphi)-1+\varepsilon}).\end{aligned} \tag{20}$$

We can now select a sufficiently small ε that satisfies

$$0<2\varepsilon<\min\{\underline{\tau}(A_l,\varphi)-\underline{\tau}(A_k,\varphi),\mu(A_l,\varphi)-\beta,\mu(A_l,\varphi)-\lambda(\frac{1}{A_l},\varphi)\}$$

then from (20), for sufficiently large $(r\in E_4\setminus([0,1]\cup E_1\cup E_2))$, we can write

$$(\underline{\tau}(A_l,\varphi)-\underline{\tau}(A_k,\varphi)-2\varepsilon))(\varphi(r))^{\mu(A_l,\varphi)-\varepsilon}\leqslant(\varphi(r))^{\rho(f,\varphi)+\varepsilon}.$$

Then, by making use of Remark 1.2, Definition 1.1, we get

$$\mu(A_l,\varphi)\leqslant\rho(f,\varphi)+2\varepsilon.$$

Since $\varepsilon>0$ is arbitrary, we deduce that $\rho(f,\varphi)\geqslant\mu(A_l,\varphi)$.

Case 2. If

$$\mu(A_k,\varphi)<\max\{\rho(A_j,\varphi)\ :\ j\neq k,l\}=\mu(A_l,\varphi)$$

and

$$\sum_{\rho(A_j,\varphi)=\mu(A_l,\varphi)>0,\quad j\neq k,l}\tau(A_j,\varphi)<\underline{\tau}(A_l,\varphi)<+\infty$$

Then, we can find a set $I\subseteq\{0,1,\ldots,n+1\}\setminus\{k,l\}$, such that for $j\in I$, we can write $\rho(A_j,\varphi)=\mu(A_l,\varphi)$ with

$$\sum_{j\in I}\tau(A_j,\varphi)=\tau_1<\tau(A_l,\varphi),$$

and for $j\in\{0,1,\ldots,n+1\}\setminus(I\cup\{k,l\})$, we have $\rho(A_j,\varphi)<\mu(A_l,\varphi)$. Using the definitions of the φ -order and the lower φ -order and the φ -type, for any given $\varepsilon>0$ and sufficiently large r, we get

$$T\left(r,A_j\right)\leqslant(\tau(A_j,\varphi)+\varepsilon)\varphi(r)^{\mu(A_l,\varphi)},j\in I, \tag{21}$$

and

$$T\left(r,A_j\right)\leqslant\varphi(r)^{\mu(A_l,\varphi)-\varepsilon},j\in\{0,1,\ldots,n+1\}\setminus(I\cup\{k,l\}). \tag{22}$$

Through the use of the definition of $\mu(A_k,\varphi)$ and Lemma 2.7, for any given $\varepsilon(>0)$, there exists a set $E_5\subset(1,+\infty)$ with $m_l=+\infty$ such that for all $r\in E_5$, we have

$$T(r,A_k)\leqslant(\varphi(r))^{\mu(A_k,\varphi)+\varepsilon}. \tag{23}$$

By replacing (15), (16), (18),(19), (21), (22), (23) into (14), we get for all z satisfying $|z|=r\in E_5$ sufficiently large

$$\begin{aligned}(\underline{\tau}(A_l,\varphi)-\varepsilon)(\varphi(r))^{\mu(A_l,\varphi)}&\leqslant\sum_{j\in I}(\tau(A_j,\varphi)+\varepsilon)(\varphi(r))^{\mu(A_l,\varphi)}\\&+\sum_{j\in\{0,1,\ldots,n+1\}\setminus(I\cup\{k,l\})}(\varphi(r))^{\mu(A_l,\varphi)-\varepsilon}+(\varphi(r))^{\mu(A_k,\varphi)+\varepsilon}\\&+(\varphi(r))^{\lambda(\frac{1}{A_l},\varphi)+\varepsilon)}+2(\varphi(2r))^{\rho(f,\varphi)+\varepsilon}+O(r^{\rho(f,\varphi)-1+\varepsilon})\\&\leqslant(\tau_1+n\varepsilon)(\varphi(r))^{\mu(A_l,\varphi)}+O((\varphi(r))^{\mu(A_l,\varphi)-\varepsilon})+(\varphi(r))^{\mu(A_k,\varphi)+\varepsilon)}\\&+(\varphi(r))^{\lambda(\frac{1}{A_l},\varphi)+\varepsilon)}+2(\varphi(2r))^{\rho(f,\varphi)+\varepsilon}+O(r^{\rho(f,\varphi)-1+\varepsilon}).\end{aligned} \tag{24}$$

We can now select a sufficiently small ε that satisfies

$$0<\varepsilon<\min\{\frac{\mu(A_l,\varphi)-\mu(A_k,\varphi)}{2},\frac{\mu(A_l,\varphi)-\lambda(\frac{1}{A_l},\varphi)}{2},\frac{\underline{\tau}(A_l,\varphi)-\tau_1}{n+1}\}$$

As a result, from (24) and for all z satisfying $|z|=r\in E_5$ sufficiently large

$$(\underline{\tau}(A_l,\varphi)-\tau_1-(n+1)\varepsilon)\varphi(r)^{\mu(A_l,\varphi)-\varepsilon)}\leqslant\varphi(r)^{\rho(f,\varphi)+\varepsilon}.$$

Then, by making use of Remark 1.2, Definition 1.1, we get

$$\mu(A_l,\varphi)-2\varepsilon\leqslant\rho(f,\varphi).$$

Since $\varepsilon>0$ is arbitrary, we deduce that $\rho(f,\varphi)\geqslant\mu(A_l,\varphi)$.

Case 3. If

$$\max\{\rho(A_j,\varphi),j\neq k,l\}=\mu(A_k,\varphi)=\mu(A_l,\varphi)$$

and

$$\sum_{\rho(A_j,\varphi)=\mu(A_l,\varphi)>0,j\neq k,l}\tau(A_j,\varphi)+\underline{\tau}(A_k,\varphi)<\underline{\tau}(A_l,\varphi)<+\infty.$$

Then, by substituting (15), (16),(17), (18),(19), (21), (22), into (14), for all z satisfying $|z|=r\in E_4$ sufficiently large, we have

$$\begin{aligned}(\underline{\tau}(A_l,\varphi)-\varepsilon)(\varphi(r))^{\mu(A_l,\varphi)}&\leqslant\sum_{j\in I}(\tau(A_j,\varphi)+\varepsilon)(\varphi(r))^{\mu(A_l,\varphi)}+\sum_{j\in\{0,1,\ldots,n+1\}\setminus(I\cup\{k,l\})}(\varphi(r))^{\mu(A_l,\varphi)-\varepsilon}\\&+(\underline{\tau}(A_k,\varphi)+\varepsilon)(\varphi(r))^{\mu(A_l,\varphi)}+(\varphi(r))^{\lambda(\frac{1}{A_l},\varphi)+\varepsilon}+2(2\varphi(r))^{\rho(f,\varphi)+\varepsilon}+O((\varphi(r))^{\rho(f,\varphi)-1+\varepsilon})\\&\leqslant(\tau_1+\underline{\tau}(A_k,\varphi)+(n+1)\varepsilon)r^{\mu(A_l,\varphi)}+O(\varphi(r)^{\mu(A_l,\varphi)-\varepsilon})\\&+\varphi(r)^{\lambda(\frac{1}{A_l},\varphi)+\varepsilon}+2(2\varphi(r))^{\rho(f,\varphi)+\varepsilon}+O(\varphi(r)^{\rho(f,\varphi)-1+\varepsilon}).\end{aligned} \tag{25}$$

We can now select a sufficiently small ε that satisfies

$$0<\varepsilon<\min\{\frac{\mu(A_l,\varphi)-\lambda(\frac{1}{A_l},\varphi)}{2},\frac{\underline{\tau}(A_l,\varphi)-\tau_1-\underline{\tau}(A_k,\varphi)}{n+2}\}$$

As a result, from (25) and for all z satisfying $|z|=r\in E_4$ sufficiently large

$$(\underline{\tau}(A_l,\varphi)-\tau_1-\underline{\tau}(A_k,\varphi)-(n+2)\varepsilon)(\varphi(r))^{\mu(A_l,\varphi)-\varepsilon)}\leqslant(\varphi(r))^{\rho(f,\varphi)+\varepsilon}.$$

Then, by making use of Remark 1.2, Definition 1.1, we get

$$\mu(A_l, \varphi) - 2\varepsilon \leqslant \rho(f, \varphi).$$

Since $\varepsilon > 0$ is arbitrary, we deduce that $\rho(f, \varphi) \geqslant \mu(A_l, \varphi)$.

Acknowledgments This paper was supported by the Directorate General for Scientific Research and Technological Development (DGRSD).

References

[1] A. Bandyopadhyay, C. Ghosh, S.K. Datta, *Growth of Solutions of Linear Difference Equations with Meromorphic Coefficients in Terms of Iterated $p - \varphi$ Order* , [Submitted on 17 Jun 2022 (v1), last revised 22 Jun 2022 (this version, v2)] http://arxiv.org/abs/2206.08741v2.

[2] B. Belaïdi and R. Bellaama, *Meromorphic Solutions of Higher Order Non-Homogeneous Linear Difference Equations*, Bulletin of th Transilvania University of Brasov, Volume 13(62), Issue 2- 2020, Series III: Mathematics, Informatics and Physics, pages 433-450.

[3] R. Bouabdelli and B. Belaïdi, *Growth and complex oscillation of linear differential equations with meromorphic coefficients of $[p, q] - \varphi$ order.* Internat. J. Anal. Appl. 2014, 6, 178-194.

[4] Z. Chen and X. M. Zheng, *Growth of meromorphic solutions of general complex linear differential-difference equation.* Acta Univ. Apulensis Math. Inform. No. 56 (2018), 1-12.

[5]J. Choi, S.K. Datta and N. Biswas, *Growth analysis of meromorphic solutions of linear difference equations with entire or meromorphic coefficients of finite φ-order*, Symmetry (2021), 13, 267.

[6] I. Chyzhykov, J. Heittokangas, J. Rattya, *Finiteness of φ-order of solutions of linear differential equations in the unit disc.* J. Anal. Math. 2009, 109, 163-198.

[7] S.K. Datta; N. Biswas, *Growth properties of solutions of complex linear differential-difference equations with coefficients having the same φ-order.* Bull. Calcutta Math. Soc. 2019, 111, 253-266.

[8] A. A. Goldberg, I. V. Ostrovskii, *The distribution of values of meromorphic functions*, Irdat Nauk, Moscow, 1970 (in Russian), Transl. Math. Monogr., vol. 236, Amer. Math. Soc., Providence RI, 2008.

[9] G. G. Gundersen, *Estimates for the logarithmic derivative of a meromorphic function*, plus similar estimates, J. London Math. Soc. (2) 37 (1988), no. 1, 88-104.

[10] W. K. Hayman, *Meromorphic functions.* Oxford Mathematical Monographs, Clarendon Press, Oxford 1964.

[11] M. Saidani, F. M. Benguettat and B. Belaïdi , *Study of Complex Oscillation of Solutions to Higher Linear Differential Equations with Meromorphic Coefficients of Finite $[p, q]\varphi$* order Aust. J. Math. Anal. Appl. Vol. 21 (2024), No. 2, Art. 10, 23 pp. AJMAA.

[12] L.M. Sánchez-Ruiz, S.K. Datta, N. Biswas and M. Legua, *Picturing the growth order of solutions in complex linear differential-Difference with coefficients of φ order,* Axiom 2023, 12, 239.

[12] X. Shen, J.Tu, H.Y. Xu, *Complex oscillation of a second-order linear differential equation with entire coefficients of [p, q]-φ order,* Shen et al. Advances in Difference Equations 2014.

OPTIMIZING LESSONS THROUGH MATHEMATICAL MODELS OF ATTENTION AND RETENTION

Maria-Giulia GHEORGHIU[1,5], Nicola Alexandra NICOLAE[2], Simona Mihaela BIBIC[3,5], Ioana-Corina BOGDAN[4,5]

[1]Faculty of Electrical Engineering, National University of Science and Technology Politehnica Bucharest, Romania
[2]"Virgil Madgearu" College of Economics, Bucharest, Romania,
[3]Department of Applied Mathematics, National University of Science and Technology Politehnica Bucharest, Romania,
[4]Faculty of Electrical Engineering and Computer Science, Transilvania University of Brasov, Brasov, Romania,
[5]Center for Research and Training in Innovative Techniques of Applied Mathematics in Engineering, National University of Science and Technology Politehnica Bucharest, Romania

Corresponding author email: maria.gheorghiu@stud.electro.upb.ro, nicolaenicola72@gmail.com, simona.bibic@upb.ro, corina.bogdan@unitbv.ro

Abstract
The effectiveness of the learning process depends largely on students' ability to maintain attention during instruction and to retain knowledge over time. While educational psychology has long documented the forgetting curve and the benefits of repetition. This paper proposes a mathematical framework for modeling both retention and attention in the educational process. Retention is described through an exponential decay function, extended with impulse-like reinforcement to represent spaced repetition, while attention dynamics are approximated using Gaussian and exponential models. Numerical simulations illustrate the differences between simple forgetting, forgetting with repetition, and learning scenarios influenced by attention. The results indicate that strategic reviews can significantly increase long-term knowledge retention, while shorter, well-timed lessons optimize attention. Beyond theoretical insights, the proposed equations have practical applicability in lesson planning, scheduling effective repetitions, and optimizing the duration of teaching sessions and breaks.
Key words*: Educational data analysis; Learning optimization; Mathematical modeling; Forgetting curve.*

1. INTRODUCTION

Education relies on two key cognitive mechanisms: attention and retention. Research over the past century has shown that learning depends on how the brain processes, stores, and retrieves information. Ebbinghaus's forgetting curve (1885) revealed that memory decays exponentially, but repetition improves long-term retention. Attention, in contrast, varies dynamically, rising at the start of a lesson, peaking, then declining with fatigue or distraction. Combining models of attention and retention offers a valuable framework for applying mathematics and computer science to education, enabling data-driven strategies for lesson design, review scheduling, and digital tool integration.

2. CONTENT

Learning is strongly influenced by two cognitive processes: retention, which reflects the ability to store knowledge, and attention, which determines the capacity to focus during instruction. Mathematical models of these phenomena allow researchers to describe and predict how information is remembered or forgotten, and how concentration fluctuates over time.

The Forgetting Curve

The process of forgetting information was first systematically studied by Hermann Ebbinghaus in 1885. Through experiments based on memorizing nonsense syllables, he observed that information is lost rapidly immediately after learning, and that the rate of forgetting then slows progressively. This

phenomenon was graphically represented in the so-called "forgetting curve," which describes the exponential decline of memory retention [1, 3]. From a mathematical perspective, this dynamic can be approximated by the equation:

$$R(t) = R_0 e^{-\lambda t} \quad (1)$$

where R_0 represents the initial level of retention, t is the time elapsed since learning, and λ is the forgetting rate.

Spaced Repetition

To analyze the phenomenon of forgetting, educational psychology introduced the concept of spaced repetition [2]. This principle states that information is retained more effectively when reviews are performed at increasing intervals, rather than when they are concentrated in a single session.

$$R(t) = R_0 e^{-\lambda(t-t_i)} + \sum_{i=1}^{n} \alpha_i e^{-\lambda(t-t_i)} \quad (2)$$

where t indicates the moments when reviews occur, and α represents the contribution of each review to memory consolidation. Thus, after every review, the retention curve rises again close to its initial level, and the rate of decline becomes slower.

Attention Models

Students' attention during a lesson is not constant but rather fluctuate over time. In literature, several mathematical formulas have been proposed to approximate this dynamic. In this paper, two models are analyzed: the logistic function and the Gaussian function.

Logistic function

$$f(t) = \frac{1}{1 + e^{-\beta(t-t_0)}} \quad (3)$$

This equation describes a gradual increase in attention from a low level to a maximum. The parameter β controls the rate of growth, while t_0 indicates the moment when attention reaches 50% of its maximum value. The logistic model is suitable for capturing the initial phase of the lesson, when students shift from distraction or lack of focus to a high level of concentration. However, its limitation is that attention tends toward a constant value, without describing the natural decline that occurs in the later stages of a lesson.

Gaussian function

$$A(t) = A_0 e^{-\frac{(t-\mu)^2}{2\sigma^2}} \quad (4)$$

The Gaussian function represents attention as a bell-shaped distribution: it increases until it reaches a maximum μ, then progressively decreases. The parameter σ controls the width of the attention window. This model is more realistic for full lessons, as it captures both the activation of attention at the beginning and its decline due to fatigue or loss of interest.

3. CONCLUSIONS

This study highlighted how mathematical models can describe two essential dimensions of learning: memory retention and student attention. The forgetting curve, reinforced through spaced repetition, and the Gaussian or logistic functions for attention provide useful tools for predicting and optimizing learning outcomes.

REFERENCES

[1] Anderson, J. R. (2000). *Learning and Memory: An Integrated Approach* (2nd ed.). Wiley.

[2] Wickens, C. D., Hollands, J. G., Banbury, S., & Parasuraman, R. (2015). Engineering Psychology and Human Performance (4th ed.). Psychology Press.

[3] Pavlik, P. I., & Anderson, J. R. (2005). *Practice and forgetting effects on vocabulary memory*

A Variational Approach to Optimal Control with Generalized Invariant Convex Interval-Valued Functionals

Marilena Ciontescu[1]

[1]Faculty of Applied Sciences, National University of Science and Technology POLITEHNICA Bucharest, 060042 Bucharest, Romania;

Abstract

This paper studies some results on solutions associated with interval-valued optimal control problems driven by generalized invariant convex functionals. Necessary conditions of optimality are stated for the considered optimization problem. Also, the sufficiency of the necessary optimality conditions is investigated.

Keywords: optimization problem; interval-valued functionals; $(q, w) - \pi$-invexity; LU-optimal solution.

1 Introduction

Most of the real-world problems have arisen related to measurement errors due to uncertainty or imprecision of the data. The branches most affected by these errors are industry, economics, and science. Thus, there appeared the necessity to optimize various real-world problems. Interval-valued optimization is an emerging branch of mathematics that deals with the uncertainty of optimization problems. Optimality conditions and duality theory play an essential role in the optimization model. The present paper studies some results on solutions associated with a class of interval-valued optimal control problems driven by generalized invex functionals. The topic covered in this article is a developing area of operations research that plays a vital role in addressing uncertainty in optimization problems.

2 Preliminaries and problem formulation

In the following, we establish the notations and elements in order to formulate the main results stated in the present study.

Let I be the family of closed bounded real intervals. If $A \in I$, then $A = [a^L, a^U]$, with a^L and a^U as the lower and upper bounds for A, respectively.

For $a^L = a^U = a$, we get $A = [a, a] = a$ is a real scalar. If $A = \left[a^L, a^U\right]$, $B = \left[b^L, b^U\right] \in I$, we define:

(i) $A + B = \{a + b : a \in A \text{ and } b \in B\} = \left[a^L + b^L, a^U + b^U\right]$,

(ii) $-A = \{-a : a \in A\} = \left[-a^U, -a^L\right]$.

We notice that $A - B = A + (-B) = \left[a^L - b^U, a^U - b^L\right]$. We also have

(i) $k + A = \{k + a : a \in A\} = \left[k + a^L, k + a^U\right]$,

(ii) $kA = \{ka : a \in A\} = \begin{cases} \left[ka^L, ka^U\right] & \text{if } k \geq 0 \\ \left[ka^U, ka^L\right] & \text{if } k < 0, \end{cases}$ where $k \in \mathbb{R}$.

Let $\mathbb{R}^n$ denote the classical real n-dimensional Euclidean space. The function $\mathrm{K} : \mathbb{R}^n \times \mathbb{R}^p \to I$ is an interval-valued continuously differentiable functional, that is, $\mathrm{K}(x, u) = \mathrm{K}(x_1, x_2, \ldots, x_n, u_1, u_2, \ldots, u_p)$ is a closed bounded real interval, for each piecewise smooth state function $x : [a, b] \subset \mathbb{R} \to \mathbb{R}^n$, $x = x(t) \in \mathbb{R}^n$, and piecewise continuous control function $u : [a, b] \subset \mathbb{R} \to \mathbb{R}^p$, $u = u(t) \in \mathbb{R}^p$. The interval-valued functional K can be formulated as $\mathrm{K}(x, u) = \left[\mathrm{K}^L(x, u), \mathrm{K}^U(x, u)\right]$, with $\mathrm{K}^L(x, u)$, $\mathrm{K}^U(x, u)$ two real-valued functionals defined on $\mathbb{R}^n \times \mathbb{R}^p$ and satisfy the condition $\mathrm{K}^L(x, u) \leq \mathrm{K}^U(x, u)$, for each $x = x(t) \in \mathbb{R}^n$ and $u = u(t) \in \mathbb{R}^p$, with $t \in [a, b]$. Let $\mathcal{X}$ be the space of piecewise smooth state functions $x : [a, b] \subset \mathbb{R} \to \mathbb{R}^n$ such that $x(a) = \alpha$ and $x(b) = \beta$ and consider it is equipped with the norm $\| x \| = \| x \|_\infty + \| \dot{x} \|_\infty$. Also, let $\mathcal{U}$ be the space of piecewise continuous control functions $u : [a, b] \subset \mathbb{R} \to \mathbb{R}^p$, endowed with the uniform norm, as well.

In the following, for $A = \left[a^L, a^U\right]$ and $B = \left[b^L, b^U\right]$, we use the partial ordering $A \leq_{LU} B$ if and only if $a^L \leq b^L$ and $a^U \leq b^U$. Also, we write $A <_{LU} B$ if and only if $A \leq_{LU} B$ but $A \neq B$. This means that $A <_{LU} B$ if and only if

$$\begin{array}{lll} a^L < b^L, & a^U \leq b^U, & \text{or} \\ a^L \leq b^L, & a^U < b^U, & \text{or} \\ a^L < b^L, & a^U < b^U. & \end{array}$$

We use the notations: $f_x(t, z, r) := \frac{\partial f}{\partial x}(t, z, r)$, $f_u(t, z, r) := \frac{\partial f}{\partial u}(t, z, r)$, $\mathbf{1}_x := (1, 1, \cdots, 1) \in \mathbb{R}^n$, $\mathbf{1}_u := (1, 1, \cdots, 1) \in \mathbb{R}^p$, $\mathbf{K}(x, u) := \int_a^b f(t, x(t), u(t))dt$, with $f : [a, b] \times \mathbb{R}^n \times \mathbb{R}^p \to \mathbb{R}$, $\mathbf{K} : \mathcal{X} \times \mathcal{U} \to \mathbb{R}$.

The following definitions will be used in the sequel in order to formulate and prove the main results derived in the present paper.

Definition 2.1 Consider q, w are two real scalars and $f : [a, b] \times \mathbb{R}^n \times \mathbb{R}^p \to \mathbb{R}$ is a smooth function. If there exist the functions $\tau : (\mathbb{R}^n \times \mathbb{R}^p)^2 \to \mathbb{R}^n$, $\nu : (\mathbb{R}^n \times \mathbb{R}^p)^2 \to \mathbb{R}^p$, $\sigma : (\mathbb{R}^n \times \mathbb{R}^p)^2 \to \mathbb{R}^n$ and the real scalar $\pi \in \mathbb{R}$, with

$\tau(a) = \tau(b) = \nu(a) = \nu(b) = 0$, such that the following inequalities

$$\frac{1}{w}\left(\mathrm{e}^{w(\mathbf{K}(x,u)-\mathbf{K}(z,r))}-1\right)(>) \geq \frac{1}{q}\int_a^b f_x(t,z,r)\left(\mathrm{e}^{q\tau(x,u,z,r)}-\mathbf{1}_x\right)dt$$
$$+\frac{1}{q}\int_a^b f_u(t,z,r)\left(\mathrm{e}^{q\nu(x,u,z,r)}-\mathbf{1}_u\right)dt+\pi\|\sigma(x,u,z,r)\|^2, \quad \text{for } q\neq 0,\ w\neq 0,$$
$$\frac{1}{w}\left(\mathrm{e}^{w(\mathbf{K}(x,u)-\mathbf{K}(z,r))}-1\right)(>) \geq \int_a^b f_x(t,z,r)\tau(x,u,z,r)dt$$
$$+\int_a^b f_u(t,z,r)\nu(x,u,z,r)dt+\pi\|\sigma(x,u,z,r)\|^2, \quad \text{for } q=0,\ w\neq 0,$$
$$\mathbf{K}(x,u)-\mathbf{K}(z,r)(>) \geq \frac{1}{q}\int_a^b f_x(t,z,r)\left(\mathrm{e}^{q\tau(x,u,z,r)}-\mathbf{1}_x\right)dt$$
$$+\frac{1}{q}\int_a^b f_u(t,z,r)\left(\mathrm{e}^{q\nu(x,u,z,r)}-\mathbf{1}_u\right)dt+\pi\|\sigma(x,u,z,r)\|^2, \quad \text{for } q\neq 0,\ w=0,$$
$$\mathbf{K}(x,u)-\mathbf{K}(z,r)(>) \geq \int_a^b f_x(t,z,r)\tau(x,u,z,r)dt+\int_a^b f_u(t,z,r)\nu(x,u,z,r)dt$$
$$+\pi\|\sigma(x,u,z,r)\|^2, \quad \text{for } q=0,\ w=0$$

are satisfied, then the real-valued functional $\mathbf{K}$ is named *(strictly)* $(q,w)-\pi$-*invex at* (z,r) *on* $\mathcal{X}\times\mathcal{U}$ *with respect to* τ,ν *and* σ.

Definition 2.2 Consider q, w are two real scalars and $f : [a,b]\times\mathbb{R}^n\times\mathbb{R}^p \to \mathbb{R}$ is a smooth function. If there exist the functions $\tau : (\mathbb{R}^n\times\mathbb{R}^p)^2 \to \mathbb{R}^n$, $\nu : (\mathbb{R}^n\times\mathbb{R}^p)^2 \to \mathbb{R}^p$, $\sigma : (\mathbb{R}^n\times\mathbb{R}^p)^2 \to \mathbb{R}^n$ and the real scalar $\pi\in\mathbb{R}$, with

$\tau(a) = \tau(b) = \nu(a) = \nu(b) = 0$, such that the following inequalities

$$\begin{aligned}
&\frac{1}{q}\int_a^b f_x(t,z,r)\left(\mathrm{e}^{q\tau(x,u,z,r)} - \mathbf{1}_x\right)dt \\
&+ \frac{1}{q}\int_a^b f_u(t,z,r)\left(\mathrm{e}^{q\nu(x,u,z,r)} - \mathbf{1}_u\right)dt + \pi\|\sigma(x,u,z,r)\|^2 \geq 0 \\
&\Rightarrow \frac{1}{w}\left(\mathrm{e}^{w(\mathbf{K}(x,u)-\mathbf{K}(z,r))} - 1\right)(>) \geq 0, \quad \text{for } q \neq 0,\ w \neq 0, \\
&\int_a^b f_x(t,z,r)\tau(x,u,z,r)dt \\
&+ \int_a^b f_u(t,z,r)\nu(x,u,z,r)dt + \pi\|\sigma(x,u,z,r)\|^2 \geq 0 \\
&\Rightarrow \frac{1}{w}\left(\mathrm{e}^{w(\mathbf{K}(x,u)-\mathbf{K}(z,r))} - 1\right)(>) \geq 0, \quad \text{for } q = 0,\ w \neq 0, \\
&\frac{1}{q}\int_a^b f_x(t,z,r)\left(\mathrm{e}^{q\tau(x,u,z,r)} - \mathbf{1}_x\right)dt \\
&+ \frac{1}{q}\int_a^b f_u(t,z,r)\left(\mathrm{e}^{q\nu(x,u,z,r)} - \mathbf{1}_u\right)dt + \pi\|\sigma(x,u,z,r)\|^2 \geq 0 \\
&\Rightarrow \mathbf{K}(x,u) - \mathbf{K}(z,r)(>) \geq 0, \quad \text{for } q \neq 0,\ w = 0, \\
&\int_a^b f_x(t,z,r)\tau(x,u,z,r)dt + \int_a^b f_u(t,z,r)\nu(x,u,z,r)dt \\
&+ \pi\|\sigma(x,u,z,r)\|^2 \geq 0 \\
&\Rightarrow \mathbf{K}(x,u) - \mathbf{K}(z,r)(>) \geq 0, \quad \text{for } q = 0,\ w = 0
\end{aligned}$$

are satisfied, then the real-valued functional $\mathbf{K}$ is named *(strictly)* $(q,w) - \pi$-*pseudoinvex at* (z,r) *on* $\mathcal{X} \times \mathcal{U}$ *with respect to* τ, ν *and* σ.

Definition 2.3 Consider q, w are two real scalars and $f : [a,b] \times \mathbb{R}^n \times \mathbb{R}^p \to \mathbb{R}$ is a smooth function. If there exist the functions $\tau : (\mathbb{R}^n \times \mathbb{R}^p)^2 \to \mathbb{R}^n$, $\nu : (\mathbb{R}^n \times \mathbb{R}^p)^2 \to \mathbb{R}^p$, $\sigma : (\mathbb{R}^n \times \mathbb{R}^p)^2 \to \mathbb{R}^n$ and the real scalar $\pi \in \mathbb{R}$, with

$\tau(a) = \tau(b) = \nu(a) = \nu(b) = 0$, such that the following inequalities

$$\frac{1}{w}\left(\mathrm{e}^{w(\mathbf{K}(x,u)-\mathbf{K}(z,r))} - 1\right) \leq 0 \Rightarrow \frac{1}{q}\int_a^b f_x(t,z,r)\left(\mathrm{e}^{q\tau(x,u,z,r)} - \mathbf{1}_x\right)dt$$
$$+ \frac{1}{q}\int_a^b f_u(t,z,r)\left(\mathrm{e}^{q\nu(x,u,z,r)} - \mathbf{1}_u\right)dt \leq -\pi\|\sigma(x,u,z,r)\|^2, \quad \text{for } q \neq 0,\ w \neq 0,$$
$$\frac{1}{w}\left(\mathrm{e}^{w(\mathbf{K}(x,u)-\mathbf{K}(z,r))} - 1\right) \leq 0 \Rightarrow \int_a^b f_x(t,z,r)\tau(x,u,z,r)dt$$
$$+ \int_a^b f_u(t,z,r)\nu(x,u,z,r)dt \leq -\pi\|\sigma(x,u,z,r)\|^2, \quad \text{for } q = 0,\ w \neq 0,$$
$$\mathbf{K}(x,u) - \mathbf{K}(z,r) \leq 0 \Rightarrow \frac{1}{q}\int_a^b f_x(t,z,r)\left(\mathrm{e}^{q\tau(x,u,z,r)} - \mathbf{1}_x\right)dt$$
$$+ \frac{1}{q}\int_a^b f_u(t,z,r)\left(\mathrm{e}^{q\nu(x,u,z,r)} - \mathbf{1}_u\right)dt \leq -\pi\|\sigma(x,u,z,r)\|^2, \quad \text{for } q \neq 0,\ w = 0,$$
$$\mathbf{K}(x,u) - \mathbf{K}(z,r) \leq 0 \Rightarrow \int_a^b f_x(t,z,r)\tau(x,u,z,r)dt + \int_a^b f_u(t,z,r)\nu(x,u,z,r)dt$$
$$\leq -\pi\|\sigma(x,u,z,r)\|^2, \quad \text{for } q = 0,\ w = 0$$

are satisfied, then the real-valued functional $\mathbf{K}$ is called $(q,w) - \pi$-*quasiinvex at* (z,r) *on* $\mathcal{X} \times \mathcal{U}$ *with respect to* τ, ν *and* σ.

Remark 2.1 We notice that the exponentials in the right-hand sides of the above-mentioned inequalities are considered componentwise.

Remark 2.2 Without loss of generality, in the rest of this paper, we assume that $w > 0, q > 0$.

In this study, we investigate the primal optimization problem driven by an interval-valued cost functional:

$$\text{(P)} \quad \min_{(x,u)\in\mathcal{X}\times\mathcal{U}} \left\{K(x,u) = \left[K^L(x,u), K^U(x,u)\right]\right\}$$

subject to
$g_j(t,x,u) \leq 0, \quad t \in [a,b],\ j = 1,2,\ldots,m$
$\dfrac{dx_i}{dt} = h_i(t,x,u), \quad t \in [a,b],\ i = 1,2,\ldots,n$
$x(a) = \alpha,\ x(b) = \beta,$

where $K : \mathcal{X} \times \mathcal{U} \to I$ is a C^1-class interval-valued functional,

$$K^L(x,u) := \int_a^b f^L(t,x(t),u(t))dt, \quad K^U(x,u) := \int_a^b f^U(t,x(t),u(t))dt,$$

with $f : [a,b] \times \mathbb{R}^n \times \mathbb{R}^p \to I,\ f = [f^L, f^U]$, a differentiable interval-valued function, $g_j : [a,b] \times \mathbb{R}^n \times \mathbb{R}^p \to \mathbb{R},\ j = 1,2,\ldots,m$, a differentiable real-valued function, and $\alpha, \beta \in \mathbb{R}$ as fixed real numbers.

The next definition, by using the partial ordering defined at the beginning of this section, introduces the concept of optimal solution for the considered variational control problem.

Let Ω be the set of all feasible solutions of (P).

Definition 2.4 The pair $(x^*, u^*) \in \Omega$ is an *LU-optimal solution* of problem (P) if there exists no $(x_0, u_0) \in \Omega$ satisfying $K(x_0, u_0) <_{LU} K(x^*, u^*)$.

The following result (see, for instance, Treanţă [**?**]) presents the Karush-Kuhn-Tucker-type necessary optimality conditions associated with (P).

Theorem 2.1 *If $(x^*, u^*) \in \Omega$ is an LU-optimal solution of primal variational control problem (P) and the constraint functions satisfy constraint qualification at (x^*, u^*), then there exist multipliers (functions on $[a, b]$) $0 < \gamma^L, \gamma^U \in \mathbb{R}$, $0 \leq \zeta_j \in \mathbb{R}$, $j = 1, 2, \ldots, m$, and $\lambda_i \in \mathbb{R}$, $i = 1, 2, \ldots, n$, such that the next relations*

$$\gamma^L \frac{\partial f^L}{\partial x_i}(t, x^*, u^*) + \gamma^U \frac{\partial f^U}{\partial x_i}(t, x^*, u^*) + \sum_{j=1}^{m} \zeta_j \frac{\partial g_j}{\partial x_i}(t, x^*, u^*)$$

$$+ \sum_{i=1}^{n} \lambda_i \frac{h_i}{\partial x_i}(t, x^*, u^*) + \frac{d\lambda_i}{dt}(t) = 0, \quad i = \overline{1, n} \tag{1}$$

$$\gamma^L \frac{\partial f^L}{\partial u_s}(t, x^*, u^*) + \gamma^U \frac{\partial f^U}{\partial u_s}(t, x^*, u^*) + \sum_{j=1}^{m} \zeta_j \frac{\partial g_j}{\partial u_s}(t, x^*, u^*)$$

$$+ \sum_{i=1}^{n} \lambda_i \frac{h_i}{\partial u_s}(t, x^*, u^*) = 0, \quad s = \overline{1, p} \tag{2}$$

$$\zeta_j g_j(t, x^*, u^*) = 0, \quad j = \overline{1, m} \tag{3}$$

are fulfilled for all $t \in [a, b]$, except at discontinuities.

Remark 2.3 The Lagrange multipliers $0 \leq \zeta_j \in \mathbb{R}$, $j = 1, 2, \ldots, m$, and $\lambda_i \in \mathbb{R}$, $i = 1, 2, \ldots, n$, mentioned in the above theorem, are assumed to be piecewise smooth functions on $[a, b]$. The Euler-Lagrange partial differential equations, given in (1) and (2), are not considered for the discontinuity points associated with the functions mentioned above.

3 Sufficient conditions of optimality associated with (P)

In the present section, we formulate and prove two results on sufficient conditions of optimality for (P).

The next result, by considering only the $(q, w) - \pi$-invexity assumptions of the involved functionals, introduces sufficient conditions of optimality for (P).

Theorem 3.1 *Let $(x^*, u^*) \in \Omega$, the constraint functions satisfy the suitable Kuhn-Tucker constraint qualification at (x^*, u^*), and the relations (1)-(3) from Theorem 2.1 are satisfied for $t \in [a, b]$, except at discontinuities. Moreover, we assume that K^L and K^U are $(q, w) - \pi_1$-invex and $(q, w) - \pi_2$-invex at (x^*, u^*) with respect to τ, ν and σ, respectively, and $G(x, u) := \int_a^b \sum_{j=1}^m \zeta_j g_j(t, x, u)dt$ and $H(x, u) := \int_a^b \sum_{i=1}^n \lambda_i[h_i(t, x, u) - \dot{x}_i]dt$ are $(q, w) - \pi_3$-invex and $(q, w) - \pi_4$-invex at (x^*, u^*) with respect to τ, ν and σ, respectively. If $\gamma^L\pi_1 + \gamma^U\pi_2 + \pi_3 + \pi_4 \geq 0$, then (x^*, u^*) is an LU-optimal solution to the problem (P).*

Proof. We assume that (x^*, u^*) is not an LU-optimal solution of (P). This fact implies there exists $(x_0, u_0) \in \Omega$ such that

$$K\left(x_0, u_0\right) <_{LU} K\left(x^*, u^*\right),$$

that is,

$$\left\{ \begin{array}{l} K^L(x_0, u_0) < K^L(x^*, u^*) \\ K^U(x_0, u_0) < K^U(x^*, u^*), \end{array} \right. \text{ or } \left\{ \begin{array}{l} K^L(x_0, u_0) \leq K^L(x^*, u^*) \\ K^U(x_0, u_0) < K^U(x^*, u^*), \end{array} \right.$$

$$\text{or } \left\{ \begin{array}{l} K^L\left(x_0, u_0\right) < K^L\left(x^*, u^*\right) \\ K^U\left(x_0, u_0\right) \leq K^U\left(x^*, u^*\right). \end{array} \right.$$

Since we have $w > 0$, by using the properties of exponential functions, we get

$$\left\{ \begin{array}{l} \frac{1}{w}[e^{w\{K^L(x_0,u_0) - K^L(x^*,u^*)\}} - 1] < 0 \\ \frac{1}{w}[e^{w\{K^U(x_0,u_0) - K^U(x^*,u^*)\}} - 1] < 0, \end{array} \right. \text{ or}$$

$$\left\{ \begin{array}{l} \frac{1}{w}\left[e^{w\left\{K^L(x_0,u_0) - K^L(x^*,u^*)\right\}} - 1\right] \leq 0 \\ \frac{1}{w}\left[e^{w\left\{K^U(x_0,u_0) - K^U(x^*,u^*)\right\}} - 1\right] < 0, \end{array} \right. \text{ or}$$

$$\left\{ \begin{array}{l} \frac{1}{w}\left[e^{w\left\{K^L(x_0,u_0) - K^L(x^*,u^*)\right\}} - 1\right] < 0 \\ \frac{1}{w}\left[e^{w\left\{K^U(x_0,u_0) - K^U(x^*,u^*)\right\}} - 1\right] \leq 0. \end{array} \right.$$

Using the $(q, w) - \pi_1$-invexity property of K^L and the $(q, w) - \pi_2$-invexity property of K^U with respect to τ, ν and σ at (x^*, u^*) at (x^*, u^*), the above inequalities imply

$$\frac{1}{q}\int_a^b f_x^L(t, x^*, u^*)\left(\mathrm{e}^{q\tau(x_0,u_0,x^*,u^*)} - \mathbf{1}_x\right)dt$$

$$+\frac{1}{q}\int_a^b f_u^L(t, x^*, u^*)\left(\mathrm{e}^{q\nu(x_0,u_0,x^*,u^*)} - \mathbf{1}_u\right)dt + \pi_1\|\sigma(x_0, u_0, x^*, u^*)\|^2 < 0,$$

$$\frac{1}{q}\int_a^b f_x^U(t, x^*, u^*)\left(\mathrm{e}^{q\tau(x_0,u_0,x^*,u^*)} - \mathbf{1}_x\right)dt$$

$$+\frac{1}{q}\int_a^b f_u^U(t, x^*, u^*)\left(\mathrm{e}^{q\nu(x_0,u_0,x^*,u^*)} - \mathbf{1}_u\right)dt + \pi_2\|\sigma(x_0, u_0, x^*, u^*)\|^2 < 0,$$

or

$$\frac{1}{q}\int_a^b f_x^L(t,x^*,u^*)\left(\mathrm{e}^{q\tau(x_0,u_0,x^*,u^*)}-\mathbf{1}_x\right)dt$$

$$+\frac{1}{q}\int_a^b f_u^L(t,x^*,u^*)\left(\mathrm{e}^{q\nu(x_0,u_0,x^*,u^*)}-\mathbf{1}_u\right)dt+\pi_1\|\sigma(x_0,u_0,x^*,u^*)\|^2\leq 0,$$

$$\frac{1}{q}\int_a^b f_x^U(t,x^*,u^*)\left(\mathrm{e}^{q\tau(x_0,u_0,x^*,u^*)}-\mathbf{1}_x\right)dt$$

$$+\frac{1}{q}\int_a^b f_u^U(t,x^*,u^*)\left(\mathrm{e}^{q\nu(x_0,u_0,x^*,u^*)}-\mathbf{1}_u\right)dt+\pi_2\|\sigma(x_0,u_0,x^*,u^*)\|^2<0,$$

or

$$\frac{1}{q}\int_a^b f_x^L(t,x^*,u^*)\left(\mathrm{e}^{q\tau(x_0,u_0,x^*,u^*)}-\mathbf{1}_x\right)dt$$

$$+\frac{1}{q}\int_a^b f_u^L(t,x^*,u^*)\left(\mathrm{e}^{q\nu(x_0,u_0,x^*,u^*)}-\mathbf{1}_u\right)dt+\pi_1\|\sigma(x_0,u_0,x^*,u^*)\|^2<0,$$

$$\frac{1}{q}\int_a^b f_x^U(t,x^*,u^*)\left(\mathrm{e}^{q\tau(x_0,u_0,x^*,u^*)}-\mathbf{1}_x\right)dt$$

$$+\frac{1}{q}\int_a^b f_u^U(t,x^*,u^*)\left(\mathrm{e}^{q\nu(x_0,u_0,x^*,u^*)}-\mathbf{1}_u\right)dt+\pi_2\|\sigma(x_0,u_0,x^*,u^*)\|^2\leq 0.$$

Since $\gamma^L>0$ and $\gamma^U>0$, from the above inequalities, we get

$$\frac{1}{q}\gamma^L\int_a^b f_x^L(t,x^*,u^*)\left(\mathrm{e}^{q\tau(x_0,u_0,x^*,u^*)}-\mathbf{1}_x\right)dt$$

$$+\frac{1}{q}\gamma^L\int_a^b f_u^L(t,x^*,u^*)\left(\mathrm{e}^{q\nu(x_0,u_0,x^*,u^*)}-\mathbf{1}_u\right)dt+\gamma^L\pi_1\|\sigma(x_0,u_0,x^*,u^*)\|^2$$

$$+\frac{1}{q}\gamma^U\int_a^b f_x^U(t,x^*,u^*)\left(\mathrm{e}^{q\tau(x_0,u_0,x^*,u^*)}-\mathbf{1}_x\right)dt$$

$$+\frac{1}{q}\gamma^U\int_a^b f_u^U(t,x^*,u^*)\left(\mathrm{e}^{q\nu(x_0,u_0,x^*,u^*)}-\mathbf{1}_u\right)dt+\gamma^U\pi_2\|\sigma(x_0,u_0,x^*,u^*)\|^2<0. \tag{4}$$

Next, by considering the feasibility property of (x_0,u_0) to (P), we obtain

$$g_j\left(t,x_0,u_0\right)\leq 0,\quad t\in[a,b],\ j=\overline{1,m}.$$

Since we have $\zeta_j\geq 0,\ j=\overline{1,m}$, then the relation (3) and the above inequality involve

$$\sum_{j=1}^m \zeta_j g_j\left(t,x_0,u_0\right)\leq\sum_{j=1}^m \zeta_j g_j\left(t,x^*,u^*\right),\quad t\in[a,b],$$

which implies

$$\int_a^b \sum_{j=1}^m \zeta_j g_j\left(t, x_0, u_0\right) dt \leq \int_a^b \sum_{j=1}^m \zeta_j g_j\left(t, x^*, u^*\right) dt, \quad t \in [a, b],$$

Since we have $w > 0$, by using the properties of exponential functions, we obtain

$$\frac{1}{w}\left[e^{w\left\{\int_a^b \sum_{j=1}^m \zeta_j g_j(t,x_0,u_0)dt - \int_a^b \sum_{j=1}^m \zeta_j g_j(t,x^*,u^*)dt\right\}} - 1\right] \leq 0,$$

and by considering that $G(x,u)$ is $(q,w)-\pi_3$-invex at (x^*,u^*), with respect to τ, ν and σ, we get

$$\frac{1}{q}\int_a^b \sum_{j=1}^m \zeta_j \frac{\partial g_j}{\partial x}\left(t, x^*, u^*\right)\left(e^{q\tau(x_0,u_0,x^*,u^*)} - \mathbf{1}_x\right) dt$$

$$+\frac{1}{q}\int_a^b \sum_{j=1}^m \zeta_j \frac{\partial g_j}{\partial u}\left(t, x^*, u^*\right)\left(e^{q\tau(x_0,u_0,x^*,u^*)} - \mathbf{1}_u\right) dt + \pi_3 \left\|\sigma\left(x_0, u_0, x^*, u^*\right)\right\|^2 \leq 0. \tag{5}$$

In a similar way, by considering the assumption that $H(x,u)$ is $(q,w)-\pi_4$-invex at (x^*,u^*), with respect to τ, ν and σ, we get

$$\frac{1}{q}\int_a^b \sum_{i=1}^n \lambda_i \frac{\partial(h_i - \dot{x}_i)}{\partial x}\left(t, x^*, u^*\right)\left(e^{q\tau(x_0,u_0,x^*,u^*)} - \mathbf{1}_x\right) dt$$

$$+\frac{1}{q}\int_a^b \sum_{i=1}^n \lambda_i \frac{\partial(h_i - \dot{x}_i)}{\partial u}\left(t, x^*, u^*\right)\left(e^{q\tau(x_0,u_0,x^*,u^*)} - \mathbf{1}_u\right) dt$$

$$+\pi_4 \left\|\sigma\left(x_0, u_0, x^*, u^*\right)\right\|^2 \leq 0. \tag{6}$$

On adding (4), (5) and (6), from the hypothesis that $\left(\gamma^L \pi_1 + \gamma^U \pi_2 + \pi_3 + \pi_4\right) \geq 0$, and by considering (1), we get a contradiction. This completes the proof. □

The next result, by considering the $(q,w)-\pi$-pseudoinvexity and quasiinvexity assumptions of the involved functionals, introduces sufficient conditions of optimality for (P).

Theorem 3.2 *Let $(x^*,u^*) \in \Omega$, the constraint functions satisfy the suitable Kuhn-Tucker constraint qualification at (x^*,u^*), and the relations (1)-(3) from Theorem 2.1 are satisfied for $t \in [a,b]$, except at discontinuities. Moreover, we consider $\gamma^L K^L + \gamma^U K^U$ is $(q,w)-\pi_1$-pseudoinvex at (x^*,u^*) with respect to τ, ν and σ, and $G(x,u) := \int_a^b \sum_{j=1}^m \zeta_j g_j(t,x,u)dt$ and $H(x,u) := \int_a^b \sum_{i=1}^n \lambda_i [h_i(t,x,u) - \dot{x}_i]dt$ are $(q,w)-\pi_2$-quasiinvex and $(q,w)-\pi_3$-quasiinvex at (x^*,u^*) with respect to τ, ν and σ, respectively. If $\pi_1 + \pi_2 + \pi_3 \geq 0$, then (x^*,u^*) is an LU-optimal solution to the problem (P).*

Proof. Consider (x^*, u^*) is not an LU-optimal solution of (P) and, consequently, there exists $(x_0, u_0) \in \Omega$ such that

$$K\left(x_0, u_0\right) <_{LU} K\left(x^*, u^*\right),$$

that is,

$$\left\{ \begin{array}{l} K^L(x_0, u_0) < K^L(x^*, u^*) \\ K^U(x_0, u_0) < K^U(x^*, u^*), \end{array} \right. \text{ or } \left\{ \begin{array}{l} K^L(x_0, u_0) \leq K^L(x^*, u^*) \\ K^U(x_0, u_0) < K^U(x^*, u^*), \end{array} \right.$$

$$\text{or } \left\{ \begin{array}{l} K^L\left(x_0, u_0\right) < K^L\left(x^*, u^*\right) \\ K^U\left(x_0, u_0\right) \leq K^U\left(x^*, u^*\right). \end{array} \right.$$

Since $\gamma^L > 0$ and $\gamma^U > 0$, from the above inequalities, we have

$$\gamma^L K^L\left(x_0, u_0\right) + \gamma^U K^U\left(x_0, u_0\right) < \gamma^L K^L\left(x^*, u^*\right) + \gamma^U K^U\left(x^*, u^*\right),$$

or, equivalently,

$$\int_a^b [\gamma^L f^L\left(t, x_0, u_0\right) + \gamma^U f^U\left(t, x_0, u_0\right)]dt < \int_a^b [\gamma^L f^L\left(t, x^*, u^*\right) + \gamma^U f^U\left(t, x^*, u^*\right)]dt.$$

Since we have $w > 0$, by using the properties of exponential functions, it follows

$$\frac{1}{w}\left[e^{w\left\{\left(\gamma^L K^L(x_0,u_0)+\gamma^U K^U(x_0,u_0)\right)-\left(\gamma^L K^L(x^*,u^*)+\gamma^U K^U(x^*,u^*)\right)\right\}} - 1\right] < 0,$$

which together with the assumption that $\gamma^L K^L + \gamma^U K^U$ is $(q, w)-\pi_1$-pseudoinvex at (x^*, u^*), with respect to τ, ν and σ, gives

$$\frac{1}{q}\gamma^L \int_a^b f_x^L(t, x^*, u^*)\left(\mathrm{e}^{q\tau(x_0,u_0,x^*,u^*)} - \mathbf{1}_x\right) dt$$

$$+\frac{1}{q}\gamma^L \int_a^b f_u^L(t, x^*, u^*)\left(\mathrm{e}^{q\nu(x_0,u_0,x^*,u^*)} - \mathbf{1}_u\right) dt + \pi_1 \|\sigma(x_0, u_0, x^*, u^*)\|^2$$

$$+\frac{1}{q}\gamma^U \int_a^b f_x^U(t, x^*, u^*)\left(\mathrm{e}^{q\tau(x_0,u_0,x^*,u^*)} - \mathbf{1}_x\right) dt$$

$$+\frac{1}{q}\gamma^U \int_a^b f_u^U(t, x^*, u^*)\left(\mathrm{e}^{q\nu(x_0,u_0,x^*,u^*)} - \mathbf{1}_u\right) dt < 0. \tag{7}$$

Next, by considering the feasibility property of (x_0, u_0) to (P), we get

$$g_j\left(t, x_0, u_0\right) \leq 0, \quad t \in [a, b],\ j = 1, 2, \ldots, m.$$

But, we have $\zeta_j \geq 0, j = 1, 2, \ldots, m$, and the relation (3) and the above inequality yield

$$\sum_{j=1}^m \zeta_j g_j\left(t, x_0, u_0\right) \leq \sum_{j=1}^m \zeta_j g_j\left(t, x^*, u^*\right), \quad t \in [a, b],$$

which involves

$$\int_a^b \sum_{j=1}^m \zeta_j g_j\left(t, x_0, u_0\right) dt \leq \int_a^b \sum_{j=1}^m \zeta_j g_j\left(t, x^*, u^*\right) dt, \quad t \in [a, b],$$

Since we have $w > 0$, by using the properties associated with exponential functions, we get

$$\frac{1}{w}\left[e^{w\left\{\int_a^b \sum_{j=1}^m \zeta_j g_j(t,x_0,u_0)dt - \int_a^b \sum_{j=1}^m \zeta_j g_j(t,x^*,u^*)dt\right\}} - 1\right] \leq 0,$$

which together with the assumption that $G(x, u)$ is $(q, w) - \pi_2$-quasiinvex at (x^*, u^*), with respect to τ, ν and σ, involves

$$\frac{1}{q}\int_a^b \sum_{j=1}^m \zeta_j \frac{\partial g_j}{\partial x}\left(t, x^*, u^*\right)\left(e^{q\tau\left(x_0, u_0, x^*, u^*\right)} - \mathbf{1}_x\right) dt$$

$$+\frac{1}{q}\int_a^b \sum_{j=1}^m \zeta_j \frac{\partial g_j}{\partial u}\left(t, x^*, u^*\right)\left(e^{q\tau\left(x_0, u_0, x^*, u^*\right)} - \mathbf{1}_u\right) dt + \pi_2 \left\|\sigma\left(x_0, u_0, x^*, u^*\right)\right\|^2 \leq 0. \tag{8}$$

In a similar way, by considering the assumption that $H(x, u)$ is $(q, w) - \pi_3$-quasiinvex at (x^*, u^*), with respect to τ, ν and σ, we get

$$\frac{1}{q}\int_a^b \sum_{i=1}^n \lambda_i \frac{\partial(h_i - \dot{x}_i)}{\partial x}\left(t, x^*, u^*\right)\left(e^{q\tau\left(x_0, u_0, x^*, u^*\right)} - \mathbf{1}_x\right) dt$$

$$+\frac{1}{q}\int_a^b \sum_{i=1}^n \lambda_i \frac{\partial(h_i - \dot{x}_i)}{\partial u}\left(t, x^*, u^*\right)\left(e^{q\tau\left(x_0, u_0, x^*, u^*\right)} - \mathbf{1}_u\right) dt$$

$$+\pi_3 \left\|\sigma\left(x_0, u_0, x^*, u^*\right)\right\|^2 \leq 0. \tag{9}$$

On adding (7), (8) and (9), from the hypothesis that $(\pi_1 + \pi_2 + \pi_3) \geq 0$, and by considering (1), we get a contradiction. This completes the proof. □

4 Conclusions

In this paper, some generalizations of the invexity notion and their applications to optimization and control theory have been established. Concretely, motivated by the continued research in this area, we have investigated the solutions for a class of optimal control problems under interval-valued generalized invexity assumptions for the involved functionals. Also, the research will continue and various duality relations between the associated dual problems and the primal optimization problem will be found.

References

[1] Antczak, T.: (p, r)-Invex sets and functions. J. Math. Anal. Appl. 263, 355-379, (2001).

[2] Ahmad, I., Jayswal, A., Banerjee, J.: On interval-valued optimization problems with generalized invex functions. J. Ineq. Appl. 2013, 313, (2013).

[3] Arrow, K.J., Enthoven, A.C.: Quasi-Concave Programming. Econometrica. 29, 779-800, (1961).

[4] Ciontescu, M., Treanţă, S.: On some connections between interval-valued variational control problems and the associated inequalities. Res. Control Optim. 12, 100300, (2023).

[5] Craven, B.D.: Invex functions and constrained local minima. Bull. Austral. Math. Soc. 24, 357-366, (1981).

[6] Hanson, M.A.: On sufficiency of the Kuhn-Tucker conditions. J. Math. Anal. Appl. 80, 545-550, (1981).

[7] Hanson, M.A., Mond, B.: Necessary and sufficient conditions in constrained optimization, FSU Statistics Report M683, Florida State University, Department of Statistics, Tallahassee, Florida, U.S.A. (1984).

[8] Jeyakumar, V.: Strong and weak invexity in mathematical programming. Method. Oper. Res. 55, 109-125, (1985).

[9] Mond, B., Hanson, M.A.: On duality with generalized convexity. Pure Math. Res. Paper, 80-3. La Trobe University, Bundoora, Australia. (1980).

[10] Treanţă, S., Arana-Jiménez, M.: On generalized KT-pseudoinvex control problems involving multiple integral functionals. Eur. J. Control 43, 39–45, (2018).

[11] Treanţă, S.: Characterization results of solutions in interval-valued optimization problems with mixed constraints. J. Global Optim. 82(4), 951-964, (2022).

On a tumoral growth model with constrained curvilinear integral functionals and gradient-type variations

Marius-Alin Dragu [1]

[1] Department of Bioengineering and Biotechnology, National University of Science and Technology Politehnica Bucharest, 060042 Bucharest, Romania;

Corresponding author email: marius_alin.dragu@upb.ro (M.A. Dragu)

Abstract

The present work addresses new classes of variational problems involving curvilinear integral-type functionals and equality constraints, developing a novel framework based on gradient-type variations. The main results highlight the nonhomogeneous Euler-Lagrange-type partial differential equations. Compared to classical variations, in this context we are led to controlled right-hand member equations, creating a novel perspective in the field of variational calculus. In addition, several illustrative biomedical applications are provided to validate the theoretical outcomes. In relation to the functionals of curvilinear integral type, a dynamical model for tumor growth is proposed, in which we investigate how a cancer cell should optimally distribute its available resources between metabolism and growth so that the applied therapy intervention achieves significant efficacy.

Key words*: constrained variational problems; curvilinear integral functionals; gradient-type variations; non-homogeneous Euler-Lagrange equations; tumor growth model.*

1. INTRODUCTION

Optimization problems are widely used to model different real-life applications from many areas of science and engineering, such as classification algorithms, decision theory, game theory, mechanics or the abstraction of medical processes (see, for example, brain electrical activity). The accuracy of the designed model is influenced by the proposed architecture to represent data (mathematical statements), so that, in numerous cases, the computational results cannot include all details of the original problem. To overcome this limitation, functional optimization theory has been extended. In this way, gradient-type variations and needle-type variations have been introduced, becoming a useful mathematical tool to investigate several variational or control problems.

2. CONTENT

Consider the complete integrable Lagrange 1-form of C^2-class

$$G_\nu\big(h(\omega), h_\gamma(\omega), \omega\big)d\omega^\nu$$

$$:= G_1\big(h(\omega), h_\gamma(\omega), \omega\big)d\omega^1 + \cdots + G_m\big(h(\omega), h_\gamma(\omega), \omega\big)d\omega^m,$$

where $\omega = (\omega^\gamma) \in \Omega_{0,\omega_0} \subset \mathbb{R}_+^m,\ h = (h^\iota): \Omega_{0,\omega_0} \to \mathbb{R}^n$, $h_\gamma(\omega) := \frac{\partial h}{\partial \omega^\gamma}(\omega),\ \gamma \in \{1, \dots, m\}$, and Ω_{0,ω_0} represents a m-dimensional interval from $\mathbb{R}_+^m$. Additionally, let $\Gamma_{0,\omega_0} \subset \Omega_{0,\omega_0}$ be an arbitrary curve (piecewise differentiable) linking the end-points $0 = (0, \dots, 0)$ and $\omega_0 = (\omega_0^1, \dots, \omega_0^m)$ in $\mathbb{R}_+^m$.

Further, we state a new optimization problem.

Multi-dimensional extremization model. Let us assume there exists a Lagrangean G such that $D_\nu G = G_\nu$, find a m-sheet $h^*: \Omega_{0,\omega_0} \to \mathbb{R}^n$ that minimizes the path-independent curvilinear integral functional

$$E\,(h(\cdot)) = \int_{\Gamma_{0,\omega_0}} G_\nu\,\big(h(\omega), h_\gamma(\omega), \omega\big)\,d\omega^\nu$$

between all C^2-class functions satisfying

$$h(0) = h_0, \quad h(\omega_0) = h_{\omega_0},$$

and the following PDE constraints

$$f_\nu^\phi\big(h(\omega), h_\gamma(\omega), \omega\big) = 0, \quad \phi = \overline{1,w},\ w \le n,\ \nu = \overline{1,m}$$

by considering gradient variations satisfying boundary and complete integrability hypotheses.

Theorem 3.1. If $\big(h^*(\cdot), p^*(\cdot)\big)$ minimizes (P_2') and the 1-form

$$\left(\frac{\partial G_\nu}{\partial h^\iota}\delta_\sigma^\gamma - D_\sigma \frac{\partial G_\nu}{\partial h_\gamma^\iota}\right) d\omega^\sigma$$

is a pullback for the 1-form $d\big(B_{\nu\iota}^\gamma\big)$, then $\big(h^*(\cdot), p^*(\cdot)\big)$ is a solution of

$$\frac{\partial G_\nu}{\partial h^\iota} - D_\gamma \frac{\partial G_\nu}{\partial h_\gamma^\iota} = c_{\nu\iota}, \quad \iota = \overline{1,n},$$

$$\frac{\partial G_\nu}{\partial p_\phi} - D_\gamma \frac{\partial G_\nu}{\partial p_{\phi,\gamma}} = 0, \quad \phi = \overline{1,w}, \quad \nu,\gamma = \overline{1,m},$$

(non-homogeneous Euler-Lagrange PDEs) where $c_{\nu\iota}$ are real constants. and $\nu, \mu = \overline{1,m}$, and

$$D_\gamma := \frac{\partial}{\partial \omega^\gamma} + \frac{\partial}{\partial h^\iota}\left(\frac{\partial h^\iota}{\partial \omega^{\pi\gamma}}\right) + \frac{\partial}{\partial h_\gamma^\iota}\left(\frac{\partial h_\gamma^\iota}{\partial \omega^\gamma}\right), \gamma = \overline{1,m},$$

is the operator of total derivative.

Illustrative application. The formulation of an optimal dynamical model for tumor growth begins with the following question: How should a cancer cell optimally allocate available resources (oxygen and nutrients) between metabolism (immediate energy consumption) and growth (leading to the release of metastatic cells) for a given therapy to have a significant effect? To address this problem, we consider a two-dimensional dynamical system that describes the temporal evolution of the effects of tumor growth. We assume $\omega = (\omega^1, \omega^2)$ refers to an observer time and an intrinsic evolution, respectively. In addition, we introduce the following functions: K(ω), seen as a dynamical variable proportional to the amount of neovascularization. The tumor is supposed to have a large number of cells so that neovascularisation becomes the primary factor governing oxygen and nutrient availability. L(ω) is regarded as labour force and T(ω) is chemotherapy treatment concentration, where $T_1(\omega)$ is associated with the concentration of anticancer agent in the central compartment (blood), while $T_2(\omega)$ is linked to the concentration of anticancer agent in the peripheral compartment (tumoral tissue).

3. CONCLUSIONS

The proposed framework, formulated in accordance with the considered class of perturbed functions governed by gradient-type variations, highlights the right-hand controlled Euler-Lagrange systems, which are very useful in modelling various applications that involve electromagnetic fields with greater accuracy. In this regard, future directions should consider studying biomedical signals as optimal control problems. Fetal electrocardiography, or the inverse problem of electroencephalography, represents a milestone in applying the foregoing theory.

A Hybrid Differential Framework for Horizontal and Horizontal–Vertical Transmissions

Maroua Amel Boubekeur[1]

[1]Ahmed Zabana University of Relizane, Algeria

Corresponding author email: marouaamel.boubekeur@gmail.com

Abstract
This research explores the practical use of piecewise differential equations, a versatile mathematical framework designed to model systems that evolve over distinct time intervals. The work primarily focuses on hybrid horizontal–vertical transmission models, with a particular application to the dynamics of HIV infection. By considering both horizontal (person-to-person) and vertical (mother-to-child) transmission routes, the study provides deeper insight into the behavior of infection spread when an infected newborn enters a population. In addition to establishing the global existence and uniqueness of solutions for piecewise systems, the investigation addresses the mathematical conditions ensuring their validity. Furthermore, the study explores cases where fractional derivatives are incorporated, revealing complex dynamical patterns that arise from such extensions. To support this theoretical framework, a parameterized method is developed for solving piecewise differential equations describing vertical and horizontal transmissions. Finally, a series of numerical simulations is conducted to demonstrate how these models behave under various conditions, offering a comprehensive view of the dynamics and illustrating the effectiveness of the piecewise modeling approach in capturing hybrid transmission mechanisms.
Keywords*:fractional calculus; piecewise differential equations; HIV infection; vertical; horizontal*

1. INTRODUCTION

The transmission of viruses occurs mainly through two pathways: horizontal and vertical. Horizontal transmission refers to the spread of infection among individuals within the same generation, while vertical transmission occurs from mother to child during pregnancy, childbirth, or breastfeeding. Several viruses, including HIV, Hepatitis B, Zika, dengue, and syphilis, can be transmitted through both routes. Asymptomatic carriers play an important role in the spread of infections such as HIV and Hepatitis B. Environmental factors, host susceptibility, and immunity also influence the simultaneous presence of multiple infections. Recent research has shown that COVID-19 may also involve vertical transmission, as newborns of infected mothers have tested positive for SARS-CoV-2, suggesting the coexistence of horizontal and vertical spread. Several mathematical models have been proposed to study these transmission mechanisms. For example, fractional-order models have been used to analyze Hepatitis B, Zika, HIV, and dengue dynamics, highlighting the contribution of asymptomatic carriers and vertical transmission to disease persistence. However, existing models often consider either horizontal or vertical transmission separately. To address this limitation, the present study introduces a piecewise differential equation model that integrates vertical transmission into a population already experiencing horizontal transmission. The model incorporates fractional and fractal–fractional derivatives, solved using a generalized parameterized method, and establishes existence and uniqueness conditions for its solutions. This approach provides a deeper understanding of hybrid transmission dynamics in infectious diseases.

2. CONTENT

When a disease first emerges within a population, it is not necessarily capable of spreading through both horizontal and vertical transmission. For instance, during the early stages of the COVID-19 outbreak, it was initially believed that transmission occurred only horizontally. However, as the pandemic evolved, evidence revealed that vertical transmission was also possible. In light of this, the present section focuses on the situation in which vertical transmission appears after a period of purely horizontal spread. To represent this process mathematically, we construct a model based on the concept of piecewise differential equations. This framework allows us to describe how vertical

transmission becomes active following horizontal spread. For this purpose, we adapt and extend the mathematical model developed by Yusuf et al. [20], which captures both vertical and horizontal transmission dynamics of HIV infection over time.

To fulfill our objective, the model proposed in [20] is reformulated using the framework of piecewise differential equations. During the first time interval, $0 \leq t \leq t_0$, the population consists of susceptible adults, HIV-infected adults, and newborns, but there are no HIV-infected newborns present. In the subsequent interval, $t_0 \leq t \leq T$, the class of HIV-infected newborns is introduced into the population, reflecting the onset of vertical transmission alongside the pre-existing horizontal transmission dynamics.

For $0 \leq t \leq t_0$:

$$\begin{cases} dS(t)/dt = \Pi - \lambda S - (\delta_1 + \mu)S \\ dI(t)/dt = \lambda S - (\alpha_1 + \delta_2 + \delta_3 + \mu)I \\ dC(t)/dt = \delta_1 S + \delta_2 I - \mu C \end{cases}$$

For $t_0 \leq t \leq T$:

$$\begin{cases} dS(t)/dt = \Pi - \lambda S - (\delta_1 + \mu)S \\ dI(t)/dt = \lambda S - (\alpha_1 + \delta_2 + \delta_3 + \mu)I \\ dC(t)/dt = \delta_1 S + \delta_2 I - \mu C \\ dI\_c(t)/dt = \delta_3 I - (\mu + \alpha_2)I\_c \end{cases}$$

3. CONCLUSIONS

In existing models addressing horizontal–vertical HIV transmission, an increase in the adult population often results in a rise in the number of susceptible newborns, which in turn reduces the proportion of susceptible adults. While several studies have examined horizontal, vertical, and combined transmission routes, none have specifically considered the case where vertical transmission emerges later, through the introduction of an infected newborn into a population already experiencing horizontal transmission. The present study investigates this situation using an innovative framework based on piecewise differential equations to analyze the resulting epidemic dynamics. We establish the existence and uniqueness of solutions to the proposed model and design a numerical scheme founded on parameterized integer–fractional derivatives to solve it. Numerical simulations are then performed to assess how the onset of vertical transmission affects the overall behavior of the system in a population previously governed by horizontal transmission.

Dimensional Scaling for Solving Diverse Computational Problems

Mihnea Andrei Vitejeanu[1], Matei Buliga[2], Paul – Andrei Ungureanu[3]

National University of Science and Technology Politehnica Bucharest, 313 Splaiul Independentei, District 6, Bucharest, Romania

Corresponding author email: 15mihneaandrei@gmail.com[1], bmatei137@gmail.com[2], ungureanu378@gmail.com[3],

Abstract

The physical interpretation of scaling spatial dimensions, from 3D Euclidean space (SO(3)) to 4D spaces (SO(4)), relies fundamentally on the mathematical framework of coordinate representations and matrix transformations. Our goal is to unpack these transformations to gain a precise understanding of what it means to computationally handle a fourth spatial dimension. The key algebraic breakthrough enabling this extension is the linearization of translation—an inherently non-linear operation—through the use of homogeneous coordinates (N to N+1). This core affine geometry technique allows complex affine transformations (translation, rotation, scaling) to be composed and applied efficiently with a single matrix multiplication, forming the foundation of computer graphics and physical simulation. In 4D, geometric complexity shifts from rotation around an axis (3D) to rotation around a plane, producing double rotations governed by the SO(4) group. Our approach will emphasize practical software implementations to illustrate these 4x4 matrix transformations, showing how they can be applied to solve real-world problems in advanced robotic navigation, simulation optimization, and multi-dimensional data visualization. We will convert the abstract grasp of dimensional scaling into a computational toolkit applicable in engineering and computer science.

Key words*: Dimensional scaling; Affine transformations; Homogeneous coordinates; Matrix multiplication; SO(4) group; Computational methods.*

1. INTRODUCTION

The physical interpretation of scaling spatial dimensions, from 3D Euclidean space (SO(3)) to 4D spaces (SO(4)), relies fundamentally on the mathematical framework of coordinate representations and matrix transformations. Our goal is to unpack these transformations to gain a precise understanding of what it means to computationally handle a fourth spatial dimension.

2. CONTENT

The key algebraic breakthrough that enables efficient extension from 3D to 4D is the linearization of translation—an inherently non-linear operation—through the use of homogeneous coordinates (N to N+1). This core technique from affine geometry allows complex sets of affine transformations (translation, rotation, scaling) to be composed and applied efficiently with a single matrix multiplication. It forms the foundation of all computer graphics software, geometric modelling, and physical simulation applications.

In higher-dimensional spaces (4D), geometric complexity shifts dramatically. Rotations no longer occur around an axis (as in 3D) but around a plane, producing double rotations governed by the SO(4) group. This behaviour is handled through algebraic geometry and the concept of bivectors.

3. CONCLUSIONS

Our approach will emphasize practical software implementations to illustrate these 4x4 matrix transformations. We will delve into the underlying intuition behind these matrices and show how they can be applied to solve real-world problems, such as:

1. Advanced Robotic Navigation: Modelling intricate motion and orientation.

2. Simulation Optimization: Developing more compact data structures for storing system states (position and orientation) in real-time applications.

3. Multi-Dimensional Data Visualization: Efficiently designing datasets involving four spatial variables.

In this way, we will convert the abstract grasp of dimensional scaling into a toolkit of computational methods directly applicable in engineering and computer science.

FEDERATED TinyML FRAMEWORK FOR ADAPTIVE AI AGENTS IN IMPLANTABLE NEURAL CHIPS

Mihnea-Ioan STĂNILĂ[1,3], Raul-Cosmin GURIENCU[1,3]
Simona Mihaela BIBIC[2,3]

[1]Faculty of Electrical Engineering, National University of Science and Technology POLITEHNICA Bucharest, 313 Splaiul Independentei, District 6, Bucharest, Romania

[2]Department of Applied Mathemathics, National University of Science and Technology POLITEHNICA Bucharest, 313 Splaiul Independentei, District 6, Bucharest, Romania

[3]Center for Research and Training in Innovative Techniques of Applied Mathematics in Engineering, National University of Science and Technology
POLITEHNICA Bucharest, 313 Splaiul Independentei, District 6, Bucharest, Romania

Corresponding author email: mihnea_ioan.stanila@stud.electro.upb.ro, raul.guriencu@stud.electro.upb.ro, simona.bibic@upb.ro

Abstact: ***Our research proposes the development and evaluation of a framework for incremental learning in artificial intelligence agents operating on sub-millimeter implantable neural devices. The study integrates energy and communication channel simulations with TinyML optimization techniques such as quantization, pruning, and knowledge distillation. To ensure long term adaptability under strict power and safety constraints, we introduce a federated update protocol specifically designed for ultra-low power communication environments. The framework aims to demonstrate that clinically relevant detection tasks, such as early identification of epileptic seizures, can be achieved with minimal energy expenditure while maintaining data privacy and reliability. Publicly available EEG and ECoG datasets will be used for simulation and validation. Through this approach, the work contributes to advancing embedded AI toward bio-compatible, energy efficient], and continuously learning neural implants, bridging the gap between intelligent computation and next generation brain computer interfaces****.*

Key words*: Incremental Learning, TinyML Optimization, Federated Update Protocols, Neural Implants, Energy Constrained AI Agents, Brain Computer Interfaces (BC1), Biomedial Signal Processing*

1. INTRODUCTION

Recent breakthroughs in brain computer interfaces (BCIs) have transformed neural implants from experimental prototypes into functional clinical systems. Companies such as Neuralink have already demonstrated bidirectional brain communication in human subjects, while over 150,000 individuals worldwide currently use implanted neurostimulators or neural monitoring devices for medical purposes. These systems continuously generate vast amounts of high-resolution neural data, which remain largely underutilized outside proprietary environments. Leveraging this existing data through open, federated, and privacy preserving frameworks could accelerate progress in personalized neuro AI and adaptive therapeutic models. This research builds on that vision by proposing a framework for incremental learning in sub millimeter AI enabled neural implants, aiming to minimize energy consumption while maintaining clinical reliability and data confidentiality.

2. CONTENT

The rapid evolution of neurotechnology and nanoelectronics is reshaping the interface between biological and artificial intelligence. Recent advances in brain computer interfaces (BCIs) such as Neuralink have demonstrated that neural implants can support real time signal decoding, adaptive stimulation, and bidirectional communication between biological neurons and artificial agents. Figure 1 illustrates the proposed system architecture, where an AI embedded nanochip processes neural signals locally using TinyML inference and transmits compressed updates to an external medical node for aggregation and analysis. This design supports a federated learning feedback loop, enabling the implant to adapt continuously while maintaining low energy consumption and data privacy.

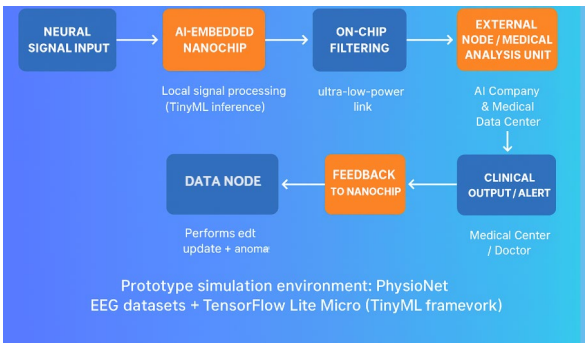

Figure 1. Prototype simulation

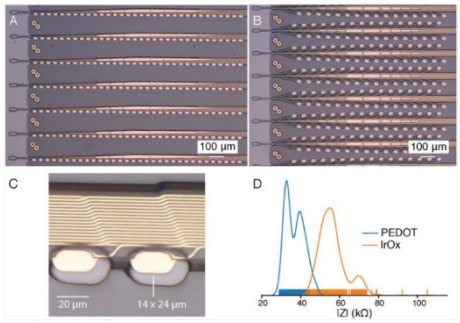

Figure 2. Novel polymer probes [2].

At the physical level, bio-compatible nanoelectrode arrays form the substrate of these learning systems. As shown in Figure 3, materials such as PEDOT and IrOx exhibit distinct impedance profiles (|Z| ranging from 20–100 kΩ), allowing stable long-term signal acquisition and fine-tuned current feedback. Each microelectrode measuring approximately 14×24 µm acts as a Data Node, capable of local adaptation through electrical feedback, forming a distributed physical learning network. Despite the growing presence of neural implants over 150,000 patients currently rely on implanted neurostimulators and neural monitoring devices the high-resolution neural data they produce remains largely siloed. Leveraging these datasets through federated, privacy preserving learning frameworks can accelerate the emergence of self-learning neural implants, capable of personalizing their behavior to each patient's neural patterns. From an economic standpoint, the convergence of AI miniaturization and neural hardware innovation is driving an unprecedented expansion in the nanochip sector. As projected in Figure 3, the global nanochip market is expected to exceed 1.5–2 trillion USD by 2040, driven by bio-integrated computing and embedded intelligence. Together, these developments mark the transition from passive, recording based implants to autonomous nano intelligent systems, where biocompatible nanochips act as active learning agents bridging living tissue and artificial cognition.

3. CONCLUSIONS

This work presents a framework for incremental learning in AI embedded neural implants, combining TinyML optimization and federated feedback protocols to enable adaptive intelligence under strict energy and safety constraints. The proposed architecture (Fig. 1) allows nanochips to perform localized inference and receive model updates through ultra-low-power communication links, achieving continuous adaptation without compromising privacy. The integration of bio compatible electrode materials such as PEDOT and IrOx (Fig. 2) demonstrates the feasibility of stable, low impedance interfaces capable of both neural recording and adaptive feedback. Each electrode operates as a Data Node, contributing to distributed, self-adjusting learning. Given the rapid expansion of the nanochip market (Fig. 3) and the growing population of implanted patients, leveraging existing neural datasets within secure, federated systems could accelerate the development of self-learning neural interfaces that evolve alongside human neural activity and redefine the boundary between biology and computation.

4. REFERENCES

[1] E. R. Musk and the Neuralink team, "An Integrated Brain-Machine Interface Platform With Thousands of Channels," *Journal of Medical Internet Research*, vol. 21, no. 10, e16194, 31 Oct. 2019. doi:10.2196/16194. PMCID:PMC6914248.

[2] P. M. Parikh and A. Venniyoor, "Neuralink and Brain–Computer Interface—Exciting Times for Artificial Intelligence," *South Asian Journal of Cancer*, vol. 13, no. 1, pp.63-65, 2024. DOI:10.1055/s-0043-1774729. PMCID:PMC11076062.

[3] D. Broom, "Microchips – their past, present and future," *World Economic Forum*, Jan. 2025.

WEAK ALMOST MONOMIAL GROUPS AND ARTIN'S CONJECTURE

Mircea CIMPOEAȘ[1]

[1]National University of Science and Technology Politehnica of Bucharest,
313 Splaiul Independentei, District 6, Bucharest, Romania

Corresponding author email: mircea.cimpoeas@imar.ro

Abstract

We introduce a new class of finite groups, called weak almost monomial, which generalize two different notions of "almost monomial" groups, and we prove it is closed under taking factor groups and direct products.

Let $K/\mathbb{Q}$ be a finite Galois extension with a weak almost monomial Galois group G and $s_0 \in C \setminus \{1\}$. We prove that Artin conjecture's is true at s_0 if and only if the monoid of holomorphic Artin L-functions at s_0 is factorial. Also, we show that if s_0 is a simple zero for some Artin L-function associated to an irreducible character of G and it is not a zero for any other L-function associated to an irreducible character, then Artin conjecture's is true at s_0.

Key words*: Finite group, Almost monomial, Galois extension, Artin L-function, Artin's conjecture.*

1. INTRODUCTION

A finite group G is called monomial, if every complex irreducible character χ of G is monomial, that is, it induced by a linear character λ of a subgroup H of G.

Let K/Q be a Galois extension. For a character of the Galois group G=Gal(K/Q), Artin associated a L-function, denoted by $L(s,\chi)$, and he conjectured that $L(s,\chi)$ is holomorphic on C\{1}. Artin proved that his conjecture holds for monomial groups G. However, the class of monomial groups is very restrictive, thus several generalizations were considered in literature:

A finite group G is called *almost monomial*, in the sense of Nicolae [4] (NAM), if for every distinct complex irreducible characters χ and $\chi'$of G, there exist a subgroup H of G and a linear character character λ of H such that the induced character λ contains χ but not χ'.

A finite group G is called *almost monomial*, in the sense of Booker [1] (BAM), if for every irreducible characters χ of G, if $\chi = \psi + \phi$ for some virtual characters ψ and ϕ, such that $\langle \psi, \sigma \rangle \geq 0$ and $\langle \phi, \sigma \rangle \geq 0$ for all monomial characters σ, then either ψ =0, either ϕ =0.

In our paper, we introduce a further generalization: We say that a finite group G is weak almost monomial (WAM), if for every distinct complex irreducible characters χ and $\chi'$of G, there exist a subgroup H of G and a linear character character λ of H such that $\langle \chi, \lambda \rangle > \langle \chi', \lambda \rangle$.

It is easy to see that if G is almost monomial (in the sense of Nicolae or in the sense of Booker), then G is weak almost monomial. However, there are examples of groups which are weak almost monomial, but are not almost monomial in the sense of Nicolae.

This presentation is based on our preprint [2].

2. CONTENT

Our main results are the following:

Theorem 1. Let N be a normal subgroup of the WAM-group G. Then G/N is a WAM.

Theorem 2. Let G, G' be two finite groups. Then $G \times G'$ is WAM if and only if G and G' are WAM.

Let $s_0 \in \mathbb{C} \setminus \{1\}$. We denote by $\mathrm{Hol}(s_0)$, the monoid of holomorphic L-functions at s_0.

Theorem 3. Let K/Q is a finite Galois extension with the Galois group G, which is WAM. Then Artin's conjecture holds, if and only if the monoid $\mathrm{Hol}(s_0)$ is factorial.

Theorem 4. Let K/Q is a finite Galois extension with the Galois group G, which is WAM. If s_0 is a simple zero for some Artin L-function associated to an irreducible character of G and it is not a zero for any other L-function associated to an irreducible character, then Artin conjecture's is true at s_0.

3. CONCLUSIONS

We introduced and studied a new class of finite groups, called weak almost monomial, which generalizes the class of monomial groups. If K/Q is a finite Galois extension with the Galois group G weak almost monomial, we proved that Artin conjecture's is true if and only if the monoid of holomorphic Artin L-functions is factorial. Also, we proved that that if s_0 is a simple zero for some Artin L-function associated to an irreducible character of G and it is not a zero for any other L-function associated to an irreducible character, then Artin conjecture's is true at s_0. Thus, we extended some previous results from [3] and [4], regarding almost monomial groups (in the sense of Nicolae).

Bibliography

[1] A. R. Booker, Artin's conjecture, *Turing's method, and the Riemann hypothesis*, Exp. Math. 15(4) (2006), 385-407.

[2] M. Cimpoeas, *Weak almost monomial groups and Artin's conjecture*, Preprint (2024), arXiv:2409.05629, 9pp.

[3] M. Cimpoeas, F. Nicolae, Artin L-functions to almost monomial Galois groups, Forum Math. 32(4) (2020), 937-940.

[4] F. Nicolae, *On holomorphic Artin L-functions,* Monatsh. Math. 186(4) (2018), 679--683.

REPRESENTATIONS OF THE BRAID GROUP AND THEIR EXTENSIONS TO THE SINGULAR BRAID MONOID

MOHAMAD N. NASSER

Abstract. Let t be indeterminate and let $\rho : B_n \to GL_m(\mathbb{Z}[t^{\pm 1}])$ be a k-local representation of the braid group B_n, where $k = m - n + 2$. We consider two types of extensions of ρ to the singular braid monoid SM_n. The first type is called the k-local extension, which is a new concept defined in this paper. The second type is called the Φ-type extension, which is given by Bardakov, Chbili, and Kozlovskaya. In order to obtain a relation between these two types of extensions, we consider two homogeneous 2-local representations of B_n, namely $\rho_B : B_n \to GL_n(\mathbb{Z}[t^{\pm 1}])$ and $\rho_S : B_n \to GL_n(\mathbb{Z}[t^{\pm 1}])$, and a homogeneous 3-local representation of B_n, namely $\rho_F : B_n \to GL_{n+1}(\mathbb{Z}[t^{\pm 1}])$. We study the relation between the two types of extensions to SM_n of these three representations of B_n. In fact, we prove that every homogeneous 2-local extension of ρ_B is also a Φ-type extension for all $n \geq 2$; which is not the case for ρ_S. Also, we prove that every homogeneous 3-local extension of ρ_F is a Φ-type extension for all $n \geq 3$. In addition, we study, in the case $n = 2$, the faithfulness of the complex specialization of all 2-local extensions of ρ_B and ρ_S.

1. Introduction

The braid group on n strings, B_n, is generated by the Artin generators $\sigma_1, \ldots, \sigma_{n-1}$. The singular braid monoid SM_n extends B_n by including additional generators $\tau_1, \ldots, \tau_{n-1}$ corresponding to singular crossings. The structure of SM_n was first introduced independently by J. Baez and J. Birman, and later Fenn, Keyman, and Rourke proved that SM_n embeds into a group SB_n, called the singular braid group.

A central topic of interest in Representation Theory is the study of linear representations of B_n, SM_n, and SB_n. One of the most notable representations of B_n is the Burau representation, known to be faithful for $n \leq 3$, unfaithful for $n \geq 5$, while the case $n = 4$ remains unresolved. Dasbach and Gemein investigated extensions of the Burau representation to SM_3 and studied their faithfulness.

Another important class of representations are the local representations. Mikhalchishina studied local and homogeneous local representations of B_n, their connection with the Burau representation, and their irreducibility properties were further examined.

Key words and phrases. Braid Group, Singular Braid Monoid, Group Representations, Burau Representation, Standard Representation, Faithfulness.

Mathematics Subject Classification. Primary: 20F36.

In analogy, the present paper introduces the notion of k-local extensions of braid group representations to the singular braid monoid SM_n. These are extensions of k-local representations of B_n preserving a similar block structure.

Another family of extensions, known as Φ-type extensions, were defined by Bardakov, Chbili, and Kozlovskaya. Given a representation $\rho : B_n \to G_n$ and a field $\mathbb{K}$, they defined

$$\Phi_{a,b,c} : SM_n \longrightarrow \mathbb{K}[G_n], \qquad \Phi_{a,b,c}(\sigma_i^{\pm 1}) = \rho(\sigma_i^{\pm 1}), \quad \Phi_{a,b,c}(\tau_i) = a\rho(\sigma_i)+b\rho(\sigma_i^{-1})+ce,$$

where $a, b, c \in \mathbb{K}$ and e is the identity in G_n. This provides a linear extension of ρ to SM_n. A special case, with $a = 1$, $b = -1$, and $c = 0$, yields the Birman representation, proved injective by L. Paris. Faithfulness of $\Phi_{a,b,c}$ in specific settings was investigated by M. Nasser.

The main objective of this work is to explore the relationship between k-local extensions and Φ-type extensions of k-local representations of B_n to SM_n. Specifically, it aims to answer:

> *If ρ is a k-local representation of B_n, what is the relation between k-local extensions and Φ-type extensions of ρ to SM_n?*

The study focuses on three homogeneous local representations of B_n:

- The **Burau representation** ρ_B (homogeneous 2-local),
- The **standard representation** ρ_S (homogeneous 2-local),
- The **F-representation** ρ_F (homogeneous 3-local).

These cases are chosen to compare behaviors for different degrees k and to highlight that even representations of the same degree may yield different types of extensions.

Conclusion. This article establishes foundational links between k-local and Φ-type extensions of braid group representations to the singular braid monoid. It shows that for several fundamental homogeneous local representations, these two types of extensions coincide, offering insight into the structure and potential faithfulness of such extensions.

Mohamad N. Nasser, Department of Mathematics and Computer Science, Beirut Arab University, P.O. Box 11-5020, Beirut, Lebanon
Email address: m.nasser@bau.edu.lb

ON THE CONTROLLABILITY OF POSITIVE FRACTIONAL 2D CONTINUOUS-TIME LINEAR SYSTEMS

Mohammed Nadjib BENAMAR [1], Mohammed Amine GHEZZAR[2] , Djillali BOUAGADA[3]

[1,3]Department of Mathematics and Computer Science, Abdelhamid Ibn Badis University, Mostaganem, Algeria

[2]"Department of Mathematics, National Higher School of Mathematics, Algiers, Algeria

Corresponding author email: nadjib.benamar.etu@univ-mosta.dz

Abstract

In this paper, we investigate the controllability of positive fractional 2D continuous-time linear systems described by Fornasini-Marchesini Model. Sufficient conditions for controllability using Gramians controllability are established. Necessary and sufficient conditions for the controllability of the considered systems, based on the matrices of the systems, are also provided. Additionally, the paper presents conditions required for the existence of a solution to the minimum energy control problem, along with a systematic approach for computing an input that minimizes the specified performance index. The effectiveness of this procedure is demonstrated through the application of a numerical example.

Keywords: *2D Fornasini-marchesini model; Controllability; Minimum energy control; Gramien Controllability.*

1. INTRODUCTION

Two-dimensional systems hold a pivotal role in modeling and controlling a wide array of phenomena spanning the physical, biological, and more. Within this domain, we find prominent models like the Roesser model [1] and the FernasiniMarchesini model [2], frequently harnessed to unravel complex dynamics.

Controllability stands as a paramount concept in control theory, serving as a linchpin for addressing diverse engineering challenges. This concept plays a pivotal role in mechanical systems, electrical circuits, and biological systems, enabling them to transition from any initial state to a desired final state within their state space through appropriate control inputs. Conversely, the minimum energy control, another facet of controllability, focuses on optimizing control inputs to facilitate seamless transitions between states. Researchers have extensively explored the controllability and minimum energy control aspects in various system types, including 1D fractional linear systems, 1D positive fractional systems [3,4], 2D continuous linear systems , 2D continuous-discrete time linear systems , positive 2D continuous-discrete systems, and fractional 2D discrete-time linear systems.

2. CONTENT

Consider the following fractional 2D continuous-time linear system described by the Fornasini-Marchesini model:

$$D_{t_{1,}\,t_2}^{\alpha,\beta} x(t_1,t_2) = A_0 x(t_1,t_2) + A_1 D_{t_1}^{\alpha} x(t_1,t_2) + A_2 D_{t_2}^{\beta} x(t_1,t_2) + Bu(t_1,t_2) \qquad (1)$$

where $D_{t_{1,}\,t_2}^{\alpha,\beta} x(t_1,t_2)$ the 2D Caputo fractional derivative operators, $0 < \alpha, \beta < 1$, $x(t_1,t_2) \in \mathrm{R}n$ is the state vector, $Bu(t_1,t_2) \in R^m$ is the input vector, matrices $A_k \in R^n$ for $k = 0, 1, 2$; $B \in R^n$.

In this article, we embark on a novel exploration: the study of controllability and minimum energy control in positive fractional 2D continuous-time linear systems utilizing the Caputo fractional derivative. Building upon the foundations laid for 1D positive fractional linear systems [10], we extend our inquiry to encompass positive fractional 2D continuous-time linear systems, particularly

those utilized in Fornasini-Marchesini models. Our investigation centers around the Gramian controllability approach and yields insights and results tailored to this contex.

3. CONCLUSIONS

In this work, we establish several key results regarding the controllability and minimum energy problems for positive fractional 2D continuous linear systems described by the Fornasini-Marchesini model. We derive sufficient conditions for the controllability of these systems, utilizing the Gramian approach.

REFERENCE

R.P. Roesser (1975) A Discrete State-Space Model for Linear Image Processing. IEEE Transactions on Automatic Control 20, No. 1: 1-10. https://doi.org/10.1109/TAC.1975.1100844

E. Fornasini, G. Marchesini (1978) Doubly-indexed dynamical systems: State-space models and structural properties. Mathematical systems theory 12: 59-72. https://doi.org/10.1007/BF01776566

T. Kaczorek (2013) Minimum energy control of fractional positive continuous-time linear systems. Bulletin of the Polish Academy of Sciences. Technical Sciences 61, No. 4, 803-807. https://doi.org/10.2478/ bpasts-2013-0087

K Benyettou, D Bouagada, MN Benamar (2025) Controllability and minimum energy control problem of two-dimensional continuous-time fractional linear systems, International Journal of Systems Science 56 (5), 966-981

Similarity in the complex plane

Nicolae MUȘUROIA

National College Gheorghe Șincai, 25 Gheorghe Șincai, Baia Mare, România

Corresponding author email: musuroianicolae@yahoo.com

Abstract

In this paper we will present some interesting applications related to the characterization of triangle similarity with complex numbers, we will get new problems and finally we will give an extension of the famous Napoleon problem.

Key words: *geometry problems, complex numbers, similar triangles.*

Proposition 2. i) Triangles ABC și $A'B'C'$, similarly oriented, are similar if and only:

$$\frac{c-a}{b-a}=\frac{c'-a'}{b'-a'}.$$

ii) Triangles ABC și $A'B'C'$, oppositely oriented, are similar if and only:

$$\frac{c-a}{b-a}=\overline{\left(\frac{c'-a'}{b'-a'}\right)}.$$

Consequence 1. i) Triangles ABC și $A'B'C'$, similarly oriented, are similar if and only:

$$a'(b-c)+b'(c-a)+c'(a-b)=0.$$

ii) Triangles ABC și $A'B'C'$, oppositely oriented, are similar if and only:

$$\overline{a'}(b-c)+\overline{b'}(c-a)+\overline{c'}(a-b)=0.$$

Proposition 3. Triangles ABC și $A'B'C'$, similarly oriented, are similar if and only:

$$(\exists)\rho>0,(\exists)\alpha\in(0,\pi):\begin{cases}c=b+(a-b)\rho\varepsilon\\ c'=b'+(a'-b')\rho\varepsilon\end{cases},\qquad \varepsilon=\cos\alpha+i\sin\alpha.$$

Proposition 4. If ABC is a triangle of affixes a,b,c then the function $f:\square\to\square$, for which triangles ABC and $A'B'C'$ are similar, where such that $a'=f(a),b'=f(b),c'=f(c)$ are

$$f_1 : \square \to C,\ f_1(z) = \alpha + \beta z,\ \alpha \neq 0,$$
$$f_2 : \square \to C,\ f_2(z) = \alpha + \beta \bar{z},\ \alpha \neq 0.$$

Problem 4. **(**Generalization of *Napoleon's* problem*)*

Let ABC be an arbitrary triangle. Show that on its sides we can construct similar triangles (and others besides equilateral triangles) and similarly oriented ABC', BCA', CAB' (all outwards or all three inwards), such that their centers of gravity form a triangle similar to the constructed triangles .

REFERENCES

[1] D. Andrica, C. Varga, D. Văcărețu, *Teme de geometrie*, Editura Promedia-Plus, Cluj Napoca, 1997.

[2] N. Bișboacă, *Transformări geometrice în planul complex*, Editura Millenium, Alba Iulia, 2004.

[3] N. Mușuroia, Rotația în planul complex, Argument, Nr.22, Baia Mare, 2020.

[4] N. Mușuroia, Gh. Boroica, V. Pop, D. Heuberger, F. Bojor, *Matematica de excelență, pentru concursuri, olimpiade și centre de excelență*, clasa a X-a, Editura Paralela 45.

[5] Vasile Pop, Geometrie pentru gimnaziu, liceu și concursuri, Editura Mediamira, Cluj Napoca, 2007.

[6] Colecția revistei *Gazeta Matematică*, seria B.

Analytical Methods for Stabilizing Fractional Multidimensional Discrete Systems

Nisrine Miliani1, Djillali Bouagada2 , Kamel Benyettou3

Departement of Mathematics and Computer Science,ACSY Team-Laboratory of Pure and Applied Mathematics.
Abdelhamid Ibn Badis University Mostaganem P.O.Box227/118,27000

Corresponding author email
nisrinemiliani95@gmail.com
Djillali.bouagada@univ-mosta.dz

Kamel.benyettou@.edu.dz

Abstract
This study focuses on the stabilization of multidimensional fractional discrete linear systems. A new method is proposed for designing control laws that ensure system stability. The approach employs gain and feedback matrices to drive the system state toward equilibrium. Several numerical examples are presented to demonstrate the validity and performance of the proposed method.

Key words: Multidimensional systems , Rosser model , Fractional systems, Gain matrix , Stabilization.

1. INTRODUCTION

The study of multidimensional (n-D) systems has attracted increasing interest over the last decades. These systems propagate their state simultaneously in several independent spatial directions. Moreover, multidimensional systems have found applications not only in systems theory but also in various engineering fields such as image processing, digital filtering, and RLC circuit analysis. It is crucial to ensure that the propagation of the state variable remains bounded over time, which implies that the model is stable.

In control theory, stabilization refers to the design of a controller capable of stabilizing an unstable system or maintaining the stability of a stable one. This is typically achieved through a careful analysis of the system dynamics and the development of a control law that appropriately adjusts the system inputs to achieve the desired behavior. A common approach to solve the stabilization problem is to use feedback control, which consists of using the system output as feedback to modify its inputs.

In this work, we study discrete-time fractional multidimensional systems of the Roesser type. The proposed solution is presented, and a new approach is introduced to achieve the stabilization of these systems based on the gain matrix. Finally, academic examples are provided to illustrate and validate the obtained results.

2. PRELIMINARIES

In this work, we focused on multidimensional fractional discrete systems described by the Roesser model. We studied the stabilization of these systems by proposing a new method based on the design of the gain matrix. The results were validated through several academic examples to demonstrate the effectiveness and relevance of the proposed approach.

Below we present a Complete formulation of multidimensional dD fractional discrete-time systems described by the Rosser model

$$\begin{bmatrix} \Delta_{\alpha 1}^{h1} x_{i_{1+1}}^{1} \\ \vdots \\ \Delta_{\alpha d}^{hd} x_{i_{d+1}}^{d} \end{bmatrix} = \begin{bmatrix} A_{11} & \dots & A_{1d} \\ A_{21} & \dots & A_{2d} \\ A_{d1} & \dots & A_{dd} \end{bmatrix} \begin{bmatrix} x_{i1,i2,\dots id}^{1} \\ \vdots \\ x_{i1,i2,\dots id}^{d} \end{bmatrix} + \begin{bmatrix} B_1 \\ \vdots \\ B_d \end{bmatrix} u_{i1,i2,id}$$

$$y_{i_1,i2,i3,\dots id} = [C_1 \quad \dots \quad C_d] \begin{bmatrix} x_{i1,i2,\dots id}^{1} \\ \vdots \\ x_{i1,i2,\dots id}^{d} \end{bmatrix} + D u_{i1,i2,\dots id}$$

$i_1, i_2, \dots i_d \in \mathbb{Z}_+$

Where

$A_d = \begin{bmatrix} A_{11} & \dots & A_{1d} \\ A_{21} & \dots & A_{2d} \\ A_{d1} & \dots & A_{dd} \end{bmatrix} \in \mathbb{R}^{n \times n}$ *is the dynamic matrix,*

$x_{i1,i2,\dots id}^{j} \in \mathbb{R}^{nj}$ $j = 1, d$ *represent state vectors,*

$u_{i1,i2,\dots id} \in \mathbb{R}^{m}$ *represent the input vectors*

$y_{i_1,i2,i3,\dots id} \in \mathbb{R}^{p}$ *represent the output vectors,*

$B_j \in \mathbb{R}^{nj \times m}$, $C_j \in \mathbb{R}^{p \times nj}$ $j = 1, d$ *and* $D \in \mathbb{R}^{p \times m}$

3. CONCLUSIONS

An analysis of the stabilization of multidimensional fractional discrete-time linear systems described by the Roesser model is presented. We conducted an extensive investigation of the conditions required to achieve stabilization in discrete-time multivariable fractional Roesser models. Our novel approach is based on a gain matrix and state feedback control, validated through linear matrix inequalities. The obtained results are demonstrated by several numerical examples to illustrate the accuracy and efficiency of the proposed method.

Topological Data Analysis for Big Data: Advances, Challenges and Applications

1st A. A. Nasef
Department of Physics and Engineering Mathematics.
Faculty of Engineering, Kafrelsheikh University.
Kafrelsheikh, Egypt.
arafa.nasif@eng.kfs.edu.eg

2nd M. A. Nasef
Department of Physics and Engineering Mathematics.
Faculty of Engineering, Tanta University.
Kafrelsheikh, Egypt.
arafa x 99@yahoo.com

3th Dina Saif
Faculty of Artificial Intelligence, Delta University for Science and Technology, Gamasa,Egypt.
DinaKazamel@deltauniv.edu.eg

4th M. M. Elbana
Department of Physics and Engineering Mathematics.
Faculty of Engineering, Kafrelsheikh University.
Kafrelsheikh, Egypt.
mehna.mohsen@eng.kfs.edu.eg

5th N.A.Hemida
Department of Electrical Engineering.
Faculty of Engineering, Kafrelsheikh University.
Kafrelsheikh, Egypt.
nada 2524b@eng.kfs.edu.eg

6rd M. E. Ayad
Department of Electrical Engineering.
Faculty of Engineering, Kafrelsheikh University.
Kafrelsheikh, Egypt.
mohamed 2716b@eng.kfs.edu.eg

***Abstract*— The rapid increase of big data in different areas has made it really necessary to have sophisticated tools for analysis that would be able to multidimensional datasets with a complex structure and uncover significant patterns. Topological Data Analysis (TDA) is one of the techniques that has been together with traditional statistics as the main mathematical framework for identifying the patterns specifying the nature of the data and that often gets overlooked by them. This document is a deep dive into TDA's principles, methods and applications in big data analytics. Among the concepts discussed are simplicial complexes, persistent homology, and Mapper algorithms with a focus on their roles in dimensionality reduction, pattern recognition and anomaly detection techniques. The paper further discusses key and existing TDA applications in the real-world scenarios of health care, finance, biology, and social networks. Current issues are raised concerning, for example, the integration of TDA and machine learning models; amongst others, keeping TDA scalable, and dealing with data noise. The article concludes by proposing future research paths and suggesting TDA's potential to act as a conduit in the interdisciplinary area between geometry, topology, and data science, ultimately revealing new insights for data-driven exploration in the age of big data.**

Keywords*— *Topological Data Analysis (TDA), Big Data, Persistent Homology, Machine Learning, Data Visualization

I. INTRODUCTION

The vast and rapid data production from different sources like social networks, smart devices, healthcare devices, and satellite imaging is the main reason for the current day data analytics scenario. This trend, which is often referred to as Big Data, is marked by its extremely high dimensionality, different forms, and huge volumes, which are the major reasons for the difficulties that classical statistics and machine learning techniques cannot cope with [1]. The classical models are not able to catch the intrinsic shapes, structure, and multi-scale relationships inside the complex datasets [2].

As a solution to these challenges, Topological Data Analysis (TDA) has risen as a powerful mathematical framework that applies concepts from algebraic topology to the extraction of qualitative geometric features from data [3]. By treating data as point clouds or networks and considering their topological invariants—ceasing components, performing loops, and creating voids—TDA allows scientists to show the overall and non-scale-dependent structural information [4]. Its key instrument, persistent homology, measures these characteristics over various levels of resolution, condensing them into persistence diagrams or barcodes that act as stable, compact representations of data structure [5-8]. Nevertheless, the application of TDA to Big Data brings up significant issues such as scalability, stability, and interpretability. The process of creating simplicial complexes like Vietoris-Rips or Čech is combinatorial in nature and grows with the size of the dataset, leading to an exponential increase in computational costs [9, 10]. To solve this problem, the development of distributed and parallel algorithms has been done, including PixHomology and GPU-accelerated frameworks that enhance performance while also preserving topological accuracy [11]. Approximation techniques based on subsampling and stochastic filtration have also been suggested for dealing with extremely large or streaming datasets [12]. What is more, still the stability of persistence diagrams with regard to noise and data variations is a matter of high concern. Really small distortions in high-dimensional inputs can in-noise the topological summaries unless some normalization or filtering strategies are properly applied [13]. The other open challenge is to work out the integration of TDA-derived topological signatures into machine learning models—this means turning qualitative features into quantitative descriptors that will aid the classification, clustering, and prediction tasks [14].

In the backdrop of these advancements, the present study intends to offer a wide-ranging review and an analytical framework for TDA in Big Data analysis. The research will

involve: (i) carrying out a systematic survey of cutting-edge algorithms along with their applications; (ii) measuring the scalability and performance of the algorithms on large-scale datasets; and finally (iii) presenting a hybrid TDA–machine learning model that combines interpretability with computational efficiency. This research, through the connection of topology and data science, is aimed at the development of a single framework that would be able to reveal hidden structures in the large, complicated data environments [15].

II. Background

A. Basics of Topology in Data Science

Topological Data Analysis (TDA) is like a magician that unveils the complex structure of data through a simple set of tools. The TDA magic is especially powerful when applied to data that is often high-dimensional, noisy, and heterogeneous. The simplicial complex is the computational topology's main character, which is a combinatorial structure made of simplices (vertices, edges, triangles, tetrahedra, etc.) that depicts relationships among data points and expands graphs to higher-order connectivity patterns. Homology theory gives a simplicial complex a series of algebraic invariants, called homology groups, whose dimensions are the Betti numbers. The 0th Betti number intuitively determines the number of connected components, the 1st Betti number determines the number of independent loops (cycles), and so on, with higher Betti numbers corresponding to higher-dimensional cavities. All these invariants together provide quick and easy-to-understand summaries of the global shape of data that are still usable after many types of deformation [13, 16].

B. Persistent Homology and the Mapper Algorithm

In contrast, the Mapper algorithm takes a different path: it does not calculate homology on a nested family of complexes but instead, Mapper creates a simplified simplicial model (a graph or simplicial complex) that represents the main shape of the data through (i) selecting a filter function on the data, (ii) covering the filter's image with overlapping intervals, (iii) clustering the pre-images of these intervals, and (iv) linking the clusters that share non-empty intersections. The Mapper provides an easy-to-understand topological summary that supports particularly well visualization and exploratory analysis—hence, it has been employed in various scientific disciplines like biology, medicine, etc., where interpretable summaries are needed[17]. The recent methodological development has propelled Mapper to new fronts where probabilistic and distribution-aware variants have been created, and its stability and statistical properties have been analyzed thereby, making it more reliable for large and noisy datasets [18].

C. Relationship between TDA and Machine Learning

Persistent homology is the core method of extracting multi-scale topological signatures from point clouds or weighted complexes. The usual constructions are based on distance thresholds and consist of Vietoris–Rips and Čech filtrations; after that, the matrix-reduction algorithms compute the homology classes and their persistence. Algorithmic improvements and efficient implementations (e.g. Ripser, GUDHI) engaged in the last decade have greatly enhanced the practicality of computing the persistence of moderately large datasets by the use of sparse representations, cohomology-based reductions, and memory-efficient data structures [19], [20]. For datasets of immense size, research on parallel and GPU-accelerated computations (including approximation schemes) supports scaling persistent homology to more or less the same levels as Big Data scenarios [21].

There is more and more proof that topological descriptors can be used along with conventional machine learning (ML) features and, in certain cases, they can even significantly improve performance and make it easier to understand the model. Usually, persistent summaries (diagrams, barcodes) are converted into machine-learnable vectors through featurization techniques like persistence landscapes, persistence images, persistence silhouettes, and statistical summaries (e.g., persistent Betti numbers) that enable topological information to be introduced to the standard classifiers or regressors [19, 20]. These vectorized topological embeddings are stable and have been applied successfully in classification tasks across various fields such as image analysis, materials science, and biomedicine with great datasets.

In addition to simply featurizing the data, topological machine learning and topological deep learning are examples of tightly coupling topology with learning architectures where the latter include persistent homology being used as an explicit regularizer, the construction of layers within neural networks that compute or approximate the topological signatures, and GNN combined with topological pooling/aggregation to represent higher-order relations. The topological ML surveys demonstrate a broad range of methods from pre-processing (topological featurization) to the end-to-end architecture that learns representations being informed by topology, where each has its own trade-off in scalability, interpretability, and theoretical guarantees [19, 22]. TDA tools are gradually turning out to be formidable partners when it comes to combining different modeling approaches, which use geometry and topology to get better generalization and explainability on difficult datasets [4, 19, 20]. This is because such tools are getting increasingly computationally efficient and are also getting better integrated (e.g., through libraries like GUDHI and optimized packages like Ripser) with ML tool-chains.

Figure 1 displays an overview of the core concepts and connections of TDA within data science. The left branch outlines the basics of topology, including simplicial complexes and homology theory that describe higher-order relationships and topological features in data. The center highlights the key algorithms—Persistent Homology and Mapper—that extract and visualize these structures. The right branch shows the relationship between TDA and machine learning, emphasizing integration with learning workflows, improved interpretability and stability, and the role of topological invariants in summarizing the global shape of data. Table 1 outlines the main conceptual pillars of TDA in data science. It summarizes how topological concepts (simplicial complexes and homology) capture the global structure of high-dimensional data, how Persistent Homology and Mapper provide multi-scale and interpretable

summaries, and how TDA integrates with machine learning to produce topology-aware features that enhance model performance and interpretability. Each row highlights the core idea, computational workflow, key outputs, strengths, representative tools, and notable references that collectively illustrate TDA's methodological framework and practical relevance across domains.

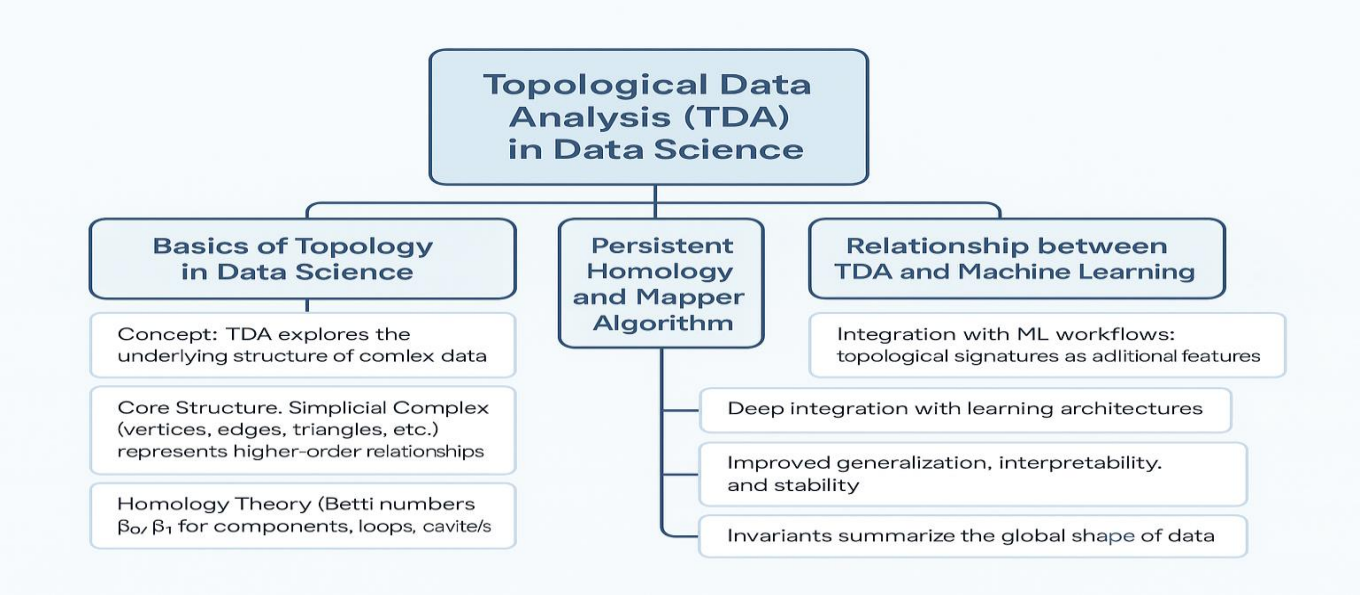

Figure 1 Topological Data Analysis (TDA) in Data Science

Table 1 Summary of Core Components and Methods in Topological Data Analysis (TDA)

Section	Core Idea	How It Works	Key Outputs	Strengths	Notable Tools/Methods	Refs
Basics of Topology in Data Science	Use topology to capture the global "shape" of complex, high-dimensional, noisy data	Build a simplicial complex from data; compute homology groups and Betti numbers (β_0 components, β_1 loops, higher-dim cavities)	Betti numbers / homological invariants summarizing connectivity and holes	Invariants are robust to many deformations; compact, interpretable summaries	Simplicial complexes; homology theory	[13], [16]
Persistent Homology & Mapper	Two complementary summaries: Persistent Homology (PH) for multi-scale features; Mapper for interpretable shape graphs	PH: build filtrations, track birth–death of features via matrix reduction. Mapper: choose filter (lens) → cover with overlapping intervals → cluster pre-images → link overlapping clusters	PH: barcodes/persistence diagrams. Mapper: simplified graph/simplicial complex	PH: stable multi-scale signatures. Mapper: intuitive visualization and exploratory analysis	PH filtrations (VR/Čech), reduction algorithms; Mapper variants (probabilistic, distribution-aware), stability/statistics	[17], [18]
Relationship between TDA & ML	Inject topological signatures into ML pipelines; scale computations to big data	Compute persistence, features (images, landscapes, vectors) → feed to ML models, leverage optimized libraries and accelerators	Topology-aware features for classification, clustering, regression, anomaly detection	Captures global structure ML often misses; modern implementations make PH practical and scalable	Ripser, GUDHI; sparse/cohomology reductions; parallel/GPU & approximation schemes	[19], [20], [21]

III. Methodological Framework

A. Data Preprocessing for TDA in Big Data Environments

The application of Topological Data Analysis (TDA) to modern high-dimensional as well as large-scale datasets depends greatly on an efficient data pre-processing step. The data from the real world are usually full of noise as well as missing values and redundancy, which can bury the underlying topological structures. Therefore, preprocessing is usually a combination of data cleaning, normalization, and dimensionality reduction; this can be done by using different approaches like Principal Component Analysis (PCA), t-distributed Stochastic Neighbor Embedding (t-SNE), and Uniform Manifold Approximation and Projection (UMAP). The last two techniques retain local geometric relations while also reducing the computational complexity for the persistent homology computation [18, 23].

To deal with the Big Data environment, methods such as subsampling and random projection are usually employed which yield point clouds that are representative of the topology. It has been experimentally found that persistence diagrams obtained through stratified subsampling and distance-preserving embedding resemble those computed on full datasets with a great saving in time and memory. In addition, topological denoising algorithms based on local manifold approximations along with density-based filtering have proved to be very effective in avoiding outliers and noise caused by measurements[24] . In a distributed data pipeline, Apache Spark, Dask, and TensorFlow Data Service can be used as the scalable frameworks which would support the application of the preprocessing stages beforehand TDA feature extraction [25]. Before applying TDA to large and heterogeneous datasets, careful preprocessing is required to ensure that the extracted topological features are meaningful and computationally tractable. The workflow displays in figure 2 begins with raw data, which are often noisy, incomplete, and high-dimensional. The cleaning and normalization stage addresses missing values, standardizes scales, and reduces redundancy to produce consistent input representations. Next, denoising techniques—such as manifold approximation and density-based filtering—help to remove spurious variations while maintaining intrinsic structure. Dimensionality reduction (e.g., PCA, t-SNE, UMAP) projects data onto a low-dimensional manifold suitable for simplicial complex construction. To handle large-scale data, scalable execution frameworks (e.g., Apache Spark, TensorFlow Data Service) are employed for distributed or parallel computation. The processed data are then ready for the TDA stage, where persistent homology and related algorithms are computed to uncover global shape and connectivity patterns in big data environments.

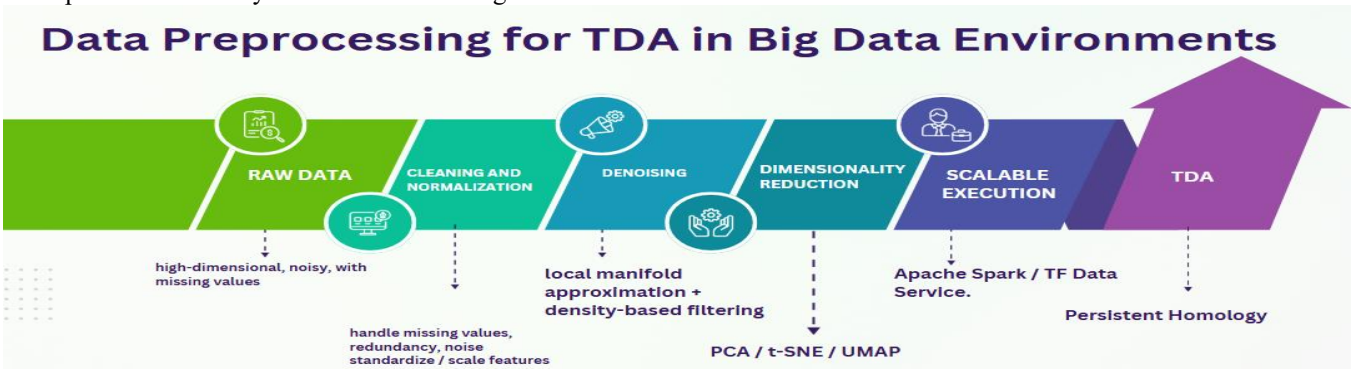

Figure 2 Data Preprocessing for TDA in Big Data Environments.

B. Scalable Algorithms for TDA

The importance of effective data preprocessing cannot be overemphasized in applying Topological Data Analysis (TDA) of modern high-dimensional and large-scale datasets. The real-life data is a mix of various problems like noise, missing values, and redundant dimensions that could hide the topological structures. Preprocessing consists of data cleaning, normalization, and dimensionality reduction through the application of Principal Component Analysis (PCA), t-distributed Stochastic Neighbor Embedding (t-SNE), and Uniform Manifold Approximation and Projection (UMAP) that keep the local geometric relations and lessen the computational complexity for persistent homology computation [18, 23]. Classic persistent homology algorithms encounter an issue of combinatorial explosion as the data size increases. To overcome the problem of scalability, a number of algorithmic innovations have been proposed. GPU-accelerated implementations (e.g., Ripser++, PHat-GPU) utilize parallel reduction of boundary matrices to achieve a tenfold increase in speed for the computation of homology on large point clouds [26].Moreover, distributed and out-of-core algorithms have been devised for computing Vietoris–Rips filtrations over huge datasets by splitting complexes and combining intermediate results [27]. Classic persistent homology algorithms encounter an issue of combinatorial explosion as the data size increases. To overcome the problem of scalability, a number of algorithmic innovations have been proposed. GPU-accelerated implementations (e.g., Ripser++, PHat-GPU) utilize parallel reduction of boundary matrices to achieve a tenfold increase in speed for the computation of homology on large point clouds [10]. Moreover, distributed and out-of-core algorithms have been devised for computing Vietoris–Rips filtrations over huge datasets by splitting complexes and combining intermediate results [27]. Recent studies bring forth approximation-based TDA, including witness complexes and sparsified filtrations, that offer provable error bounds together with considerable computational efficiency [5]. The hybrid methods that merge cohomology computations with matrix factorization techniques also lessens memory needs for high-dimensional data [28]. Such scalable algorithms, which are frequently packaged in libraries like GUDHI, DIPHA, and TDAmapper, have rendered TDA practicable for the contemporary Big Data and real-time analytics situations thus making it possible to interface with AI pipelines at a large scale [29].

C. Integration with Deep Learning and Graph Neural Networks (GNNs)

The combination of TDA and Deep Learning has given birth

to the new subfield called Topological Deep Learning (TDL), which consists of the incorporation of topological invariants into neural architectures. The process of persistent homology may be utilized as a regularization constraint that guarantees topological consistency in the hidden representations learned by autoencoders or convolutional neural networks (CNNs) [30]. Changes in the persistence diagram of the encoded features would not be allowed by the topological loss functions, resulting in more structurally accurate reconstructions [31].

Persistent Betti numbers or persistence landscapes are examples of topological embeddings which have been used in Graph Neural Networks (GNNs) to include node and graph representations that are able to give higher-order interactions other than just pairwise edges [32]. Newer GNN architectures like TopoGNN, PH-GCN, and TopoDiffusion have explicitly allowed the propagation of persistence information during message passing or pooling, thus making them more expressive as well as noise resistant structurally [33]. They not only provide interpretability but also improvements in performance that span various fields such as bioinformatics, materials science, and computer vision [34].

D. Proposed Hybrid Framework

We propose a hybrid TDA–Deep Learning framework that integrates Persistent Homology with Autoencoders and Graph Neural Networks to develop topologically aware embeddings for complex datasets. The pipeline comprises five main steps:

1. *Preprocessing & Subsampling: reduction of data at scale by UMAP and stratified sampling.*
2. Topological Feature Extraction: filtered simplicial complexes technique to compute multi-scale persistent homology features.
3. Topological Autoencoder Module: unsupervised reconstruction with topological loss that retains key homological structures.
4. Graph Neural Topology Module: refinement of structure by GNN aggregation with persistence-informed node attributes.
5. Fusion & Prediction: for subsequent operations like classification or anomaly detection, latent and topological embeddings are concatenated.

The goal is to achieve a topology-preserving yet deep-represented architecture by introducing the stability of persistence diagrams and the expressiveness of neural models [35, 36]. Such hybridization is expected to lead to more robust generalization in the case of complex, structured, and noisy datasets—in particular, in the fields of biomedical, sensor, and materials data. Figure 3 presents a hybrid framework that combines topological data analysis (TDA) with deep learning to enhance representation learning and predictive performance. The process starts with data preprocessing and subsampling.

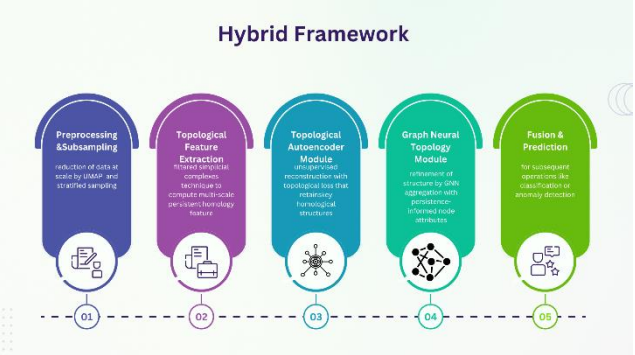

Figure 3 Hybrid Framework Integrating Topological and Neural Modules.

IV. APPLICATIONS

A. TDA in Healthcare and Bioinformatics

Topological Data Analysis (TDA) is becoming more and more popular in the medical field, where it is used to find differences in structures that are not seen easily in high-dimensional data. In medical imaging, persistent homology not only helps in the classification of textured and morphological features which are given by the pixel intensities but also has a wider scope of application. As an instance, TDA is being successfully used in radiology, where it is possible to classify the areas of the tumor and non-tumor regions based on the texture created from the images with more interpretability and robustness than when using the classic radiomic features [37]. Additionally, in detecting COVID-19, a combination of TDA and ML methods was able to extract persistent homology signatures from CT images of the lungs and use those as input for classifiers with over 97% accuracy and AUC > 0.99 [38].

In the fields of genomics and molecular biology, TDA is applied to the analysis of gene expression and interaction networks to find disease subtypes and regulatory modules. Such a comprehensive review is done by Skaf et al. where they enumerate TDA applications in various segments like cancer, neuroimaging, and proteomics among others [39]. Persistent homology has been successfully used to uncover genotype–phenotype associations by analyzing the presence of high-dimensional loops and voids in molecular data that have a correlation with disease progression.

Also, TDA is being utilized in physiological signals to analyze cardiovascular signals (e.g. ECG, PPG) and to find topological invariants that are linked with disease states, thus facilitating the diagnosis and prognosis of cardiovascular conditions [40]. These instances prove that TDA can be regarded as a strong auxiliary tool along with the traditional statistical and machine learning methods in the health and biological sciences.

B. TDA in Network and Graph Analysis

In various domains, such as social, biological and infrastructural networks, the higher-order connectivity patterns are more complex than just pairwise edges. TDA method can help identify the loops, cycles and cavities in the networks that mirror their deeper structural features. Petania et al. talk about TDA's potential to "encode interactions beyond networks" and getting mesoscopic structures in complex systems [41].

For power grid systems, persistent homology has been applied for vulnerability analysis: studying the changes in homological features through simulated failures can help identify critical topological weak points and predict cascading failures. In communication and social networks, TDA overcorrelation or adjacency-based filtrations brings out community structures, network evolution, and anomalies that

are not detectable through standard graph metrics.

A few studies have developed time-evolving correlation networks in finance or neuroscience and performed persistent homology to monitor the shifts in the topology of interconnectedness, thereby uncovering the sudden changes or regime shifts in the underlying system. This peculiar attribute of TDA encourages its application in the field of dynamic network analysis and monitoring [42].

C. TDA in Financial and Economic Data

Financial markets are intricate, nonlinear systems wherein classical linear models still struggle. TDA grants the ability to find out the structural changes and the early warning signals of the crisis. For instance, Gidea & Katz utilize TDA in the correlation networks of stock indices and analyze the topological changes evolving before the 2008 crash, with the emerging loops interpreted as warning signs [43].

With the application of sliding-window persistence landscapes to financial returns in the time series domain, it becomes evident that there are growing trends in low-frequency norms which are preceding crashes, thus serving as a predictive indicator of instability [44]. More modern research examines the possibility of using TDA to foresee financial melt-downs by locating topological features in multivariate price data, thus putting TDA in the same line as econometric and machine learning models in terms of its role [45].

In addition, in the case of macroeconomic networks—such as trade, credit, or banking networks—TDA can uncover hidden structural changes in the connectivity pattern of the network, thereby giving new perspectives on systemic risk and contagion that are not only based on standard network centralities or spectral methods[46]. Figure 3 represents the applications of Topological Data Analysis.

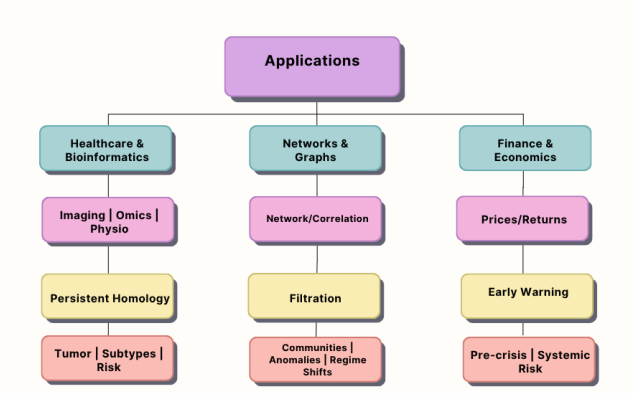

Figure 4 Applications of Topological Data Analysis (TDA).

V. CHALLENGES AND OPEN RESEARCH DIRECTIONS

Despite the growing successes and applications of TDA, numerous fundamental challenges remain to be addressed before its full potential in Big Data settings can be realized.

a) Scalability and Computational Complexity

Among the major challenges to TDA's large scale usage is the combinatorial explosion linked to simplicial complexes construction like Vietoris-Rips or Čech complexes. The increasing size and dimensionality of datasets result in exponential growth of simplices, thus the direct calculation of persistent homology becomes unfeasible for large datasets. This issue is a major limitation of TDA methods that are currently being used because they confine themselves to moderate-scale data or otherwise, require very effective dimensionality reduction or sparsification techniques [46].

The use of GPU-accelerated, parallel, and distributed implementations does help mitigate this problem but they come with memory usage, load balancing, and complexity of merging partial results trade-offs. For instance, the issue of designing scalable algorithms that maintain theoretical guarantees (e.g., upper bounds on error) while efficiently distributing large boundary matrix reductions is still left open as an area of research [47].

Furthermore, in the context of real-world Big Data pipelines, streaming, incremental, and out-of-core TDA algorithms are a must in order to process the data continuously coming in without the need of recomputing from scratch—this is a direction that is still underdeveloped and requires innovations in both algorithmic design and data structures [48].

Specialized hardware has become another important driver of energy efficiency. Edge TPUs, GPUs, and FPGAs, for example, are designed for deploying AI workloads at high throughput, but with significantly lower energy costs compared to typical CPU usage. Accelerators leverage parallelism and low-precision arithmetic to maximize throughput [49]. Additionally, neuromorphic chips, which simulate the operations of biological energy-efficient neurons, are being developed to reduce energy usage in the long run within continuous AI workloads [50].

b) Noise Sensitivity in Persistence Diagrams

Even though theorems regarding stability ensure that input with small perturbations will only result in changes that are bounded in the persistence diagrams, in reality, there are situations like noise in the data, outliers, and irregularities in sampling which cause us to break the assumptions of these theorems. The introduction of, for instance, measurement errors or non-evenly distributed samples may result in the presence of non-existent topological features that could possibly hide the real structure [51].

A study that made a focus on the problem of noise-robust topology estimation through persistent homology has shown that even very good persistent homology pipelines may undergo deterioration when subjected to structured noise or adversarial perturbations. This is especially true with images where noise at the pixel level complicates the identification of the actual cycles [52]. The methods of such as filtering out short-lived features, persistence simplification, denoising filtrations, or using probabilistic persistence might be able to help with this issue, but they would then be risking the loss of real signal or the data being over-smoothened.

The other issue that comes up is the sensitivity of parameters: the selection of filtration scale and the radius of the neighborhood, as well as the size of the sub-sample, are all factors that have a very critical impact on the diagrams produced. The development of resilient methods for the automatic selection of scale and noise-adaptive filtration remains a very active and challenging area of research.

c) Interpretability and Explanation of Topological Signatures

What TDA achieves are compact and informative summaries made possible through persistence diagrams or barcodes, yet drawing these abstract topological signatures into valuable insights for domain experts still remains a challenge. Connecting topological invariants (e.g., Betti numbers, loops, voids) to domain-level phenomena is found to be a maximum challenge by most users, particularly when data is either high-dimensional or heterogeneous.

Mapper visualizations, barcode plots, or persistence

landscapes have been suggested as intermediate interpretative tools, but very often, such methods require expert judgment to infer significance. The absence of highly interpreted frameworks or topological features that are standardized or annotated adds up to the barriers against the potential applicability of TDA in various industries like medicine, biology, etc. (e.g., medicine, biology) [3].

In the deep learning context, TDA came to the fore as an instrument for interpretability: for example, the topology of hidden-layer activations has been investigated through Mapper graphs to expose class separation and internal hierarchical structure [53]. Yet, the implementation of such methodologies on a large scale and for providing real-time explanations is still very limited.

D) Integration with AI Models (Deep Learning / Hybrid Models)

The incorporation of topological data into machine learning as well as into deep neural networks is a very promising yet challenging task. One major challenge is the issue of differentiability; the outputs of persistence computation are in the form of diagrams that are composed of discrete and combinatorial elements, which are not easy to differentiate among. Therefore, it is very difficult to apply them directly to gradient-based training. The research community has been exploring different ways such as differentiable surrogates or approximate backpropagation through persistence layers, but all these methods have some limitations in terms of scalability and theoretical foundations [54].

In addition, there are different ways of representing persistence diagrams (persistence images, landscapes, kernel embeddings), and these are still somewhat ad hoc. The performance of the chosen featureization has a strong influence, yet there is not a universally optimal method existing. Hybrid architectures (e.g., TDA + autoencoders, TDA + GNNs, etc.) confront drawbacks of either losing topological accuracy or losing the expressiveness of the new representations [55].

As the topological deep learning area is developing, the surveys indicate that there are still many isolated architectures that lack inter-task benchmarking, and that the optimal connection between topology and learning is still largely unexplored [55]. Figure 5 highlights the four major research challenges currently shaping the development of Topological Data Analysis (TDA).

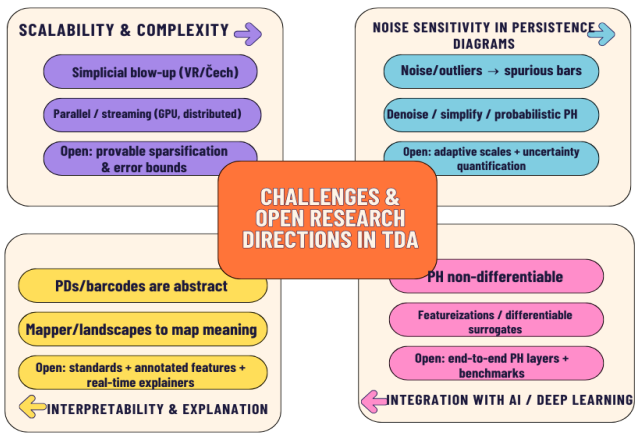

Figure 5 Challenges and Open Research Directions in Topological Data Analysis (TDA)

REFERENCES

1. Chazal, F. and B. Michel, *An introduction to topological data analysis: fundamental and practical aspects for data scientists.* Frontiers in artificial intelligence, 2021. **4**: p. 667963.
2. Wasserman, L., *Topological data analysis.* Annual review of statistics and its application, 2018. **5**(2018): p. 501-532.
3. Carlsson, G., *Topology and data.* Bulletin of the American Mathematical Society, 2009. **46**(2): p. 255-308.
4. Edelsbrunner, H. and J. Harer, *Computational topology: an introduction*. 2010: American Mathematical Soc.
5. Oudot, S.Y., *Persistence theory: from quiver representations to data analysis*. Vol. 209. 2015: American Mathematical Society Providence.
6. Skaf, Y. and R. Laubenbacher, *Topological data analysis in biomedicine: A review.* Journal of Biomedical Informatics, 2022. **130**: p. 104082.
7. Uray, M., et al., *Topological Data Analysis in smart manufacturing: State of the art and future directions.* Journal of Manufacturing Systems, 2024. **76**: p. 75-91.
8. Wee, J. and J. Jiang, *A review of topological data analysis and topological deep learning in molecular sciences.* arXiv preprint arXiv:2509.16877, 2025.
9. Wei, X. and G.-W. Wei, *Persistent topological Laplacians—a survey.* Mathematics, 2025. **13**(2): p. 208.
10. Ceccaroni, R., et al., *A distributed approach for persistent homology computation on a large scale.* The Journal of Supercomputing, 2024. **80**(17): p. 25510-25532.
11. Hajij, M., E. Munch, and P. Rosen. *Fast and scalable complex network descriptor using pagerank and persistent homology*. in *2020 International Conference on Intelligent Data Science Technologies and Applications (IDSTA)*. 2020. IEEE.
12. Cao, Y. and A. Monod, *Approximating persistent homology for large datasets.* arXiv preprint arXiv:2204.09155, 2022.
13. Cohen-Steiner, D., H. Edelsbrunner, and J. Harer. *Stability of persistence diagrams*. in *Proceedings of the twenty-first annual symposium on Computational geometry*. 2005.
14. Su, Z., et al., *Topological Data Analysis and Topological Deep Learning Beyond Persistent Homology--A Review.* arXiv preprint arXiv:2507.19504, 2025.
15. El-Yaagoubi, A.B., M.K. Chung, and H. Ombao, *Topological data analysis for multivariate time series data.* Entropy, 2023. **25**(11): p. 1509.
16. Singh, G., F. Mémoli, and G.E. Carlsson,

Topological methods for the analysis of high dimensional data sets and 3d object recognition. PBG@ Eurographics, 2007. **2**(091-100): p. 90.
17. Kerber, M., *Persistent homology: state of the art and challenges.* International Mathematische Nachrichten, 2016. **231**(15-33): p. 1.
18. McInnes, L., J. Healy, and J. Melville, *Umap: Uniform manifold approximation and projection for dimension reduction.* arXiv preprint arXiv:1802.03426, 2018.
19. Bauer, U., *Ripser: efficient computation of Vietoris–Rips persistence barcodes.* Journal of Applied and Computational Topology, 2021. **5**(3): p. 391-423.
20. Zhang, S., M. Xiao, and H. Wang, *GPU-accelerated computation of Vietoris-Rips persistence barcodes.* arXiv preprint arXiv:2003.07989, 2020.
21. Carriere, M., M. Cuturi, and S. Oudot. *Sliced Wasserstein kernel for persistence diagrams*. in *International conference on machine learning*. 2017. PMLR.
22. Hensel, F., M. Moor, and B. Rieck, *A survey of topological machine learning methods.* Frontiers in Artificial Intelligence, 2021. **4**: p. 681108.
23. Chazal, F., et al. *Subsampling methods for persistent homology*. in *International Conference on Machine Learning*. 2015. PMLR.
24. Kloke, J. and G. Carlsson, *Topological de-noising: Strengthening the topological signal.* arXiv preprint arXiv:0910.5947, 2009.
25. Kallenborn, F., et al., *GPU-accelerated homology search with MMseqs2.* Nature Methods, 2025: p. 1-4.
26. Malott, N.O., et al. *Distributed computation of persistent homology from partitioned big data*. in *2021 IEEE International Conference on Cluster Computing (CLUSTER)*. 2021. IEEE.
27. Sheehy, D.R. *Linear-size approximations to the Vietoris-Rips filtration*. in *Proceedings of the twenty-eighth annual symposium on Computational geometry*. 2012.
28. Maria, C., et al. *The gudhi library: Simplicial complexes and persistent homology*. in *International congress on mathematical software*. 2014. Springer.
29. Moor, M., et al. *Topological autoencoders*. in *International conference on machine learning*. 2020. PMLR.
30. Hofer, C., et al., *Deep learning with topological signatures.* Advances in neural information processing systems, 2017. **30**.
31. Pun, C.S., S.X. Lee, and K. Xia, *Persistent-homology-based machine learning: a survey and a comparative study.* Artificial Intelligence Review, 2022. **55**(7): p. 5169-5213.
32. Horn, M., et al., *Topological graph neural networks.* arXiv preprint arXiv:2102.07835, 2021.
33. Brüel-Gabrielsson, R., et al., *A topology layer for machine learning.* arXiv preprint arXiv:1905.12200, 2019.
34. Papamarkou, T., et al., *Position: Topological deep learning is the new frontier for relational learning.* Proceedings of machine learning research, 2024. **235**: p. 39529.
35. Maurya, A., et al., *Hybrid topological data analysis and deep learning for basal cell carcinoma diagnosis.* Journal of Imaging Informatics in Medicine, 2024. **37**(1): p. 92-106.
36. Gidea, M. and Y. Katz, *Topological data analysis of financial time series: Landscapes of crashes.* Physica A: Statistical mechanics and its applications, 2018. **491**: p. 820-834.
37. Singh, Y., et al., *Topological data analysis in medical imaging: current state of the art.* Insights into Imaging, 2023. **14**(1): p. 58.
38. Umeda, Y., J. Kaneko, and H. Kikuchi, *Topological data analysis and its application to time-series data analysis.* Fujitsu Scientific & Technical Journal, 2019. **55**(2): p. 65-71.
39. Petri, G., et al., *Topological strata of weighted complex networks.* PloS one, 2013. **8**(6): p. e66506.
40. Gidea, M. *Topological data analysis of critical transitions in financial networks*. in *International conference and school on network science*. 2017. Springer.
41. Xu, J., *Topological structure and analysis of interconnection networks*. Vol. 7. 2013: Springer Science & Business Media.
42. Andjelković, M., et al., *Topology of innovation spaces in the knowledge networks emerging through questions-and-answers.* PloS one, 2016. **11**(5): p. e0154655.
43. Emrani, S., T. Gentimis, and H. Krim, *Persistent homology of delay embeddings and its application to wheeze detection.* IEEE Signal Processing Letters, 2014. **21**(4): p. 459-463.
44. Umeda, Y., *Time series classification via topological data analysis.* Information and Media Technologies, 2017. **12**: p. 228-239.
45. Gupta, S., et al., *Topology-aware uncertainty for image segmentation.* Advances in Neural Information Processing Systems, 2023. **36**: p. 8186-8207.
46. Chen, M., et al., *Narrow band internet of things.* IEEE access, 2017. **5**: p. 20557-20577.
47. Chab, R., F. Li, and S. Setia, *Algorithmic Techniques for GPU Scheduling: A Comprehensive Survey.* Algorithms, 2025. **18**(7): p. 385.
48. Anang, A.N. and J.N. Chukwunweike, *Leveraging Topological Data Analysis and AI for Advanced Manufacturing: Integrating Machine Learning and Automation for Predictive Maintenance and Process*

Optimization. Int. J. Comput. Appl. Technol. Res, 2024. **13**: p. 27-39.
49. Suzuki, S., et al., *GPU-acceleration of sequence homology searches with database subsequence clustering.* PLoS one, 2016. **11**(8): p. e0157338.
50. Bauer, U., M. Kerber, and J. Reininghaus. *Distributed computation of persistent* homology. in 2014 proceedings of the sixteenth workshop on algorithm engineering and experiments (ALENEX). 2014. SIAM.
51. Chazal, F., et al. Convergence rates for persistence diagram estimation in topological data analysis. in International Conference on Machine Learning. 2014. PMLR.
52. Peek, D., M.P. Skerritt, and S. Chalup, Noise-Robust Topology Estimation of 2D Image Data via Neural Networks and Persistent Homology. arXiv preprint arXiv:2509.09140, 2025.
53. Dembowski, C., et al., Experimental observation of the topological structure of exceptional points. Physical review letters, 2001. 86(5): p. 787.
54. Montgomery, R.M., Topological Machine Learning and the Geometry of Neural Networks: A Comprehensive Survey of Recent Advances.
55. Zia, A., et al., Topological deep learning: a review of an emerging paradigm. Artificial Intelligence Review, 2024. 57(4): p. 77.

Stability analysis in a mutualism model with two discrete delays

Olfat Al Lakkies*[1]

[1]Department of Mathematics and Informatics, National University of Science and Technology Politehnica of Bucharest, 060042 Bucharest, Romania, olfat.al@stud.fsa.upb.ro

Abstract

This paper studies a two–species mutualism model formulated as a system of delay differential equations with two discrete lags τ_1, τ_2 that encode time–lagged self–regulation and interspecific facilitation. Focusing on the positive coexistence equilibrium, we derive computable criteria for local asymptotic stability by linearization and analysis of the associated characteristic quasipolynomial. In the zero–delay limit, stability is characterized by necessary and sufficient Routh–Hurwitz conditions expressed explicitly in the model parameters. With a single nonzero delay, the imaginary–axis crossing problem reduces to a quartic in ω^2, which yields delay–independent stability regions; when those are violated, we obtain closed–form expressions for the Hopf frequency and the corresponding threshold delays τ_{1k}. For the case of two nonzero delays, we eliminate the phase terms by expressing $\cos(\omega\tau_2)$ and $\sin(\omega\tau_2)$ and using the fundamental relation between them to characterize the crossing set and construct branches τ_{2k} as functions of the model coefficients and the fixed τ_1. Transversality of the eigenvalue crossing is verified via $d\,\mathrm{Re}\,\lambda/d\tau \neq 0$, ensuring the occurrence of Hopf bifurcations and the emergence of small–amplitude periodic orbits. Time–domain simulations corroborate the analytical boundaries, illustrating delay–induced loss of stability and the birth of stable oscillations for parameter values relevant to ecological mutualism. Collectively, the results quantify how delayed mutualistic feedback interact, with nonlinear density dependence, to describe stability regions in the (τ_1, τ_2)–plane, providing practical algebraic tests for stability and bifurcation in a broad class of delayed mutualism models.

*This paper is a joint work with Laurance Fakih, Paul Georgescu, and Andrei Halanay.

IMPLEMENTING C++ COMPUTER PROGRAMS FOR SOME CLASSES OF COMPLEX ELLIPTIC CURVES

Radu Gaba[1], Vlad Olteanu[2], Bogdan Canepa[3]

[1]Institute of Mathematics "Simion Stoilow" of the Romanian Academy, Calea Grivitei 21 and University Politehnica of Bucharest, 313 Splaiul Independentei, District 6, Bucharest, Romania

[2]"unaffiliated

[3]M.Guguianu Highschool, Vaslui

Corresponding author email: radu.gaba@imar.ro

Abstract

In this note we present the C++ computer programs developed with the scope of improving the complexity orders of the algorithms of [1] by mean of which Canepa and Gaba classified on one hand the complex elliptic curves E for which there exist non-cyclic subgroups C of finite order n of the additive group (E, +) such that the elliptic curves E/C and E are isomorphic and on the other hand, upon imposing some conditions in order to include the cyclic case, the complex elliptic curves E for which there exist subgroups C of (E, +) of finite order n such that the elliptic curves E and E/C are isomorphic. We also provide a thoroughly comparison of the results we have obtained when running the two computer programs on the same machine after doubling its Random Access Memory size.

Key words*: algorithm, non-cyclic subgroup, elliptic curve, fixed point, complexity order*

1. INTRODUCTION

Let E be an elliptic curve defined over the complex numbers field and C a subgroup of finite order n of the additive group of points (E, +). That is, C is a subgroup of order n of the n-torsion subgroup of E, namely E[n]. The group E/C has a structure of Riemann variety since C acts effectively and properly discontinuous on E and the structure is compatible with the natural projection map E→E/C which is an unramifed isogeny of degree n.

2. CONTENT

This work is a follow up of [2] and deals with creating and implementing in C++ two faster computer programs developed by the authors in order to improve the complexity orders of the algorithms created by Canepa and Gaba in [1] , with the purpose of classifying on one hand the complex elliptic curves E for which there exist non-cyclic subgroups C of (E, +) of order n such that the elliptic curves E and E/C are isomorphic and on the other hand, upon imposing certain conditions in order to include the cyclic case, classifying the complex elliptic curves E for which there exist subgroups C of (E, +) of order n such that the elliptic curves E and E/C are isomorphic. We briefly recall how were the algorithms developed and we extend the results to the general case in the second computer program. We introduce several helper classes which will replace mathematical functions using dynamic programming. Using the helper classes the new algorithms are faster than the old ones, their complexity orders being $O(\sqrt{n})$ faster than the complexity orders of the old ones. We provide various examples of the above classes of complex elliptic curves. We also provide a thoroughly comparison of the results we have obtained when running the two computer programs on the same machine after doubling its Random Access Memory size. We compute the CPU time it takes to complete the calculations.

We remark that the isomorphism E isomorphic to E/C can only occur for non-singular projective curves of genus 1. In higher genus, if X is a non-singular projective curve of genus g(X) greater or equal to 2, then one can show that there is no non-trivial finite subgroup C of the group of

automorphisms of X, Aut(X), acting holomorphically and effectively on X such that X is isomorphic to X/C. Consequently, the problem we study cannot be generalized to higher genus non-singular projective curves.

The main theorem used for developing the codes is the following one:

Theorem. ([1], Theorem 2.1) Let E be a complex elliptic curve.
Then there exists a finite subgroup C of (E,+) such that $C \cong \mathbb{Z}/D_1 \times \mathbb{Z}/D_2$ and $D_1|D_2$, $D_1 \neq D_2$ and with the property that $\frac{E}{C} \cong$ E if and only if τ satisfies the equation $\tau^2 = u\tau + v, u, \tau \in \mathbb{Q}$, $\Delta = u^2 + 4v < 0$ and there exist $(a, b') \in \mathbb{Z} \times \mathbb{Z}$ with $Gcd(a, b') = D_1$ such that, if one denotes by (a, A, b, B) the numbers $(a, A, b, B) := \left(a, \frac{u_2 v_1}{d_2} b', \frac{u_2 v_2}{d_2} b', a + \frac{u_1 v_2}{d_2} b'\right)$ and by M the matrix: $M = \begin{pmatrix} a & A \\ b & B \end{pmatrix}$, then we have the relation $\det(M) = D_1 D_2$. We have denoted by $u := \frac{u_1}{u_2}$, $v := \frac{v_1}{v_2}$ with $u_2, v_2 \neq 0$ and $u_1, v_1, u_2, v_2 \in \mathbb{Z}$, $Gcd(u_1, u_2) = Gcd(v_1, v_2) = 1$, $d_2 := Gcd(u_2, v_2)$.
Moreover, the isomorphism $\frac{E}{C} \cong$ E comes from a morphism of varieties: $\phi_{a,b'}$: E → E which has the following properties:

1) $\deg(\phi_{a,b'}) = D_1 D_2$;
2) it is a group homomorphism;
3) $Ker(\phi_{a,b'}) = C$;
4) $Ker(\phi_{a,b'}) = \nu z$, ν=a+bτ.

Remark. When writing the second computer program we allow the case $D_1 = 1$ where $D_1 = Gcd(a, b')$.

3. CONCLUSIONS

The computer programs developed can be used in the theory of complex elliptic curves. We emphasize here the utility of studying quotients of complex elliptic curves and also of studying isomorphisms classes of type E isomorphic to E/C which can be further used in studying fixed points of the action of Fricke's involution on the open modular curves $Y_0(n)$. We also present several applications of Hurwitz's Theorem for compact Riemann surfaces ([3]) and of Chow's theorem for abelian varieties ([4]).

REFERENCES:

[1] B. Canepa, R. Gaba A generalization of a Fixed point theorem for CM Elliptic Curves.
U.P.B. Sci. Bull., Series A, Vol. 81, Iss. 1, (2019), p. 3-12.
[2] B. Canepa, R. Gaba A CM Complex Elliptic Curves and Algorithms Complexity.
U.P.B. Sci. Bull., Series A, Vol. 84, Iss. 4, (2022), p. 123-130.
[3] R. Miranda, Algebraic curves and Riemann surfaces, Graduate Studies in Mathematics, volume 5, AMS.
[4].W.L. Chow On the quotient variety of an abelian variety, Mathematics, volume 38, (1952). p. 1039-1044.

ARTIFICIAL INTELLIGENCE: AN URGENT NEED IN INITIAL TEACHER TRAINING

Robert Berezovski

University Politehnica of Bucharest - Pitești University Center, Str. Târgul din Vale, nr.1
110040 Pitesti, Argeș, Romania

Corresponding author email: robert.berezovski@upb.ro

Abstract

We are witnessing a rapid transformation of society, driven largely by exponential advances in Artificial Intelligence (AI). This technological revolution is also affecting the field of education, bringing with it unprecedented challenges and opportunities. In order to prepare future generations of students for a world shaped by AI, it is imperative that teachers themselves be equipped with solid knowledge and skills in this field. Thus, the integration of AI into the initial training of teachers is a fundamental necessity in the development of teaching skills.

Key words*: Artificial Intelligence, initial teacher training, teaching competence*

We are witnessing a rapid transformation of society, driven largely by exponential advances in Artificial Intelligence (AI). This technological revolution is also affecting the field of education, bringing with it unprecedented challenges and opportunities. In order to prepare future generations of students for a world shaped by AI, it is imperative that teachers themselves are equipped with solid knowledge and skills in this field. Thus, the integration of AI into initial teacher training is a fundamental necessity in the development of teachers' skills.

At the European level [1], a series of significant investments have been made in numerous research and innovation activities related to the digitization of education. These investments have been made through various European programs, such as the Horizon 2020 program [2]. The Horizon 2020 program covered the following areas:

- mentoring programs for schools: integrating innovation by spreading advanced ICT-based teaching practices across a wide range of schools (DT-TRANSFORMATIONS-21-2020); a new generation internet that's good for empowerment and inclusion (ICT-2019-30);
- building international partnerships in low- and middle-income countries (ICT-39-2016-2017);
- technologies for learning and skills (ICT-22-2016);
- technologies for better human learning and teaching (ICT 20-2015);
- advanced gaming/digital gamification technologies (ICT 21-2014).

The European Commission aims to modernize education and training by funding research and innovation and promoting digital technologies used for learning. Thus, through the Digital Education Action Plan (2021-2027) [3], the EU wants to support the sustainable and effective adaptation of EU Member States' education and training systems to the digital age by establishing 13 actions in two priority areas:

- promoting the development of a high-performance digital education ecosystem;
- strengthening digital skills and competences for digital transformation.

Within the first priority area, a group of experts was tasked with developing ethical guidelines on artificial intelligence and the use of data in education and training[4] and for the second priority area, another group of experts was tasked with developing common guidelines for teachers and educators to promote digital literacy and combat disinformation through education and training[5].

Following an initiative by the European Parliament, the European Commission is co-financing a series of pilot projects on digital education. A concrete example is the pilot project "Girls 4 STEM in Europe" [6], which aims to increase girls' interest in science, technology, engineering, and mathematics (STEM) subjects, studies, and careers by promoting and teaching STEM subjects in attractive and engaging ways.

The world in which today's students will live and work will be profoundly influenced by AI. From automating repetitive tasks to analyzing complex data and generating content, AI is reshaping industries, economies, and, implicitly, the skills needed for success. Teachers are central pillars in preparing students for

this reality. Without a solid understanding of AI, teachers risk providing students with an education that is out of sync with the demands of the future.

Here are some key reasons why initial teacher training in AI is important:

1. Preparing students for the future.

Future teachers need to understand how AI will affect the job market in order to guide students in choosing relevant educational and career paths. They need to teach students not only about AI, but also how to work alongside AI, developing complementary skills such as critical thinking, creativity, complex problem solving, and emotional intelligence—areas where AI is still lacking.

2. Optimizing the teaching process.

AI offers powerful tools to personalize learning and streamline classroom management. Teachers trained in AI will be able to use adaptive platforms that adjust content and teaching pace to each student's needs, use AI systems for quick and personalized feedback, and automate administrative tasks, freeing up valuable time for direct interaction with students.

3. Developing critical and ethical thinking.

As AI becomes more prevalent, ethical challenges related to bias, data privacy, and social impact are also emerging. Teachers need to be able to initiate informed discussions with students about these issues, encouraging responsible and ethical use of technology. Without their own understanding of these dilemmas, it will be difficult for them to guide students in developing critical and ethical behavior.

4. Innovation and research in education.

Teachers who understand AI can contribute to pedagogical innovation. They can experiment with new AI-based teaching approaches, participate in research on the effectiveness of AI tools in education, and become developers of AI-assisted educational solutions themselves.

5. Combating technological anxiety.

Poor integration of AI can cause anxiety and reluctance among teachers. Solid initial training will demystify AI, reduce unfounded fears about its negative influence on the human psyche, and encourage a proactive attitude of exploration and adaptation to new technologies.

Before we can develop effective training programs, we need to understand where we stand at the moment. A questionnaire on the use of AI in the teaching activities of future teachers, administered to students enrolled in initial teacher training programs (bachelor's, master's degrees in education), could provide a clear picture of the current situation.

In addition to providing an overview, the use of a questionnaire has multiple benefits, including:

-**Supporting curriculum decisions**: The data collected will provide a solid basis for adapting and updating initial training programs. Thus, education science faculties can develop specific modules, optional courses, or practical workshops that meet the real needs of future teachers.

-**Development of personalized educational resources**: Based on the profiles identified, differentiated learning resources can be created—from introductory guides for those with little experience to advanced materials for those already familiar with AI.

-**Evaluating the impact of training**: By applying the questionnaire at both the beginning and end of training programs, the effectiveness of educational interventions and their impact on students' knowledge and attitudes can be measured.

-**Anticipating future needs**: Monitoring perceptions and use of AI among young teachers will allow the education system to anticipate trends and prepare teachers for upcoming AI innovations.

-**Creating a responsible pro-AI culture**: By openly addressing the topic and encouraging reflection on AI, the questionnaire contributes to creating an organizational culture in which AI is seen as an educational partner, not a threat.

REFERENCES:

[1] https://digital-strategy.ec.europa.eu/ro/policies/digital-learning ;
[2] https://digital-strategy.ec.europa.eu/ro/policies/digital-learning ;
[3] https://education.ec.europa.eu/focus-topics/digital-education/plan ;
[4]https://ec.europa.eu/transparency/expert-groups-register/screen/expert-groups/consult?lang=en&do=groupDetail.groupDetail&groupID=3774;
[5]https://ec.europa.eu/transparency/expert-groups-register/screen/expert-groups/consult?lang=en&do=groupDetail.groupDetail&groupID=3774;
[6] https://icse.eu/international-projects/gem/;

AVERAGE OVERSHOOT OF JUMP-DIFFUSION PROCESSES

Romain Mrad[1] and Mario Lefebvre[3]

Fie $\tau(x)$ prima dată când procesul unidimensional de difuzie prin salturi $\{X(t), t \geq 0\}$ părăsește intervalul (c_1, c_2). Studiem depășirea medie deasupra frontierei la c_2 în cazul salturilor ascendente. Mai întâi, derivăm ecuația integro-diferențială satisfăcută de funcția $R(x) = E[(X(\tau(x)) - c_2)_+]$ care denotă depășirea medie. Apoi, arătăm că, în cazul salturilor exponențiale, această ecuație integro-diferențială poate fi transformată într-o ecuație diferențială ordinară de ordinul trei. În cele din urmă, soluții explicite ale ecuației diferențiale se obțin în cazul în care partea continuă a procesului de difuzie prin salturi este un proces Wiener particular și când este un proces CIR particular.

Let $\tau(x)$ be the first time that the one-dimensional jump-diffusion process $\{X(t), t \geq 0\}$ leaves the interval (c_1, c_2). We study the average overshoot above the boundary at c_2 in the case of upward jumps. First, we derive the integro-differential equation satisfied by the function $R(x) = E[(X(\tau(x)) - c_2)_+]$ that denotes the average overshoot. Then, we show that, in the case of exponential jumps, this integro-differential equation can be transformed into a third-order ordinary differential equation. Finally, explicit solutions to the differential equation are obtained in the case when the continuous part of the jump-diffusion process is a particular Wiener process, and when it is a particular CIR process.

Keywords: integro-differential equation, Brownian motion, infinitesimal generator, Dynkin's formula.

2010 Mathematics Subject Clasification: 60J 75, 60J 70.

1. Introduction

We consider the one-dimensional jump-diffusion process $\{X(t), t \geq 0\}$ defined by

$$X(t) = X(0) + \int_0^t \mu[X(s)]\mathrm{d}s + \int_0^t \sigma[X(s)]\mathrm{d}W(s) + \sum_{k=1}^{N(t)} Y_k, \qquad (1)$$

where $\{W(t), t \geq 0\}$ is a standard Brownian motion, $\{N(t), t \geq 0\}$ is a Poisson process with rate λ (independent of the Brownian motion), and $Y_1, Y_2, \ldots$ are independent random variables that are distributed as the random variable Y having the probability density function $f_Y(y)$, and are independent of the

[1]Master's student, Polytechnique Montréal, Canada, e-mail: romain.mrad@polymtl.ca
[2]Full professor, Polytechnique Montréal, Canada, e-mail: mlefebvre@polymtl.ca

Poisson process. The functions $\mu(\cdot) \in \mathbb{R}$ and $\sigma(\cdot) \geq 0$ are assumed to be such that the stochastic differential equation

$$\mathrm{d}X(t) = \mu[X(t)]\mathrm{d}t + \sigma[X(t)]\mathrm{d}W(t) \tag{2}$$

has a unique solution (which is a diffusion process).

Next, let $\tau(x)$ be the first-passage time defined by

$$\tau(x) = \inf\{t \geq 0 : X(t) \notin (c_1, c_2) \mid X(0) = x \in [c_1, c_2]\}. \tag{3}$$

We are interested in the average overshoot

$$R(x) := E[(X(\tau(x)) - c_2)_+], \tag{4}$$

where $(x-c_2)_+ := \max\{x-c_2, 0\}$. This type of quantity arises in the valuation of path-dependent financial products, such as lookback options or barrier-type structured products, where the average overshoot models the expected payoff associated with the underlying crossing a critical level.

For a jump-diffusion process with double exponential jumps, Kou and Wang [6] derived closed-form expressions for the moment-generating function of the first-passage time and for the joint distribution of the first-passage time and the overshoot. They showed that the overshoot is exponentially distributed, conditional on being positive, and that conditional independence between the first-passage time and the overshoot can be used to simplify computations.

Yin *et al.* [8] extended this framework to jumps following a mixed exponential distribution, also obtaining explicit formulas for the joint moment-generating function of the first-passage time and the overshoot. In addition, Klüppelberg *et al.* [4] investigated Lévy processes with heavy-tailed jumps and established an explicit asymptotic expression for the overshoot, conditional on crossing a high level.

These contributions represent some of the few cases where analytical expressions are available, and they serve as useful benchmarks for the study of the Cox-Ingersoll-Ross (CIR) process with jumps.

In the next section, the integro-differential equation (IDE) satisfied by the function $R(x)$ will be derived. Moreover, we will show that when the jump size Y has an exponential distribution, it is possible to transform the IDE into an ordinary differential equation (ODE). In Section 3, two particular processes will be considered: a Wiener process and a CIR process, with exponential jumps. We will end with a few remarks in Section 4.

2. **The general case**

First, we will derive the IDE satisfied by the function $R(x)$.

Proposition 2.1. *The function $R(x)$ defined in Eq. (4) satisfies the integro-differential equation*

$$\mathcal{L}R(x) = -\int_{c_2-x}^{\infty} (x + y - c_2) f_Y(y)\mathrm{d}y, \tag{5}$$

where $\mathcal{L}$ is the infinitesimal generator of the jump-diffusion process $\{X(t), t \geq 0\}$:

$$\mathcal{L}f(x) = \frac{1}{2}\sigma^2(x)f''(x) + \mu(x)f'(x) + \lambda \int_{-\infty}^{\infty} [f(x+y) - f(x)]f_Y(y)\mathrm{d}y \quad (6)$$

for functions f that are twice differentiable with continuous second derivative. The equation is valid for $x \in (c_1, c_2)$. The boundary conditions are $R(c_1) = R(c_2) = 0$.

Proof. Let $f(x) := (x - c_2)_+ = \max\{x - c_2, 0\}$. Then, by applying Dynkin's formula (see [3]), we obtain

$$\mathbb{E}[f(X(\tau(x)))] = f(x) + \mathbb{E}\left[\int_0^{\tau(x)} \mathcal{L}f(X(s))\mathrm{d}s\right]. \quad (7)$$

For $x \in (c_1, c_2)$, we have $f(x) \equiv 0$, which implies that

$$\mathcal{L}f(x) = \lambda \int_{-\infty}^{\infty} f(x+y)f_Y(y)\mathrm{d}y = \lambda \int_{c_2-x}^{+\infty} (x + y - c_2)f_Y(y)\mathrm{d}y. \quad (8)$$

The average overshoot is then given by

$$R(x) := \mathbb{E}\left[(X(\tau(x)) - c_2)_+\right] = \mathbb{E}[f(X(\tau(x)))] = \mathbb{E}\left[\int_0^{\tau(x)} U(X(s))\mathrm{d}s\right], \quad (9)$$

with $U(x)$ defined as follows:

$$U(x) = \lambda \int_{c_2-x}^{\infty} (x + y - c_2)f_Y(y)\mathrm{d}y. \quad (10)$$

Finally, Abundo [1] has shown that $R(x)$ satisfies

$$\mathcal{L}R(x) = -U(x), \quad (11)$$

with $R(c_1) = R(c_2) = 0$. □

Remark 2.1. *The mathematical expectation in the definition of the function $R(x)$ is only of interest in the case when $x \in (c_1, c_2)$. For $x \notin (c_1, c_2)$, we set $R(x) = 0$. Since the jumps are positive, we can write that $R(x) = 0$ for $x \geq c_2$.*

Next, we consider the case when the random variable Y is exponentially distributed.

Proposition 2.2. *Suppose that the jump size Y has an exponential distribution with parameter θ; that is,*

$$f_Y(y) = \theta e^{-\theta y} \quad \text{for } y > 0 \quad (12)$$

Then the function $R(x)$ satisfies the linear third-order ODE

$$\begin{aligned} &\sigma^2(x)R'''(x) + \{2\mu(x) + \sigma(x)[2\sigma'(x) - \theta\sigma(x)]\}R''(x) \\ &-2[\lambda - \mu'(x) + \theta\mu(x)]R'(x) = 0, \end{aligned} \quad (13)$$

subject to $R(c_1) = R(c_2) = 0$.

Remark 2.2. *(i) Notice that Eq. (13) is actually a second-order ODE for $R'(x)$. (ii) We assume that the functions $\mu(x)$ and $\sigma(x)$ are differentiable. (iii) We need a third condition on the function $R(x)$ to obtain a unique solution to the differential equation. (iv) The boundary conditions in the proposition are valid if the boundaries at c_1 and c_2 are both attainable. For example, if the continuous part of the jump-diffusion process $\{X(t), t \geq 0\}$ is a geometric Brownian motion, then the origin is unattainable.*

Proof. The IDE in Eq. (5) becomes

$$\frac{1}{2}\sigma^2(x)R''(x) + \mu(x)R'(x) + \lambda \int_0^{c_2-x} R(x+y)\theta e^{-\theta y}\mathrm{d}y - \lambda R(x) = -\frac{\lambda}{\theta}e^{\theta(x-c_2)}. \tag{14}$$

That is,

$$\frac{1}{2}\sigma^2(x)R''(x) + \mu(x)R'(x) + \lambda\Delta(x) - \lambda R(x) = -\frac{\lambda}{\theta}e^{\theta(x-c_2)}, \tag{15}$$

where

$$\Delta(x) := \theta e^{\theta x}\int_x^{c_2} R(z)e^{-\theta z}\mathrm{d}z. \tag{16}$$

From Eq. (15), we have

$$\lambda\Delta(x) = -\frac{1}{2}\sigma^2(x)R''(x) - \mu(x)R'(x) + \lambda R(x) - \frac{\lambda}{\theta}e^{\theta(x-c_2)}, \tag{17}$$

and we calculate

$$\Delta'(x) = \theta\left[\Delta(x) - R(x)\right]. \tag{18}$$

Hence, differentiating Eq. (15), we find (after simplification) that

$$\begin{aligned}&\frac{1}{2}\sigma^2(x)R'''(x) + R''(x)\left\{\mu(x) + \frac{1}{2}[\sigma^2(x)]' - \frac{\theta}{2}\sigma^2(x)\right\}\\ &+R'(x)\left[\mu'(x) - \lambda - \theta\mu(x)\right] = 0.\end{aligned} \tag{19}$$

As in Proposition 2.1, the boundary conditions are $R(c_1) = R(c_2) = 0$, which follows at once from the definition of the function $R(x)$. □

In the next section, Eq. (13) will be solved explicitly in the case when the continuous part of $\{X(t), t \geq 0\}$ is a particular Wiener process, and also when it is a particular CIR process.

3. **Particular cases**

Let us denote by $\{X_c(t), t \geq 0\}$ the continuous part of $\{X(t), t \geq 0\}$.

3.1. The Wiener process

The first particular case that we consider in the one when Eq. (1) is given by

$$X(t) = X(0) + \mu t + \sigma W(t) + \sum_{k=1}^{N(t)} Y_k, \tag{20}$$

where $\mu \in \mathbb{R}$ and $\sigma > 0$. Then, $\{X_c(t), t \geq 0\}$ is a Wiener process with drift μ and dispersion parameter σ. The third-order ODE (19) becomes

$$\sigma^2 R'''(x) - \left(\theta\sigma^2 - 2\mu\right) R''(x) - 2(\lambda + \mu\theta)R'(x) = 0, \tag{21}$$

whose closed-form solution exists, but is rather involved. Therefore, we will consider a special case.

Setting $\mu = \lambda = \theta = 1$ and $\sigma = \sqrt{2}$, we obtain

$$R'''(x) - 2R'(x) = 0. \tag{22}$$

We take $c_1 = 0$ and $c_2 = 1$. In addition to the boundary conditions $R(0) = R(1) = 0$, we impose a third condition: $R(1/2) = r$, where r is to be determined. We then find the following solution to Eq. (22):

$$R(x) = -r \operatorname{csch}^2\left(\frac{1}{2\sqrt{2}}\right) \sinh\left(\frac{x-1}{\sqrt{2}}\right) \sinh\left(\frac{x}{\sqrt{2}}\right). \tag{23}$$

Substituting the above function into the integro-differential equation (11), we can find the value of the constant r. The final solution is

$$R(x) = -\frac{2\sinh\left(\frac{x-1}{\sqrt{2}}\right)\sinh\left(\frac{x}{\sqrt{2}}\right)}{\sqrt{2}\sinh\left(\frac{1}{\sqrt{2}}\right) + 2\cosh\left(\frac{1}{\sqrt{2}}\right)}. \tag{24}$$

Remark 3.1. *In the general case, we can use a mathematical software package such as* Maple *to find (numerically) the value of* r.

To confirm the above expression for the function $R(x)$, we ran simulations of the overshoot for two values of the parameter λ, and we compared them to the exact function; see Figures 1 and 2. The simulation results clearly agree with the theoretical findings.

3.2. The Cox-Ingersoll-Ross process

Next, we assume that Eq. (1) takes the form

$$X(t) = X(0) + \int_0^t a[b - X(s)]\,\mathrm{d}s + \int_0^t \sigma\sqrt{X(s)}\,\mathrm{d}W(s) + \sum_{k=1}^{N(t)} Y_k. \tag{25}$$

This time, $\{X_c(t), t \geq 0\}$ is a CIR process. The third-order ODE (19) becomes

$$\sigma^2 x R'''(x) + R''(x)\left[2a(b-x) + \sigma^2 - \theta\sigma^2 x\right] - 2R'(x)\left[a\theta(b-x) + a + \lambda\right] = 0. \tag{26}$$

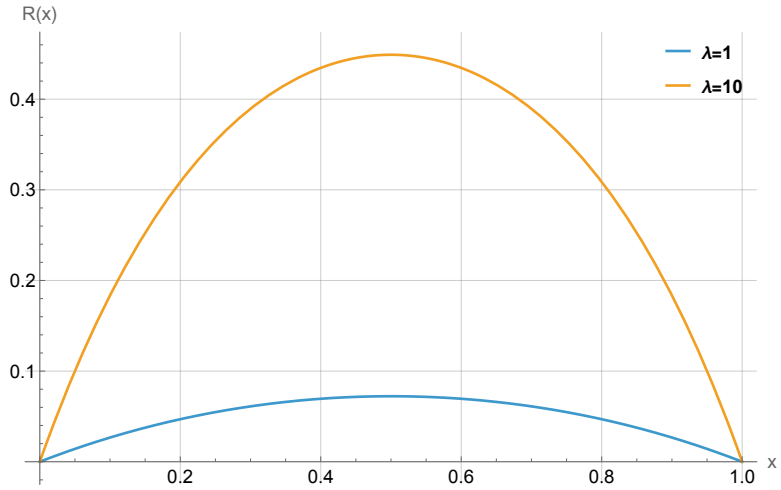

FIGURE 1. Exact function $R(x)$ for the particular Wiener process with jumps considered.

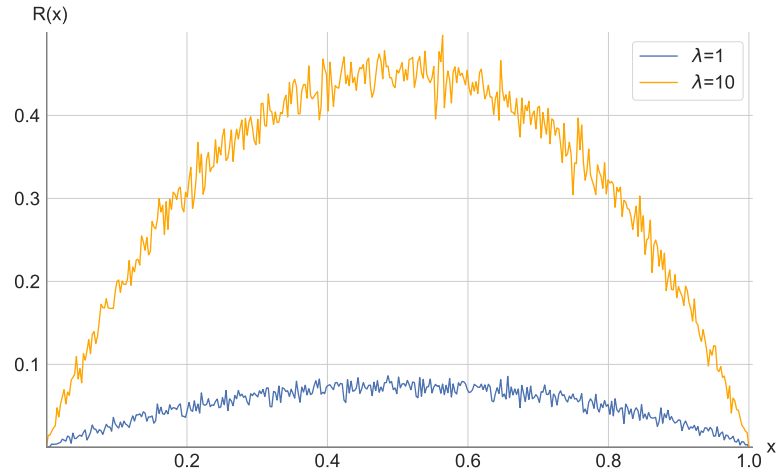

FIGURE 2. Simulation results for the particular Wiener process with jumps considered.

We will treat a special case, namely the one when $a = 0$, so that

$$xR'''(x) - (\theta x - 1)R''(x) - 2\frac{\lambda}{\sigma^2}R'(x) = 0. \tag{27}$$

The above ODE is a Kummer equation for $R'(x)$. Its general solution is known to be (see [7])

$$R'(x) = k_1\Phi\left(\frac{2\lambda}{\theta\sigma^2}, 1, \frac{x}{\theta}\right) + k_2\Psi\left(\frac{2\lambda}{\theta\sigma^2}, 1, \frac{x}{\theta}\right), \tag{28}$$

where k_1 and k_2 are constants, and $\Phi(\cdot,\cdot,\cdot)$ and $\Psi(\cdot,\cdot,\cdot)$ are confluent hypergeometric functions of the first and second kind, respectively.

Integrating Eq. (28), we obtain (assuming that $\theta\sigma^2 \neq 2\lambda$)

$$R(x) = k_1 x\Phi\left(\frac{2\lambda}{\theta\sigma^2}, 2, \frac{x}{\theta}\right) + k_2\frac{\theta^2\sigma^2}{\theta\sigma^2 - 2\lambda}\Psi\left(\frac{2\lambda}{\theta\sigma^2} - 1, 0, \frac{x}{\theta}\right) + k_3. \tag{29}$$

Now, with $a = 0$, the origin is attainable. We set $c_1 = 0$ and $c_2 \equiv c$. Then, making use of the boundary conditions $R(0) = R(c) = 0$ and the third condition $R(c/2) = r$, we can determine the three constants and obtain the final form of the solution:

$$R(x) = \frac{2r\left\{k_0 x\phi(x) + c\phi(c)\left[x\Gamma\left(\frac{2\lambda}{\theta\sigma^2}\right)\psi(x) - \theta\right]\right\}}{c\left\{k_0\phi\left(\frac{c}{2}\right) + \phi(c)\left[c\Gamma\left(\frac{2\lambda}{\theta\sigma^2}\right)\psi(\frac{c}{2}) - 2\theta\right]\right\}}, \tag{30}$$

with $\phi(z)$, $\psi(z)$ and k_0 defined as follows:

$$\begin{aligned} \phi(z) &= \Phi\left(\frac{2\lambda}{\theta\sigma^2}, 2, \frac{z}{\theta}\right), \\ \psi(z) &= \Psi\left(\frac{2\lambda}{\theta\sigma^2}, 2, \frac{z}{\theta}\right), \\ k_0 &= \theta - c\Gamma\left(\frac{2\lambda}{\theta\sigma^2}\right)\psi(c), \end{aligned} \tag{31}$$

where $\Gamma(\cdot)$ is the gamma function.

Finally, choosing numerical values for θ, λ, σ and c, we can try to use Eq. (11) to solve for r and hence obtain an exact solution. When $\theta = \lambda = \sigma = c = 1$, we find that

$$R(x) = xe^x\left[\mathrm{Ei}(-1) - \mathrm{Ei}(-x)\right], \tag{32}$$

where $\mathrm{Ei}(x)$ is the exponential integral function defined by

$$\mathrm{Ei}(x) = -\int_{-x}^{\infty}\frac{e^{-t}}{t}\mathrm{d}t = \int_{-\infty}^{x}\frac{e^t}{t}\mathrm{d}t. \tag{33}$$

As in the case of the Wiener process with jumps, we ran simulations to confirm our results; see Figures 3 and 4. Again, the simulation results agree with the theoretical findings. Moreover, the effect of a larger jump rate λ is also observed.

Remark 3.2. *In* [2]*, Bondarenko introduced a new class of path-dependent options called crossover (CO) options. These contracts are defined in relation to a barrier K and their payoff increments every time the underlying crosses over the threshold (whether from above or below). Thus, the payoff is entirely built from overshoot quantities.*

Our work provides explicit characterizations of the expected overshoot for one-dimensional jump-diffusion processes above a critical level, in particular $R(x) = \mathbb{E}\left[(X(\tau(x)) - c_2)_+\right]$ (the same can be done for a lower threshold in case of downwards jumps). In this sense, our framework complements the theory of CO options by offering analytical tools for evaluating their payoff in models

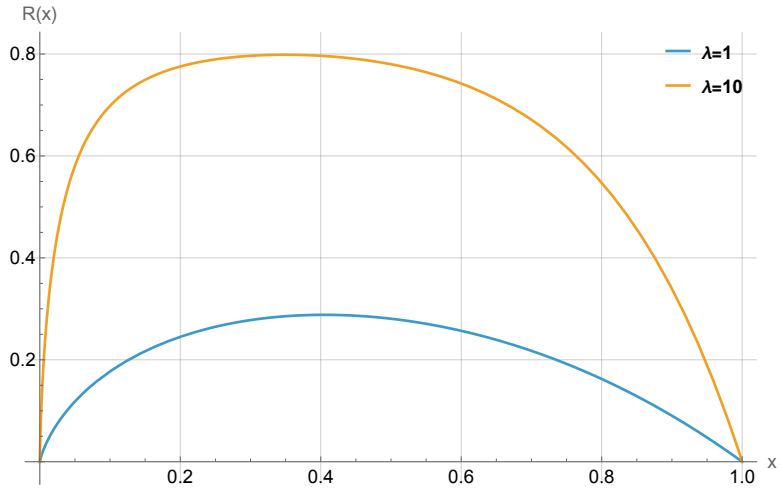

FIGURE 3. Exact function $R(x)$ for the particular CIR process with jumps considered.

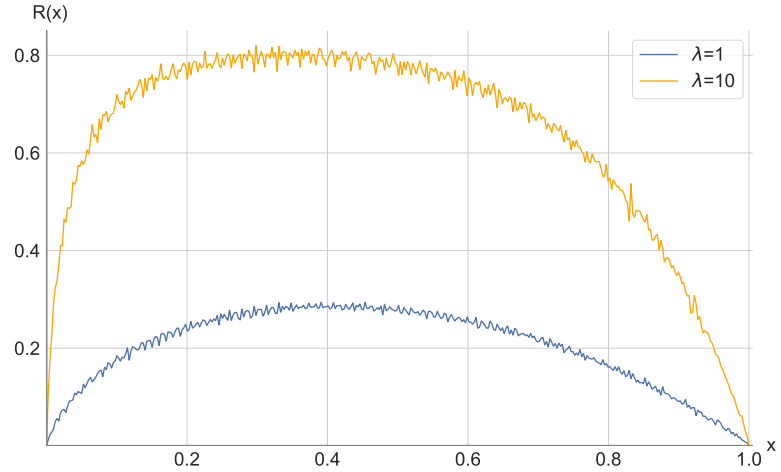

FIGURE 4. Simulation results for the particular CIR process with jumps considered.

with jumps. It provides closed-form or semi-closed-form expressions for the expected overshoot, which directly enters into the valuation of CO options.

4. Conclusion

In this paper, we have investigated the overshoot of a jump-diffusion process at the first-exit time from an arbitrary interval. In the general case, we have derived an integro-differential equation governing the average overshoot above the upper boundary of the interval. Then, in the case of exponentially distributed jumps, the problem was reduced to solving a third-order linear ordinary differential equation. We applied this framework to Wiener and CIR

processes with jumps, and we obtained closed-form solutions in special cases. Furthermore, the theoretical findings were confirmed through numerical simulations.

The results that we obtained provide analytical tools that can be applied in the general theory of stochastic processes or in mathematical finance, where this type of quantity arises in the valuation of path-dependant barrier or look-back structured products. Future works could extend this approach to other diffusion dynamics, such as geometric Brownian motion, and/or incorporate downward jumps, as in the jump-diffusion model considered by Kou [5].

REFERENCES

[1] *M. Abundo*, On the first-passage area of a one-dimensional jump-diffusion process, Methodol. Comput. Appl. Probab., **15**(2013), No. 1, 85-103 (DOI 10.1007/s11009-011-9223-1).

[2] *O. Bondarenko*, Cross-over options, SSRN Electronic Journal, (2023). (DOI 10.2139/ssrn.4592789). Available at https://ssrn.com/abstract=4592789.

[3] *E. B. Dynkin*, Markov Processes, Springer, Berlin, Heidelberg, 1965 (DOI 10.1007/978-3-662-00031-1).

[4] *C. Klüppelberg, A. E. Kyprianou and R. A. Maller*, Ruin probabilities and overshoots for general Lévy insurance risk processes, Ann. Appl. Probab., **14**(2004), 1766-1801 (DOI 10.1214/105051604000000927).

[5] *S. G. Kou*. A jump-diffusion model for option pricing, Manag. Sci., **48**(2002), No. 8, 1086-1101 (DOI 10.1287/mnsc.48.8.1086.166).

[6] *S. Kou and H. Wang*, First passage times of a jump diffusion process, Adv. Appl. Probab., **35**(2003), No. 2, 504-531 (DOI 10.1239/aap/1051201658).

[7] *W. Magnus, F. Oberhettinger and R. P. Soni*, Formulas and Theorems for the Special Functions of Mathematical Physics, Springer, Berlin, Heidelberg, 1966 (DOI 10.1007/978-3-662-11761-3).

[8] *C. Yin, Y. Wen, Z. Zong and Y. Shen*, The first passage time problem for mixed-exponential jump processes with applications in insurance and finance, Abstr. Appl. Anal., **2014**, Article ID 571724, 9 pages (DOI 10.1155/2014/571724).

USING THE DISCOVERY METHOD TO UNCOVER THE MATHEMATICS BEHIND A MAGIC CARD TRICK

FOLOSIREA ALGORITMULUI METODEI DESCOPERIRII PENTRU A DEZVĂLUI MATEMATICA DIN SPATELE UNUI TRUC MAGIC

Simona BUCURENCIU

„Marin Preda" Theoretical Highschool, Bucharest

Ph.D. student, State Pedagogical University of Chisinau

simonabucurenciu@yahoo.com

Abstract:
Over the time, various teaching methods have been proposed, studied, applied and improved. In this article I want to present the application of the discovery method in real life: discovering the math behind a magic card trick. Using this teaching method, students must discover the concepts themselves, discover formulas, mathematical rules. The students do not discover something that has not been studied before, but for them it represents a novelty, which will be discovered in the classroom, organized and supervised by the teacher. The purpose of this article is to explore the subtle connections between mathematics and magic, through a practical example that show how mathematical structures can generate "magical" effects.

Abstract:
De-a lungul timpului, au fost propuse, studiate, aplicate și îmbunătățite diverse metode de predare. În acest articol vreau să prezint aplicarea algoritmului metodei descoperirii în viața reală: descoperirea matematicii din spatele unui truc magic cu cărți. Folosind această metodă de predare, elevii trebuie să descopere singuri conceptele, să descopere formule, reguli matematice. Elevii nu descoperă ceva ce nu a mai fost studiat anterior, doar pentru ei reprezintă o noutate, care va fi descoperită în sala de clasă, în formă organizată și supravegheată de profesor. Scopul acestui articol este de a explora legăturile subtile dintre matematică și magie, printr-un exemplu practic care să arate cum structurile matematice pot genera efecte „magice".

Key words: *mathematics, discovery method, magic trick, problem solving, real life*

De-a lungul istoriei, matematica a fost privită nu doar ca o știință a rațiunii și a logicii, ci și un domeniu capabil să dezvăluie ordinea universului. Matematica reușește să descrie fenomene aparent inexplicabile printr-un limbaj abstract, dar riguros, transformând necunoscutul într-un sistem coerent de reguli. De-a lungul istoriei până în zilele noastre, civilizațiile s-au dezvoltat folosind matematica. La polul opus, magia reprezintă o practică simbolică și imaginară ce caută să ofere o punte între vizibil și invizibil, între concret și transcendent. Trucurile „magice" cu cărți nu sunt doar iluzii vizuale, ci și demonstrații ingenioase de matematică aplicată, pentru a distra auditoriul, pentru a produce surpriză, suspans și chiar iluzia de imposibil. Scopul acestui articol este de a explora conexiunile subtile dintre matematică și magie, printr-un exemplu practic, un truc „magic" cu cărți de joc, integrat unei lecții de matematică.

Predarea unei lecții reprezintă un proces creativ, creat de profesor, luând în considerare programa care trebuie urmată, planificarea concepută, metodele, mijloacele și resursele adecvate elevilor cărora le este destinată, cu scopul de a atinge obiectivele lecției și de a forma elevilor abilitățile dorite, la cel mai înalt nivel, în modul cel mai eficient posibil. Dintre metodele de predare, cea care oferă elevilor atât autonomie, cât și încredere în sine este metoda descoperirii. Succesul pe care îl simt atunci când reușesc să finalizeze o problemă le crește stima de sine, creativitatea, gândirea critică și capacitatea de a rezolva probleme pe parcursul întregii vieți.

Aplicarea *algoritmului metodei descoperirii* începe înainte de lecția propriu-zisă, cu *selectarea problemei de studiat*. Problema este întotdeauna derivată dintr-un context real. *Determinarea strategiei de abordare a problemei* revine în sarcina profesorilor școlii ce trebuie să ia în considerare elevii cărora li se adresează. Problema trebuie aleasă cu atenție, astfel încât să poată fi rezolvată de toți elevii, inclusiv de cei cu performanțe mai scăzute. De asemenea, trebuie selectată astfel încât să faciliteze soluții diverse și o formă de generalizare. Este de dorit să se ofere cât mai puține detalii, pentru a permite elevilor să ajungă la propriile soluții prin gândire proprie, în acest fel elevii își vor crea metode personale de reflecție. Strategia de abordare a problemei necesită răbdare și atenție, deoarece trebuie să se alinieze cu modul de gândire al elevilor. *Elaborarea planului de aplicare a metodei descoperirii* reprezintă o etapă de discuții și negocieri între profesorii școlii în care se hotărăsc asupra unui plan unitar pentru toate clasele la care vor prezenta problema aleasă și pașii de urmat în timpul lecției, ceea ce rezultă în *elaborarea proiectului didactic al lecției*. Atunci când se elaborează un plan de lecție, resursele didactice necesare sunt alese cu mare atenție. Nu doar că problema prezentată pentru soluționare ar trebui să fie legată de cunoștințele lor anterioare, dar din aceasta elevii ar trebui să dobândească și noi cunoștințe funcționând astfel ca o conexiune între ceea ce știau și ceea ce vor învăța în sesiunile viitoare.

O dată ce toate detaliile sunt decise, planul de lecție se poate aplica. Prima parte a lecției debutează cu *prezentarea problemei*, a contextului din care a fost luată, setarea cadrului real din care face parte, precum și ce li se cere elevilor, ce înseamnă exact să rezolve problema. După ce profesorul răspunde eventualelor întrebări ale elevilor, urmează *realizarea activității individuale,* o perioadă de lucru independent, perioadă în care elevii reflectă asupra cerințelor și se străduiesc să găsească soluții. Profesorul își notează care dintre elevi au rezolvări obișnuite, mai des întâlnite, care elevi au făcut greșeli, și care au rezolvări originale. După trecerea timpului alocat acestei etape, profesorul conduce etapa de *discutare în plen a metodelor de soluționare a problemei*. Elevii sunt invitați să prezinte la tablă soluțiile descoperite. Profesorul dă ocazia elevilor să colaboreze și să se ajute reciproc, elevii discută, compară soluția lor cu a celorlalți, pot observa diferențele și pot învăța din ele.

În ultimele minute ale lecției profesorul trebuie să realizeze o încheiere a lecției, realizând un rezumat a ceea ce s-a prezentat și s-a discutat pe parcursul desfășurării lecției, într-un mod cât mai firesc și natural prin *evidențierea produsului matematic descoperit.* Profesorul prezintă elevilor notațiile general valabile, denumește noțiunile teoretice descoperite de elevi, prezintă regula de generalizare sau formula căutată. De asemenea se poate evidenția *aplicarea produsului descoperit în diferite contexte* la sugestia profesorului sau a elevilor. Lecția se încheie prin *formularea concluziilor și a recomandărilor rezultate din activitatea desfășurată*, momente în care elevii notează observații în caiete sau pe fișele de lucru referitoare la ora recent încheiată. Aceste observații contribuie la dezvoltarea gândirii critice a elevilor. Prin examinarea acestor notițe, profesorul poate evalua

înțelegerea lecției de către elevi și poate identifica conceptele greșite sau neclarificate care ar putea persista. Astfel, el poate începe următoarea lecție prin clarificarea acestor aspecte.

Un exemplu de aplicare a algoritmului de mai sus o reprezintă următorul truc „magic”, care reprezintă problema de rezolvat:

Se iau la întâmplare 21 cărți dintr-un pachet de cărți de joc. Un jucător alege o carte pe care magicianul nu o vede dar o va „ghici prin magie”.

✓ Magicianul distribuie cărțile pe masă, cu fața în sus, în ordine, în trei coloane, astfel încât să fie vizibile și identificabile de către jucător, ca în figura de mai jos.

✓ Jucătorul indică respectiva coloană, pe cea în care se află cartea aleasă.

✓ Magicianul strânge cele trei coloane de cărți, în ordine, plasând coloana cu cartea aleasă la mijloc, între celelalte două coloane.

După 3 astfel de secvențe, magicianul distribuie pe masă cărțile cu fața în jos și „ghicește” cartea aleasă de jucător.

Figura 1. Cărți de joc distribuite în trei coloane

CERINȚE:

- Explicați matematic trucul magicianului?
- Care sunt pozițiile posibile ale cărții alese după prima secvență de joc?
- Care sunt pozițiile posibile ale cărții alese după a doua secvență de joc?
- Care sunt pozițiile posibile ale cărții alese după a treia secvență de joc?
- Care este numărul minim de cărți pentru care trucul funcționează din trei secvențe?
- Care este numărul maxim de cărți pentru care trucul funcționează din trei secvențe?
- Ce puteți spune despre n, numărul de cărți?
- Funcționează trucul pentru *n* cărți?

Explicația trucului este una matematică: prin distribuirea în trei coloane a cărților, se restrâng pozițiile în șirul de cărți. După prima secvență de joc, din douăzeci și unu de poziții posibile, se restrâng la doar șapte, de la 14 la 8, în ordine descrescătoare. După cea de-a doua secvență de joc, pozițiile posibile se restrâng mai mult, la doar trei, de la 12 la 10. După cea de-a treia secvență, poziția posibilă a cărții este una singură, cea din mijloc, adică a unsprezecea. De exemplu, în figură, jokerul se află pe poziția a șaptea, iar cartea trei de inimă roșie se află pe poziția a opta.

Trucul funcționează pentru mai multe variante ale lui *n*, pentru *n* cărți de joc, unde *n* este multiplu impar de 3. În acest caz, după prima secvență de joc, pozițiile posibile ale cărții sunt de la $\frac{2n}{3}$ la $\frac{n}{3}+1$, în ordine descrescătoare. După a doua secvență de joc, pozițiile posibile ale cărții sunt $\frac{n-1}{2}$, $\frac{n+1}{2}$ sau $\frac{n+3}{2}$. După a treia secvență de joc, singura poziție posibilă va fi $\frac{n+1}{2}$.

În cazul în care profesorul dorește să aplice acest truc unor elevi de vârstă mai mică, acesta funcționează și cu nouă cărți. Cartea ajunge pe poziția, unică, a cincea, după doar două secvențe de joc.

În cazul în care elevii doresc să exploreze mai mult matematica din spatele trucului, se pot formula alte întrebări cum ar fi:

- Care este valoarea maximă pe care o poate lua *n* pentru ca jocul să funcționeze din exact 3 secvențe?
- Care sunt valorile pe care le poate lua *n* pentru ca jocul să funcționeze din exact 4 secvențe?
- Care sunt valorile pe care le poate lua *n* pentru ca jocul să funcționeze din exact *s* secvențe?

Atunci când magicianul „ghicește" cartea sau „prezice" rezultatul, auditoriul trebuie să știe faptul că există o explicație logică. Trucul nu este magic, este o demonstrație elegantă, distractivă și subtilă a matematicii în realitate. Pornind de la experiențele trăirii trucurilor, elevii pot fi interesați să descopere, să înțeleagă ceea ce se întâmplă în spatele magiei. Astfel magia devine doar un instrument de aplicare distractivă a matematicii, stimulând motivația și interesul pentru studiul acestei discipline.

Deși, la o primă vedere, magia și matematica par să nu aibă nimic în comun, descoperim încă un domeniu în spatele căruia se află matematica. Folosind metoda descoperirii, elevii își îmbunătățesc abilitățile matematice, își dezvoltă gândirea logico-matematică, ajută la crearea unei atitudini pozitive către această disciplină.

Bibliografie

DIACONIS, Persi; GRAHAM, Ron. Magical Mathematics: The Mathematical Ideas That Animate Great Magic Tricks. New Jersey: Princeton University Press, 2012. ISBN 9780691169774

GARDNER, Martin. Mathematics, Magic and Mystery. New York: Dover Publications, 1956. ISBN 486-20335-2

MULCALHY, Colm. Mathematical Card Magic: Fifty-Two New Effects. Boca Raton: CRC Press, 2013. ISBN 978-1-4665-0978-8

PAULOS, John Alles. Innumeracy: Mathematical Illiteracy and Its Consequences. New York: Hill and Wang, 1991. ISBN 0-679-72601-2

STROGATZ, Steven. Infinite Powers: How Calculus Reveals the Secrets of the Universe. New York: Houghton Mifflin Harcourt, 2019. ISBN 97813288880017

DESIGNING HYBRID LIBRARY SYSTEMS WITH EVOLVING TECHNOLOGIES

Simona Mihaela BIBIC[1,3], Mara MUNTENAȘU[2,3], Petru-Cristian GRĂMESCU[2,3], Flavius LUNG[2,3], Andreea-Teodora CORNEA[2,3]

[1] Department of Applied Mathematics, National University of Science and Technology Politehnica Bucharest, 313 Splaiul Independentei, District 6, Bucharest, Romania

[2] Faculty of Electrical Engineering, National University of Science and Technology POLITEHNICA Bucharest, 313 Splaiul Independentei, District 6, Bucharest, Romania

[3]Center for Research and Training in Innovative Techniques of Applied Mathematics in Engineering, National University of Science and Technology POLITEHNICA Bucharest, 313 Splaiul Independentei, District 6, Bucharest, Romania

Corresponding author email: simona.bibic@upb.ro, mara.muntenasu@stud.electro.upb.ro, petru.gramescu@stud.electro.upb.ro, flavius.lung@stud.electro.upb.ro, andreea.cornea@stud.electro.upb.ro

Abstract
The purpose of this paper is to analyse the architecture of a hybrid library, which is regarded as an automated system meant to combine digital and physical resources with artificial intelligence technologies. Some examples of comprehensive features include adaptive search, user behaviour understanding, built-in recommendations, and robotic assistance. These can transform conventional library functions into dynamic and responsive ones, appropriate for current information environments. Therefore, certain algorithms are integrated, including content recommendation, real-time assessment, and feedback. The proposed application will focus on pathfinding and optimization algorithms, using an SQL database to manage and retrieve information. The outcome of the entire process consists of simplified access to specific knowledge, reduced workload, and motivation for self-directed learning, which is achieved through real-time booking and availability.
Key words*: Automation; Digitalization; Pathfinding Algorithms; SQL Data Base; Content-Based Filtering; Collaborative Filtering; Data Processing*

1. INTRODUCTION

The digital era can be traced back to early radio broadcasts and the first television flickering images, and it marked a turning point in how people interacted with the outside world. However, the implementation was gradual, starting with the progressive computerization of workplaces and schools. This stage was followed by the creation of software systems adapted to the requirements of each institution, initially accessible only to well-funded organizations and governments, and subsequently, they have become affordable and widely used.

The main purpose of this paper is to design a high-performance network between physical and virtual spaces, preserving the advantages of both. Therefore, to satisfy the demands of users, a model is proposed in the form of a hybrid library, which combines physical collections with digital resources. Methods such as binary search and sorting algorithms [1,2] are fundamental to processing, organizing, and accessing information more easily, and allowing fast data retrieval, indexing, and classification of distinct items that can be physical documents or digital formats. Additionally, within the hybrid library, there is an autonomous robot capable of physical delivery by using the A* pathfinding algorithm, accompanied by sensors, to detect obstacles [4].

2. CONTENT

The COVID-19 pandemic represents a historic change from two perspectives: human interactions and the way society functions. In the context of lockdowns and social distancing, social media platforms have become the only way to connect. This period has faced multiple challenges, including job losses caused by unequal access to technology, exposure to cybersecurity risks, and the need for

digital literacy. At the same time, it revealed opportunities that have ever since become standards in everyday life.

Conventional libraries have considerable limitations, and this model aims to provide a solution by combining the attributes from the physical and digital spaces. Due to all the tasks being done manually, there are multiple shortcomings, such as space constraints, low efficiency, slower information retrieval, and resource sharing risks. The system's goal is to automate cataloguing and indexing, user authentication and access control, search, lending, and return. Moreover, it has the objective of reducing the time spent looking for specific content and academic resources while also allowing real-time access.

The robot prototype is based on a movable frame with two electric motors, which allow it to navigate inside the library. Book handling is carried out using a robotic arm equipped with a gripper and a pressure sensor to prevent any damage to the books. Upon completing its task, the robot automatically returns to a charging station. To ensure the proper operation of the robots used to deliver and retrieve documents, the hybrid library is structured as a graph, allowing the implementation of these complex and specialized algorithms:

- **Document Retrieval and Search Logic:** this algorithm checks if the requested document exists in the physical database. If found, its location is being added to the robot's path; otherwise, it searches for the digital format. The output depends on existing physical or digital documents.

- **A* Path with Document Collection:** the robot's path is based on the A* search technique [3] an analysis algorithm that uses a heuristic function to allocate the optimal path in a graph

- **Recommendation Process:** the last algorithm recommends similar documents if the requested one is neither physically nor digitally available. It lists the top 3 documents by the same author and the top 3 documents in the same genre, based on popularity. The popularity system uses two primary criteria: content-based filtering and collaborative filtering.

3. CONCLUSIONS

The integration of digitalization in educational environments has transformed the way information is accessed, stored, and shared. Libraries have evolved into hybrid spaces and environments that support academic research by merging physical collections with digital resources. The transition not only improves accessibility and productivity but also enriches user experience by providing customized assistance and instant access to documents.

For future improvements, a customized database is proposed for each user in which data related to their behaviour on the platform will be stored. At the end of each month, a report will be formed summarizing the activity (preferred authors, favourite topics, preferred format type) and suggestions.

4. REFERENCES

[1] Nowak, R. (2008). Generalized binary search. Proc. of the 46th annual Allerton conference on Communication, Control, and Computing, IEEE, pp. 568-574.

[2] Martin, W.A., et al. (1972). Optimizing binary trees grown with a sorting algorithm. Communications of the ACM, 15(2), pp. 88-93.

[3] Duchon, F., et al. (2014). Path planning with modified a star algorithm for a mobile robot. Procedia Engineering, vol. 96, pp.59–69.

[4] Bogdan, I.C., et al. (2025). The Future of Social Robots in Education, Healthcare and Engineering. Proc of the 27th Int. Conf. on Inter. Collaborative Learning, vol. 4, pp. 577-588, Springer.

A NEW ERA OF LEARNING: AI DIGITAL SUPPORT FOR ACADEMIC COMMUNITIES

Simona Mihaela BIBIC[1,3], Nicoleta POPA[2,3], Vlad DICU[2,3]

[1]Department of Applied Mathemathics, National University of Science and Technology POLITEHNICA Bucharest, 313 Splaiul Independentei, District 6, Bucharest, Romania

[2]Faculty of Applied Sciences, National University of Science and Technology POLITEHNICA Bucharest, 313 Splaiul Independentei, District 6, Bucharest, Romania

[3]Center for Research and Training in Innovative Techniques of Applied Mathematics in Engineering, National University of Science and Technology POLITEHNICA Bucharest, 313 Splaiul Independentei, District 6, Bucharest, Romania

Corresponding author email: simona.bibic@upb.ro, nicoleta.popa2102@stud.fsa.upb.ro,

vlad.dicu@stud.fsa.upb.ro

Abstract

Even though digitization has highly advanced education, many students still find it difficult to organize their study materials, including notes, publications, websites, and educational platforms, in one convenient location. Because of this lack of centralization, they frequently require artificial intelligence-based solutions, which are helpful but don't always offer reliable or correct information. In response to this need, our goal is to provide an integrated learning environment with an AI-powered platform (AIP). This AIP has three significant characteristics: learning, training, and assessment. Thus, it will allow easy access to documents, generating summaries, customized learning, and evaluation. Additionally, teachers and tutors will be able to track students' progress, identify groups at risk of low performance, and set important deadlines. To achieve this initiative, we combine theoretical research with data obtained through a questionnaire applied to students, focusing on study habits, exam preparation methods, and use of artificial intelligence (AI).

Key words*: Artificial Intelligence, education, personalized learning, accessibility, digital platform.*

1. INTRODUCTION

Education has undergone constant changes when it comes to digitalization. However, students often face challenges to organize and access their study materials in one place. During their study they have a variety of resources they use simultaneously, such as course notes, articles, websites, or external platforms. Thus, students are tempted to turn to AI, this being one of the few places where information can be found in one place. However, AI often generates unverified or inaccurate information. It is a useful tool, but it's frequently misused [1].

2. CONTENT

Our goal is to create a space where AI is used in an educational way through various facilities. The AIP is assisted by artificial intelligence and organizes, sorts, and structures learning materials for students, generating information for each subject they choose to study. AI filters each document, and students can request instant summaries, personalized learning plans, quizzes, and other exercises to support their learning process. In addition, the AIP supports the installation of various browser extensions that enhance the learning experience across multiple resources. These include grammar and style correction tools, which help students and teachers generate explanatory texts, essays, or create test questions. Productivity and time-management extensions assist in organizing schoolwork and managing schedules effectively, offering intelligent suggestions for prioritizing tasks and optimizing time allocation. Other extensions support language learning by providing automatic translations and vocabulary recommendations. To make learning more accessible, text-to-speech

extensions read aloud the content on a page, which is especially useful for students with reading difficulties or visual impairments. Accessibility tools allow users to adjust contrast, text size, and other display features to facilitate reading for those with visual or learning disabilities. Teachers also benefit from extensions that analyze student responses, such as essays or tests, and provide personalized feedback, helping them save time and identify each student's strengths and weaknesses more effectively. To achieve this goal, we combine theoretical research with primary data collection. We analyze existing academic articles that examine students' behavior in a digitalized era. We study students' learning habits, compare the results, and design an AIP that generates summaries of course content, sorts information, suggests study plans, and supports the learning process through exercises and quizzes [2].

3. CONCLUSIONS

Following this study, we aim to enhance learning methodology, increase student engagement, and evaluate as well as improve current learning methods and platforms. The proposed AI-powered platform (AIP) contributes to a more organized and personalized educational process, offering both students and teachers intelligent tools that simplify study management, feedback, and accessibility [3]. Moreover, the integration of artificial intelligence into education encourages the development of digital skills and critical thinking, preparing students for the technological demands of the modern world.

REFERENCES

[1] Wheatley, A., Hervieux, S. (2019). Artificial intelligence in academic libraries: An environmental scan. Information Services and Use, vol. 39(4), pp. 347–356.

[2] Ozer, M. (2024). Potential benefits and risks of artificial intelligence in education. Bartın University Journal of Faculty of Education, vol. 13(2), pp. 232–244.

[3] Ali, W., et al. (2024). Consensus or Controversy: Examining AI's Impact on Academic Integrity, Student Learning, and Inclusivity Within Higher Education Envi ronments. Proc. of the 2nd Int. Conf. on Cyber Resilience (ICCR), pp. 1–5, IEEE

A NEW PERSPECTIVE ON THE $\mathcal{LMI}$ REGION AND $\mathcal{D}_d$ STABILITY OF FRACTIONAL MULTIDIMENSIONAL STATE-SPACE MODELS

Souad SALMI[1], Djillali BOUAGADA[2]

[1,2] Department of Mathematics and Computer Science, ACSY Team-Laboratory of Pure and Applied Mathematics.
Abdelhamid Ibn Badis University Mostaganem, P.O.Box 227/118, 27000

Corresponding author email:
[1]souad.salmi.etu@univ-mosta.dz
[2] Djillali.bouagada@univ-mosta.dz .

Abstract

In this work, we study the stability region of a new class of fractional generalized multidimensional state-space systems described by the Roesser model. The analysis aims to determine the sufficient conditions, in a specific region of the complex plane, to guarantee the desired stability properties of the system under consideration. Numerical examples are provided to illustrate the validity and effectiveness of the proposed results.

Key words*: Fractional calculus; fractional dD systems; Stability Region ; Linear Matrix Inequalities.*

1. INTRODUCTION

Fractional multidimensional systems have gained much interest in recent years because they can describe complex dynamic systems that include memory and interactions between different variables. These systems are an extension of classical models to fractional orders, which makes them more flexible and accurate for representing real processes. Studying such systems is important for understanding their stability and for improving control performance in practical applications.

In dynamic systems, stability depends on the location of the poles in the complex plane. Some systems are naturally stable because their poles lie inside a stability region, which allows them to resist small changes or disturbances. Other systems have poles close to the boundary of the stability region, so even a small perturbation can move them outside this region and make the system unstable.

In this context, the study of the stability region becomes essential to determine where the system poles are located in the complex plane and to ensure that the system remains stable under different conditions. Numerous efforts have been dedicated to the development of stability criteria. Motivated by the work of D. Bouagada and P. Vandooren (2006), the present study focuses on analyzing the stability region of fractional multidimensional systems described by the Roesser model and on providing sufficient conditions to guarantee their stability.

2. PRELIMINARIES

In the following, we introduce a general formulation of multidimensional dD fractional continuous-time systems described by the Roesser model

$$K^{\alpha_1,\cdots,\alpha_d} E_d X_d(t_1,\cdots,t_d) = A_d X_d(t_1,\cdots,t_d) + B_d u_d(t_1,\cdots,t_d)$$
$$y_d(t_1,\cdots,t_d) = C_d X_d(t_1,\cdots,t_d) + D_d u_d(t_1,\cdots,t_d) \quad (1)$$

where,

$E_d = \begin{pmatrix} E_{11} & \cdots & E_{1d} \\ \vdots & \ddots & \vdots \\ E_{d1} & \cdots & E_{dd} \end{pmatrix} \in \mathbb{R}^{n\times n}$, which be assumed invertible.

$A_d = \begin{pmatrix} A_{11} & \cdots & A_{1d} \\ \vdots & \ddots & \vdots \\ A_{d1} & \cdots & A_{dd} \end{pmatrix} \in \mathbb{R}^{n\times n}$, is the dynamic matrix.

$B_d = \begin{pmatrix} B_1 \\ \vdots \\ B_d \end{pmatrix} \in \mathbb{R}^{n\times m}$, is the control matrix.

$C_d = [C_1, \cdots, C_d] \in \mathbb{R}^{p\times n}$, is the output matrix

$D_d \in \mathbb{R}^{p\times m}$, is the transmission matrix

$X_d = \begin{pmatrix} x_1(t_1, \cdots, t_d) \\ \vdots \\ x_d(t_1, \cdots, t_d) \end{pmatrix} \in \mathbb{R}^{n}$, represent the state of the sub-vectors,

$K_d^{\alpha_1,\cdots,\alpha_d} = \begin{pmatrix} \lambda_1^{\alpha_1} I_{n_1} & \cdots & 0 \\ \vdots & \ddots & \vdots \\ 0 & \cdots & \lambda_d^{\alpha_d} I_{n_d} \end{pmatrix} \in \mathbb{R}^{n\times n}$, represent matrix of differentials operators

$diag_{i=1}^{d}\, s_i^{\alpha_1} I_{n_i}$ in the Laplace transform when (1) in the continuous-time and $diag_{i=1}^{d}\, z_i^{\alpha_1} I_{n_i}$ is the Z-transform when (1) in the discrete-time.

$u(t_1, \cdots, t_d) \in \mathbb{R}^{m}$, is the input vector.

$y(t_1, \cdots, t_d) \in \mathbb{R}^{p}$, is the output vector.

3. CONCLUSIONS

In this work, we constructed a new $\mathcal{D}_{\mathrm{d}}$-region in the complex plane, formulated through Linear Matrix Inequalities ($\mathcal{LMI}s$). This region defines where the poles of the system should be located to ensure stability. Based on this formulation, we derived sufficient conditions that guarantee the stability of the fractional multidimensional system within the proposed region. Finally, several numerical examples were presented to demonstrate the validity and effectiveness of the obtained results.

Uncertainty-Aware Dynamic Cost Maps for Real-Time Autonomous Navigation — Extended Abstract

1. Introduction and Motivation

Autonomous navigation in dynamic and uncertain environments remains one of the most challenging problems in robotics. Traditional planners rely heavily on deterministic cost maps that assume perfect sensor accuracy and static surroundings. In practice, however, perception noise, occlusions, and rapidly changing elements such as vehicles, pedestrians, and traffic lights continuously distort the environment’s representation. When uncertainty is ignored, these distortions propagate downstream—leading to erratic planning behavior, unsafe motion, and brittle performance under real-world conditions. This work introduces a probabilistic framework for dynamic cost mapping and uncertainty-aware control. The method fuses heterogeneous sensory information into a unified spatial potential field that captures both the expected traversal cost and its associated uncertainty. By diffusing this probabilistic field and using its gradients as the substrate for control and reinforcement learning, the system achieves smooth, interpretable, and computationally efficient motion even on low-power embedded platforms.

2. Probabilistic Field Construction

2.1 Environment Representation The environment is modeled as a 2D lattice, where each grid cell stores an expected cost value and an uncertainty estimate. Static factors include geometric and regulatory information such as curvature, lane topology, and stop-line positions. Dynamic factors arise from real-time perception: moving objects, pedestrian heatmaps, and traffic-light states. Each is treated as a stochastic feature represented by a Gaussian variable with mean and variance estimated online. ### 2.2 Precision-Weighted Fusion To integrate multiple uncertain features into a single coherent map, a precision-weighted fusion operator is employed. Each feature contributes proportionally to its reliability, so high-confidence detections dominate while noisy or ambiguous inputs are naturally down-weighted. This process produces a dynamic cost field that explicitly encodes uncertainty and remains robust under perception errors or partial observability. ### 2.3 Diffusion-Based Regularization The fused field may contain discontinuities due to sensor sparsity or asynchronous updates. A diffusion step, implemented as Gaussian convolution, enforces spatial coherence and ensures the field is differentiable and smooth. High-cost regions (obstacles, occupied zones) act as repulsive potentials, while low-cost goal regions form attractive basins. The diffusion guarantees Lipschitz continuity, which stabilizes gradient-based control and ensures well-behaved vector fields across the environment.

3. Reinforcement Learning over Diffused Fields

3.1 Local Patch Encoding The navigation policy does not operate on the full global map. Instead, it receives an ego-centric local field patch, centered on the vehicle’s position and aligned with its heading. This patch is normalized and resampled to a fixed grid size, preserving relative gradients and reward structures while maintaining invariance to absolute cost scale. ### 3.2

Discrete Control Policy A lightweight reinforcement learning (RL) controller governs vehicle behavior. The policy observes the local field patch and the current state vector—position, velocity, heading, and curvature—and outputs small discrete increments in acceleration and curvature. This discretization simplifies training, guarantees physical feasibility, and enhances interpretability of the learned behavior. The policy is trained using Proximal Policy Optimization (PPO). The reward signal is derived directly from the potential field, encouraging motion along descending gradients while penalizing excessive curvature and acceleration. During deployment, a safety projection layer clips infeasible actions and enforces adherence to physical and environmental constraints. The final actions are passed to a spline-based trajectory generator, which interpolates them into continuous motion commands executable by the vehicle's low-level controller.

4. Real-Time Implementation and Performance

The proposed framework is designed for embedded real-time operation. Field fusion, diffusion, and reward updates are computed at 10–20 Hz, while the control policy operates at 50 Hz with an average end-to-end latency below 15 ms. All computations are performed on a Raspberry Pi 5 CPU without GPU acceleration, and the neural policy occupies less than 1 MB of memory. This efficiency stems from two design choices: (1) separable Gaussian kernels for the diffusion operator, which reduce complexity to linear in map size, and (2) small, fixed-size field patches for inference, which allow constant-time policy evaluation regardless of global map dimensions. Together, these enable high-frequency updates and deterministic timing guarantees, critical for closed-loop control in real systems.

5. Discussion and Contributions

This work introduces three core contributions to uncertainty-aware navigation: 1. Probabilistic Cost Fusion — a principled approach to combining uncertain perceptual evidence via precision-weighted estimation, ensuring consistent propagation of uncertainty. 2. Diffused Potential Representation — a mathematically grounded smoothing process that converts noisy cost maps into continuous differentiable fields with well-defined gradients. 3. Field-Aware Reinforcement Learning — a discrete-action policy architecture that interprets potential-field structure to make safe, smooth, and efficient motion decisions in real time. These components collectively yield a navigation pipeline that is interpretable, data-efficient, and robust to noise, bridging the gap between perception-driven mapping and control-theoretic planning.

6. Conclusion and Future Work

This research establishes a unified probabilistic foundation for dynamic cost maps in autonomous navigation. By modeling each perception-derived layer as a stochastic observation and fusing them under uncertainty, the framework captures both the spatial and epistemic structure of the driving environment. Through Gaussian diffusion, these maps become continuous potential fields suitable for smooth gradient-based control. When paired with a lightweight RL controller, the result is a real-time system that balances interpretability, adaptability, and computational efficiency. Future work will focus on multi-agent interactions,

active uncertainty minimization, and large-scale testing in simulation environments such as CARLA or Gazebo. The principles outlined here—precision-weighted fusion, field diffusion, and field-aware reinforcement learning—provide a strong theoretical and practical foundation for scalable, uncertainty-aware autonomy.

Mathematical Modeling and Machine Learning Approaches for Predicting Online Course Dropout Probability

Ștefan-Cătălin PETRESCU[1,2], Elena Corina CIPU[1,3]

[1] National University of Science and Technology Politehnica of Bucharest (UNSTPB), Centre for Research and Training in Innovative Techniques of Applied Mathematics in Engineering "Traian Lalescu" (CiTi), Bucharest, Romania

[2] Faculty of Automatic Control and Computer Science, Systems Engineering Domain, UNSTPB
[3] Department of Applied Mathematics, Faculty of Applied Sciences, UNSTPB

Corresponding author email: pcatalinp47@gmail.com

Abstract
The increasing utilization of online learning platforms has given rise to novel challenges in the analysis and management of student attrition. The present paper proposes a predictive model for evaluating the likelihood of course desertion. This model utilizes behavioral and academic markers, including login frequency, duration on the platform, assessment scores, and interaction patterns. The model utilizes supervised machine learning methodologies, including Logistic Regression, Random Forest, and Naïve Bayes, to identify critical variables that determine persistence in e-learning environments. A mathematical framework is employed to select features and estimate probabilities. This framework is designed to enhance the interpretability and accuracy of the model. Statistical indicators such as accuracy, recall, and ROC-AUC are employed to evaluate performance. The present study focuses on two primary areas: the algorithmic optimization of the prediction process and the mathematical underpinnings of the aforementioned process. Insights gained from this study offer significant potential for the development of early intervention tactics that promote student retention.

Key words*: E-learning, machine learning, probability modeling, Logistic Regression, Random Forest, Naïve Bayes, mathematical modeling, feature selection, algorithmic optimization.*

1. INTRODUCTION

The accelerated growth of digital education has profoundly altered the manner in which individuals' access and engage with knowledge. The advent of Massive Open Online Courses (MOOCs) and institutional e-learning systems has precipitated a democratization of education, yet concomitantly engendered a substantial predicament: the prevalence of high attrition rates. It is imperative to comprehend the elements that contribute to student disengagement to enhance the efficacy of course design, retention strategies, and overall learning outcomes. In this regard, predictive modeling emerges as a pivotal analytical instrument for identifying students who are at risk of withdrawing from their courses.

Machine learning algorithms can quantify the probability of abandonment and identifying the variables most strongly associated with persistence by leveraging behavioral and performance data. This approach serves to establish a connection between data-driven insights and pedagogical interventions. From a mathematical and algorithmic perspective, the present study explores the construction of predictive models using classification techniques such as Logistic Regression, Random Forest, and Naïve Bayes.

The analysis of these methods encompasses not only their predictive capacity but also an examination of their underlying mathematical principles, including probability estimation, decision boundaries, and feature importance weighting. The integration of rigorous data preprocessing, feature selection, and probabilistic reasoning establishes a foundation for the development of interpretable and robust predictive systems in educational analytics. This work aims to contribute to the field of learning analytics by integrating algorithmic efficiency with mathematical rigor, offering insights that support adaptive learning environments and reduce dropout rates in online education.

2. CONTENT

1. *Collection and Preprocessing of Data*

The dataset utilized in this research derives from an open e-learning analytics platform containing engagement and performance data of online learners. The preprocessing phase entailed the cleansing of missing values, the encoding of categorical variables, and the normalization of numerical attributes through the utilization of the z-score method. To ensure data integrity, outliers and redundant features were removed through a variance-based filtration process. All measurements are expressed in accordance with the International System of Units (SI). A statistical analysis was conducted to identify dependencies between variables such as activity frequency, time on platform, and assessment results.

2. *Mathematical and Algorithmic Framework*

The predictive model is predicated on supervised classification techniques that are underpinned by probabilistic and statistical learning theory. Logistic regression was implemented to estimate the probability of user attrition using the logistic function: β_0

$$P(y = 1 \mid x) = \frac{1}{\left(1 + e^{-(\beta_0 + \sum_{i=1}^{n} \beta_i x_i)}\right)} \quad (1)$$

The Random Forest algorithm, which is based on ensemble decision trees, was applied to capture nonlinear relationships. In contrast, the Naïve Bayes algorithm provided a mathematically tractable baseline, assuming conditional independence of predictors. The training of models was conducted using k-fold. The K-fold cross-validation and hyperparameters were optimized through grid search. The performance of the model was evaluated using several performance metrics, including accuracy, precision, recall, F1-score, and ROC-AUC.

3. *Experimental Results and Analysis*

A comparative analysis of the experimental results indicated that the Random Forest model achieved the highest predictive accuracy, followed by Logistic Regression and Naïve Bayes. A thorough examination of feature importance revealed that engagement-related features, specifically the frequency of logins and the duration spent on course materials, exerted the most significant influence on the probability of dropout. Logistic regression was characterized by its high interpretability, enabling direct quantification of the influence of the predictors. Conversely, Naïve Bayes demonstrated its efficacy in terms of computational efficiency, particularly when dealing with large datasets.

3. CONCLUSIONS

The present study demonstrated the feasibility and effectiveness of using supervised machine learning algorithms to predict the probability of student dropout in online learning environments. The application of Logistic Regression, Random Forest, and Naïve Bayes classifiers to metrics and academic data led to the identification of key variables influencing course completion, including engagement frequency and assessment performance. The integration of mathematical modeling, particularly probabilistic estimation and statistical inference, has been demonstrated to enhance the interpretability and precision of predictive models.

The findings emphasize the importance of integrating algorithmic optimization with a robust mathematical foundation in the domain of educational analytics. The proposed models have the potential to be integrated into e-learning systems as early warning tools, thereby providing instructors and institutions with the capacity to develop adaptive interventions aimed at improving student retention. Subsequent research endeavors will center on the extension of the framework to encompass temporal dynamics, ensemble hybridization, and real-time prediction for large-scale online platforms.

REFERENCES

[1] Goldberg, D. E. (1989). Genetic Algorithms in Search, Optimization, and Machine Learning. Addison-Wesley.

[2] M.J. Kochenderfer, T.A. Wheeler, Algorithms for Optimization, The MIT Press Cambrigde, Massachusetts, London, England, 2019.

[3] Yang, X. S. (2020). Nature-Inspired Optimization Algorithms. Elsevier.

FRACTIONAL PARAMETER FUSION FOR CNN MODEL VERSION MERGING

Ștefan-Răzvan ANTON[1]

[1]University Politehnica of Bucharest, 313 Splaiul Independentei, District 6, Bucharest, Romania

Corresponding author email: antonstefan000@gmail.com

Abstract

This paper proposes Fractional Parameter Fusion (FPF), a new merging approach inspired by fractional calculus, which allow non-integer order interpolation between CNN parameter sets. FPF interprets successive CNN versions as points along a continuous trajectory in weight space and applies fractional-order operations to produce a merged model that encodes both the spatial and historical dependencies between these versions. We compare FPF with traditional weight averaging and logit ensemble approaches on the CIFAR-10 dataset, using a ResNet-18 architecture exploring both fusing checkpoints from different epochs within the same training run (intra-run fusion) and fusing final models from independent runs (inter-run fusion).Our findings indicate that fractional fusion produces smoother model transitions and higher representation coherence compared to conventional methods.

Key words*: fractional calculus; ensembling; model merging; parameter fusion; CNN.*

1. INTRODUCTION

Traditional model merging approaches, such as parameter averaging, are simple and computationally efficient but rely on the assumption that model parameters occupy similar regions in weight space. In practice, model trained independently often diverge to different local minima. Directly averaging their weights can lead to destructive interference, resulting in degraded accuracy. Similarly, logit ensembling can achieve strong performance but has the overhead of running all models separately and then combining the results, limiting practicality.

Recent work in machine learning theory suggests that the training trajectory of a model can be viewed as a dynamical system evolving in a high-dimensional manifold [1]. From this perspective, merging different versions of the same model, from different epochs of independent runs, can be seen as combining different points along this manifold. Traditional linear interpolation neglects the temporal and nonlinear dependencies between these points. In contrast, fractional calculus provides a mathematical framework for modelling systems with memory and nonlocal behaviour, offering a richer representation of the relationships between model states. In this paper, we propose Fractional Parameter Fusion (FPF), a new technique for merging CNN versions based on fractional differential operators. The central idea is to treat the sequence of model weights as a discrete signal indexed by training progress and apply a fractional derivative operator to interpolate between them. This enables smoother and more coherent parameter blending.

2. CONTENT

The methodology of this paper focuses on three distinct merging strategies: (1) logit ensemble, (2) weight averaging, and (3) fractional parameter fusion. Each method combines multiple versions of the same CNN model but with either temporal or stochastic variations

The logit ensemble method operates at the prediction level. Given a set of trained models $\{f_i(x)\}_{i=1}^{N}$, each producing logits for the input x, the ensemble prediction is computed as:

$$y_{LE} = \frac{1}{N}\sum_{i=1}^{N} f_{i(x)} \tag{1}$$

This approach averages decision-level outputs, yielding stable predictions but requires multiple forward passes during inference

The resulting model is structurally identical to its components but relies on the assumption that the models occupy approximately the same space in the loss landscape. When this assumption is violated, the merged model may preform worse than any individual constituent.

The proposed Fractional Parameter Fusion introduces a non-integer order interpolation between model parameters. We treat the sequence of model weights $\{W_i\}$ as discrete signal evolving over training time. Using the Grünwald-Letnikov definition of the fractional derivative [2], the fractional differential operator D^{α} acting on a discrete sequence is expressed as:

$$D^{\alpha}W_i = \sum_{k=0}^{K}(-1)^k\binom{\alpha}{k}W_{i-k} \tag{3}$$

The operator introduces memory across past model states, allowing the merged model to encode historical information about the training trajectory.

The final merged model is obtained as a weighted contribution of these fractional derivatives:

$$W_{FPF} = \sum_{i=1}^{N}\omega_i D^{\alpha}(W_i) \tag{4}$$

Where ω_i are blending coefficients. The fractional order α governs how strongly earlier versions influence the merged model. This formulation allows FPF to merge models obtained either from the same training run (capturing temporal continuity across epochs) or from independent runs (capturing stochastic diversity).

3. CONCLUSIONS

This paper introduced Fractional Parameter Fusion (FPF), a framework for merging multiple CNN model versions using concepts from fractional calculus. By treating the evolution of model parameters as a discrete temporal process, FPF employs non-integers order differential operator to capture long-range dependencies and memory effects between successive model states. When applied to both intra-run and inter-run fusion scenarios on the CIFAR-10 dataset, FPF demonstrated its potential to improve accuracy metrics while maintaining computational efficiency at inference time.

References

[1] Zhang, Yukun, and Qi Dong. "Dynamic Manifold Evolution Theory: Modeling and Stability Analysis of Latent Representations in Large Language Models." *arXiv preprint arXiv:2505.20340* (2025).

[2] Scherer, Rudolf, et al. "The Grünwald–Letnikov method for fractional differential equations." *Computers & Mathematics with Applications* 62.3 (2011): 902-917.

FRACTAL PARAMETER STEGANOGRAPHY: ENCODING INFORMATION IN THE MATHEMATICS OF IMAGES

Teodora-Georgiana BANU[1], Elena-Sorina NICULĂESA, Emil SIMION[1,2]

[1]National University of Science and Technology POLITEHNICA Bucharest, 313 Splaiul Independenței, District 6, Bucharest, Romania
[2]Department of Mathematical Methods and Models, Centre for Research and Training in Innovative Techniques of Applied Mathematics in Engineering, Bucharest, Romania

Corresponding authors email: banu.teodora21@gmail.com, niculaesa.sorina20@gmail.com

Abstract
Steganography is the art of concealing information within ordinary data, traditionally by modifying digital media such as images, audio, or video. Although effective, such methods are often vulnerable to steganalysis, compression artifacts, or format conversions. This paper proposes a conceptual shift: instead of hiding information in the image itself, the data is embedded in the mathematical parameters that generate the image. Using the Julia set fractals as a model, the method encodes binary data in high-precision numerical parameters that control fractal generation. Each parameter can be slightly perturbed within a precision of 2^{-24} to 2^{-26}, representing encoded bits while keeping the resulting fractal visually indistinguishable from the original. The data is encrypted using AES-GCM, then permuted according to a key. The hidden information thus resides entirely in the parametric domain rather than in the image pixels. The implementation demonstrates both the potential and the limitations of this approach, showing that while it achieves complete invisibility and resistance to conventional steganalysis, the encoded data cannot be recovered from the image alone.

Key words: *steganography; fractals; Julia set; information hiding; cryptography; mathematical modeling; digital art.*

1. INTRODUCTION

The field of steganography has evolved from simple pixel-based manipulations to more sophisticated mathematical and algorithmic approaches. Traditional digital image steganography techniques hide secret messages within the least significant bits (LSB) of pixels, which allows for large payloads but leaves detectable traces under forensic analysis or statistical tests. Furthermore, such methods are fragile when the carrier image undergoes transformations such as compression, scaling, or format conversion.

In this context, fractal parameter steganography introduces a fundamentally new direction. The core idea is to hide information not in the rendered pixels of an image, but in the mathematical parameters that generate it. Fractals, especially those belonging to the Julia and Mandelbrot families, are governed by iterative complex equations that are extremely sensitive to parameter variations. This sensitivity is exploited here as a medium for information embedding. By making minute, high-precision changes to the parameters — on the order of 2^{-24} or smaller — it is possible to encode binary data without inducing any perceptible alteration in the fractal's rendered appearance. Thus, the image itself remains identical to human vision and to most signal-domain analyses.

This paradigm shift brings steganography into a new mathematical domain, one that is independent of digital signal processing limitations. The following sections describe the encoding procedure, experimental setup, and results obtained using a Python implementation of this concept.

2. CONTENT

The proposed implementation is based on the Julia set, defined by the iterative complex equation $z_{n+1} = z_n^2 + c$, where c is a complex constant controlling the structure of the fractal. A base set of parameters defines the original image: the real and imaginary parts of c, the center coordinates, the zoom scale, and the maximum iteration count. To embed information, each of these parameters is perturbed by a very small delta (Δ), representing an encoded subset of bits.

Before embedding, the plaintext message is compressed and encrypted using AES-GCM algorithm. This ensures both confidentiality and integrity of the payload. The encryption key is derived from the user's password through a one-way hash function combined with a randomly generated salt. The encrypted data is then converted to a bit sequence and distributed among the delta values using a pseudorandom permutation based on the same password-derived key. Each JuliaRecipe data structure in the Python implementation can store approximately 110 bits of information. For longer messages, the data is split into multiple recipes, each corresponding to a slightly modified fractal instance. The encoded parameters are stored in JSON format to enable perfect reconstruction and decoding.

To further analyze the results, three comparative visualizations were generated in order to assess the visual and statistical effects of parameter embedding. In the figure below, the original fractal image is compared with the encoded version and with their RGB difference map. It can be observed that the two images are visually identical, with no perceptible distortion or colour deviation introduced by the embedding process. The difference map confirms that the perturbations applied to the fractal parameters remain below the visible threshold, ensuring the complete imperceptibility of the hidden message.

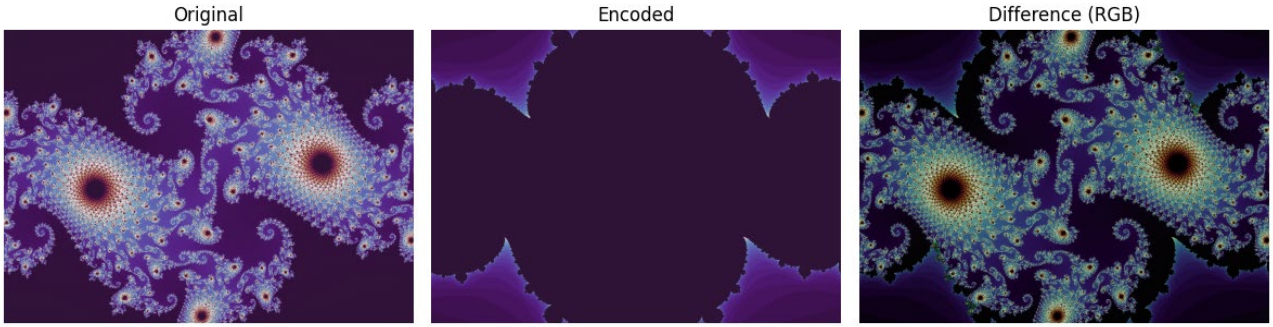

Figure 1. Comparison between the original, encoded fractal images and their RGB difference map

In the following figure, the statistical distributions of pixel intensities and escape-iteration counts are presented. Both histograms maintain an almost identical profile, indicating that the encoding process does not distort the natural dynamics of the Julia set generation. This stability of the distributions demonstrates that the hidden data modifies only the underlying numerical precision of the parameters, without affecting the global visual or statistical structure of the fractal image.

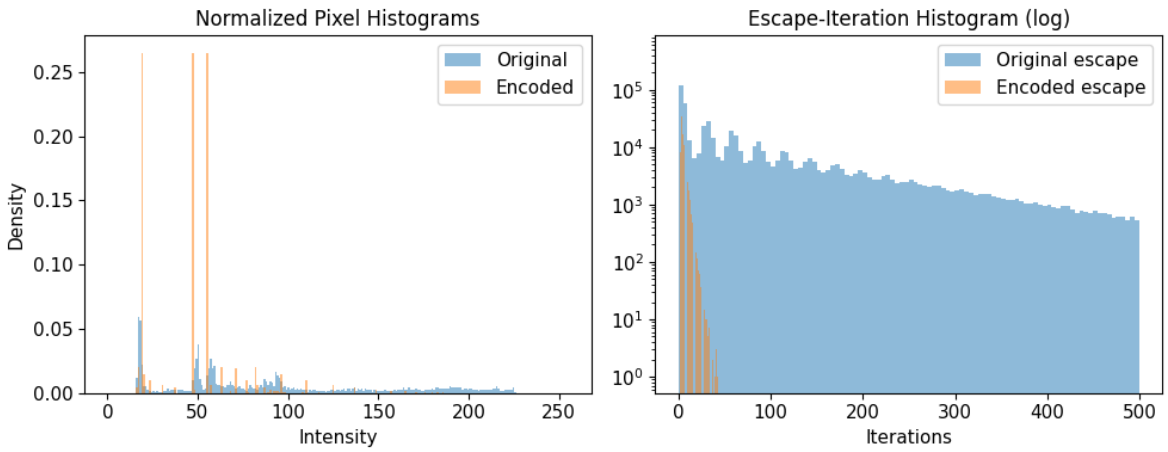

Figure 2. Normalized pixel intensity and escape-iteration histograms

A more detailed numerical perspective is offered in the next figure, where the $\Delta - iteration$ heatmap reveals the internal computational differences between the two fractals. Although these variations are mathematically measurable, they remain invisible in the rendered output, being distributed harmoniously within the fractal geometry itself. This proves that the message is embedded at the parameter level rather than in the visual texture, representing a true parametric steganographic process.

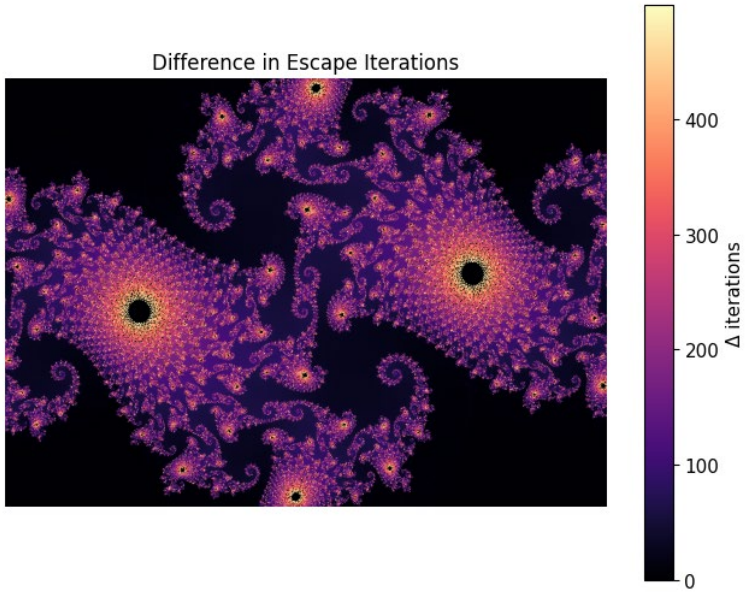

Figure 3. $\Delta - iterations$ heatmap showing internal parameter differences

The quantitative evaluation confirms these observations. For an encoded image of 900×640 pixels, the embedding capacity reaches 110 bits per recipe, while the Peak Signal-to-Noise Ratio (PSNR) and the Structural Similarity Index (SSIM) register values of 10.13 dB and 0.374074 respectively. Despite the measurable numerical deviations, the image remains visually unchanged, confirming that the embedding of encrypted data within fractal parameters preserves complete perceptual fidelity.

```
Capacity_per_recipe_bits: 110
PSNR_dB: 10.13
SSIM: 0.374074
Image_size: 900x640
```

Figure 4. Quantitative metrics of the encoded fractal

Overall, these analyses demonstrate that the hidden information is located exclusively in the high-precision numerical space of the fractal parameters. The resulting images are visually indistinguishable from one another, yet correspond to distinct mathematical seeds that encapsulate the encrypted payload. Without access to the exact parameter configuration and the correct decryption password, the embedded message cannot be recovered, providing a double layer of protection that combines cryptographic robustness with visual invisibility.

3. CONCLUSIONS

Fractal parameter steganography extends the boundaries of information hiding by operating entirely in the parametric domain. Instead of modifying digital media at the pixel level, it embeds encrypted information in the numerical parameters that define a fractal image. The resulting image is a faithful visual reproduction of the original, indistinguishable both to the human eye and to statistical image analysis tools.

The method's advantages include complete visual transparency, resilience to compression and format conversion, and the ability to combine with modern cryptographic algorithms for enhanced confidentiality. Its limitations lie in the requirement for exact parameter recovery and the relatively low bit capacity per fractal recipe. However, for small payloads such as cryptographic keys, metadata, or authentication tags, the method is highly suitable.

Beyond its technical value, the approach also illustrates an intersection between mathematics, art, and computer science. It demonstrates how abstract mathematical constructs like fractals can act as carriers of digital information, blurring the line between data encoding and creative visualization. Future work may explore multi-fractal embeddings, adaptive bit allocation, and integration with procedural graphics engines to achieve larger capacities while preserving invisibility.

One compelling use case is the secure embedding of cryptographic keys, blockchain metadata, or authentication tokens directly into visual artifacts, enabling dual-purpose media that functions both aesthetically and as a secure data container. This approach could be leveraged in digital art authentication and NFT provenance, where the fractal parameters serve as an immutable and visually invisible signature tied to ownership or identity.

In conclusion, fractal parameter steganography provides both a secure and conceptually elegant medium for hidden communication, representing an innovative educational tool and a novel research direction within information security and digital art.

A COMPREHENSIVE REVIEW OF CONVEX FUNCTIONS: CLASSIFICATIONS, PROPERTIES, AND APPLICATIONS

Valeria Șutu _Cîrlan[1, 2]

[1]University Politehnica of Bucharest, 313 Splaiul Independentei, District 6, Bucharest, Romania
[2]"Ștefan cel Mare" University of Suceava, 13 University street, Suceava, Romania

valeria.sutu_cirlan@yahoo.com

Abstract

The theory of convex functions represent one of the most fundamental and rich areas in mathematical analysis and has significant impact in optimization theory, functional analysis, and applied mathematics. Our study offer a systematic classifications of various types of convex functions, exploring their theoretical foundations, characterizations, and practical applications. We examine classical convex functions along their numerous generalizations, such as s-convex, η-convex functions, h-convex, harmonically convex, logarithmically convex, strongly convex functions, among others. Corroborating existing literature, our work illustrate their relationships, similarities, and directions between different classes of convex functions, providing researchers with a unified framework for understanding these mathematical structures. Our analysis expose how various convexity concepts emerge naturally from different mathematical contexts and evidence their interconnected nature. This classification serves as a valuable resource for optimization practitioners, and researchers working in related fields, facilitating better understanding and application of convex function theory.

Key words*: convex functions, s-convex, η-convex functions, h-convex, harmonically convex, logarithmically convex, strongly convex functions, duality, optimization*

1. INTRODUCTION

The theory of convex functions is a cornerstone of contemporary mathematical analysis, strongly bonding deep geometric intuitions and rigorous analytical frameworks. These functions are not merely abstract constructs; they encapsulate the variational basis of numerous disciplines, ranging from the calculus of variations and nonlinear PDEs to modern optimization, machine learning, and information theory (Rockafellar, 1970; Borwein & Vanderwerff, 2010). Far from being monolithic, convex functions open a spectrum of complexity that mirrors the structural richness of the functional spaces on which they are defined. Their classification constitutes both a practical necessity and a profound theoretical endeavor (Boyd & Vandenberghe, 2004; Bauschke & Combettes, 2017).

The convex analysis lies the notion of convexity to functions: mappings from vector spaces (often Banach or Hilbert spaces) into the extended real line whose epigraphs are convex sets. While seemingly simple, this definition carries a vast analytic depth, bridging topological, geometrical, and variational perspectives (Ekeland & Temam, 1999; Brézis, 2010). Convexity in infinite dimensional spaces is nuanced by weak topologies, duality pairings, and the geometry of functional spaces, such as reflexive Banach spaces and uniformly convex Hilbert spaces (Rudin, 1991; Barbu & Precupanu, 2012). The toolkit here is vast and subtle: Hahn–Banach separation theorems, Fenchel–Legendre transforms, and monotonicity theory form the backbone of many later classifications (Fenchel, 1949; Moreau, 1965). These foundational results are not isolated curiosities but are deeply embedded in variational formulations, optimal transport, and even equilibrium theories in physics and economics.

2. CONTENT

Convex functions are not a homogeneous types. Their classification grounded on a host of properties: lower semicontinuity, differentiability (in various senses), strict, lower and strong convexity, as well as representability via dualization techniques such as the Legendre–Fenchel transform (Rockafellar, 1974; Clarke, 1983). Lower semicontinuity, for example, ensures the attainment of minima under coercivity, a principle central to the direct method in the calculus of variations (Minty, 1962; Fitzpatrick, 1988). Equally, one distinguishes between functions operating over classical Sobolev or BV spaces and those defined in the context of measure theory or abstract metric spaces, where standard tools may no longer apply (Villani, 2003). With the development of convexity in nonlinear spaces, particularly Hadamard spaces, novel notions of geodesic convexity and non-smooth analysis have emerged (Treanță, 2015). Differentiability categories, such as Gâteaux versus Fréchet differentiability, are essential in understanding not just regularity, but the very geometry of the minimization landscape (Luenberger, 1997; Hiriart-Urruty & Lemaréchal, 2001).

A refined typology of convex functions reveals multiple intersecting families. Strict convexity, often invoked to guarantee uniqueness of minimizers, is indispensable in both theoretical analysis and computational algorithms (Borwein & Vanderwerff, 2010). Strong convexity introduces a modulus that quantifies curvature, yielding robust convergence properties and error bounds in numerical optimization (Nesterov, 2003). Polyhedral and sub linear functions, often arising in piecewise linear settings, connect with dual polyhedral geometry and support function representations (Clarke, 1983; Aubin & Frankowska, 2009). Meanwhile, theoretic formulations such as entropy, information divergence, and transport energies, suggest deep involvement between convex analysis, geometry, and probability (Santambrogio, 2015; Peyré & Cuturi, 2019).

The duality of convex functions theory lies in the Fenchel–Moreau theorem: every proper, lower semicontinuous convex functional is the biconjugate of its convex conjugate (Fenchel, 1949; Rockafellar, 1974). This result is foundational. Duality theory facilitates the transition between primal and dual variational formulations, often simplifying complex constrained problems into solvable dual ones (Ekeland & Temam, 1999). Subdifferential calculus, maximal monotonicity, and the geometry of dual cones are deeply woven into this framework (Fitzpatrick, 1988). Moreau's decomposition theorem and vaste theory offer operational mechanisms for regularization and projection in convex settings (Moreau, 1965). In nonlinear metric contexts like Hadamard spaces, these tools require significant generalization, and recent advances, such as those by (Treanță, 2015) and many others analogues.

3. CONCLUSIONS

This review has light the huge and complex taxonomy of convex functions, grounding their classification in rigorous mathematical frameworks while highlighting their vast applicability. From duality theory to the concrete exigencies of numerical optimization and variational modeling, convex functions serve as a connective tissue across diverse domains. Recent explorations, especially in non-Euclidean and geometric contexts such as Hadamard spaces, underscore the vitality and evolution of this field (Rockafellar, 1970; Treanță, 2015; Ekeland & Temam, 1999). The journey from epigraphs to entropy, from sub-differentials to geodesics, reveals not just a theory, but a dynamic, unifying vision of mathematical structure and its application.

INTEGER MATRICES THAT LEAVE REMARKABLE FUNCTIONS INVARIANT

Vasile POP[1]

[1]Technical University of Cluj-Napoca, C. Daicoviciu 15, 400020 Cluj-Napoca, Romania

Corresponding author email: vasile.pop@math.utcluj.ro

Abstract

In the last 10 years, various mathematical competitions have featured several linear algebra problems requiring the determination of matrices from $\mathcal{M}$ ($\mathbb{R}$), $\mathcal{M}$ ($\mathbb{C}$) or $\mathcal{M}$ ($\mathbb{Z}$) that are invariant under certain functions of n variables. In most studied cases, the sought-after sets form important algebraic structures, like finite groups or classical matrix groups. In this paper, we study several classes of such matrices that leave several remarkable functions invariant.

Key words: *integer matrices; invariant; matrix groups; mathematical competitions.*

1. INTRODUCTION

Let $n \in \mathbb{N}$, $n \geq 2$. We denote $\mathcal{M}_{n,1}(\mathbb{Z}) = \mathbb{Z}^n = \{X = [x_1 x_2 \dots x_n]^t, x_1, x_2, \dots, x_n \in \mathbb{Z}\}$.

Consider the functions $f_k: \mathbb{Z}^n \to \mathbb{Z}$, $k = 1,2,\dots,6$, defined by: $f_1(X) = \gcd\{x_1, x_2, \dots, x_n\}$ (O.N.M. 2018), $f_2(X) = \sum_{i=1}^{n} |x_i|$ (O.N.M. 2007), $f_3(X) = \max\{|x_i|, i = 1, n\}$ (SEEMOUS 2007), $f_4(X) = \sum_{i=1}^{n} x_i^2$ (G.M.A. 2008), $f_5(X) = \sum_{i=1}^{n} x_i$, $f_6(X) = \prod_{i=1}^{n} x_i$.

We say that a matrix $A \in \mathcal{M}_n(\mathbb{Z})$ leaves the function f_k invariant if $f_k(X) = f_k(AX)$, for all $X \in \mathbb{Z}^n$. We denote by $G_k \subset \mathcal{M}_n(\mathbb{Z})$ the set of matrices that leave the function f_k invariant.

The purpose of this paper is to characterize or explicitly determine the sets G_k, $k = 1,2,\dots,6$.

2. MAIN RESULTS

Theorem 1. A matrix $A \in \mathcal{M}_n(\mathbb{Z})$ leaves the function f_1 invariant if and only if $\det A \in \{-1, +1\}$.

Corollary 1. $G_1 = (\mathrm{GL}_n(\mathbb{Z}), \cdot)$.

Theorem 2. Fix $k \in \{2,3,4\}$. A matrix $A \in \mathcal{M}_n(\mathbb{Z})$ leaves the function f_k invariant if and only if it has exactly one non-zero element, equal to +1 or -1, in each row and each column.

Corollary 2. $G_2 = G_3 = G_4 = (\mathrm{O}_n(\mathbb{Z}), \cdot)$, the multiplicative group (with $2^n n!$ elements) of orthogonal matrices ($A \cdot A^t = A^t \cdot A = I_n$), which is a subgroup of $(\mathrm{GL}_n(\mathbb{Z}), \cdot)$.

Theorem 3. A matrix $A \in \mathcal{M}_n(\mathbb{Z})$ leaves the function f_5 invariant if and only if the sum of the entries in each column is equal to 1.

Remark 1. G_5 is infinite and does not form a group in either $\mathcal{M}_n(\mathbb{Z})$ or $(\mathrm{GL}_n(\mathbb{Z}), \cdot)$.

Theorem 4. A matrix $A \in \mathcal{M}_n(\mathbb{Z})$ leaves the function f_6 invariant if and only if on each row and on each column, there is exactly one nonzero entry equal to 1 or -1, and the number of entries equal to -1 is even.

Corollary 3. G_6 is a multiplicative group (with $2^{n-1} n!$ elements) and a subgroup of $(\mathrm{GL}_n(\mathbb{Z}), \cdot)$.

3. REFERENCES

[1] *Gazeta Matematică Seria B*: the Supplement of the National Mathematics Olympiad, Satu Mare, 2018 (in Romanian).

[2] *Gazeta Matematică Seria B*, 2007 (6), p. 283-295: The National Mathematics Olympiad 2007, 11th grade, problem 3 (in Romanian).

[3] *South Eastern European Mathematical Olympiad for University Students* - SEEMOUS 2007: problem 2 (https://www.massee-org.eu/mathematical/seemous/item/21-seemous-2007-cyprus)

[4] Vasile Pop, *Linear Isometries in* $\mathbb{R}^n$ *and* $\mathbb{C}^n$ (in Romanian). Gazeta Matematică Seria A, 2008 (4), pp. 308-314.

[5] Vasile Pop (coordinator), *Topics and Problems for Student Mathematics Competitions*, vol. 1 (problems 3.27, 3.28), Studis Publishing, Iași, 2013 (in Romanian).

An Application of Perron–Frobenius Theory for Positive Matrices

Vlad-Andrei PERPELEA

University of Bucharest, The Faculty of Mathematics and Computer Science, 14 Strada Academiei, District 5, Bucharest, Romania

Corresponding author email: perpelea.vlad@gmail.com

Abstract

We present an example illustrating how existing restrictions on the form of a matrix can yield substantial information when combined with appropriate analytical tools. An initial approach based on elementary algebraic manipulations and maximality principles provides a correct solution but offers limited insight into the matrix's structure. In contrast, by applying the Perron–Frobenius Theorem, we demonstrate how one can extract meaningful information about the eigenvalues and eigenvectors of a positive matrix solely from its form. The Perron–Frobenius Theorem plays a central role in the study of positive matrices and has led to significant results in both theoretical and applied mathematics, including Markov chain theory and the PageRank algorithm. This paper aims to illustrate how the theorem provides deep insight into the intrinsic properties of positive matrices, information that would otherwise remain inaccessible through basic algebraic methods.

Key words*: positive matrices, Perron–Frobenius theorem, linear algebra, spectral radius, eigenvalues.*

1. INTRODUCTION

The Perron–Frobenius Theorem is a fundamental result in the study of positive matrices, with numerous consequences that allow one to derive deep structural properties of such matrices. In many disciplines, including probability theory, statistics, and algorithmic analysis, the theory of positive matrices has proven essential to solving major problems, notably in Markov chain theory and the PageRank algorithm. The purpose of this paper is to illustrate how the Perron–Frobenius Theorem can be employed to extract additional information about a matrix based solely on its positivity. To this end, we examine a problem involving positive matrices and vectors, presenting two approaches: a classical method that provides a correct solution but no further structural insight, and an approach grounded in the theory of positive matrices, which reveals substantial information about the matrix's internal structure.

2. CONTENT

Our application focuses on the following problem:

Let $A \in M_n(\mathbb{R})$ be such that all entries are strictly positive real numbers, and let $\boldsymbol{u}, \boldsymbol{v} \in \mathbb{R}^n$ be two vectors also with strictly positive elements, such that:

$$A\boldsymbol{u} = \boldsymbol{v} \; and \; A\boldsymbol{v} = \boldsymbol{u}$$

Prove that $\boldsymbol{u} = \boldsymbol{v}$.

The original solution splits the problem into two cases. The first case, where $\boldsymbol{u}$ *and* $\boldsymbol{v}$ are linearly dependent and then the second case where they are linearly independent.

This solution only utilizes elementary ideas and relations and does not dive so deep into the theory of positive matrices and advanced linear algebra.

The second solution we present looks at the problem from the point of view of the theory of positive matrices and gives deeper insight into the relations between the given problem and the spectrum of the matrix A, thus highlighting the utility of the Perron-Frobenius Theorem for positive matrices.

We will first state the problem we want to analyze.

After this we will look at the first solution to the problem.

After the first solution we will give the statement for the Perron-Frobenius Theorem for Positive Matrices.

And finally, we will present the second solution to the problem utilizing the previously discussed theorem.

3. CONCLUSIONS

By exploiting the particular form of the given matrix and vectors we can derive a lot of information about the spectrum of the matrix utilizing the rich theory of positive matrices and the Perron-Frobenius Theorem. The Perron-Frobenius Theorem provides a foundation for the study of eigenvalues and eigenvectors of positive matrices as can be seen in the example we presented. This emphasizes how important it is to consider the information that can be extracted from the restrictions present on a given matrix's form.

BIBLIOGRAPHY

1. S. Axler, *Linear Algebra Done Right*, Springer, 2024.
2. R.A. Horn, C.R. Johnson, *Matrix Analysis*, Second Edition, Cambridge University Press, 2012.
3. A. Negrescu, *Algebră liniară. O abordare prietenoasă*, Editura Politehnica Press, 2023.
4. V. Pop, *Algebră liniară şi geometrie analitică*, Editura Mega, 2017.